PREDICTIONS OF THE INELASTIC SEISMIC RESPONSE OF CONCRETE STRUCTURES INCLUDING SHEAR DEFORMATIONS AND ANCHORAGE SLIP

by

NESTOR ROBERTO RUBIANO-BENAVIDES

Ingeniero Civil, Magister en Ingenieria Civil, M.S.E.

DISSERTATION

Presented to the Faculty of the Graduate School of

the University of Texas at Austin

in Partial Fulfillment

of the Requirements

for the Degree of

DOCTOR OF PHILOSOPHY

THE UNIVERSITY OF TEXAS AT AUSTIN

August 1998

PREDICTIONS OF THE INELASTIC SEISMIC RESPONSE OF CONCRETE STRUCTURES INCLUDING SHEAR DEFORMATIONS AND ANCHORAGE SLIP

Approved by

Dissertation Committee:

Michael E. Kreger, co-supervisor

Jose M. Roesset, co-supervisor

Kenneth H. Stokoe

Ramon Carrasquillo

Ronald O. Stearman

To the woman who left her career, her family and
her country to become my ‘compañera’

To ‘those two little fellows’:
Néstor Raul and Paulo Julián

A mis padres, por el cariño y soporte
durante todos estos años.

ACKNOWLEDGMENTS

The computer program developed as part of this research was based on that written by Dr. Pablo Armendariz who, in turn, used code originally implemented by Dr. Chryssis Papaleontiou, both former doctoral students at the Department of Civil Engineering of the University of Texas at Austin.

The support, guidance and fellowship given by Dr. Michael E. Kreger and Dr. Jose M. Roesset during the course of this research is deeply appreciated.

Many thanks are also extended to Dr. Kenneth H. Stokoe, Dr. Ramon Carrasquillo and Dr. Ronald Stearman for serving in the doctoral committee.

The author is indebted to the Department of Civil Engineering of the University of Texas at Austin for the continuous support given to him during his doctoral studies through a Teaching Assistantship.

The author also wishes to express his gratitude to the "Fundación para el Futuro de Colombia, COLFUTURO", for granting him a license to continue his doctoral studies before returning to Colombia.

Nestor Roberto Rubiano-Benavides
August, 1998

PREDICTIONS OF THE INELASTIC SEISMIC RESPONSE OF CONCRETE STRUCTURES INCLUDING SHEAR DEFORMATIONS AND ANCHORAGE SLIP

Publication No.________

Nestor Roberto Rubiano-Benavides, Ph.D.
The University of Texas at Austin, 1998
Supervisors: Michael E. Kreger and Jose M. Roesset

The behavior of reinforced concrete frame structures under seismic loads is analyzed using a number of mathematical models of increasing levels of complexity. The first model, represented by the program DRAIN-2DX, idealizes plasticity in members as concentrated at the member ends and governed by a simple elastoplastic hysteretic rule with no strength or stiffness degradation. The second model, implemented in program IDARC2D, permits yield penetration into the member and accounts for stiffness and strength degradation as well as pinching of the hysteresis loops. The last model is based on a fiber formulation and is implemented in the program FIBERC.

Several large-scale member and frame laboratory specimens are analyzed with the three models under static and dynamic loading. It was found that in general the beam-column element of program DRAIN-2DX does not reproduce well the member behavior, particularly in terms of stiffness and energy dissipation. In contrast, program IDARC2D generally provides a good estimate of member and frame behavior, including pinching of the hysteresis loops, thanks to a set of parameters used to adjust the predicted response. Finally, program FIBERC simulates closely the member response when it is governed primarily by flexure and axial forces. It does not, however, provide good predictions when pinching of the hysteresis loops occurs.

To extend and improve the performance of the fiber element model implemented in program FIBERC, a simple model that accounts for the effects of shear deformations is added. Such a model is based on a truss analogy of the cracked structural members. A series of runs using some of the members and frames studied previously is performed to assess the validity of the model as well as its influence on the predicted response.

Additionally, a model that estimates the effects of anchorage slip on member deformation and stiffness is introduced into the program. Again, a series of runs is performed on the same specimens to evaluate the effectiveness of the model as well as the impact on the computed response.

TABLE OF CONTENTS

CHAPTER 1

CHAPTER 2

CHAPTER 3

CHAPTER 4

CHAPTER 5

CHAPTER 6

CHAPTER 7

APPENDIX A

APPENDIX B

CHAPTER 1

Introduction

1.1 General Remarks

A large number of nonlinear models have been developed and used in research to compute the inelastic dynamic behavior of reinforced-concrete building structures subjected to earthquake excitation. One of the most common of such models considers localized yielding at the ends of the members (point hinges) and is represented by the computer program DRAIN-2D, which is widely used in practice. Another example uses again point hinges for linear members, but adds the possibility of spreading of yielding through a fiber model in certain elements. This model is represented by the computer program IDARC which has been gaining acceptance and more widespread use. The third approach to be considered in this work is a complete fiber model. In this case, all the elements of the structure are divided into a number of segments composed of longitudinal fibers. Yielding can spread all along these elements.

Studies of the seismic response of structures in the time domain using complete fiber models and accounting for combined horizontal and vertical seismic excitations have been conducted previously by Papaleontiou (1-12) for steel frames and by Armendariz (1-3) for high-strength concrete frames. A computer program originally developed by Papaleontiou and then extended by Armendariz was used to evaluate the dynamic response of concrete structures.

1.2 Earlier Studies Using Fiber Formulations

Several studies have used fiber formulations in the past. The studies by Latona (1-8), Adams (1-1) and Mark (1-11) at MIT are among the initial applications of the method to static and dynamic analysis of steel and concrete frames. Park, Paulay and their associates (1-13, 1-14) at the University of Canterbury in New Zealand have used the fiber model to study Reinforced Concrete Sections. More recently Mahin and his associates (1-5, 1-6, 1-

18) and Filippou and his associates (1-16) at the University of California, Berkeley, have used the fiber model to analyze reinforced concrete sections and members under static and dynamic loads. The versatility of this approach is further demostrated by its application to the analysis of composite steel concrete conducted by Kim and Lu (1-7).

1.3 Previous Research Work

Papaleontiou developed the program *Fiber* to predict the inelastic dynamic behavior of steel building structures under seismic loads using a fiber formulation. He compared this response in the linear range to those obtained by frequency-domain, time-domain and modal analyses. He used an elastoplastic (bilinear) model to simulate the stress-strain behavior of the steel fibers.

Armendariz extended the *Fiber* program to enable analysis of reinforced concrete buildings. The new program was named *FEP*. He developed several mathematical models to predict the cyclic stress-strain response of concrete and steel following the findings and proposed models of other researchers. Then, he conducted a series of analyses comparing the theoretical prediction of these models to the experimental response of standard concrete cylinders and reinforcing steel coupons subjected to repeated and cyclic loads.

Yu (1-17) used the program *FEP* to analyze the effect of vertical earthquake accelerations in the response of bridges.

1.3.1 Material Models

Several models such as those proposed by Mander et al. (1-10), Ahmad and Shah (1-2) and Madas and Elnashai (1-9) were considered by Armendariz for modelling the hysteretic behavior of concrete. The model by Mander (1-10) for concrete was found to predict closely the cyclic experimental results (for normal- and high-strength concrete) using few parameters and fewer computations than the other models. Although the Mander model produces a stiffer initial response, the subsequent cycles of repeated loading are predicted reasonably well.

As for the reinforcement, a bilinear model with kinematic hardening, a modified bilinear model, and a model based on the Richard-Abbott equation (1-15) were considered and used by Armendariz to predict the results of repeated and cyclic loading of low- high- and ultra high-strength steel coupons. In general, the bilinear and modified-bilinear models predict poorly the cyclic response primarily because of their inability to model the Bauschinger effect. However, for cases involving small strains and repeated loading (no reversals of load), these two models provide a good prediction. The model based on the Richard and Abbott equation (1-15) produces a close prediction to both the repeated and cyclic behavior of all types of steel.

1.3.2 Moment Curvature Behavior of Sections

Moment-curvature analysis of several reinforced concrete beam sections were conducted by Armendariz. Initially, a parametric study was performed in which the optimum number of concrete fibers and increment in curvature for analysis were investigated. With as little as 10 concrete fibers, the experimental moment-curvature behavior of several sections could be reproduced closely. Also, close simulation was obtained when the curvature increment was between $\phi_y/50$ and $\phi_y/100$, where ϕ_y is the curvature at first yield of the section.

Three sets of simply-supported beams under concentrated loads were selected by Armendariz to evaluate the accuracy of the fiber model to predict their moment-curvature behavior using the Mander model for the concrete fibers and the Richard-Abbott and bilinear models for the steel fibers. In general, the moment-curvature response of the beams was predicted well when the Richard-Abbott model was used. However, using that model, the peak moments were occasionally overestimated. Peak moments were always closely predicted when the bilinear models were used, but the theoretical reloading branches were very different from the experimental reloading branches.

An additional parametric study at this stage demonstrated that the fiber formulation reproduces the effects of an axial force on the section, such as the increase in moment capacity and the pinching of hysteresis loops. Furthermore, it was found that if the tensile strength of concrete is accounted for, the moment capacity is significantly overestimated. In order to correct this problem, an iteration scheme must be applied once the section has cracked. Armendariz concluded that tensile strength should better be neglected.

1.3.3 Load-Displacement Behavior of Members

Using the Mander model for concrete fibers and both the bilinear and Richard-Abbott models for the reinforcing bars, a series of load reversals on beam subassemblages was simulated by Armendariz and compared to experimental results obtained by different researchers. For these analyses, members were divided into 19 sections and each section was discretized into 20 concrete fibers. Due to numerical problems in the algorithm, Armendariz did not include the descending branch of the concrete model and introduced a 1% post-yield stiffness in the steel stress-strain curve.

Results of three sets of cyclic tests on cantilever beams were simulated using the fiber formulation. Generally, the theoretical predictions were close to the experimental results. However, the peaks of the hysteretic response of some of the specimens were overestimated when the Richard-Abbott steel model was used. In contrast, peaks were usually predicted well when the bilinear model was used, in spite of the poor prediction of the overall shape of the hysteresis loops.

1.3.4 Time-Domain Dynamic Behavior of Frames

Finally, Armendariz conducted a series of simulations in the time domain of the response of several complete structures subjected to earthquake ground motions. However, the actual response of the structures was generally unavailable, and thus, verification of the program predictions was not possible. Nevertheless, many features of the program were evaluated. For these runs, the Mander model for concrete fibers and the modified bilinear model for steel were used. The frames studied were two one-bay one-story frames, one one-bay three-story buiding frame, and one three-bay ten-story building frame.

Top displacement of the frames and the internal forces on certain columns were used as control variables. Several parametric studies were conducted in order to evaluate the effect on response of the time increment used in the computation, mass matrix formulation (lumped or consistent), step-by-step integration scheme, damping model (mass-proportional, stiffness-proportional or Rayleigh), type of ground motion (horizontal, vertical, or both), concrete compressive strength (normal- or high-strength), etc.

Results obtained by Armedariz indicated that the optimum time increment was 0.001 sec. This means that if a smaller time increment is used, the program will yield the same prediction. On the other hand if a larger time step is used, results will differ.

Slight differences in response, if any, were observed by changing the mass matrix formulation. When lumped masses were used, the displacement amplitude tended to increase; and when consistent masses were used, higher axial forces in columns were obtained.

Two different step-by-step integration methods were considered: the Constant Average Acceleration and the Central Difference Formula. Similar responses were obtained for both integration schemes.

For one of the one-bay one-story frames all damping models gave the same prediction. This was interpreted as meaning that the response was controlled by the fundamental mode. For the one-bay three-story frame studied, when the mass-proportional damping idealization was considered, a smaller displacement amplitude was observed as compared to when stiffness-proportional damping was included.

For several of the frames the concrete compressive strength was arbitrarily increased from 5 ksi to 12 ksi. However, no change in member dimensions or reinforcement was performed. In general, significant reductions in the displacement amplitude took place as the strength was increased. Internal member forces increased in cases and decreased in others. Finally, the response of some of the frames to different types of ground motions was investigated.

1.4 Objectives and Scope of this Study

The main overall objective of this research study is to improve the state-of-the-art modeling of the dynamic inelastic behavior of reinforced concrete structures subjected to earthquake ground motions. For this purpose, several specific objectives are to be met:

a. Verify the response obtained by the existing program *FEP* as developed by Armendariz and then, introduce corrections and/or modifications to the program as necessary.

b. Compare the performance of program *FEP* to that of other programs which have been previously calibrated with experimental results. Such programs should be based on phenomenological hysteretic rules or finite-element programs based on plasticity constitutive models.

c. Overcome current program limitations and introduce new modelling capacities. In particular, the following modelling capabilities are to be introduced:

    Inelastic shear deformations of beams and columns,

    Anchorage slip of reinforcing bars.

d. Perform a series of studies on large-scale specimens to evaluate the effect of those models on the response of members and frame structures.

CHAPTER 2

Fiber-Element Formulation for Dynamic Analysis

2.1 General Remarks

In the first two sections of this chapter, the theoretical development of the Fiber Element model is described including the step-by-step numerical integration of the dynamic equations of motion. The force-displacement relation of the members as well as the assembly of the member flexibility and stiffness matrices follow the original development by Latona (2-3) and are presented here in a concise form for completeness. Likewise, a brief presentation of the solution to the dynamic equations of motion developed by Armendariz (2-1) is given. The last section of this chapter introduces the material cyclic constitutive models for concrete and steel used throughout this study.

2.2 Member Incremental Stiffness Matrix

The analytical approach followed in this study to simulate the inelastic response of reinforced concrete building structures to seismic loads is based on the uniaxial stress-strain behavior of the materials, namely concrete and reinforcing steel.

At a given section of a frame element the section forces are given by

$$dN = \int_A d\sigma \, dA \tag{2.1}$$

$$dM = -\int_A d\sigma \, y \, dA \tag{2.2}$$

in which dN is the normal force and dM the bending moment acting on the section, while $d\sigma$ is the normal stress on the section. This stress is related to the strain at any point in the section by the following relation

$$d\sigma = E_T \, d\varepsilon \tag{2.3}$$

where E_T is the tangent modulus of elasticity. The strain is in turn a function of the curvature and the centroidal strain of the section as shown below

$$d\varepsilon = d\varepsilon_o - y\,d\phi \tag{2.4}$$

Replacing the expressions for stress and strain into the equilibrium equations, the final set of relationships relating forces and strains are obtained below

$$dN = \int_A \left(d\varepsilon_o - y d\phi\right) E_T \, dA \tag{2.5}$$

$$dM = -\int_A \left(d\varepsilon_o - y\, d\phi\right) y\, E_T \, dA \tag{2.6}$$

If the cross section is divided into n uniaxial fibers or filaments parallel to the longitudinal centroidal axis of the member, these expressions can be discretized as follows

$$dN = \sum_{i=1}^{n} E_{Ti} d\varepsilon_o A_i - \sum_{i=1}^{n} E_{Ti} y_i d\phi\, A_i \tag{2.7}$$

$$dM = -\sum_{i=1}^{n} E_{Ti} d\varepsilon_o y_i A_i + \sum_{i=1}^{n} E_{Ti}\, y_i^{\,2} d\phi\, A_i \tag{2.8}$$

where A_i is the area of fiber i, y_i is the distance from the centroid of the section to fiber i, and E_Ti is the tangent modulus of elasticity of fiber i.

For a given cross section, the centroidal strain and curvature are constants, and therefore, the previous expressions can be rearranged as

$$dN = d\varepsilon_o \sum_{i=1}^{n} E_{Ti}\; A_i - d\phi \sum_{i=1}^{n} E_{Ti}\; y_i\; A_i \tag{2.9}$$

$$dM = -d\varepsilon_o \sum_{i=1}^{n} E_{Ti}\; y_i A_i + d\phi \sum_{i=1}^{n} E_{Ti}\; y_i^{\,2} A_i \tag{2.10}$$

Finally, a matrix equality can be established using these two expressions

$$\begin{bmatrix} dN \\ dM \end{bmatrix} = \begin{bmatrix} a_{11} & a_{12} \\ a_{21} & a_{22} \end{bmatrix} \begin{bmatrix} d\varepsilon_o \\ d\phi \end{bmatrix} \tag{2.11}$$

where the matrix components are

$$a_{11} = \sum_{i=1}^{n} E_{Ti} \ A_i \tag{2.12}$$

$$a_{12} = a_{21} = -\sum_{i=1}^{n} E_{Ti} \ y_i \ A_i \tag{2.13}$$

$$a_{22} = \sum_{i=1}^{n} E_{Ti} \ y_i^{\ 2} \ A_i \tag{2.14}$$

In incremental form, the above matrix can be rewritten approximately as follows

$$\begin{bmatrix} \Delta N \\ \Delta M \end{bmatrix} = \begin{bmatrix} a_{11} & a_{12} \\ a_{21} & a_{22} \end{bmatrix} \begin{bmatrix} \Delta\varepsilon_o \\ \Delta\phi \end{bmatrix} \tag{2.15}$$

The increments of strain and curvature can then be found from the force increments by inverting the matrix of coefficients a_{ii} to obtain a new matrix of coefficients b_{ii} as shown below

$$\begin{bmatrix} \Delta\varepsilon_o \\ \Delta\varphi \end{bmatrix} = \begin{bmatrix} b_{11} & b_{12} \\ b_{21} & b_{22} \end{bmatrix} \begin{bmatrix} \Delta N \\ \Delta M \end{bmatrix} \tag{2.16}$$

These coefficients a_{ii} and b_{ii} are related by the following expressions (found by Cramer's rule):

$$b_{11} = \frac{a_{22}}{Det} \tag{2.17}$$

$$b_{12} = b_{21} = -\frac{a_{12}}{Det} \tag{2.18}$$

$$b_{22} = \frac{a_{11}}{Det} \tag{2.19}$$

where *Det* is the determinant of the first matrix,

$$Det = a_{11}a_{22} - a_{12}a_{21} \tag{2.20}$$

Equations 2.21 enforce equilibrium between the section forces and the forces at member end A (see Figure 2.1)

$$\begin{aligned} \Delta N &= -\Delta X_A \\ \Delta M &= x\left(\Delta Y_A\right) - \Delta M_A \end{aligned} \tag{2.21}$$

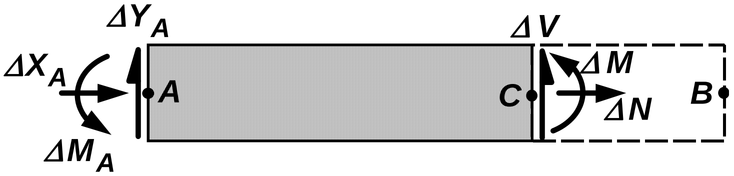

Figure 2.1 - Internal forces acting in Member

Therefore, a relationship can be drawn between the member end forces and the strain and curvature at any section along the member by combining Equations 2.16 and 2.21

$$\begin{bmatrix} \Delta\varepsilon_0 \\ \Delta\varphi \end{bmatrix} = \begin{bmatrix} b_{11} & b_{12} \\ b_{21} & b_{22} \end{bmatrix} \begin{bmatrix} -\Delta X_A \\ x\left(\Delta Y_A\right) - \Delta M_A \end{bmatrix} \tag{2.22}$$

Expanding Equation 2.22, separate expressions for the increments of strain and curvature are obtained

$$\Delta\varepsilon_o = -b_{11}\left(\Delta X_A\right) + b_{12}\, x\left(\Delta Y_A\right) - b_{12}\left(\Delta M_A\right) \tag{2.23}$$

$$\Delta\varphi = -b_{21}\left(\Delta X_A\right) + b_{22}\, x\left(\Delta Y_A\right) - b_{22}\left(\Delta M_A\right) \tag{2.24}$$

Using the definitions of these two variables, the axial and transverse displacements can be involved in the expressions developed so far.

$$\Delta\varepsilon_o = \frac{d\left(\Delta u\right)}{dx} \tag{2.25}$$

$$\Delta\varphi = \frac{d\left(\Delta\theta\right)}{dx} = \frac{d}{dx}\left[\frac{d}{dx}\left(\Delta v\right)\right] = \frac{d^2}{dx^2}\left(\Delta v\right) \tag{2.26}$$

Integrating the displacement differentials along the length of the member (from the initial end to the section under consideration)

$$\int_{\Delta u_a}^{\Delta u} d(\Delta u) = \int_0^x (\Delta \varepsilon_o)\, dx = \Delta u - \Delta u_A \tag{2.27}$$

In a similar fashion, the strains of Equation 2.23 are integrated from the member end to the cross section

$$\int_0^x (\Delta \varepsilon_o)\, dx = -(\Delta X_A)\int_0^x b_{11}\, dx + (\Delta Y_A)\int_0^x b_{12}\, x\, dx - (\Delta M_A)\int_0^x b_{12}\, dx \tag{2.28}$$

Then, equating the last two expressions, a direct relationship between member end forces and member end axial displacements is obtained in Equation 2.29.

$$\Delta u = \Delta u_A - (\Delta X_A)\int_0^x b_{11}\, dx + (\Delta Y_A)\int_0^x b_{12}\, x\, dx - (\Delta M_A)\int_0^x b_{12}\, dx \tag{2.29}$$

If this integral is carried out over the whole member, an expression relating the axial displacements at both member ends is found in Equations 2.30 and 2.31

$$\Delta u_B - \Delta u_A = -(\Delta X_A)\int_0^L b_{11}\, dx + (\Delta Y_A)\int_0^L b_{12}\, x\, dx - (\Delta M_A)\int_0^L b_{12}\, dx \tag{2.30}$$

$$\Delta u_A - \Delta u_B = (\Delta X_A)\int_0^L b_{11}\, dx - (\Delta Y_A)\int_0^L b_{12}\, x\, dx + (\Delta M_A)\int_0^L b_{12}\, dx \tag{2.31}$$

Using Equation 2.26, the differential of the member rotation can be found in terms of the curvature as shown below

$$d(\Delta\theta) = \Delta\varphi\, dx = d\left[\frac{d}{dx}(\Delta v)\right] \tag{2.32}$$

If Equation 2.32 is integrated once from the member end to the section under consideration, a relationship between cross-sectional rotation (at that section and at the member end) and the end forces is obtained (Equation 2.34)

$$\int d\left[\frac{d}{dx}(\Delta v)\right] = \int_{\Delta\theta_A}^{\Delta\theta} d(\Delta\theta) = \int_0^x (\Delta\varphi)\, dx \tag{2.33}$$

$$\frac{d}{dx}(\Delta v) = \Delta\theta - \Delta\theta_A = -(\Delta X_A)\int_0^x b_{21}\,dx + (\Delta Y_A)\int_0^x b_{22}\,x\,dx - (\Delta M_A)\int_0^x b_{22}\,dx \tag{2.34}$$

If this integration is carried out along the entire length of the member, a relationship between the rotations at both member ends and the member-end forces is obtained (Equations 2.35 and 2.36)

$$\Delta\theta_B - \Delta\theta_A = -(\Delta X_A)\int_0^L b_{21}\,dx + (\Delta Y_A)\int_0^L b_{22}\,x\,dx - (\Delta M_A)\int_0^L b_{22}\,dx \tag{2.35}$$

$$\Delta\theta_A - \Delta\theta_B = (\Delta X_A)\int_0^L b_{21}\,dx - (\Delta Y_A)\int_0^L b_{22}\,x\,dx + (\Delta M_A)\int_0^L b_{22}\,dx \tag{2.36}$$

Integrating Equation 2.32 once more, or more precisely Equation 2.34, it is possible to relate the member-end forces to the transverse deflection of the element at both ends (Equations 2.38 and 2.39)

$$\int_{\Delta v_A}^{\Delta v} d(\Delta v) = \int_0^L \left\{ \Delta\theta_A - (\Delta X_A)\int_0^x b_{21}\,dx + (\Delta Y_A)\int_0^x b_{22}\,x\,dx - (\Delta M_A)\int_0^x b_{22}\,dx \right\} dx \tag{2.37}$$

$$\begin{aligned} \Delta v_B - \Delta v_A = L\Delta\theta_A - (\Delta X_A)\int_0^L (L-x)b_{21}dx + (\Delta Y_A)\int_0^L x b_{22}(L-x)\,dx \\ - (\Delta M_A)\int_0^L (L-x)b_{22}dx \end{aligned} \tag{2.38}$$

or,

$$\begin{aligned} \Delta v_A - \Delta v_B + L(\Delta\theta_A) = (\Delta X_A)\int_0^L (L-x)b_{21}dx - (\Delta Y_A)\int_0^L x b_{22}(L-x)\,dx \\ + (\Delta M_A)\int_0^L (L-x)b_{22}dx \end{aligned} \tag{2.39}$$

In order to relate all member end forces to all member end displacements in a matrix form, two vectors, one of displacements and one of forces, are defined in Equations 2.40 and 2.41

$$\Delta U^{*} = \begin{Bmatrix} \Delta u_A - \Delta u_B \\ \Delta v_A - \Delta v_B + L\left(\Delta\theta_A\right) \\ \Delta\theta_A - \Delta\theta_B \end{Bmatrix} \tag{2.40}$$

$$\left\{\Delta F_A\right\} = \begin{Bmatrix} \Delta X_A \\ \Delta Y_A \\ \Delta M_A \end{Bmatrix} \tag{2.41}$$

These two vectors are related to each other by a flexibility matrix (Equations 2.42 and 2.43)

$$\left\{ \Delta U^{*} \right\} = \left[f \right] \left\{ \Delta F_A \right\} \tag{2.42}$$

$$\begin{Bmatrix} \Delta u_A - \Delta u_B \\ \Delta v_A - \Delta v_B + L\left(\Delta\theta_A\right) \\ \Delta\theta_A - \Delta\theta_B \end{Bmatrix} = \begin{bmatrix} f_{11} & f_{12} & f_{13} \\ f_{21} & f_{22} & f_{23} \\ f_{31} & f_{32} & f_{33} \end{bmatrix} \begin{Bmatrix} \Delta X_A \\ \Delta Y_A \\ \Delta M_A \end{Bmatrix} \tag{2.43}$$

where the flexibility matrix is given by Equation 2.44

$$\begin{bmatrix} f_{11} & f_{12} & f_{13} \\ f_{21} & f_{22} & f_{23} \\ f_{31} & f_{32} & f_{33} \end{bmatrix} = \begin{bmatrix} \int_0^L b_{11} dx & -\int_0^L x b_{12} dx & \int_0^L b_{12} dx \\ \int_0^L \left(L - x\right) b_{21} dx & -\int_0^L x\left(L - x\right) b_{22} dx & \int_0^L \left(L - x\right) b_{22} dx \\ \int_0^L b_{21} dx & -\int_0^L x b_{22} dx & \int_0^L b_{22} dx \end{bmatrix} \tag{2.44}$$

It is more useful, from a computer programming standpoint, to express forces in terms of displacements via a stiffness matrix. This is done in Equation 2.53 by inverting the flexibility matrix

$$\left\{\Delta F_A\right\} = \left[f \right]^{-1} \left\{ \Delta U^{*} \right\} = \left[K\right] \left\{ \Delta U^{*} \right\} \tag{2.53}$$

or

$$\begin{Bmatrix} \Delta X_A \\ \Delta Y_A \\ \Delta M_A \end{Bmatrix} = \begin{bmatrix} k_{11} & k_{12} & k_{13} \\ k_{21} & k_{22} & k_{23} \\ k_{31} & k_{32} & k_{33} \end{bmatrix} \begin{Bmatrix} \Delta u_A - \Delta u_B \\ \Delta v_A - \Delta v_B + L(\Delta\theta_A) \\ \Delta\theta_A - \Delta\theta_B \end{Bmatrix} \tag{2.54}$$

This stiffness matrix can be separated into two components

$$\begin{Bmatrix} \Delta X_A \\ \Delta Y_A \\ \Delta M_A \end{Bmatrix} = \begin{bmatrix} k_{11} & k_{12} & (Lk_{12} + k_{13}) \\ k_{21} & k_{22} & (Lk_{22} + k_{23}) \\ k_{31} & k_{32} & (Lk_{32} + k_{33}) \end{bmatrix} \begin{Bmatrix} \Delta u_A \\ \Delta v_A \\ \Delta\theta_A \end{Bmatrix} + \begin{bmatrix} -k_{11} & -k_{12} & -k_{13} \\ -k_{21} & -k_{22} & -k_{23} \\ -k_{31} & -k_{32} & -k_{33} \end{bmatrix} \begin{Bmatrix} \Delta u_B \\ \Delta v_B \\ \Delta\theta_b \end{Bmatrix} \tag{2.55}$$

$$\{\Delta F_A\} = [K_{AA}]\{\Delta U_A\} + [K_{AB}]\{\Delta U_B\} \tag{2.56}$$

The forces at the end *B* of the member are related to the forces at end *A* by Equations 2.57

$$\begin{aligned} \Delta X_B &= -\Delta X_A \\ \Delta Y_B &= -\Delta Y_A \\ \Delta M_B &= L(\Delta Y_A) - \Delta M_A \end{aligned} \tag{2.57}$$

or in matrix form

$$\begin{Bmatrix} \Delta X_B \\ \Delta Y_B \\ \Delta M_B \end{Bmatrix} = \begin{bmatrix} -1 & 0 & 0 \\ 0 & -1 & 0 \\ 0 & L & -1 \end{bmatrix} \begin{Bmatrix} \Delta X_A \\ \Delta Y_A \\ \Delta M_A \end{Bmatrix} \tag{2.58}$$

$$\{\Delta F_B\} = [T]\{\Delta F_A\} \tag{2.59}$$

And, using the separation of the stiffness matrix shown in Equation 2.56

$$\begin{aligned} \{\Delta F_B\} &= [T]\{\Delta F_A\} \\ \{\Delta F_B\} &= [T]\{[K_{AA}]\{\Delta U_A\} + [K_{AB}]\{\Delta U_B\}\} \\ \{\Delta F_B\} &= [T]\,[K_{AA}]\{\Delta U_A\} + [T]\,[K_{AB}]\,\{\Delta U_B\} \\ \{\Delta F_B\} &= [K_{BA}]\{\Delta U_A\} + [K_{BB}]\,\{\Delta U_B\} \end{aligned} \tag{2.60}$$

where

$$\left[K_{BA}\right]=\begin{bmatrix} -k_{11} & -k_{12} & -\left(Lk_{12}+k_{13}\right) \\ -k_{21} & -k_{22} & -\left(Lk_{22}+k_{23}\right) \\ \left(Lk_{21}-k_{31}\right) & \left(Lk_{22}-k_{32}\right) & \left(L^2k_{22}+Lk_{23}-Lk_{32}-k_{33}\right) \end{bmatrix} \tag{2.61}$$

$$\left[K_{BB}\right]=\begin{bmatrix} k_{11} & k_{12} & k_{13} \\ k_{21} & k_{22} & k_{23} \\ \left(-Lk_{21}+k_{31}\right) & \left(-Lk_{22}+k_{32}\right) & \left(-Lk_{23}+k_{33}\right) \end{bmatrix} \tag{2.62}$$

Finally the member stiffness matrix is

$$\begin{bmatrix} \Delta F_A \\ \Delta F_B \end{bmatrix}=\begin{bmatrix} K_{AA} & K_{AB} \\ K_{BA} & K_{BB} \end{bmatrix}\begin{bmatrix} \Delta U_A \\ \Delta U_B \end{bmatrix} \tag{2.63}$$

$$\left[\Delta F\right]=\left[K\right]\left[\Delta U\right] \tag{2.64}$$

2.3 Solution of the Dynamic Equations of Motion

Equation 2.65 is the general equation of motion for a multi-degree of freedom system subjected to an acceleration at its base. This expression can be applied to a nonlinear system since the restoring force F_{n+1} may not be proportional to the system displacements (as in a linear system).

$$M\ddot{U}_{n+1}+C\dot{U}_{n+1}+F_{n+1}=-M\ J\left(\ddot{u}_G\right)_{n+1} \tag{2.65}$$

where,

$$J=\begin{bmatrix} 1 & 0 \\ 0 & 1 \\ 0 & 0 \\ 1 & 0 \\ 0 & 1 \\ 0 & 0 \\ \vdots & \vdots \end{bmatrix} \tag{2.66}$$

and the ground acceleration vector is given by Equation 2.67. It includes both horizontal and vertical motions.

$$\ddot{u}_G = \begin{bmatrix} \ddot{u}_h \\ \ddot{u}_v \end{bmatrix} \tag{2.67}$$

2.3.1 Constant Average Acceleration Method

$\dot{U}_{n+1}$ and $\ddot{U}_{n+1}$ are the nodal relative velocities and accelerations respectively of the system at time t_{n+1}. F_{n+1} is a vector of nodal forces at time t_{n+1}, and can be defined approximately in terms of the forces at the previous step plus a linear incremental response from time t_n to time t_{n+1} by means of a tangent stiffness matrix as shown in Equation 2.68.

$$F_{n+1} = F_n + K_{\tan}\left(U_{n+1} - U_n\right) \tag{2.68}$$

Introducing this expression into the equation of motion of the system (Equation 2.65), the following expression is found

$$M\ddot{U}_{n+1} + C\dot{U}_{n+1} + F_n + K_{\tan}\left(U_{n+1} - U_n\right) = -M\ J\left(\ddot{u}_G\right)_{n+1} \tag{2.69}$$

One of the simplest and most commonly used methods of solution of this problem is the so-called Constant Average Acceleration Method given by Equations 2.70 and 2.71.

$$\dot{U}_{n+1} = \dot{U}_n + \frac{1}{2}\Delta t\,\ddot{U}_n + \frac{1}{2}\Delta t\,\ddot{U}_{n+1} \tag{2.70}$$

$$U_{n+1} = U_n + \Delta t\,\dot{U}_n + \frac{1}{4}\Delta t^2\,\ddot{U}_n + \frac{1}{4}\Delta t^2\,\ddot{U}_{n+1} \tag{2.71}$$

Introducing these two expressions into Equation 2.69, a relationship between the accelerations of the system at time t_{n+1} and the accelerations, velocities and displacements at time t_n is obtained (Equation 2.72)

$$\left(M+\frac{1}{2}\Delta t\,C+\frac{1}{4}\Delta t^2\,K_{\tan}\right)\ddot{U}_{n+1}=-M\,J\left(\ddot{u}_G\right)_{n+1}-C\left(\dot{U}_n+\frac{1}{2}\Delta t\,\ddot{U}_n\right)-$$
$$-K_{\tan}\left(U_n+\Delta t\,\dot{U}_n+\frac{1}{4}\Delta t^2\,\ddot{U}_n\right)-F_n+K_{\tan}U_n \tag{2.72}$$

Using the definition of an equivalent load vector P^*_n, given by Equation 2.73, and an equivalent stiffness matrix K^*_n, given by Equation 2.74, a final simplified expression is obtained (Equation 2.75) in which the only unknowns are the accelerations at time t_{n+1}

$$P^*_n=-M\,J\left(\ddot{u}_G\right)_{n+1}-C\left(\dot{U}_n+\frac{1}{2}\Delta t\,\ddot{U}_n\right)-K_{\tan}\left(U_n+\Delta t\,\dot{U}_n+\frac{1}{4}\Delta t^2\,\ddot{U}_n\right) \tag{2.73}$$

$$K^*_n=M+\frac{1}{2}\Delta t\,C+\frac{1}{4}\Delta t^2\,K_{\tan} \tag{2.74}$$

$$K^*_n\,\ddot{U}_{n+1}=P^*_n-F_n+K_{\tan}\,U_n \tag{2.75}$$

This last expression is solved for $\ddot{U}_{n+1}$ as a linear set of simultaneous equations. Then, the relative velocities and displacements at time t_{n+1} are found using the original Constant Average Acceleration expressions (Equations 2.70 and 2.71).

2.3.2 Mass and Damping Matrices

The mass matrix for the element can be obtained by assuming that its mass is concentrated at the member ends (nodes of structure) or by evaluating a set of mass influence coefficients (in a similar fashion as a stiffness matrix is formed). The first procedure generates the lumped-mass matrix given in Equation 2.76. In this equation, μ is the mass per unit length and L is the length of the element.

The second approach results in the so-called consistent-mass matrices of the element using the principle of virtual work (Armendariz, 1995). Equations 2.77 and 2.78 show the member consistent mass matrices for translational and rotational inertia, respectively. In Equation 2.78, r is the radius of gyration of the section.

$$M_L = \frac{1}{2}\begin{bmatrix} \mu L & 0 & 0 & 0 & 0 & 0 \\ 0 & \mu L & 0 & 0 & 0 & 0 \\ 0 & 0 & 2I_o & 0 & 0 & 0 \\ 0 & 0 & 0 & \mu L & 0 & 0 \\ 0 & 0 & 0 & 0 & \mu L & 0 \\ 0 & 0 & 0 & 0 & 0 & 2I_o \end{bmatrix} \tag{2.76}$$

$$M_T = \frac{\mu L}{420}\begin{bmatrix} 140 & 0 & 0 & 70 & 0 & 0 \\ 0 & 156 & 22L & 0 & 56 & -13L \\ 0 & 22L & 4L^2 & 0 & 13L & -3L^2 \\ 70 & 0 & 0 & 140 & 0 & 0 \\ 0 & 56 & 13L & 0 & 156 & -22L \\ 0 & -13L & -3L^2 & 0 & -22L & 4L^2 \end{bmatrix} \tag{2.77}$$

$$M_R = \frac{\mu r^2}{30L}\begin{bmatrix} 0 & 0 & 0 & 0 & 0 & 0 \\ 0 & 36 & 3L & 0 & -36 & 3L \\ 0 & 3L & 4L^2 & 0 & -3L & -L^2 \\ 0 & 0 & 0 & 0 & 0 & 0 \\ 0 & -36 & -3L & 0 & 36 & -3L \\ 0 & -3L & -L^2 & 0 & -3L & 4L^2 \end{bmatrix} \tag{2.78}$$

The damping matrix, C, follows an equivalent viscous damping formulation so that the orthogonality condition of the mode shapes to the damping matrix, given by Equation 2.79, is maintained (X_i and X_j are the i^{th} and j^{th} mode shapes or eigenvectors of the structure, respectively) and a modal damping for each mode of vibration can be computed (Equation 2.80) as a function of the i^{th} natural frequency ω_i.

$$X_i^T C X_j = 0 \quad for \quad i \neq j \tag{2.79}$$

$$\beta_i = \frac{X_i^T C X_i}{2\omega_i} \tag{2.80}$$

Three types of damping matrices that comply with the orthogonality condition are often specified, namely a mass-proportional matrix, a stiffness-proportional matrix and a Rayleigh matrix.

The mass-proportional damping matrix is given by $C = a\,M$ in which a is a constant. If the mode shapes are normalized with respect to the mass matrix (that is, $X_i^{\,T} M\, X_i = 1$) the modal damping becomes

$$\beta_i = \frac{a}{2\omega_i} \tag{2.81}$$

and the mass-proportional damping matrix is given by Equation 2.82 (using the first mode).

$$C = 2\omega_1\beta_1 M \tag{2.82}$$

The stiffness-proportional damping is defined by $C = b\,K$ in which b is a constant.

Using Equation 2.80 and the fact that $K\,X_i = \omega_i^{\,2}\, M\, X_i$, the modal damping becomes

$$\beta_i = \frac{b\,\omega_i}{2} \tag{2.83}$$

and therefore, the stiffness-proportional matrix is given by Equation 2.84.

$$C = \frac{2\beta_1}{\omega_1} K \tag{2.84}$$

Finally, the Rayleigh damping matrix is defined as a linear combination of both the mass and stiffness matrices as shown in Equation 2.85. The modal damping is then given by Equation 2.86.

$$C = aM + bK \tag{2.85}$$

$$\beta_i = \frac{a}{2\omega_i} + \frac{b\omega_i}{2} \tag{2.86}$$

Setting β to a constant value, it can be related to two different frequencies Ω_1 and Ω_2, as shown in Equations 2.87 and 2.88.

$$\beta = \frac{a}{2\Omega_1} + \frac{b\Omega_1}{2} \tag{2.87}$$

$$\beta = \frac{a}{2\Omega_2} + \frac{b\Omega_2}{2} \tag{2.88}$$

and then, from these two equations, the values of the constants *a* and *b* can be obtained as follows

$$a = \frac{2\beta\ \Omega_1\,\Omega_2}{\Omega_1 + \Omega_2} \tag{2.89}$$

$$b = \frac{2\beta}{\Omega_1 + \Omega_2} \tag{2.90}$$

Finally, the damping matrix can be written as Equation 2.91. In this case, damping in the structure increases for frequencies lower than Ω_1 and larger than Ω_2.

$$C = \left(\frac{2\beta\ \Omega_1\,\Omega_2}{\Omega_1 + \Omega_2}\right) M + \left(\frac{2\beta}{\Omega_1 + \Omega_2}\right) K \tag{2.91}$$

2.4 Material Constitutive Models

2.4.1 Modified Mander Model for Concrete

A large number of cyclic uniaxial constitutive models for unconfined and confined concrete under compression and tension have been developed in recent decades. One of the most general and versatile ones is that presented by Tsai (2-9). In this study, a particular form of the Tsai model developed by Mander, Priestley and Park (2-4) is used.

The stress-strain relationship for monotonic and cyclic loading suggested by Mander et al (2-4) for normal strength concrete was modified by Armendariz (2-1) to accommodate the behavior of high-strength concrete. The original Mander stress-strain constitutive equation (for monotonic quasi-static loading) is

$$f_c = \frac{f'_{cc} x r}{r - 1 + x^r} \tag{2.92}$$

where, f_c is the compressive stress corresponding to strain ε_c, f'_{cc} is the compressive strength of confined concrete and x and r are defined as follows

$$x = \frac{\varepsilon_c}{\varepsilon_{cc}} \tag{2.93}$$

$$r = \frac{E_c}{E_c - E_{\sec}} \tag{2.94}$$

In Equation 2.93, ε_{cc} is the strain corresponding with the confined concrete strength f'_{cc} and is described in turn by Equation 2.95. E_c in Equation 2.94 is the initial tangent modulus of concrete in compression, and E_{sec} is the secant modulus at peak stress f'_{cc}.

$$\varepsilon_{cc} = \varepsilon_{co}\left[1 + R\left(\frac{f'_{cc}}{f'_{co}} - 1\right)\right] \tag{2.95}$$

$$E_c = 57{,}000\sqrt{f'_{co}} \qquad \text{for } f'_{co} \le 6000\, psi \tag{2.96a}$$

$$E_c = (40{,}000\sqrt{f'_{co}} + 1{,}000{,}000) \qquad \text{for } 6000\, psi \le f'_{co} \le 12000\, psi \tag{2.96b}$$

$$E_{\sec} = \frac{f'_{cc}}{\varepsilon_{cc}} \tag{2.97}$$

The unconfined concrete compressive strength is f'_{co} and ε_{co} is the corresponding strain, which is given by Equation 2.98 (2-1)

$$\varepsilon_{co} = \frac{f'_{co}}{E_c}\frac{k_a}{\sqrt[4]{f'_{co}}} \tag{2.98}$$

where, k_a is taken as *4.26* for crushed aggregate concrete and *3.78* for river gravel aggregate concrete.

In general terms, the confined concrete strength is given by

$$f'_{cc} = f'_{co} + k_1 f'_l \tag{2.99}$$

where f'_l is the lateral stress induced by the confinement and k_1 is a constant that depends on the concrete mix and the lateral confining pressure (2-4).

The compression unloading branch is given by Equation 2.100 and illustrated in Figure 2.2

$$f_c = f_{un} - \frac{f_{un} x r}{r - 1 + x^r} \tag{2.100}$$

where,

$$x = \frac{\varepsilon_c - \varepsilon_{un}}{\varepsilon_{pl} - \varepsilon_{un}} \tag{2.101}$$

$$r = \frac{E_u}{E_u - E_{\sec}} \tag{2.102}$$

$$E_{\sec} = \frac{f_{un}}{\varepsilon_{un} - \varepsilon_{pl}} \tag{2.103}$$

and ($\varepsilon_{\mathrm{un}}$, f_{un}) is the point on the curve at which unloading starts. E_{u} is the tangent modulus of elasticity at the onset of unloading and is given by $E_{\mathrm{u}} = bcE_{\mathrm{c}}$, where $b = f_{\mathrm{un}}/f'_{\mathrm{co}} \geq 1.0$ and $c = (\varepsilon_{\mathrm{cc}}/\varepsilon_{\mathrm{un}})^{0.5} \leq 1.0$.

Some of the above expressions depend on the plastic strain ε_{pl}. This strain is computed as follows:

$$\varepsilon_{pl} = \varepsilon_{un} - \frac{\left(\varepsilon_{un} + \varepsilon_a\right) f_{un}}{\left(f_{un} + E_c \varepsilon_a\right)} \tag{2.104}$$

$$\varepsilon_a = a\sqrt{\varepsilon_{un}\varepsilon_o} \tag{2.105}$$

$$a = \frac{\varepsilon_o}{\left(\varepsilon_o + \varepsilon_{un}\right)} \quad \text{or} \quad a = \frac{0.09\varepsilon_{un}}{\varepsilon_o} \tag{2.106}$$

Tension loading after compressive unloading is given by

$$f_t = f_t'\left(1 - \frac{\varepsilon_{pl}}{\varepsilon_{cc}}\right) \tag{2.107}$$

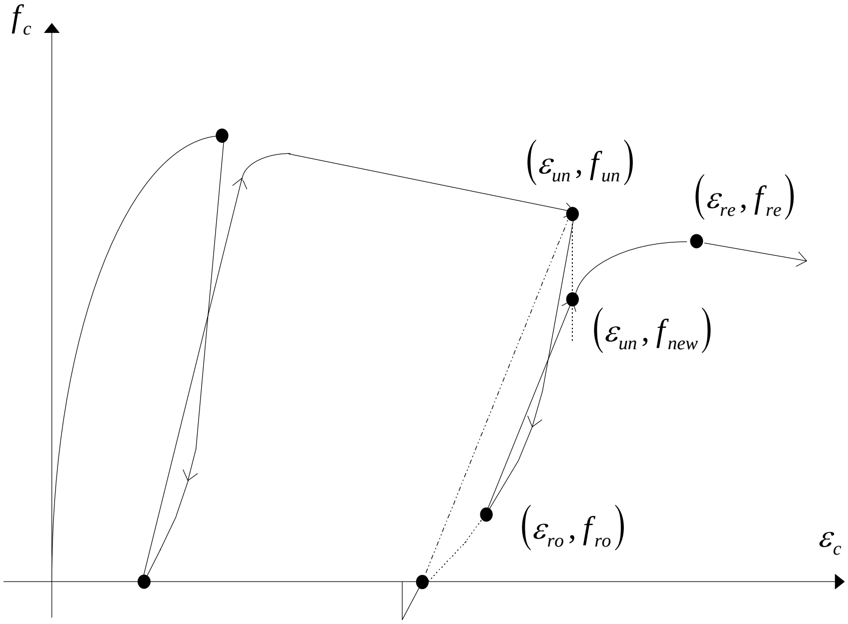

Figure 2.2 - Unloading and Reloading Rules (taken from 2-1)

If $\varepsilon_{pl} > \varepsilon_{cc}$, then $f_t = 0$. The tensile stress-strain relationship can then be written as

$$f_t = E_t\left(\varepsilon_c - \varepsilon_{pl}\right) \tag{2.108}$$

$$E_t = \frac{f_t}{\varepsilon_t} \tag{2.109}$$

$$\varepsilon_t = \frac{f_t'}{E_c} \tag{2.110}$$

For reloading, a linear stress-strain relationship, given by Equation 2.111, is followed between the point of reloading (ε_{ro}, f_{ro}) and the revised unloading point (ε_{un}, f_{new}), where f_{new} is given by Equation 2.112. This is illustrated in Figure 2.2.

$$f_c = f_{ro} + E_r\left(\varepsilon_c - \varepsilon_{ro}\right) \tag{2.111}$$

$$f_{new} = 0.92 f_{un} + 0.08 f_{ro} \tag{2.112}$$

$$E_r = \frac{f_{ro} - f_{new}}{\varepsilon_{ro} - \varepsilon_{un}} \tag{2.113}$$

The transition between the linear reloading curve and the monotonic stress-strain envelope (Equation 2.92) is a third-degree polynomial curve given by Equation 2.114 (2-1).

$$f_c = A_2 + B_2 X + C_2 X^2 + D_2 X^3 \tag{2.114}$$

where,

$$X = \left(\varepsilon_c - \varepsilon_{re}\right) \tag{2.115}$$

$$A_2 = f_{re} \tag{2.116}$$

$$B_2 = E_{re} \tag{2.117}$$

$$C_2 = \left[f_{new} - \left(f_{re} + E_{re} X_o \right) - D_2 X_o^{\,3} \right] \frac{1}{X_o^{\,2}} \tag{2.118}$$

$$D_2 = \frac{\left(E_r + E_{re}\right) X_o - 2\left(f_{new} - f_{re}\right)}{X_o^{\,3}} \tag{2.119}$$

$$X_o = \varepsilon_{un} - \varepsilon_{re} \tag{2.120}$$

E_{re} and f_{re} are the tangent modulus and stress at the return point, respectively, and correspond to the strain ε_{re} given by Equation 2.121. Both E_{re} and f_{re} are computed using the monotonic stress-strain curve (Equation 2.92).

$$\varepsilon_{re} = \varepsilon_{un} + \frac{f_{un} - f_{new}}{E_r \left(\frac{f_o}{f'_c} \right)} \tag{2.121}$$

Figure 2.3 illustrates the performance of the model under cyclic straining. Note the progressive deterioration in stiffness and stress at large deformations.

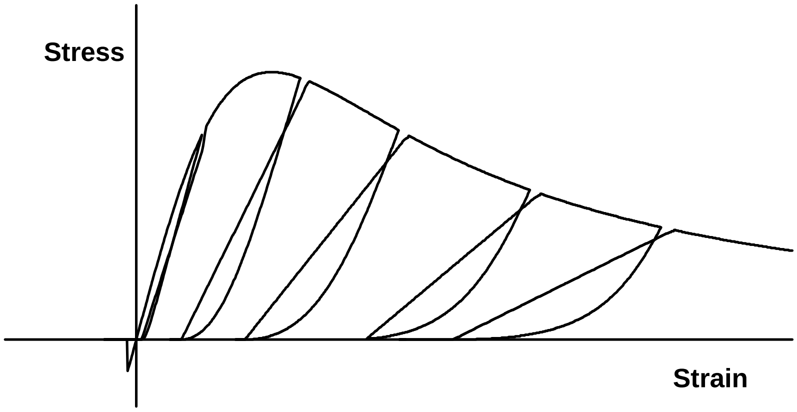

Figure 2.3 - Model's Performance under Cyclic Straining

2.4.2 Menegotto-Pinto Model for Reinforcing Steel

As in the case of concrete, a large number of cyclic constitutive models for steel have been developed in recent decades. However, the model proposed by Menegotto and Pinto (2-6, 2-7) has been found to give very good predictions of the hysteretic behavior of steel (2-5, 2-8), including the Bauschinger effect, while retaining a very simple formulation (with very few parameters).

One of the main advantages of the Menegotto-Pinto model is that it explicitly formulates the stress and tangent modulus as a function of strain and therefore, it is ideal for use in algorithms driven by deformations like those developed in this study. In addition to these features, the model requires essentially a single nonlinear expression for loading and unloading branches both in tension and compression, making its implementation in a computer program a very simple task.

The basic expression of the model, given by Equation 2.122, is fundamentally a curved transition between two asymptotes: one with an elastic slope E_s, and another with a post-elastic slope E_p. The normalized stress σ^* corresponds to the normalized current strain ε^*. These two depend on the location of the intersection of the two asymptotes (ε_o, σ_o), and on the point at which the last strain reversal with stress of equal sign occurred (ε_r, σ_r).

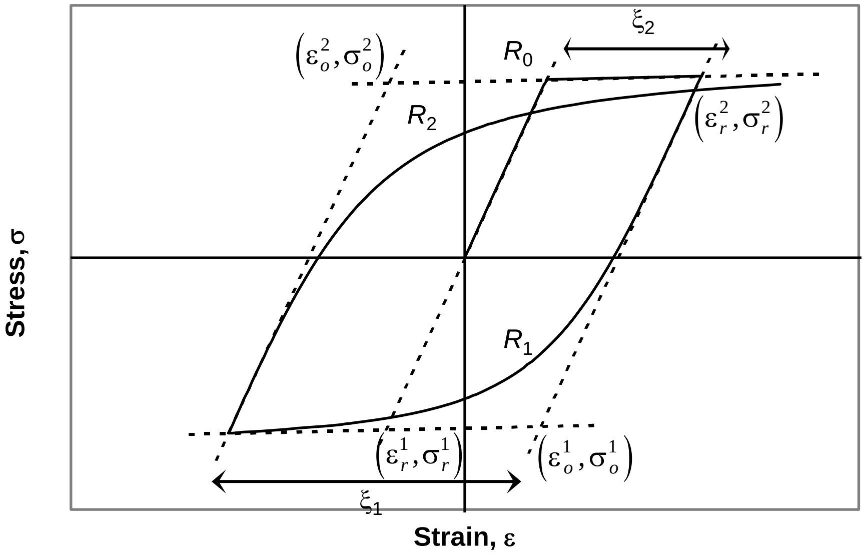

Figure 2.4 - Definition of the Menegotto-Pinto Model (Adapted from 2-6)

$$\sigma^* = b\varepsilon^* + \frac{(1+b)\varepsilon^*}{\left(1+\varepsilon^{*R}\right)^{\frac{1}{R}}} \tag{2.122}$$

$$\varepsilon^* = \frac{\varepsilon - \varepsilon_r}{\varepsilon_o - \varepsilon_r} \tag{2.123}$$

$$\sigma^* = \frac{\sigma - \sigma_r}{\sigma_o - \sigma_r} \tag{2.124}$$

The parameter constant b in Equation 2.122 represents the strain hardening or post-elastic slope as a fraction of the elastic modulus.

$$b = \frac{E_p}{E_s} \tag{2.125}$$

R is the parameter that controls the transition curve between asymptotes and therefore, models the Bauschinger effect, as shown in Figure 2.4. R depends on the parameter constants R_0, a_1 and a_2, that are determined by curve-fitting experimental results, and on ξ, the difference between the strain at the current asymptote intersection point and the strain at the previous maximum (or minimum) load reversal point.

$$R = R_o - \frac{a_1 \xi}{a_2 + \xi} \tag{2.126}$$

The model, as described above, corresponds to the original formulation by Menegotto and Pinto (2-6) and, as mentioned before, reproduces very well the experimental cyclic behavior of steel loaded uniaxially. This is particularly true when kinematic hardening is developed, which is precisely the case of reinforcing bars in reinforced concrete members, which tend to be strained mainly in tension, as shown in Figure 2.5.

However, in certain situations some isotropic hardening can develop, such as for bottom reinforcing bars in a section when the bars are 50% or less of the area of top bars. These bars may be subjected to compression yielding upon crack closure. In such cases, the original Menegotto-Pinto model will give a poor prediction of the stress-strain response of the bottom bars.

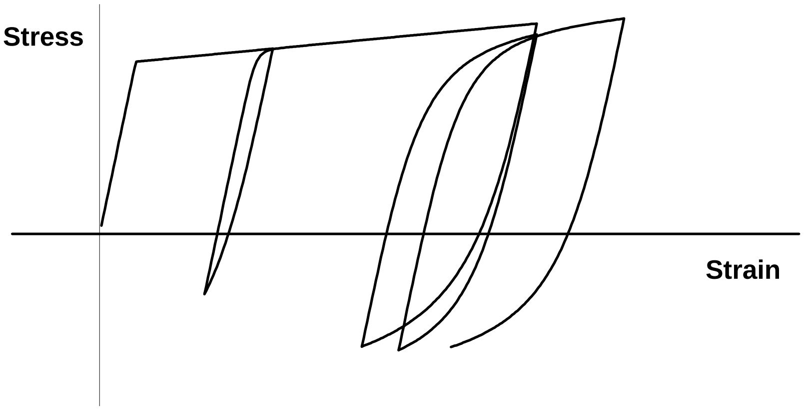

Figure 2.5 -Performance of Menegotto-Pinto Model under Cyclic Straining in Tension

Filippou et al (2-2), following an idea by Stanton and McNiven (2-8), developed a modified Menegotto-Pinto model that allows for isotropic hardening. The modification consists of imposing a stress shift σ_{st} in the position of the post-elastic asymptote after a strain reversal.

$$\sigma_{st} = a_3 \sigma_y \left(\frac{\varepsilon_{\max}}{\varepsilon_y} - a_4 \right) \tag{2.127}$$

CHAPTER 3

Idealizations for Nonlinear Dynamic Analysis

3.1 General

In this chapter the main features of several discrete member models for nonlinear dynamic time-history analysis of reinforced concrete structures are presented. The first such model is the "Lumped Plasticity Model" that assumes inelastic behavior is concentrated exclusively at the ends of the members while the remaining portions of members continue to be elastic. The second is the "Distributed Plasticity Model", that allows part of the length of the member to experience inelastic deformations. The third, and final model considered here, is the fiber model. For each of these models several computer programs have been developed in order to simulate the response of concrete structures.

Two of the most widely used computer programs for seismic analysis of reinforced concrete structures, each one representing one of the first two models discussed above, are discussed in detail in the following two sections. The first of these programs is DRAIN-2D which has been extensively used worldwide since its first release in 1973. The second program, IDARC, was initially released in 1987 and since then has been widely used.

In the last section of this chapter, the computer program FIBERC, based in the fiber element idealization described in Chapter 3, is presented. This program is based on the program *FEP* developed by Armendariz (3-3).

3.2 DRAIN-2DX

This is an improved version of the well-known DRAIN-2D program developed at the University of California, Berkeley. The original version of the program by Kanaan and Powell (3-4) included truss elements, beam-column elements, infill shear panels and semi-rigid connections. Multiple versions have been developed since the first release of the program in 1973; most of them including new and sophisticated elements used to simulate particular characteristics of certain structural elements. The version DRAIN-2DX developed by Allahabadi and Powell (3-2), which constitutes a major revision and expansion of the original program, includes several types of linear and nonlinear static and dynamic analyses, and additional types of elements. A second major revision (version 1.10) was released in 1993 (3-9, 3-10) but the element types were the same as in the previous release. Recently, a PC-based postprocessor for DRAIN-2DX running under Microsoft Windows was made commercially available (3-1).

3.2.1 Types of Elements

Several types of structural elements are available in this release of DRAIN-2DX. These are: the truss element (type 01), the beam-column element (type 02), the simple connection (type 04), the structural panel (type 06), the link (type 09) and the fiber-flexibility model (type 15).

3.2.2 Types of Analyses

While the original version of the program had a limited number of analysis types, the revised version includes an important set of analysis types: These are: a static gravity analysis (linear elastic structure), static nonlinear analysis (for static lateral load), mode shapes and periods, response spectra analysis (linear dynamic structure), ground acceleration (nonlinear dynamic) analysis, initial velocity analysis (nonlinear dynamic for impact or energy absorption capacity) and ground displacement analysis (nonlinear dynamic).

In addition to the analyses listed above, P-Delta effects can be considered, overshooting during step-by-step solution is checked, and energy balance is computed.

3.2.3 Beam-Column Element Model

The beam-column element (element type 02) has both axial and flexural stiffness, and can accommodate shear deformations and the effects of eccentric end connections and rigid joint zones. Yielding is concentrated exclusively at plastic hinges located at one or both ends of the member. Post-yield member stiffness (due to reinforcement strain hardening, for instance) is simulated by introducing an elastic element parallel to the inelastic elastoplastic member, as shown schematically in Figure 3.1.

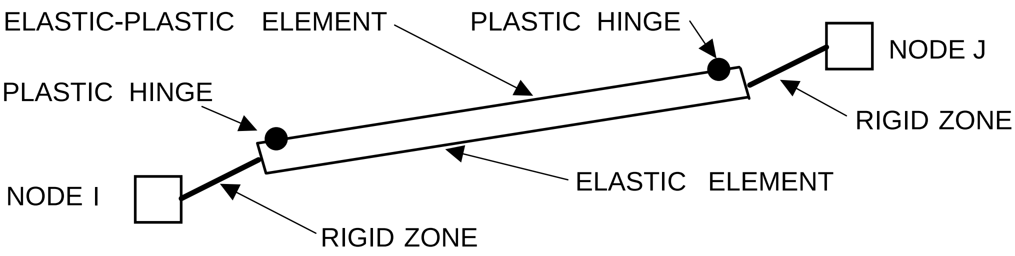

Figure 3.1 - Parallel-Component Element Model (adapted from 3-9)

The moment-curvature or moment-rotation behavior of the members is then a combination of an elastic component and an elastic-plastic component (Figure 3.2). The resultant bilinear member response is specified in terms of moment-rotation of the member ends, and therefore, the element idealization is not directly applicable if the actual applied moments or member strength vary along the length of the element.

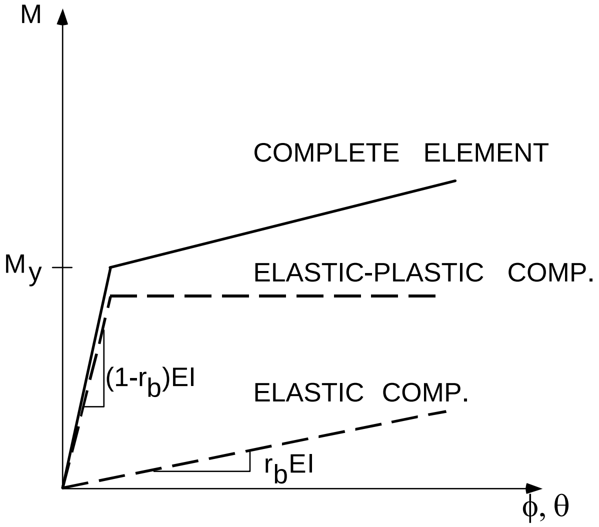

Figure 3.2 - Section response Idealization (adapted from 3-9)

Figure 3.3 shows the hysteretic moment-curvature or moment-rotation response of the member, again as a combination of the elastic and elastoplastic components. No degradation in stiffness or strength is considered during the cyclic response of the elements.

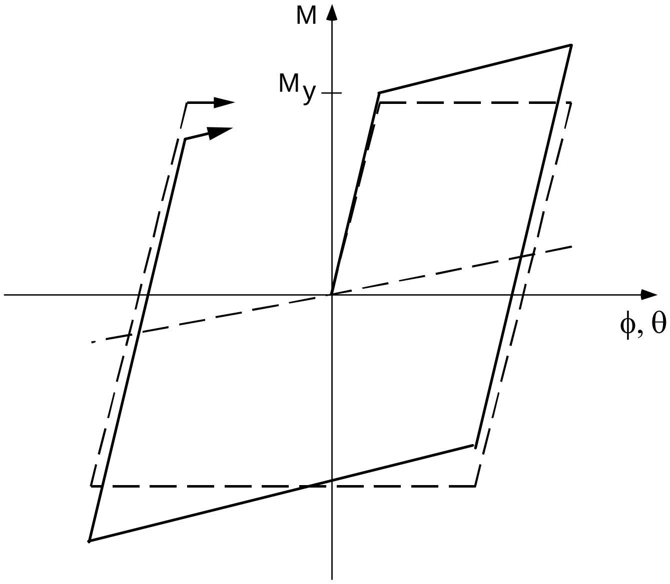

Figure 3.3 - Hysteretic Response of Parallel-Component Element (adapted from 3-9)

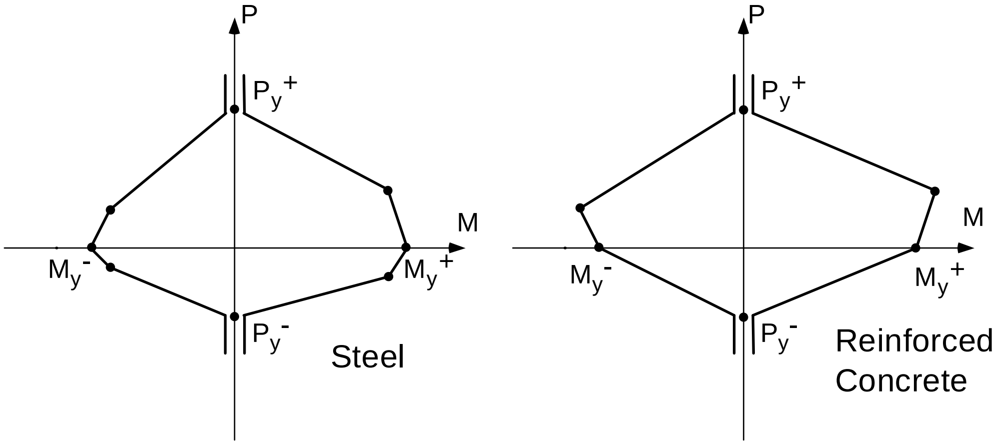

Figure 3.4 - Yield Surfaces for Steel and Reinforced Concrete Columns (adapted from 3-9)

The model does not consider inelastic axial deformations, and the axial load-moment interaction is accounted for in just an approximate manner by means of yield surfaces. The yield surfaces for steel and reinforced concrete columns are shown in Figure 3.4. Whenever a combination of bending moment and axial load in the column reaches the yield surface, a plastic hinge is formed in the member.

Figure 3.5 shows the yield surface for the beams. In this case, no interaction of moments and axial load is present, and the plastic hinge is formed as soon as the yield moment (M_y^- or M_y^+) is reached.

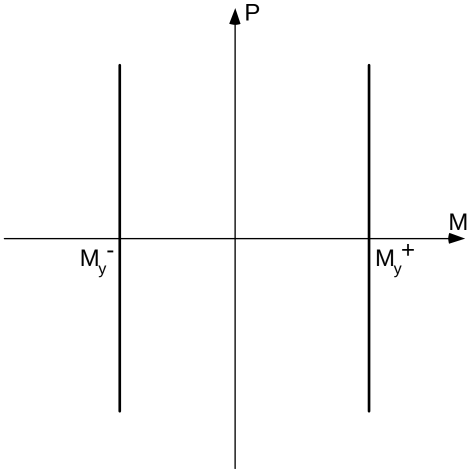

Figure 3.5 - Yield Surfaces for Beams (adapted from 3-9)

For the dynamic response, DRAIN-2DX assumes the mass lumped at the joints (nodes). The step-by-step integration uses the constant average acceleration method, and at each step an equilibrium correction is performed using the unbalanced forces of the previous step.

3.3 IDARC2D

This program was developed at the State University of New York at Buffalo as a tool to evaluate the inelastic response of a reinforced concrete structure and to estimate the damage generated in its elements. The original version of this program by Park, Reinhorn and Kunnath (3-8), called simply IDARC, was intended for analysis of reinforced concrete frame or shear-wall buildings. Most formulations for the capacity of the elements were empirical. It included element damage computation capabilities and the ability to analyze test subassemblages.

Version 3.0 by Kunnath, Reinhorn and Lobo (3-5), released in 1992, improved the evaluation of section capacities, introducing a sectional fiber model. An updated Version 3.1 (3-6) was released subsequently.

Finally, version 4.0 (3-11), renamed IDARC2D, expanded the analysis capabilities of the program to include steel structures as the result of adding new general hysteretic models. Also, new elements like braces, masonry infills and dampers were introduced.

3.3.1 Types of Elements

Most element types were originally developed to simulate the behavior of reinforced concrete members. The available elements at present are: beam-column (inelastic single-component element with distributed plasticity), shear wall (made up of shear and flexure springs connected in series), inelastic axial element (shear-wall edge column), transverse beams, discrete springs, masonry infill walls and dampers (visco-elastic, frictional and hysteretic).

3.3.2 Types of Analyses

The analysis modules are: nonlinear static (initial stress states under dead and live load), failure/collapse (monotonic lateral load or ‘pushover’), quasi-static nonlinear cyclic analysis (load or displacement controlled), incremental nonlinear dynamic response (for horizontal and vertical seismic excitations) and damage estimation.

3.3.3 Beam-Column Element

This is a simple flexural spring element that includes the effect of shear deformations. The axial deformation is considered in the column but neglected in the beams. The interaction of axial load and bending moment is not considered directly in the step-by-step analysis. However, the effect of axial load in moment capacity is included.

As shown schematically in Figure 3.6, a distributed flexibility model is used instead of concentrated plastic hinges. Figures 3.6a and 3.6b display the typical deformed shape and moment distribution, respectively, for a beam under seismic loads. The flexibility along the element is assumed to vary linearly from the member ends to the locations at which the cracking moment has been reached (Figure 3.6d), while it is assumed constant and equal to the elastic flexibility in the middle portion.

As the end moments increase, the plastified regions grow and yield penetration is modeled as shown in Figure 3.6e. Finally, the flexibility member matrix is found by numerical integration.

Perfect hinges can be specified at either end of a member (as moment releases). Also, discrete inelastic springs can be specified at member ends with their moment-rotation response characterized by a non-symmetric tri-linear envelope with degrading parameters. Using these springs, joint distortions and pull-out response can be modeled.

The mechanical properties of the elements were defined in the original version by empirical relationships (3-8). In version 3.0, these were replaced by a more rational procedure using a fiber model. Additionally, the user can input directly cross-sectional strength and rotation properties.

The hysteretic modeling in the original version was based on a three-parameter model. For version 3.0 a general-purpose versatile model was developed which uses four control parameters. The characteristics that are modeled are stiffness degradation, strength deterioration and crack closure/bond-slip/pinching. These features of the program are discussed in detail in the next section.

3.3.4 Hysteretic Modeling

The hysteresis model implemented in the program is based on a non-symmetric trilinear backbone curve and a set of rules for loading and unloading governed by four parameters defined by the user. These parameters control the stiffness degradation, the strength degradation and the pinching of the hysteresis loops for the member response. Figure 3.7 shows the general hysteretic response of the model.

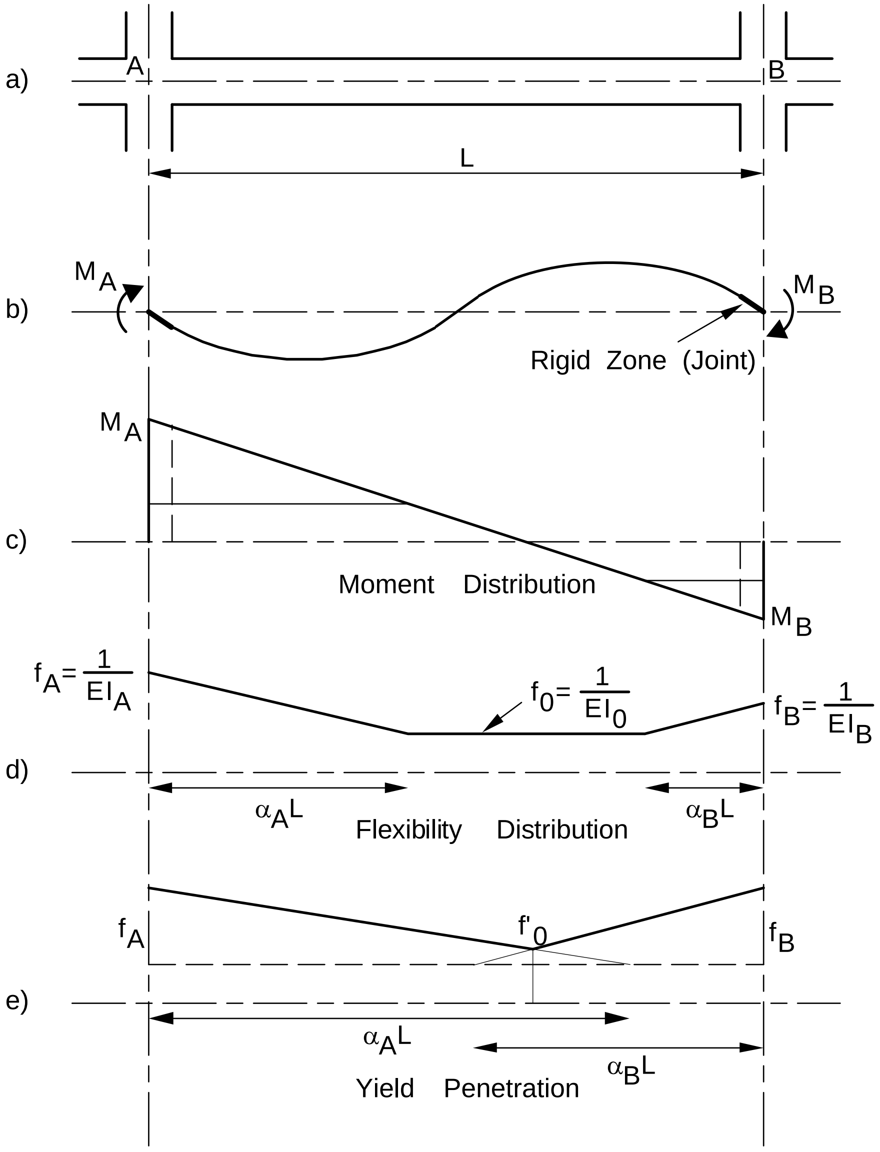

Figure 3.6 - Spread Plasticity and Yield Penetration Idealization (adapted from 3-11)

The stiffness degradation parameter HC determines the stiffness reduction as a function of the level of ductility in the member by having all unloading paths from the backbone curve aim at the same point (Figure 3.8) and therefore, resulting in degrading stiffness as deformations increase. According to the authors (3-5), HC normally lies between 1.5 and 3.0.

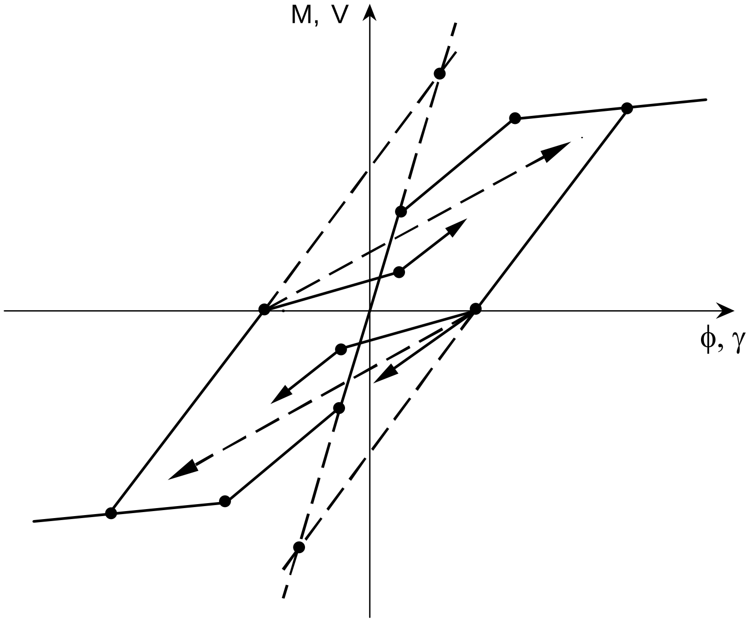

Figure 3.7 - Hysteretic Rules (adapted from 3-11)

Strength deterioration depends on the dissipated energy and the ductility attained in the member. The expression used in the program to estimate strength decay is (see Figure 3.8)

$$F_{new} = F_{\max}\left(1.0 - HBE \times \overline{E} - HBD \times \mu_c\right)$$

where HBE is a user parameter that controls the strength deterioration as a function of the dissipated energy and HBD is another user parameters that depends on the maximum attained curvature ductility. In this case, the authors recommend (3-5) using values of 0.1 for HBE and 0.0 for HBE for usual situations (or when no experimental data are available) and a value of 0.5 for both parameters when the response is expected to exhibit considerable strength deterioration.

The pinching or slip parameter reduces the stiffness of the load reversal (reloading path after crossing the zero moment axis) up to the cracking deformation, after which the loading path is re-directed towards the maximum point of the previous cycle. Such reduction in stiffness is controlled by the parameter HS as shown in Figure 3.9. The authors suggest (3-5) a value of 0.5 for the parameter HS.

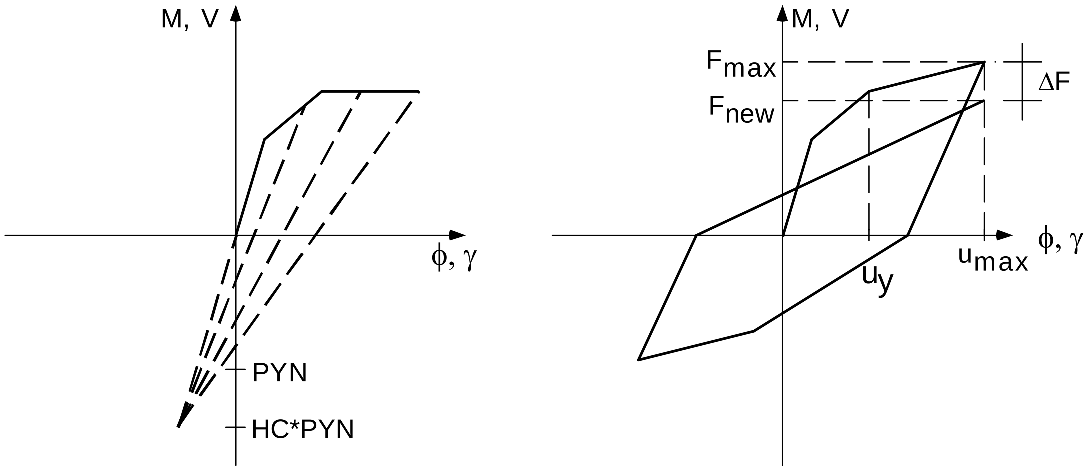

Figure 3.8 - Stiffness and Strength Degradation Parameters (adapted from 3-11)

For the dynamic response, the program IDARC2D, as DRAIN-2DX, assumes mass lumped at the joints (nodes). Also, the step-by-step integration uses the constant average acceleration method and at each step an equilibrium correction is performed using the unbalanced forces from the previous step.

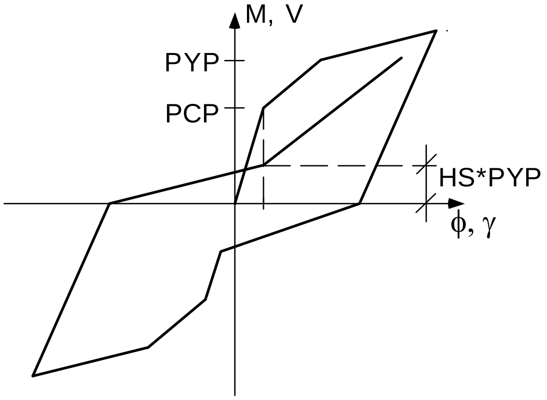

Figure 3.9 - Slip Degradation and Pinching Parameter (adapted from 3-11)

3.4 FIBERC

In contrast to the models presented in Sections 3.2 and 3.3, material nonlinearity can occur along the element in distributed plasticity models. This is achieved by monitoring the behavior of the elements at several locations (slices) along their length, where the cross-section is discretized into fibers that are assumed to be stressed and strained uniaxially in the direction parallel to the longitudinal axis of the element, as shown in Figure 3.10.

The program FIBERC was developed to implement a distributed-plasticity solution using the fiber-element model. The program is based on the program *Fiber* developed by Papaleontiou (3-7) using the Fortran computer language, and extended by Armendariz (3-3) at the University of Texas at Austin.

3.4.1 Types of Elements

The program FIBERC has a single frame member type that is used to model both reinforced concrete columns and beams. The cross section geometry of the elements is completely general since both the width an thickness of the concrete fibers are specified by the user. Likewise, the location and number of the steel reinforcement fibers is arbitrary and decided by the user.

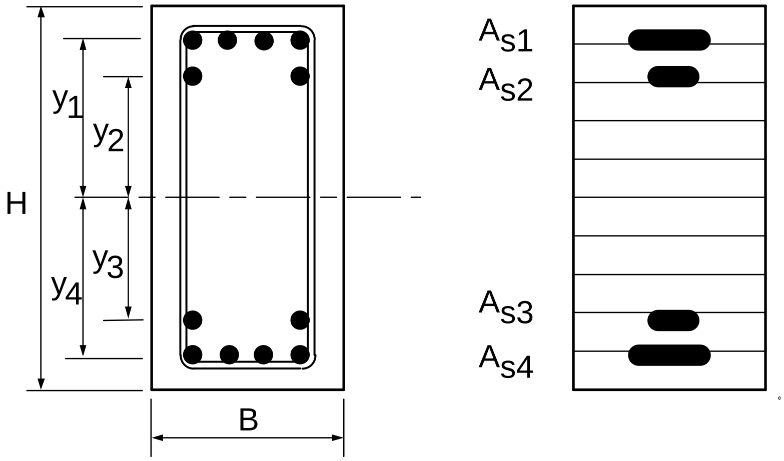

Figure 3.10 - Cross-Section Geometry and Fiber Idealization

The elements are modeled as shown in Figure 3.11. Each member is divided into three regions or “segments”. Such segments are used to define different longitudinal (and transverse) reinforcement ratios and/or patterns. The segments are divided in turn into slices or “sections”. In the current version of the program the number of sections per segment is defined by the user. However, a maximum of 20 sections for the entire member is allowed.

Finally, each section is composed of a number of concrete strips and steel filaments or “fibers” as shown in Figures 3.10 and 3.11. The concrete are rectangular and therefore, are defined by their width and depth. The steel fibers are defined by the diameter and number of bars for each layer of reinforcement. The location of concrete and steel fibers is completely arbitrary and decided by the user.

Because the behavior of the fibers can be specified to be linear elastic during the analysis, a new type of element can be created from the beam-column described above, to simulate elastic springs.

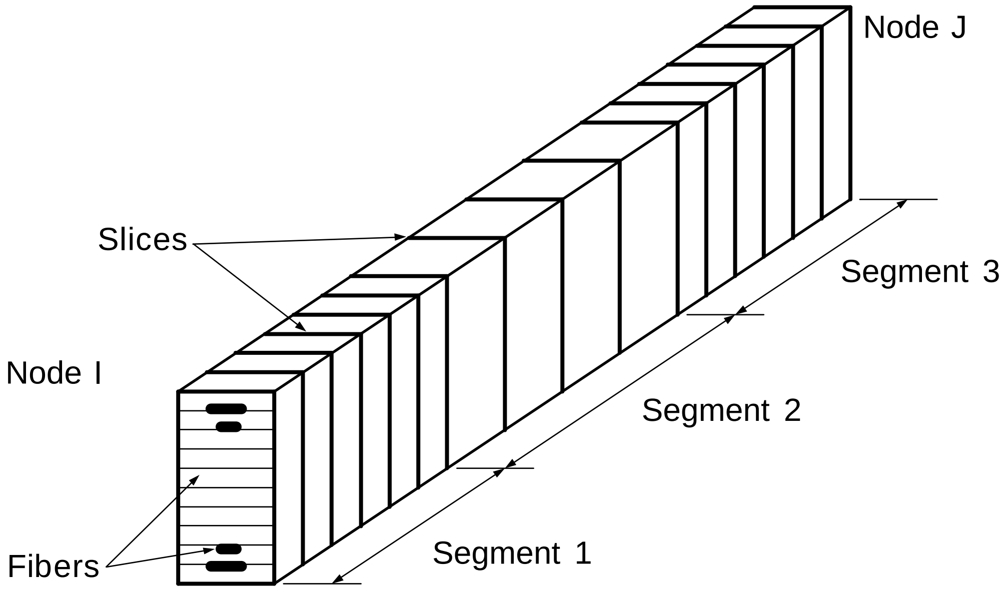

Figure 3.11 - Fiber Element Idealization

3.4.2 Types of Analysis

The analysis options available are: nonlinear static for gravity loads (all loads applied in a single step), nonlinear quasi-static cyclic analysis (load or displacement controlled) and nonlinear incremental dynamic analysis (for horizontal and vertical seismic excitations). The gravity load analysis can precede either the quasi-static or the dynamic analyses.

3.4.3 Solution Algorithm

For each structural member (beams and columns) the flexibility matrix is assembled according to Equation 2.44 using numerical integration (trapezoidal rule). Then, the member stiffness matrix is obtained as in Equation 2.63. Finally, the tangent stiffness matrix for the complete structure is assembled from the element matrices. For dynamic analysis, the damping and mass matrices are also formed as described in Section 2.3.2

The differential equations of motion are solved by direct integration using the constant average acceleration method described in Section 2.3. The tangent stiffness formulation and pure incremental procedure are used. To avoid developing large unbalanced forces during the solution, a very small time step (of the order of 0.001 second) is used.

Nonlinear material behavior is taken into account assuming that the fibers respond uniaxially in the direction parallel to the member longitudinal axis. Cyclic stress-strain relationships for concrete and for reinforcing bars follow the models described in Section 2.4. In addition, the modified bilinear model introduced by Armendariz (3-3) and a simple bilinear model with kinematic hardening are available for the reinforcing steel.

3.4.4 Transition from *FEP* to FIBERC

The following enhancements were made to the program as part of the initial phase of the research study:

An extensive reorganization and “clean up” of the code was conducted. The program was divided into three modules: FRC01, that contains the main program as well as general input and output routines; FRC02, with the main analysis subroutines; and FRC03 with the routines for material models.

The input data routine was rewritten for easier data specification. Some details of the input are given in Section 3.4.5. Output routines were also rewritten to print an echo file and up to 20 response files in a single run. Several output options were implemented (history of node displacements, member forces, equivalent EA, concrete fiber stress-strain, steel fiber stress-strain, moment-curvature of sections and moment-axial load-shear of section). Section 3.4.6 provides some details about the output files.

A new option for selecting the system of units was made available. The user can choose either US customary units or the International (SI) system of units.

A PC-based version with some user interaction running under Microsoft Windows was created.

The material models for steel and concrete were reviewed. A new model for steel bars was introduced based on the Menegotto-Pinto formulation. Section 2.4.2 describes the details of that model.

The number of sections per segment as well as the total number of sections along the member are now variable. However, they are the same for all elements.

Some or all elements can behave elastically during a run. This feature can be used to introduce elastic springs or stiff supports.

Finally, a new analysis option was introduced for quasi-static loading in a force- (or displacement-) controlled mode.

3.4.5 Input Data Description

The current version of program FIBERC allows the user to specify the structural geometry in two different forms. In the first option (MSTR = 1), the structural geometry must be a complete orthogonal frame. Elements (beams and columns) are input by blocks defined by floor and column line numbers. Furthermore, all base joints are assumed rigidly fixed and all other joints are considered free.

The second input mode (MSTR = 2) allows the user to specify the geometry of a bridge structure in a very simple fashion. In this case, each column can be given a different height. If the number of bays is greater than the number of columns, the ends of the extreme bays are supported not on columns but on simple supports to model abutments.

In Appendix A, the input files needed to run program FIBERC in mode are described in detail. Each file is specified line by line, and repeated lines are noted. A short definition of each variable is also given.

3.4.6 Output Description

One or more output files are created during the run. The file <PROJECTNAME>.ECH is always generated. This file contains an echo of the input data (parameters and structural geometry) as well as the results of the eigenvalue problem and the results of the static analysis of the structure under gravity loads.

Up to 20 additional output files corresponding to different nonlinear dynamic responses can be generated. Appendix A describes the types of responses that can be generated, together with the file extensions and the parameters required for each selection. File names are composed of the four characters of the variable PROJECTNAME plus a 2-digit counter and an extension.

CHAPTER 4

Analysis of Sections, Members and Frames

4.1 General Remarks

In the study by Armendariz (4-4), results of a number of quasi-static tests on beams and columns were presented. The program *FEP* was used to simulate the results of those tests with relative success. Armendariz also presented the response of several frames to ground motions and again, a simulation of the results using program *FEP* was performed. However, in this case, the comparison of experimental and theoretical results was not clear, as discussed in Section 1.3.4.

In this chapter, some of the member tests analyzed by Armendariz are studied again, this time using the programs IDARC2D, DRAIN-2DX, and FIBERC. Section 4.2 presents some of the analyses in terms of moment-curvature response of the critical cross-section of specimens, while Section 4.3 presents load-deflection behavior. Additionally, the results of static and dynamic frame tests are presented and then analyzed using the three programs. Emphasis is given to large-scale laboratory tests to avoid size effects on specimen response (4-1).

A literature review of recent full-scale reinforced concrete frame tests was conducted as part of the research described in this chapter. However, very few such tests were found to be available in the literature. Probably the most significant test to date is that of the 7-story building at the Building Research Institute of Japan (4-3) conducted during the early 1980s. More recently (late 1980s), a 2-story plane frame was tested by Vecchio and his associates at the University of Toronto (4-10, 4-21). At the beginning of this decade (1990s), a full-scale laboratory test of a 5-story masonry building was performed by Seible and his collaborators at the University of California at San Diego (4-20). At about the same time, a four-story building was tested at the European Laboratory for Structural Assessment (ELSA) of the European Commission in Italy (4-12, 4-14). Finally, during the mid 1990s, a series of field tests were conducted by Eberhard on an existing bridge in Washington state (4-8, 4-9).

The 7-story Japanese building contained a central structural wall that dominated, to a large extent, the response of the structure and therefore, will not be considered in this study. The bridge tests by Eberhard introduced effects of the soil in the response of the structure and therefore, increase the uncertainty in analysis of the structural behavior. The test by Seible was conducted on a masonry-wall building and thus, is beyond the scope of this research. As a result of these considerations, the only large-scale frame systems identified as suitable for use in this study were the 2-story frame tested by Vecchio, and the four-story European building. They are described and analyzed in Sections 4.4 and 4.5.

In all the comparisons presented in this chapter with two series of data, the experimental results will be represented by dashed lines and the numerical prediction by solid lines, unless otherwise stated.

4.2 Moment-Curvature Response of Sections

4.2.1 Beam #24 by Park, Kent and Sampson (4-15, 4-16)

The simply-supported beam shown in Figure 4.1 was tested at the University of Canterbury in New Zealand under displacement-controlled load reversals by means of screw jacks placed at the top and bottom of the column stub. This test was part of a large series of tests performed to investigate cyclic flexure yielding in reinforced concrete beams.

The compressive strength f'_c of the concrete used was 6.95 ksi, while the yield strengths f_y of the top and bottom reinforcing bars were 47.5 ksi and 49.2 ksi, respectively. The ultimate strengths of the top and bottom reinforcing bars f_u were 68.5 ksi and 69.7 ksi, respectively. Though the strain hardening modulus was not reported by Park et al. (4-15), the strain at the onset of strain hardening was measured as approximately 0.033 in/in for all bars.

The load history consisted of a cycle up to approximately initial yielding and then two cycles well into the inelastic range to produce ultimate response.

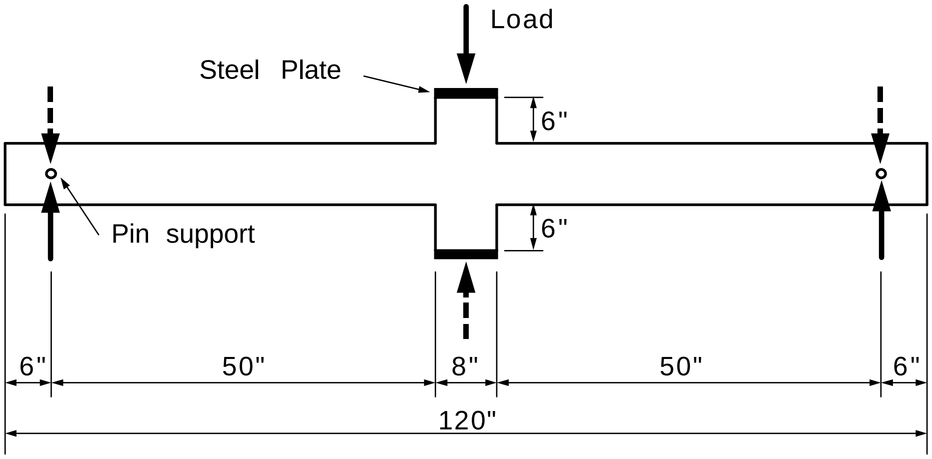

Figure 4.1 - Experimental Set-up (adapted from 4-15)

Geometry of the cross section and reinforcement of the tested beam is shown in Figure 4.2. The reinforcement was continuous along the beam, and both the positive and negative-moment reinforcement ratios ρ were equal to 0.012.

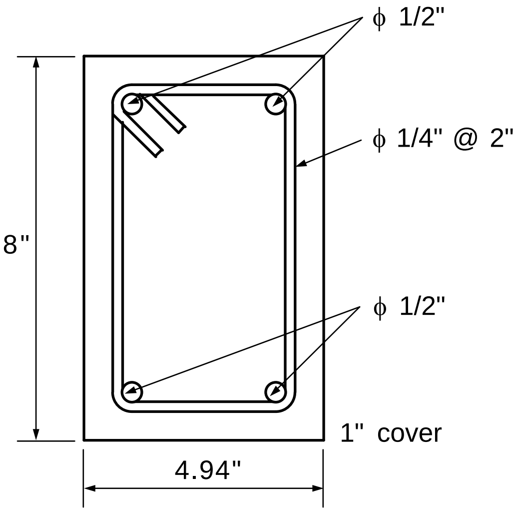

Figure 4.2 - Beam Geometry and Reinforcement (adapted from 4-15)

Figure 4.3 shows the experimental moment-curvature response at the face of the loading stub. Note that the section did not reach its expected strength in either the positive or negative directions. Using the rectangular stress block recommended in the ACI code (4-2), the resisting moments of the section (with no strength reduction factors) are 126 kip-in for positive bending and 122 kip-in for negative bending. However, the maximum experimental positive and negative moments were 110 kip-in and 95 kip-in, respectively.

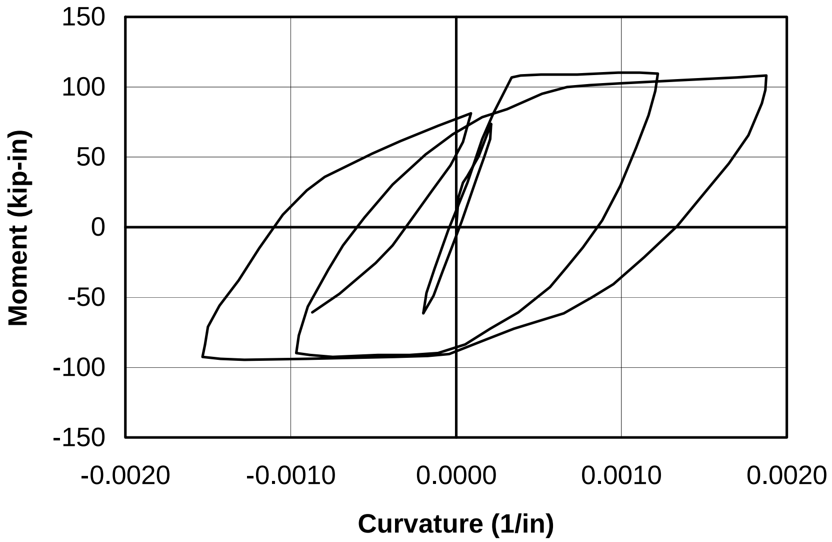

Figure 4.3 - Experimental Response (adapted from 4-15)

The analytical prediction of the response of the section provided by program IDARC2D is shown in Figure 4.4 compared to the experimental results. For this figure the IDARC2D model assumed no strain hardening in the reinforcing bars and the default values of the hysteretic parameters (provided in Section 3.3.4) were used.

The prediction of the response during the initial cycle is dominated by the uncracked stiffness which is significantly larger than the experimental stiffness. Although it is clear that the experimental strength was over-predicted (by approximately 10% in the positive direction and 25% in the negative direction), IDARC2D estimates closely the expected ACI strength.

The predicted unloading stiffnesses are generally somewhat larger than those obtained during testing. In contrast, the predicted reloading stiffnesses are considerably smaller than the experimentally measured stiffnesses, introducing pinching in the computed hysteresis loops.

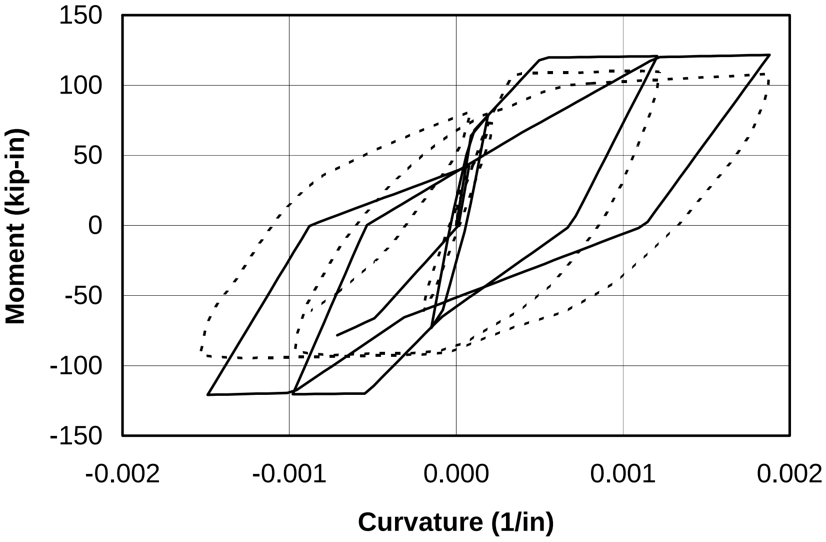

Figure 4.4 - IDARC2D Prediction (Before Adjusting Hysteretic Parameters) Compared with Measured Response

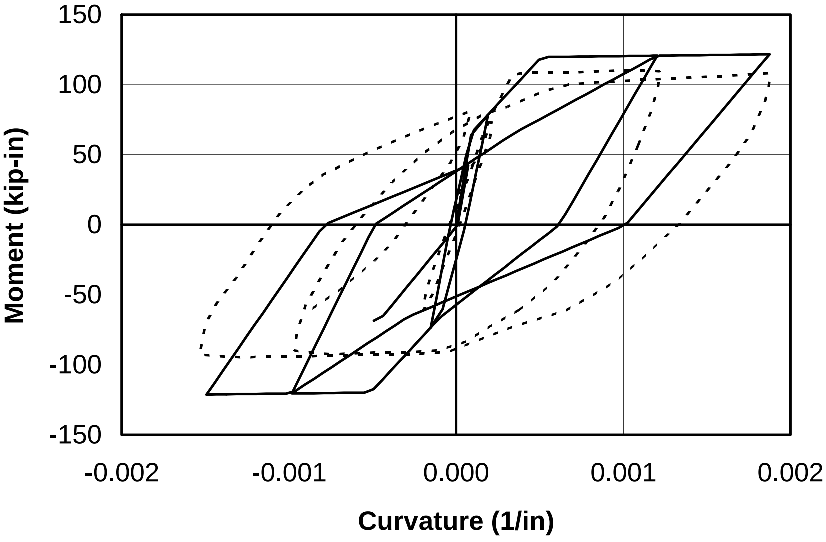

Figure 4.5 - IDARC2D Prediction (After Adjusting Hysteretic Parameters) Compared with Measured Response

These differences in unloading and reloading stiffnesses cause a significant reduction in the size of the simulated hysteresis loops and therefore, the computed response underestimates the energy dissipation of the beam.

In an attempt to match the beam's cyclic behavior the hysteretic parameters of the program were adjusted. The energy-related strength deterioration parameter HBE was set to 0.0, while the stiffness degradation parameter HC was set to 1.5. The computed response of the modified IDARC2D model is shown in Figure 4.5. Despite the fact that no slip or strength deterioration is allowed in the model (HS was still set to 1.0), the predicted stiffness upon load reversal is always lower in the IDARC2D model than in the actual test, introducing pinching into the computed response.

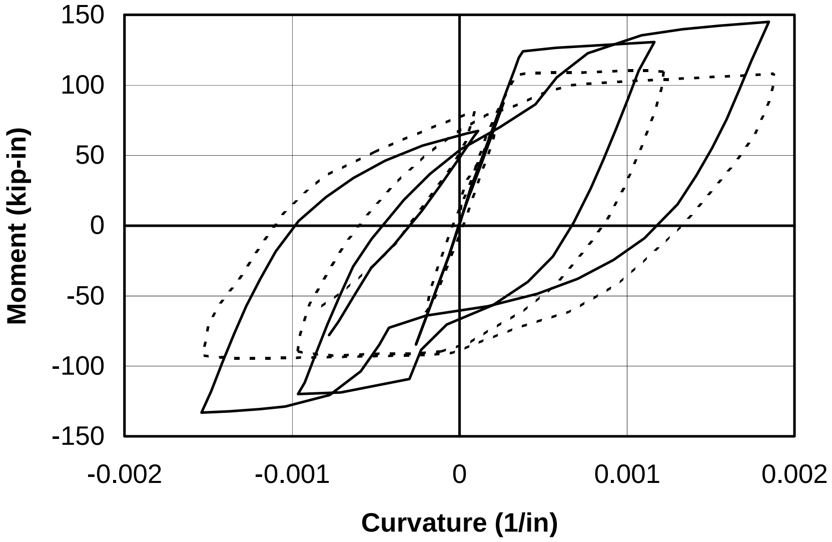

Figure 4.6 - FIBERC Prediction Compared with Measured Response

Figure 4.6 shows the prediction of the section's response provided by program FIBERC compared with the experimental result. Similarly to the previous computer model, no strength hardening in the reinforcing bars was provided. The loading and unloading stiffness during the initial cycle is very closely predicted. As before, the moment strength is over-predicted (by approximately 30%), but this time it is even larger than the ACI estimate (by approximately 15% in the positive direction and 5% in the negative direction). However, the analytical unloading stiffness for all cycles is nearly parallel to the experimentally-obtained stiffness. Likewise, the predicted stiffness upon reversal of the load, is very close to that measured in the test. Though the overall shape of the FIBERC hysteretic cycles is quite similar to the experimental loops, an abrupt stiffness change upon crack closure is evident in the computed response which is absent in the test result.

4.2.2 Beam with Axial Load by Aoyama (4-5)

The test configuration is shown in Figure 4.7. The experiment, conducted at the University of Illinois, consisted of a single displacement-controlled cycle of transverse load while maintaining a constant axial load of 36 kips, which corresponded to a compression level of approximately $0.10f'_cA_g$.

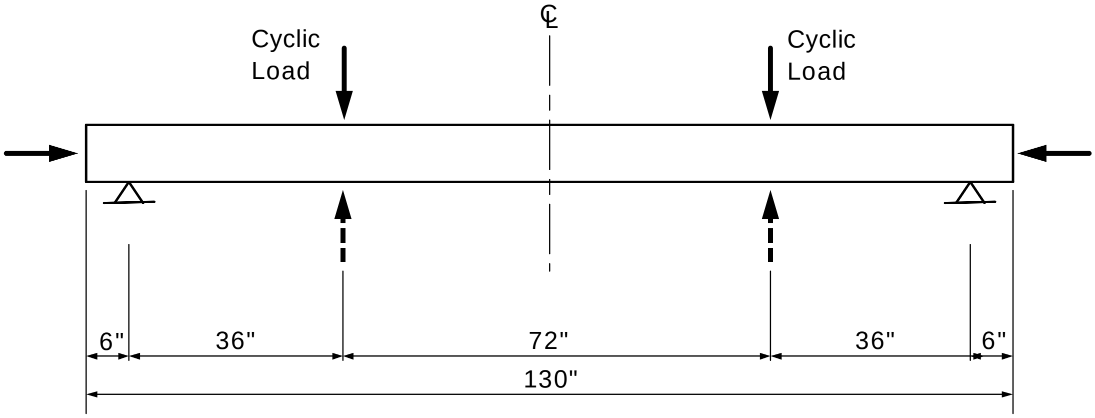

Figure 4.7 - Test Configuration (adapted from 4-5)

The average compressive strength of the concrete used was 4.9 ksi, and the average yield strength of the reinforcing steel was 50 ksi. No ultimate strength, strain at onset of strain hardening, or strain hardening modulus were reported by Aoyama (4-5).

The cross section of the tested beam is shown in Figure 4.8. Longitudinal reinforcement was continuous along the beam, and both the positive and negative reinforcement ratios ρ were equal to 0.015.

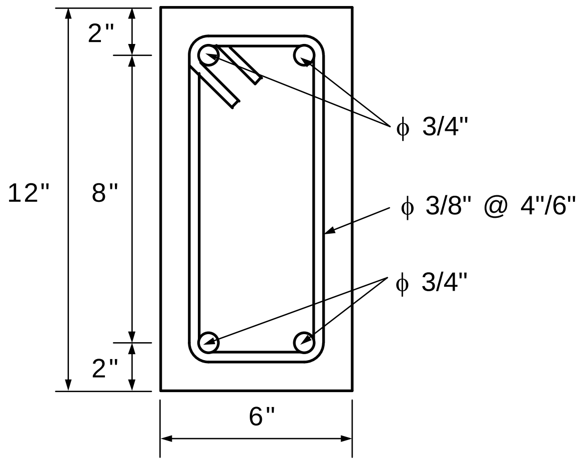

Figure 4.8 - Beam Geometry and Reinforcement (adapted from 4-5)

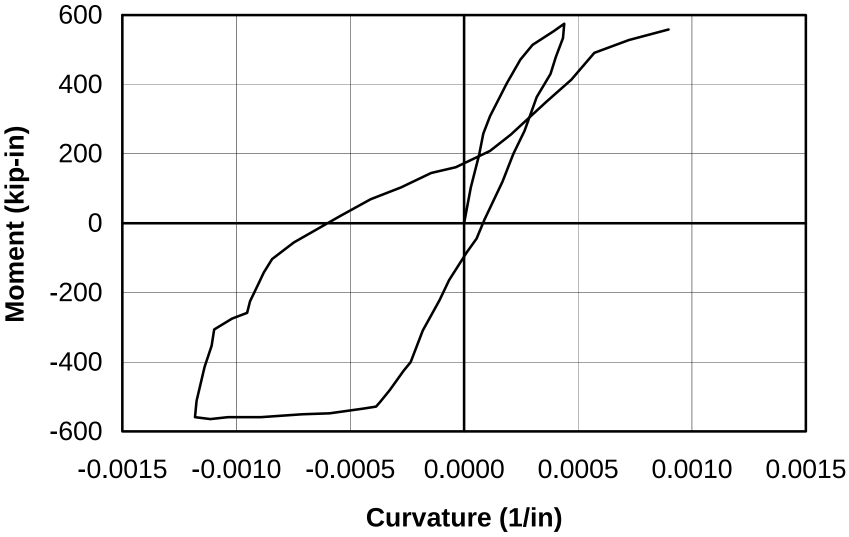

Figure 4.9 - Experimental Response (adapted from 4-5)

The hysteresis loop obtained during the test is presented in Figure 4.9, and corresponds to the moment-curvature behavior of the midspan section of the beam. The expected flexural strength for the pure bending condition (no axial load) is 396 kip-in, and is 552 kip-in for the constant axial load case. This latter strength was slightly exceeded (by 2% and 4%) for both the positive and negative directions. The response of the beam clearly exhibited some “pinching” of the hysteresis loop, which was likely a function of the axial load.

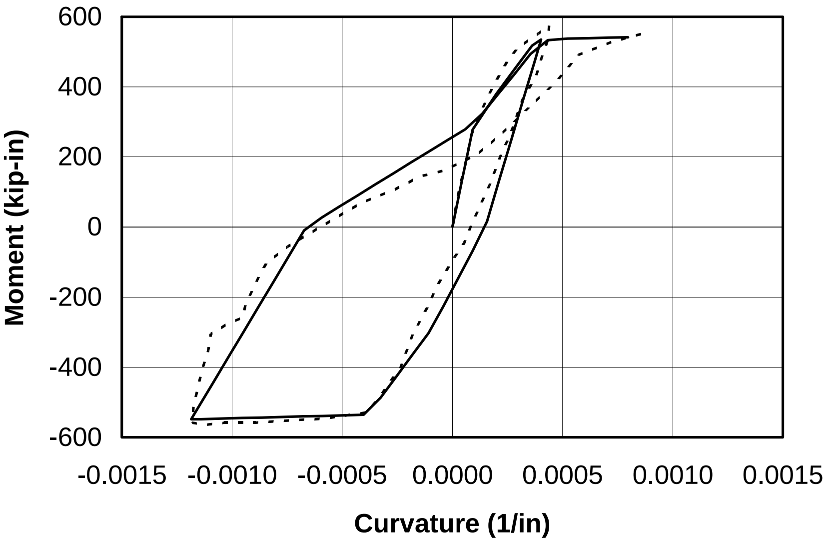

Figure 4.10 - IDARC2D Prediction (Before Adjusting Hysteretic Parameters) Compared with Measured Response

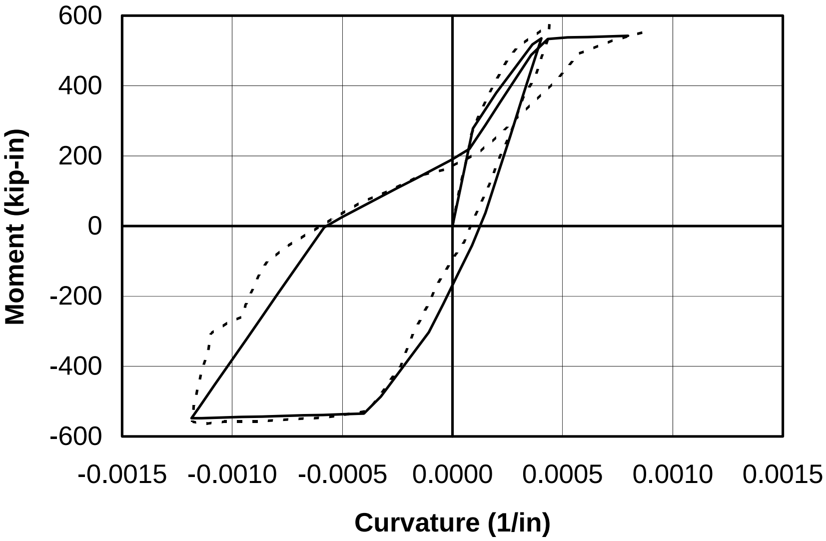

Figure 4.11 - IDARC2D Prediction (After Adjusting Hysteretic Parameters) Compared with Measured Response

Figure 4.10 presents the computed response of the beam using program IDARC2D with the hysteretic parameters set at their default values. Although the strength of the member is closely predicted, the unloading and reloading stiffnesses are overestimated. Therefore, the pinching of the computed hysteresis loops is not accurately reproduced.

The IDARC2D model was then modified in an attempt to obtain a more accurate computed response. A stiffness-degradation parameter HC of 1.4 and a pinching parameter HS of 0.4 were used in the modified model while the strength deterioration parameters were set at the default values.

As shown in Figure 4.11, after adjusting the hysteretic parameters the program IDARC2D generally predicts the experimental response of the beam section. The main differences between the predicted and actual loop are the initial strength and stiffness, which are both underestimated, and the stiffness of the second loading cycle (in the positive direction) which is overestimated.

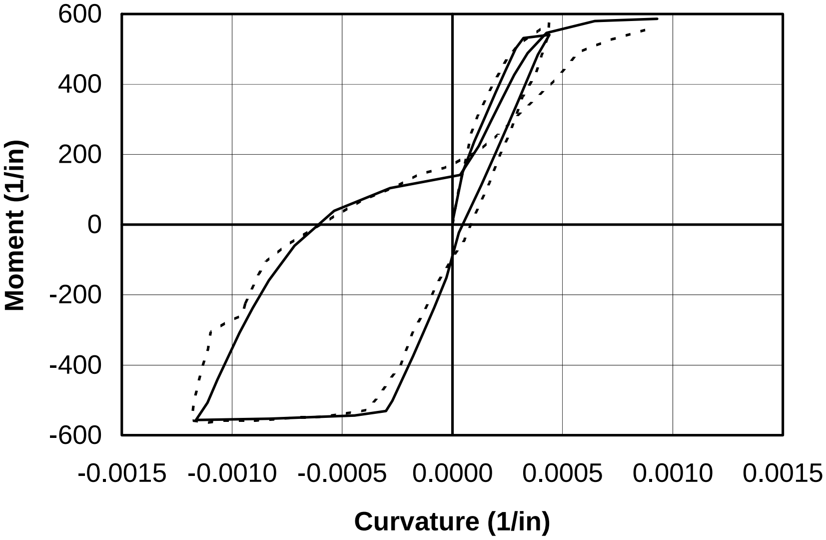

Figure 4.12 - FIBERC Prediction Compared with Measured Response

Finally, Figure 4.12 illustrates the predicted moment-curvature response produced by program FIBERC. In this case, both strength and stiffness are very closely predicted in both directions, except for the stiffness of the second loading cycle (in the positive direction) which is again overestimated. This seems to correspond with a faster crack closure in the analytical model than in the actual test.

4.3 Load-Displacement Response of Members

4.3.1 Cantilever Beam G4 by Hanks (4-11)

The test performed on this beam, shown in Figure 4.13, was part of a large testing program conducted at the University of Kansas. The compressive strength of the concrete used was 12.7 ksi, while the yield strength of the reinforcing steel was 69.4 ksi. Strain at the onset of strain hardening of the reinforcing bars was approximately 0.008 in/in, and the strain hardening modulus was approximately 1200 ksi or 4% of the elastic modulus (E_s = 29000 ksi). Ultimate strength of the reinforcing bars was not reported.

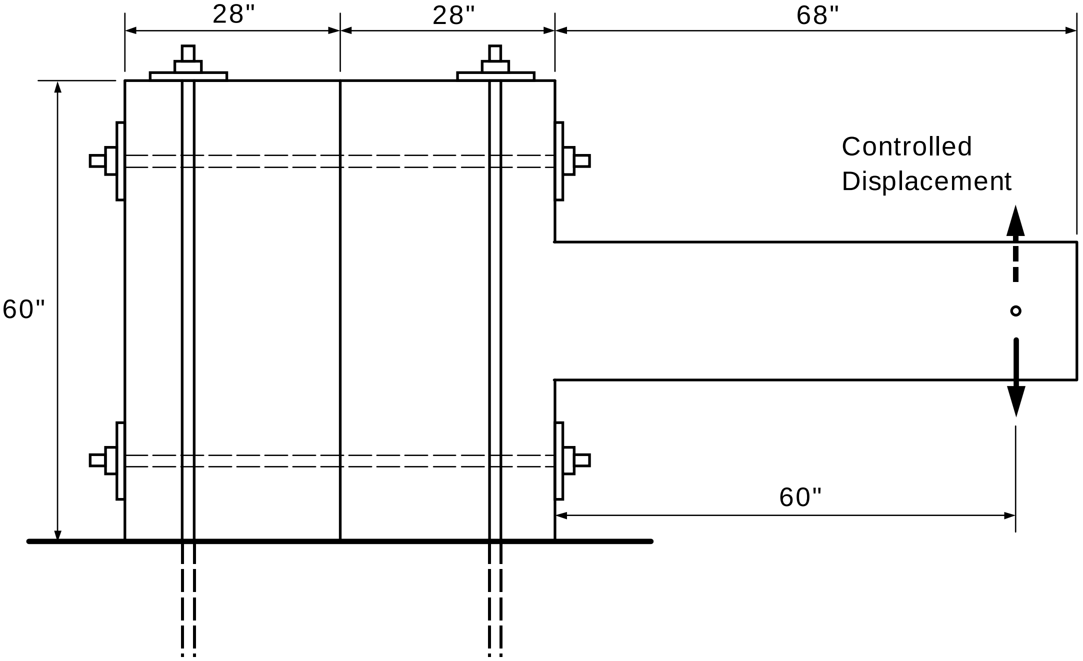

Figure 4.13 - Schematic of Experimental Set-up (adapted from 4-11)

The cross section of the tested beam is shown in Figure 4.14. The longitudinal reinforcement was continuous along the beam. The positive reinforcement ratio ρ was 0.010, while the negative reinforcement ratio was 0.005.

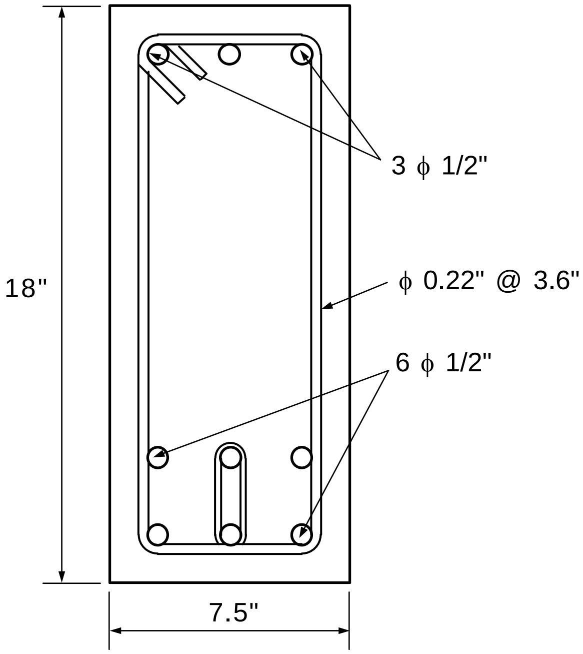

Figure 4.14 - Beam Geometry and Reinforcement (adapted from 4-11)

The load-displacement response of the beams to the first three cycles of displacement-controlled loading are shown in Figure 4.15. During the initial cycle the beam yielded, and in the two subsequent cycles a very large drift ratio of approximately 3% was imposed on the beam in both directions. These last two cycles exhibited by pinching of the hysteresis loops caused mainly by shear cracking. This was due to the fact that this was a relatively deep beam; its span to section depth ratio was 3.33.

The author of the test reported (4-11) a flexure-shear crack across the entire cross section and some spalling of concrete cover during the first cycle of load. With subsequent cycles, diagonal web cracks formed and further spalling occurred exposing the bottom reinforcement near the support face. At the end of the tests, wide inclined cracks and buckled reinforcement were clearly visible.

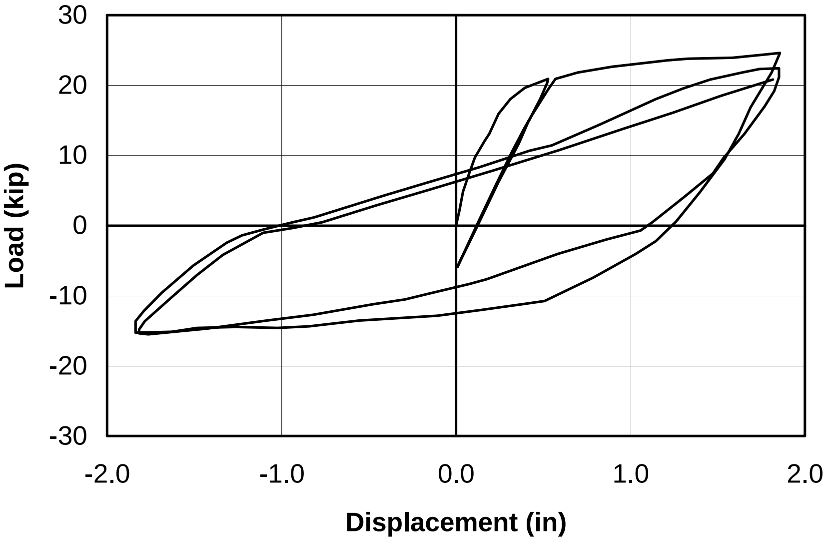

Figure 4.15 - Experimental Response (adapted from 4-11)

The computed positive flexural strength for the section was 1258 kip-in, while the negative flexural strength was 680 kip-in. These moments correspond with beam tip loads of 21.0 and 11.3 kips, respectively. However, the maximum experimental loads observed were 24.5 kips in the positive direction and 15.5 kips in the negative direction. The increase in capacity was mainly due to strain hardening of the reinforcement.

Figure 4.16 presents the prediction of the load-displacement behavior computed using program IDARC2D, together with the experimental response, for a model in which the hysteretic parameters were set to their default values.

For this model, the levels of strength for the large-displacement cycles are generally well-estimated (within 10%) in the negative direction but not very well in the positive direction (within 20%). In contrast, the stiffnesses at loading, unloading and load reversal are not accurately predicted. In particular, the loading and unloading stiffness for the first cycle are significantly overestimated by IDARC2D. On the other hand, the estimated unloading stiffness from the maximum positive moment for the two subsequent cycles is somewhat lower than the experimentally obtained stiffness. Finally, unloading stiffness from the maximum negative moments is again overestimated.

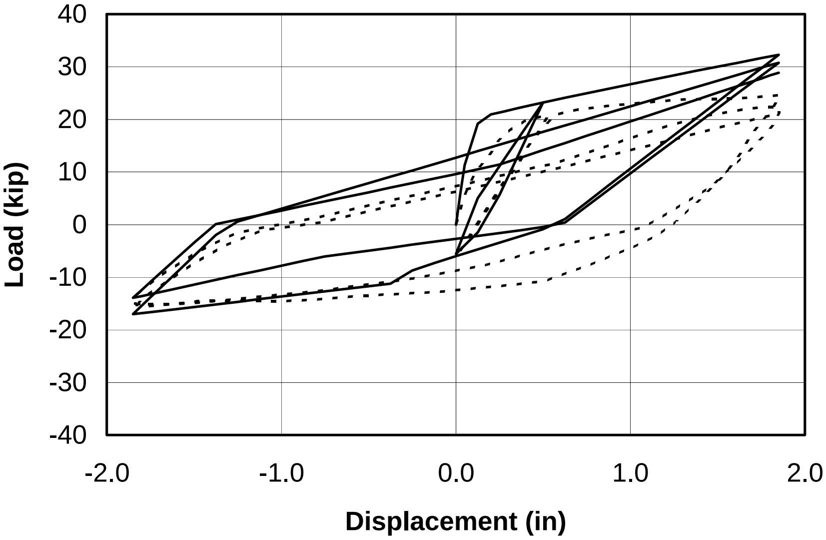

Figure 4.16 - IDARC2D Prediction (Before Adjusting Hysteretic Parameters) Compared with Measured Response

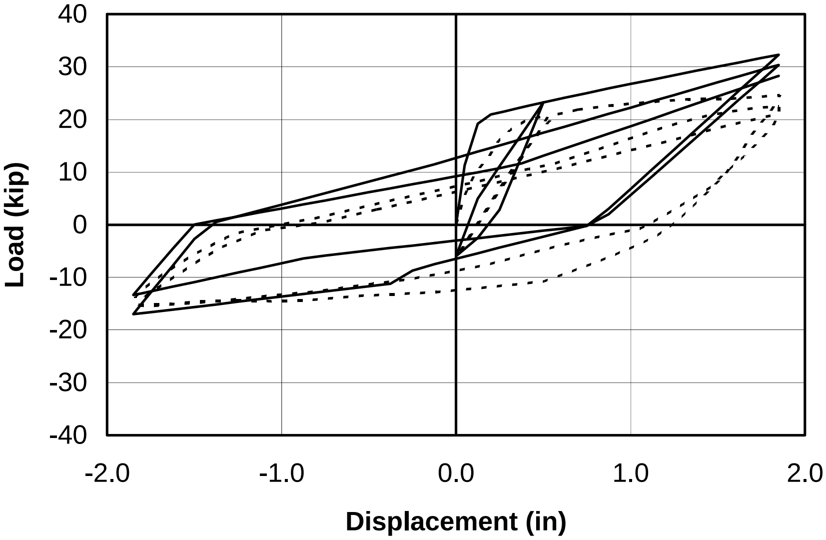

Figure 4.17 - IDARC2D Prediction (After Adjusting Hysteretic Parameters) Compared with Measured Response

Figure 4.17 shows the computed response of the beam after the original IDARC2D model was modified using a stiffness-degradation parameter HC of 3.0. The other parameters were maintained at their default values. This model gave, on average, a closer prediction (in terms of stiffness) to the experimental response.

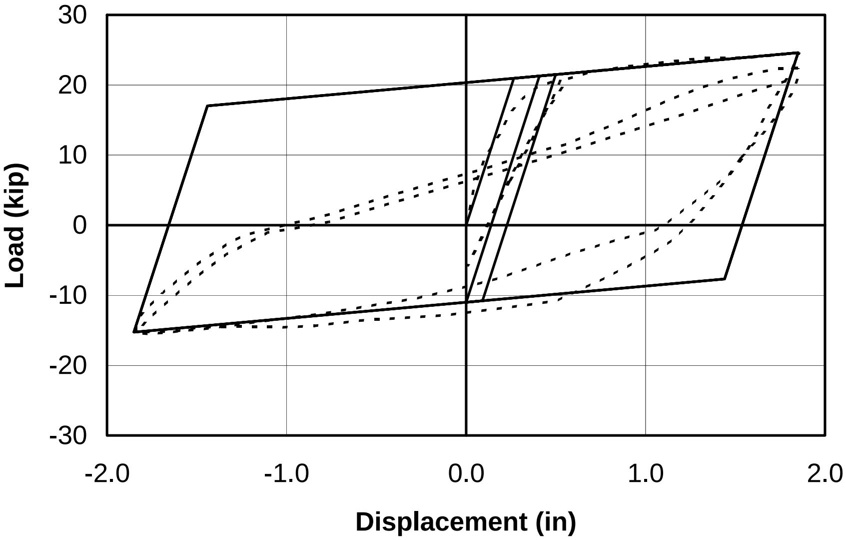

Figure 4.18 - DRAIN-2DX Prediction Compared with Measured Response

A model of the beam using the program DRAIN-2DX was developed and subjected to the same history of displacement-controlled loading as the test beam. The computed load-displacement response is shown in Figure 4.18 together with the experimental response. In general, the strength of the beam is well estimated. However, the elasto-plastic hysteresis loops do not reproduce well the stiffness degradation. Therefore, the energy absorption of the beam is grossly overestimated.

The prediction of the load-displacement behavior obtained using the program FIBERC is shown in Figure 4.19. In this case, the overall shape of the experimental and computed hysteresis loops is relatively similar. However, the stiffness and strength of the initial loading branch in the positive direction are over-estimated. During subsequent cycles, both strengths and stiffnesses in the negative direction are close to the experimental values, except for the reloading stiffness upon reversal of load after the maximum negative moment excursion. In particular, the increase in stiffness after crack closure is again overemphasized. Furthermore, the strength in the positive direction is always over-estimated by approximately 20%.

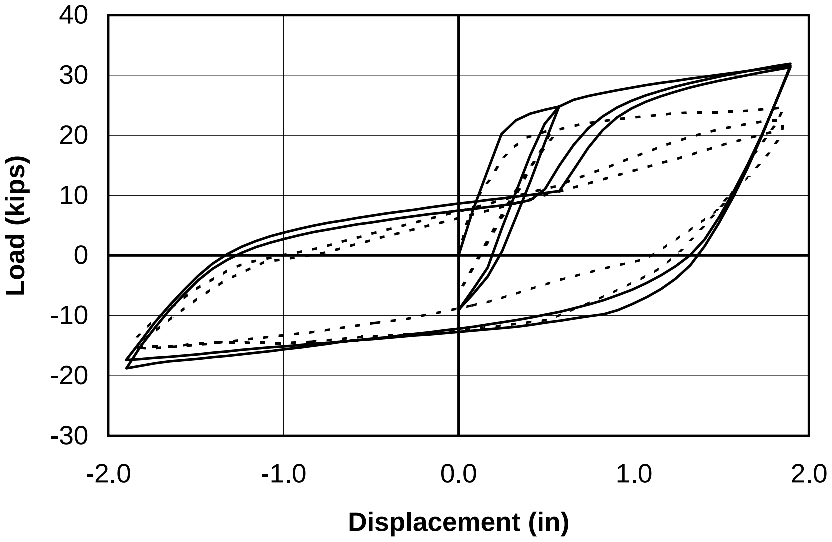

Figure 4.19 - FIBERC Prediction Compared with Measured Response

4.3.2 Cantilever Beam by Popov, Bertero and, Krawinkler (4-19)

This beam was tested at the University of California, Berkeley, to investigate the effect of large shear forces on the strength, stiffness and energy absorption capacity of reinforced concrete beams. A schematic of the test set-up as well as the geometry and reinforcement in the beam are shown in Figures 4.20 and 4.21.

The longitudinal reinforcement is continuous along the beam, and both the positive and negative reinforcement ratios ρ are equal to 0.016. The specimen analyzed here, Beam 35, is one of three tested in the study by Popov et al.

The concrete compressive strength was 3.86 ksi at the time of testing. Yield strength was 67.0 ksi for the longitudinal bars and 53.0 ksi for the stirrups. Ultimate steel strength was 103.0 ksi for the longitudinal bars and 90.0 ksi for the stirrups.

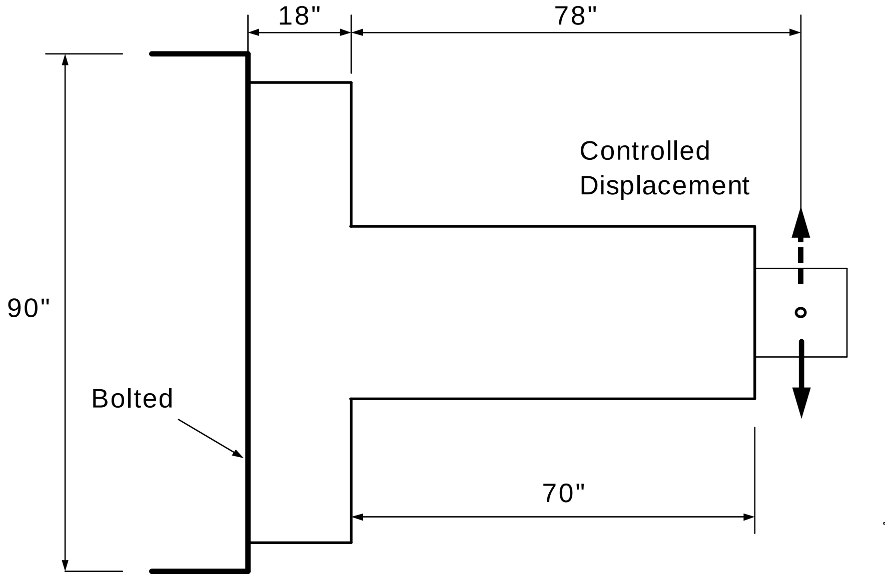

Figure 4.20 - Experimental Set-up (adapted from 4-19)

Neither the strain at the onset of strain hardening nor the strain-hardening modulus were explicitly reported. However, a tension stress-strain plot for the longitudinal reinforcement was included in an appendix of the report by Hanks (4-19). From that diagram, the strain at the end of the yield plateau was 0.009 in/in, and the strain-hardening modulus was approximately 3.6% of the elastic modulus.

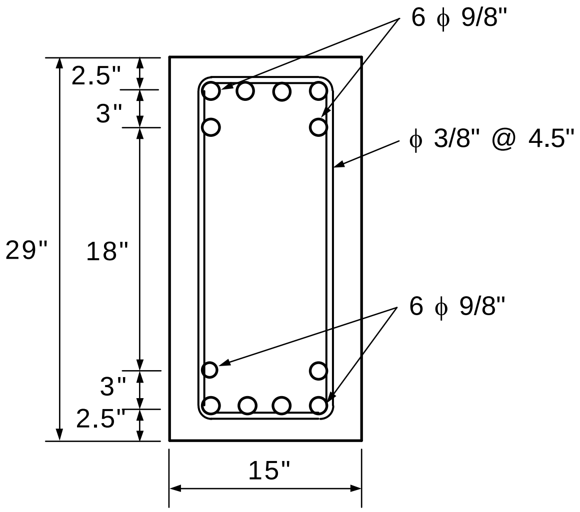

Figure 4.21 - Beam Geometry and Reinforcement (adapted from 4-19)

Figure 4.22 shows the experimental load-displacement response of the beam. Pinching of the hysteresis loops is evident and occurred due to the shear strength deterioration in the element. The computed flexural capacity of the beam is 8509 kip-in in both directions which corresponds with a tip load of 109.1 kips. However, the maximum loads obtained during the tests were 129.6 kips in the positive direction and 132.4 kips in the negative direction. This difference, of approximately 20%, can be attributed to the strain hardening of the reinforcing steel.

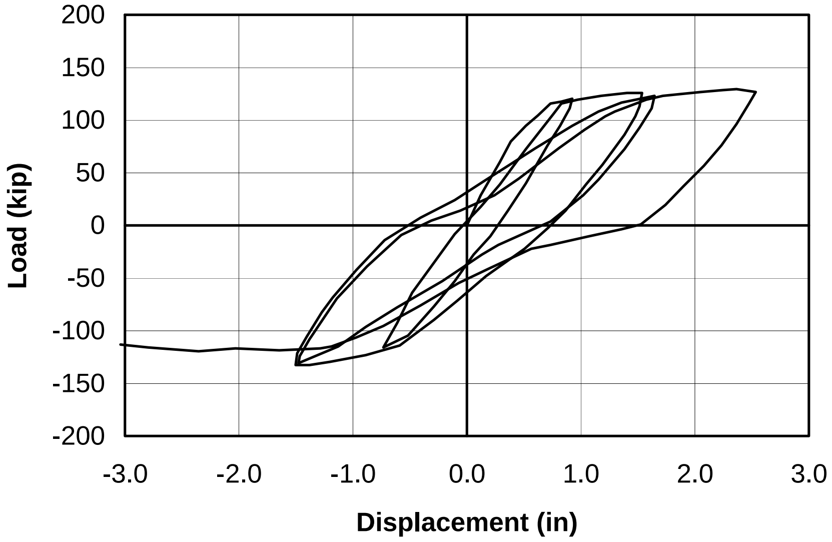

Figure 4.22 - Experimental Response (adapted from 4-19)

The load-displacement response of the beam was simulated using the program IDARC2D. The computed response obtained assuming default values for the hysteretic parameters is shown in Figure 4.23. The strain-hardening modulus used for the reinforcing bars was approximately 3.0% of the elastic modulus.

In this case, the overall shape of the hysteretic loops is reasonably accurate, both in terms of stiffness and strength. However, the initial stiffness computed by IDARC2D is significantly larger than the experimental stiffness. And, the strength in the positive direction is over-estimated by approximately 20%.

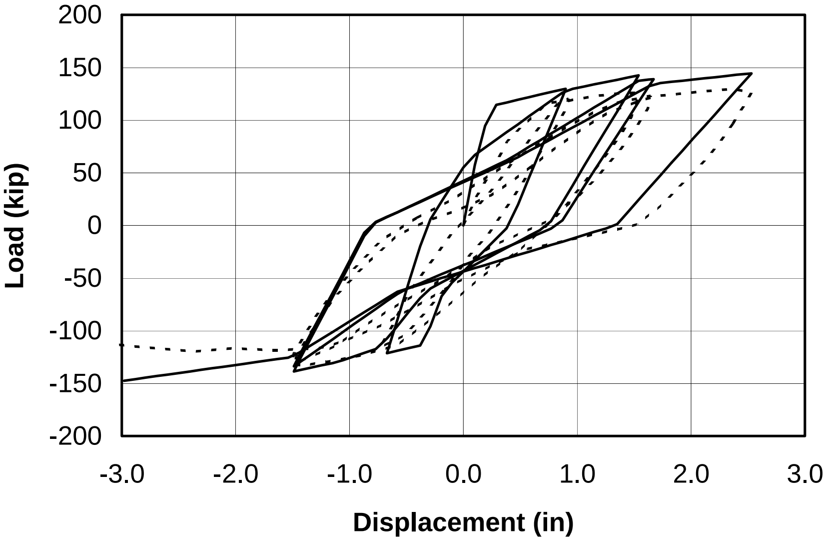

Figure 4.23 - IDARC2D Prediction (Before Adjusting Hysteretic Parameters) Compared with Measured Response

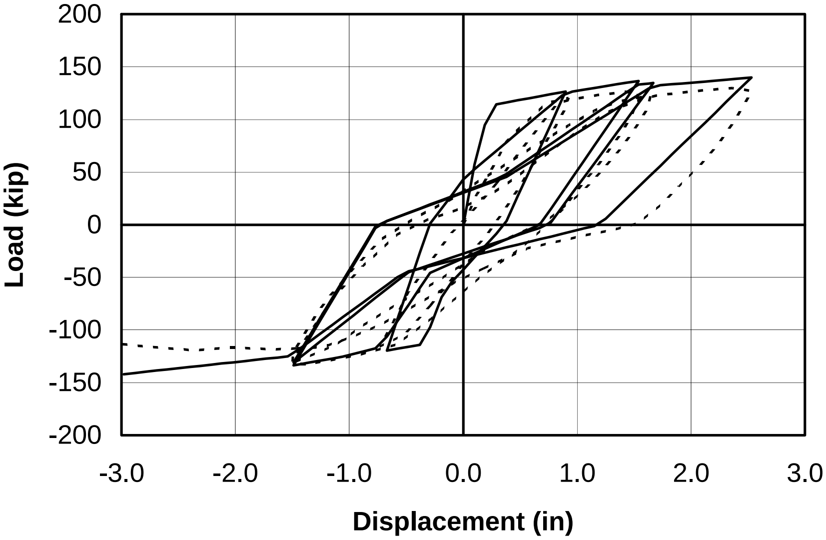

Figure 4.24 - IDARC2D Prediction (After Adjusting Hysteretic Parameters) Compared with Measured Response

In order to improve the simulation of the stiffness degradation, the parameter HC was set to 1.5. Likewise, to model the pinching of the hysteretic loops, the parameter HS was adjusted to 0.4. The computed response of the modified IDARC2D model, shown in

Figure 4.24, is slightly closer to the experimental response than that obtained by the original model.

Figure 4.25 shows the load-displacement response as predicted by program DRAIN-2DX. As in Section 4.3.1, the response computed using this program is far from the actual behavior in terms of the loading and unloading stiffnesses. However, the strength levels are very closely estimated in both directions, except at the largest displacement in the negative direction where the load reaches again approximately 150 kips.

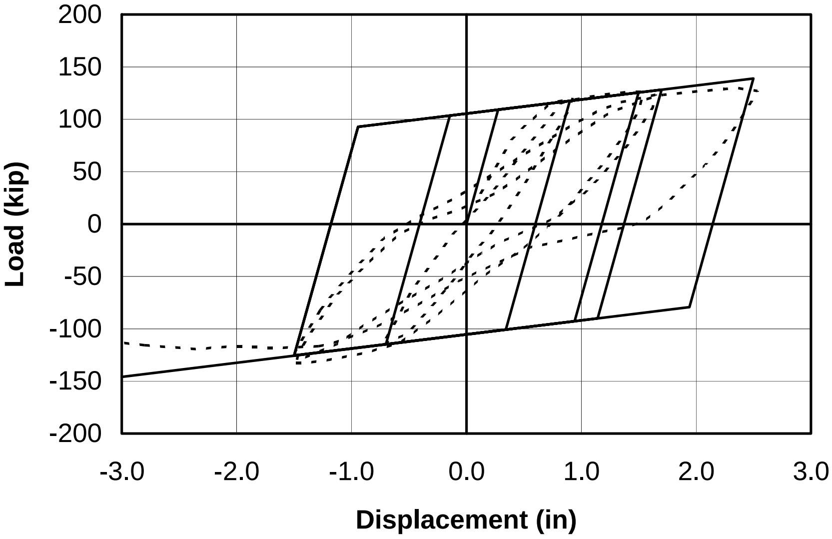

Figure 4.25 - DRAIN-2DX Prediction Compared with Measured Response

The load-displacement response computed by program FIBERC is shown in Figure 4.26. An average post-yield stiffness of 2% of the elastic modulus was chosen for the reinforcing bars in this model.

The initial stiffness as well as the unloading stiffnesses for subsequent cycles are clearly overestimated. Strength in the positive direction is also overestimated significantly (approximately 30%) while in the negative direction, it is relatively closely predicted (within approximately 10%). No pinching effect is reproduced, as is expected from a regular fiber-element idealization. Consequently, the predicted hysteretic energy dissipation is much larger than the actual energy dissipation.

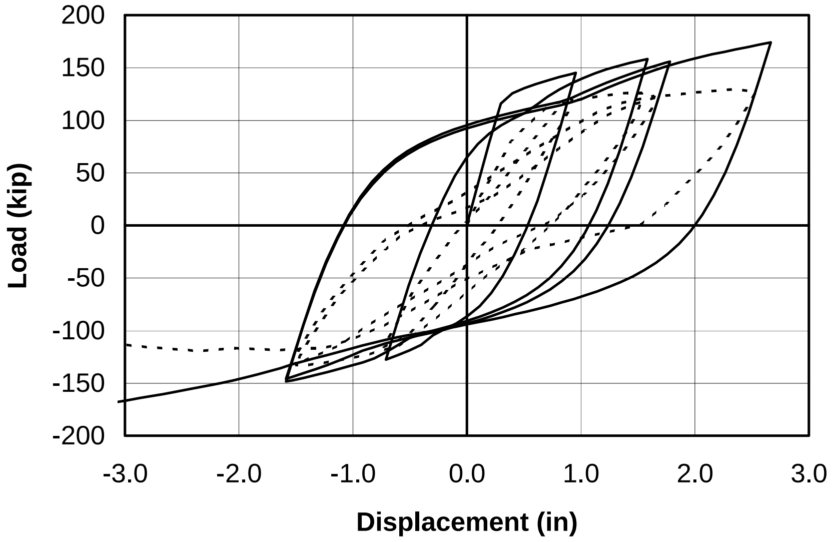

Figure 4.26 - FIBERC Prediction Compared with Measured Response

4.4 Quasi-Static Response of Two-Story Frame (4-10, 4-21)

4.4.1 Description of Structure and Test Procedure

The test structure consisted of a large-scale single span, two-story plane frame built integrally with a massive, heavily-reinforced foundation beam. It was cast horizontally and then lifted to its final vertical position after a 14-day curing period. The base beam was then post-tensioned to the laboratory strong floor, virtually fixing the column bases and preventing lateral sliding of the system. The detailed geometry of the frame is shown in Figure 4.27 (all dimensions in this figure are in millimeters).

All members had a rectangular cross section of 300 mm by 400 mm, reinforced longitudinally with No. 20 bars and transversely with No. 10 bars spaced 125 mm center to center. Typical cross sections for beams and columns are shown in Figure 4.28 (all dimensions in this figure are in millimeters).

Both concrete and reinforcement samples were tested on the first day of testing. Concrete compression tests were performed on standard cylinders using a stiff machine in stroke-control mode. A concrete compressive strength of 30 MPa was found. For the main reinforcing bars, a yield stress of 418 MPa and a modulus of elasticity of 192,500 MPa were obtained. The average strain-hardening modulus was 3100 MPa, and the onset of strain hardening occurred at approximately 0.009 in/in. For the transverse reinforcement, a yield strength of 454 MPa and an ultimate strength of 340 MPa were measured.

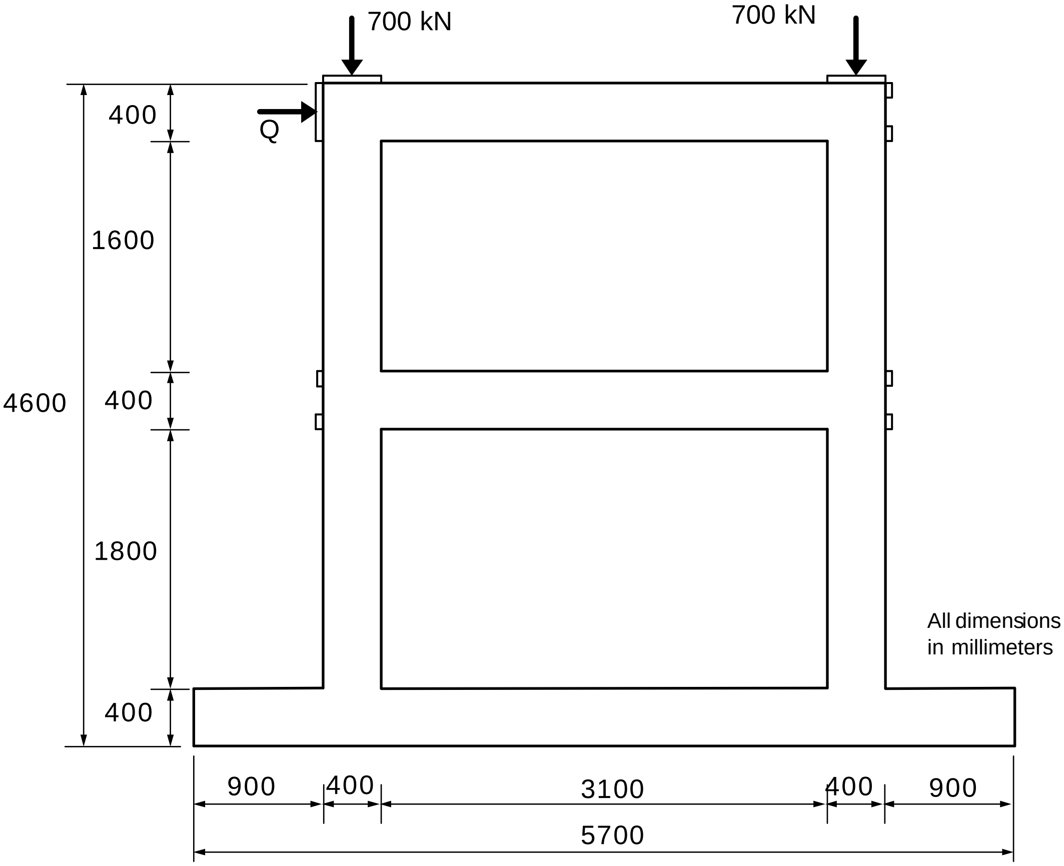

Figure 4.27 - Schematic of Experimental Set-up (adapted from 4-10)

Loading consisted of 700-kN constant axial loads on the columns and a quasi-static lateral load controlled by the horizontal displacement of the top-level beam. Instrumentation of the specimen consisted of displacement transducers for lateral deflections, demountable gages for surface strains, strain gages for reinforcing bar deformations and load cells for measuring the load applied by actuators.

The first part of the series of tests was initiated with the application of axial loads on the columns (force-controlled mode). Then, the frame was subjected to a series of repeated monotonic loadings with increasing maximum lateral displacements until the lateral capacity of the frame was reached. Details of this series are given in Section 4.4.2.

During the second part of the test series, reversed cyclic loads were applied to the frame. This was done in three stages, with several cycles and increasing maximum displacements for each stage. A complete description of this series of tests and their results are presented in Section 4.4.4.

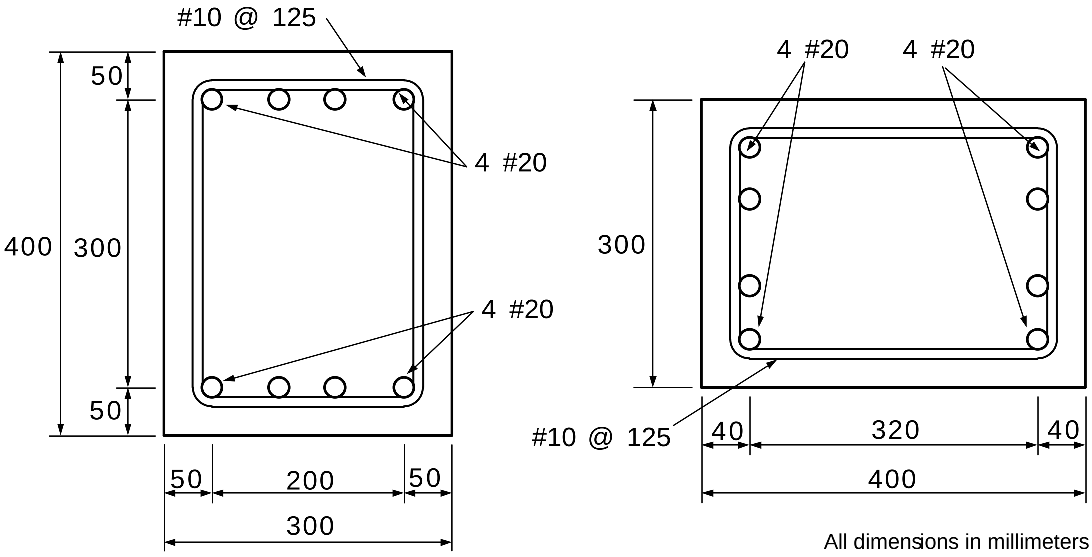

Figure 4.28 - Beam and Column Geometry and Reinforcement (adapted from 4-10)

4.4.2 Repeated Loading Test Results

The load-displacement response of the frame, in terms of applied load, Q (equal to the base shear), versus the horizontal displacement of the top beam, is shown in Figure 4.29. A similar plot is shown in Figure 4.30 comparing the load-displacement responses at the first (solid line) and second (dashed line) levels.

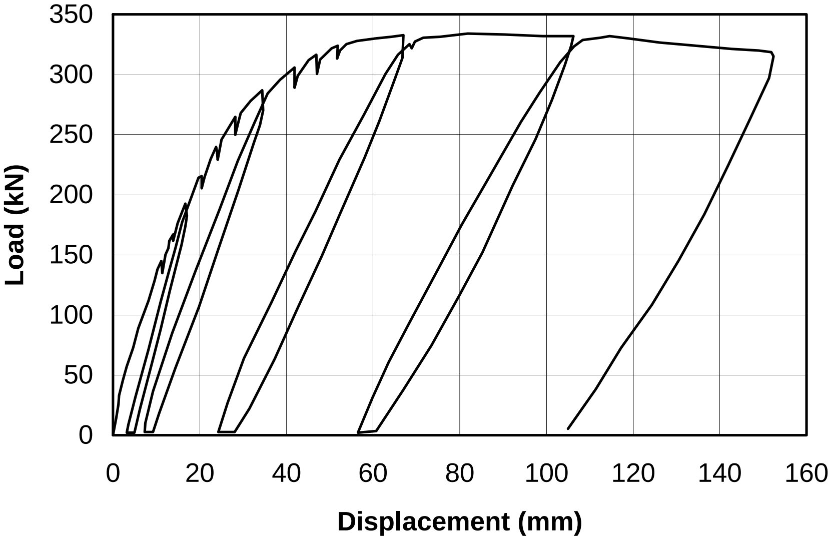

Figure 4.29 - Experimental Response at top beam (adapted from 4-10)

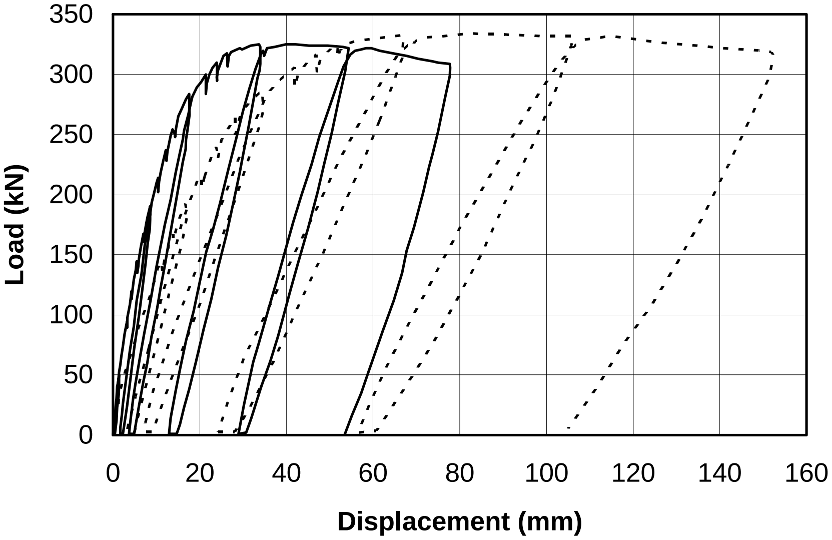

Figure 4.30 - Experimental Response at first- and second-floor beams (adapted from 4-10)

The initial experimental stiffness of the frame was approximately 20 kN/mm. First cracking was reached in the first-story beam at approximately 50 kN, causing the first noticeable reduction in stiffness to approximately 15 kN/mm. At a load of 145 kN flexural cracking at the column base occurred together with web shear cracks in the first-story beam, further reducing the stiffness to approximately 8 kN/mm.

First yielding of reinforcement in the first-story beam occurred at approximately 260 kN leading to a noticeable reduction in the lateral stiffness of the frame to approximately 5 kN/mm. As the load approached 323 kN yielding of all column-base reinforcement and concrete spalling occurred, effectively generating plastic hinges. At a slightly larger load (329 kN) hinging developed at the ends of the top-story beam. After this stage stiffness reduced to zero but strength was maintained for large deformations (an overall displacement ductility of approximately 5 was measured).

The ultimate lateral load was approximately 330 kN and was reached at a drift ratio of 2.0% (approximately 80 mm). The collapse mechanism involved hinges at the ends of the beams and at the base of first-story columns. Although response was mainly in flexure, shear cracks developed in beams and columns.

Figure 4.29 shows clearly the degradation in unloading and reloading stiffness with increasing deformations and number of cycles. For the initial cycles both the unloading and reloading stiffnesses were between 11 kN/mm and 15 kN/mm. For the large-deflection cycles, the unloading stiffness was initially approximately 8 kN/mm reducing to 5 kN/mm while the reloading stiffness was approximately 7 kN/mm.

4.4.3 Analytical Predictions of the Repeated Loading Experimental Response

First, program IDARC2D was used to simulate the response of the frame. The load-displacement response for this case is shown in Figure 4.31, for which the model assumed default values for the hysteretic parameters. The initial stiffness predicted by IDARC2D is very close to the experimental stiffness (20 kN/mm). However, this stiffness is maintained for high levels of load (up to approximately 150 kN) while the actual stiffness dropped approximately 25% at 50 kN. First yielding in the first-floor beam was detected by IDARC2D at approximately 250 kN, which was in close agreement with the experimental occurrence.

At a drift ratio of 2.0% (approximately 80 mm), the predicted lateral strength is approximately 310 kN, that is, approximately 7% less than the actual strength of the frame. However, the predicted strength of the structure grows with increasing deflection, and at approximately a drift ratio of 3.6% (approximately 150 mm), it reaches a load of 330 kN.

The predicted unloading and reloading stiffnesses are generally in good agreement with the experimental results. In particular, the degradation of stiffness with increasing deformations and number of cycles is reproduced well, although slightly underestimated.

In an attempt to match the unloading and reloading stiffness a new IDARC2D model was created using a modified set of hysteretic parameters. The parameter values used for the new simulation were HC=3.5 and HBE=HS=0. Figure 4.32 shows the computed response for this model. The stiffnesses for the initial cycles are slightly overestimated while the stiffness of final unloading branch is very close to the experimentally observed stiffness.

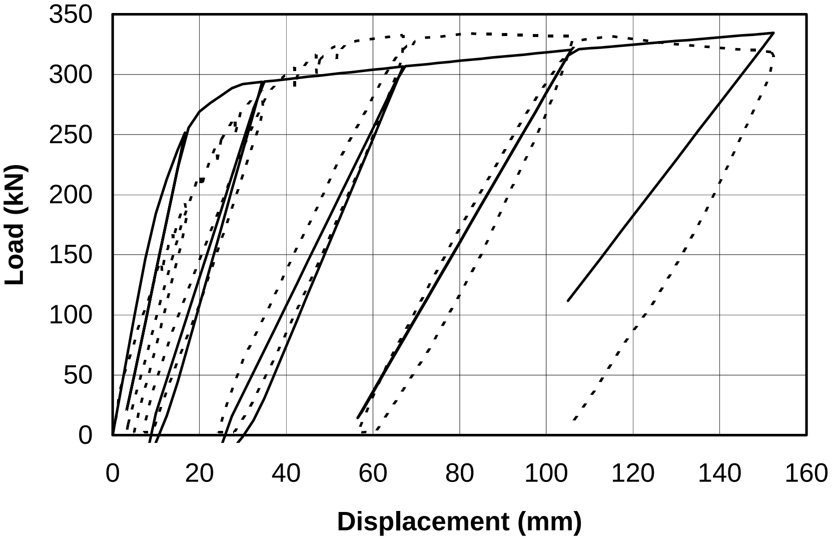

Figure 4.31 - IDARC2D Prediction (Before Adjusting Hysteretic Parameters) Compared with Measured Response

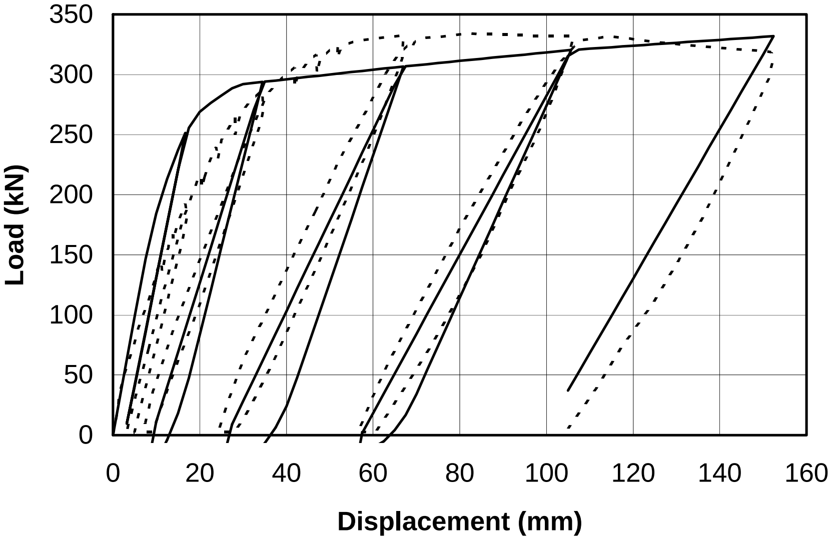

Figure 4.32 - IDARC2D Prediction (After Adjusting Hysteretic Parameters) Compared with Measured Response

The IDARC2D model develops plastic hinges in the base of the columns and at the ends of beams. The first-story column top ends are predicted to remain elastic during the response, while both ends of the second-story columns are predicted to crack. These results are in general agreement with the experimental observations discussed in Section 4.4.2.

Figure 4.33 shows the load-displacement response computed using the DRAIN-2DX program. The predicted initial stiffness is approximately 10 kN/mm, which is approximately half of the experimental initial stiffness. This stiffness is maintained for all unloading and reloading branches of subsequent cycles.

The predicted yielding of the structure takes place at only 210 kN, while in reality it occurred at approximately 260 kN. Furthermore, the estimated strength at 2.0% drift ratio (approximately 80 mm) barely reached 260 kN which corresponds to less that 80% of the actual strength at that displacement. Finally, the maximum base shear predicted by this model was slightly over 270 kN (82% of the experimental strength) at a drift ratio of 3.6% (150 mm).

The poor performance of this model is due mainly to the absence of interaction between axial loads and bending moments. Also, the elasto-plastic nature of the hysteretic element response does not permit a realistic representation of the unloading and reloading stiffness degradation.

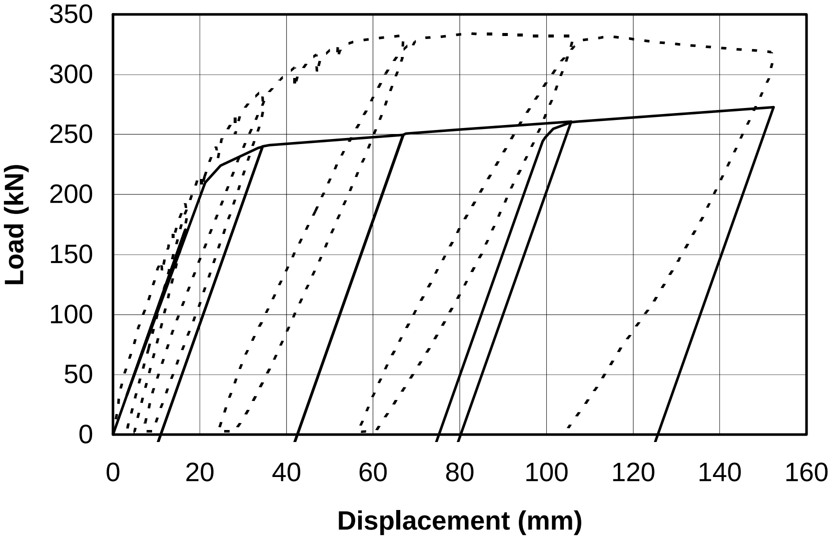

Figure 4.33 - DRAIN-2DX Prediction Compared with Measured Response

Finally, it is worth mentioning that the model predicts plastic hinges not only at the column bases and beam ends, but also at the column top ends. This again may be a consequence of the lack of axial load and moment interaction.

Figure 4.34 presents the load-displacement response computed with program FIBERC. The predicted initial stiffness of the structure is slightly lower that the experimental result. However, the program simulates closely the gradual reduction in stiffness as the applied load increases. First yield is estimated at a lateral load of approximately 240 kN (8% lower than the actual yield load). The predicted lateral capacity of the frame was nearly 310 kN (approximately 95% of the experimental strength) and was reached at a drift ratio of approximately 2.0% (80 mm). For larger deflections and subsequent cycles, the estimated capacity of the frame is maintained approximately constant up to a drift ratio of 3.6% (approximately 150 mm). The predicted unloading and reloading stiffnesses for late cycles are close to the experimentally obtained stiffnesses.

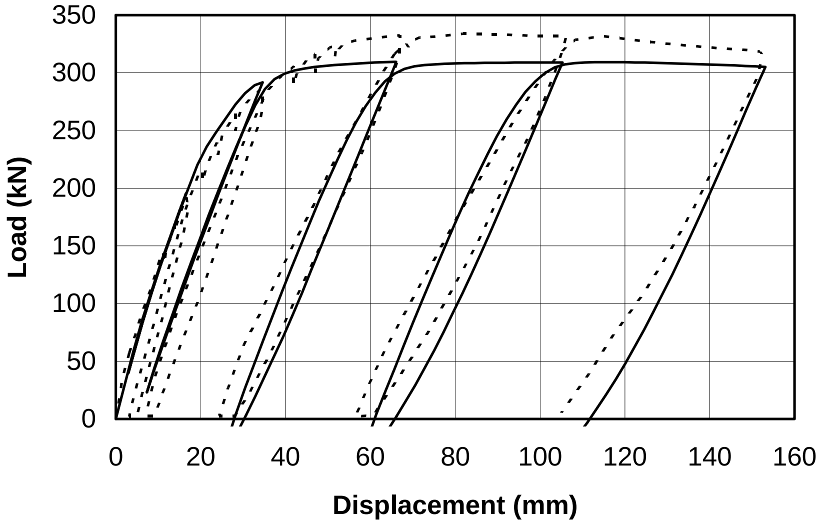

Figure 4.34 - FIBERC Prediction Compared with Measured Response

The FIBERC model exhibits significant yielding at the column bases and beam ends. The computed response at the top of the first-story and bottom of second-story columns is basically elastic, while at the top of the second-story column shows cracking and some yielding. In general, this prediction coincides with the experimental response described in Section 4.4.2.

4.4.4 Reversed Cyclic Loading Test Results

A second series of tests were conducted on the damaged structure, immediately after the repeated loading series, to evaluate its response to reversed-cyclic loads. Initially, the specimen was pulled back to a top lateral displacement of approximately 50 mm. Then, a sequence of five displacement-controlled loading cycles was applied, with a maximum displacement of ±25 mm. The second stage of the reversed-cyclic load series involved excursions of ±55 mm of top floor lateral displacement, and the last sequence of cycles was applied with excursions of ±65 mm of top floor lateral displacement. Figure 4.35 compares the typical load-displacement responses for all three levels of cyclic load displacements. The figure illustrates the reduction in stiffness that occurred with increasing displacement amplitude and number of cycles.

Observations after the series of tests (4-10) indicated that widespread crushing of concrete at the top and bottom of all beam ends had occurred. Likewise, extensive spalling of concrete at the bottom of the columns was observed. Additionally, diagonal concrete crushing in the first-story beam was detected. Finally, large permanent rotations at the ends of the beams were observed.

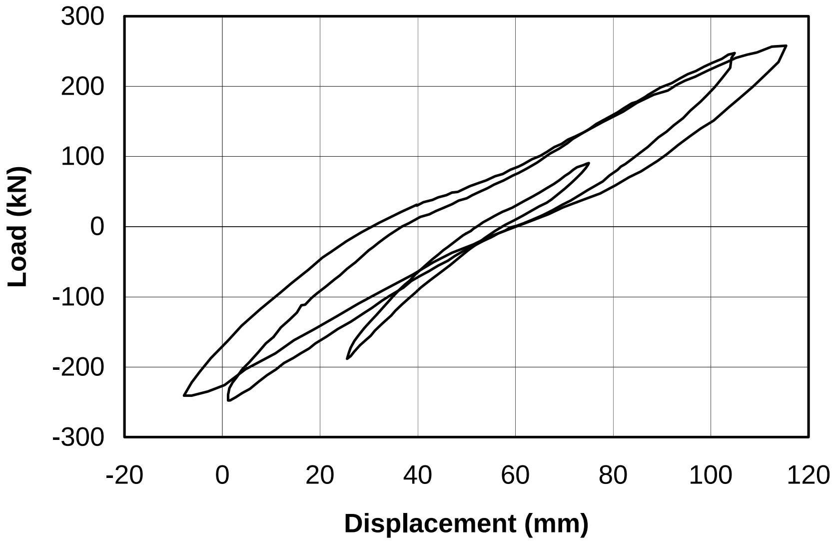

Figure 4.35 - Experimental Response (adapted from 4-10)

4.4.5 Analytical Prediction of Reversed Cyclic Loading Results

Using the programs IDARC2D, DRAIN-2DX and FIBERC, the analytical model of the damaged frame was subjected to the history of displacements corresponding with the repeated-load history before the frame was subjected to the history of cyclic displacements.

Figure 4.36 displays the computed cyclic response of the frame using the program IDARC2D compared to the experimental response (shown with a dashed line). In general, the program does not reproduce accurately the measured behavior in terms of either strength or stiffness, even though the hysteretic parameters were readjusted repeatedly to try to match the experimental response. The difference in predicted and actual strength at maximum displacement in the negative direction is more than 40%. On the other hand, the unloading stiffness from the positive side, is not too different from the experimentally observed stiffness. However, the unloading stiffness from the negative excursions is generally far too stiff. Furthermore, pinching of the hysteretic loops is not reproduced.

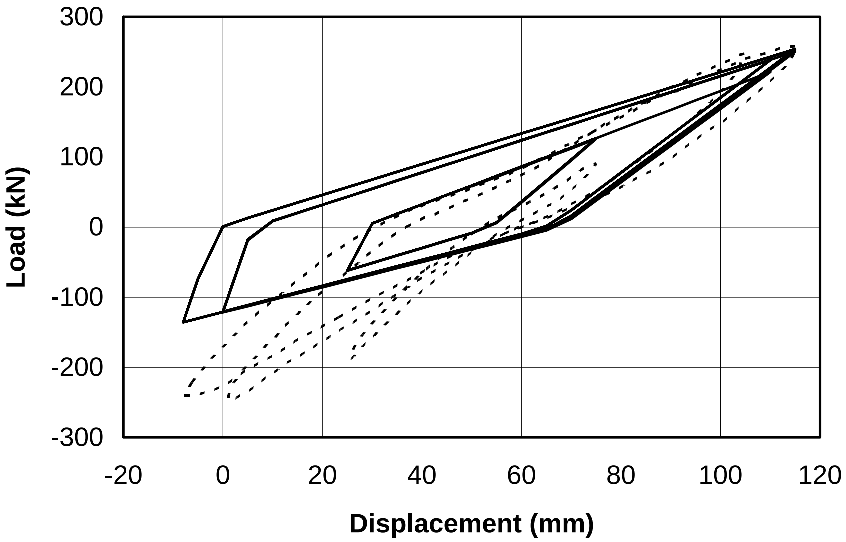

Figure 4.36 - IDARC2D Prediction of Cyclic Response (typical loops)

An explanation for the poor prediction provided by IDARC2D for the cyclic-loading case can be inferred from Figure 4.37, in which both the repeated and reversed loading cycles are included. It is clear from Figure 4.37 that the unloading stiffness in the positive direction estimated by the program IDARC2D indicates a significant degradation while the unloading stiffness for the opposite direction is very close to the elastic stiffness. In contrast, the experimental response shows similar degradation in unloading stiffness regardless of the direction of the reversed load. It is concluded then, that the IDARC2D model is unable to effectively predict the hysteretic response of the frame when the deformation history is not symmetric with respect to the zero-deflection axis.

The hysteretic response computed by the program DRAIN-2DX is shown in Figure 4.38. As expected, the response computed by this program is essentially elasto-plastic and therefore, the response is grossly misrepresented in terms of stiffness and energy dissipation (as measured by the area inside the hysteretic loops). The levels of force at maximum displacement for the large-deflection cycles, however, are closely matched by the model.

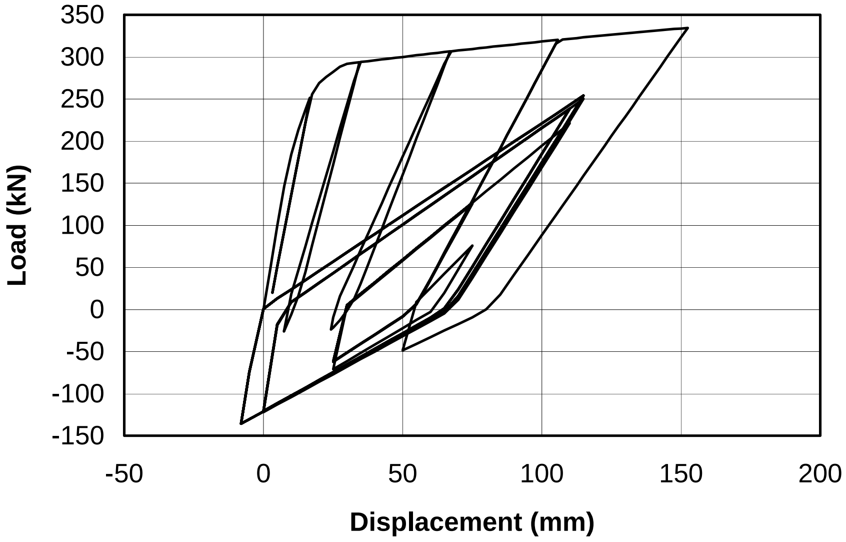

Figure 4.37 - IDARC2D Prediction of Complete Cyclic Response

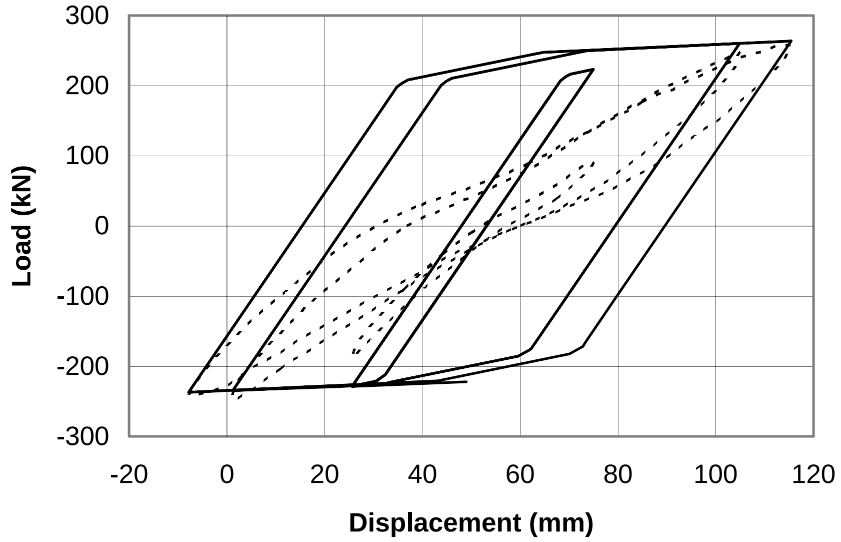

Figure 4.38 - DRAIN-2DX Prediction of Cyclic Response (typical loops)

Shown in Figure 4.39 is the hysteretic response of the frame computed by the program FIBERC together with the experimental response. For this case, the strength level and unloading stiffnesses are generally well predicted for all stages of maximum deflection. However, because of the nature of the model, the pinching of the loops (due mainly to shear deformation and anchorage slip) is not reproduced and therefore, the energy dissipation of the structure is significantly overestimated.

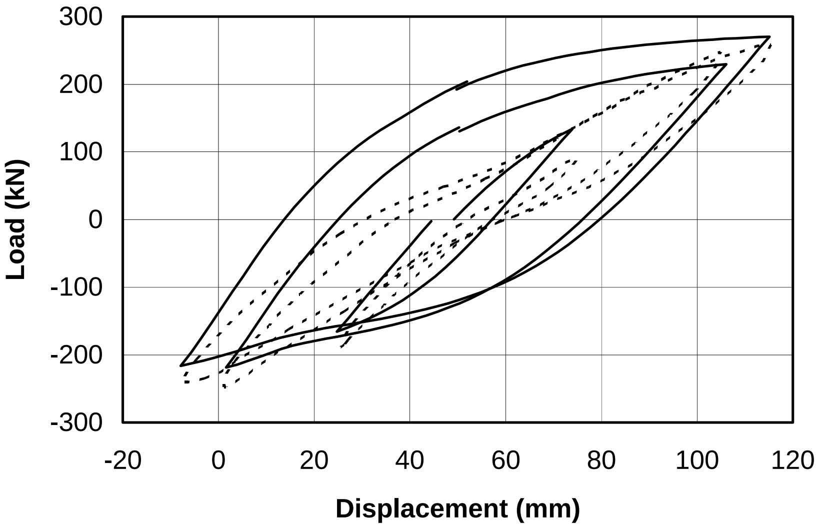

Figure 4.39 - FIBERC Prediction of Cyclic Response (typical loops)

4.5 Pseudo-Dynamic Response of Four-Story Building (4-12, 4-14)

A full-scale four-story reinforced concrete building was tested under simulated seismic loads at the European Laboratory for Structural Assessment (ELSA) of the Joint Research Center (JRC) of the European Commission as part of a comprehensive testing program “to contribute to the advancement of safety evaluation of structures subjected to seismic action by developing damage indicators and failure criteria for plastic hinge regions (4-14).” That program consisted of several phases of analytical and experimental efforts leading to the pseudo-dynamic test of the building.

Details of the structure and the base motion used to test the structure are presented in Section 4.5.1, while a brief description of the pseudo-dynamic approach is given in Section 4.5.2.

The overall experimental results are then described in Section 4.5.3. These results however, are based on preliminary reports (4-12, 4-14) and therefore, lack some aspects of the response that would be of interest for the present study. Nonetheless, a complete analysis of the results together with responses computed using the programs IDARC2D, DRAIN-2DX and FIBERC are presented in Section 4.5.4.

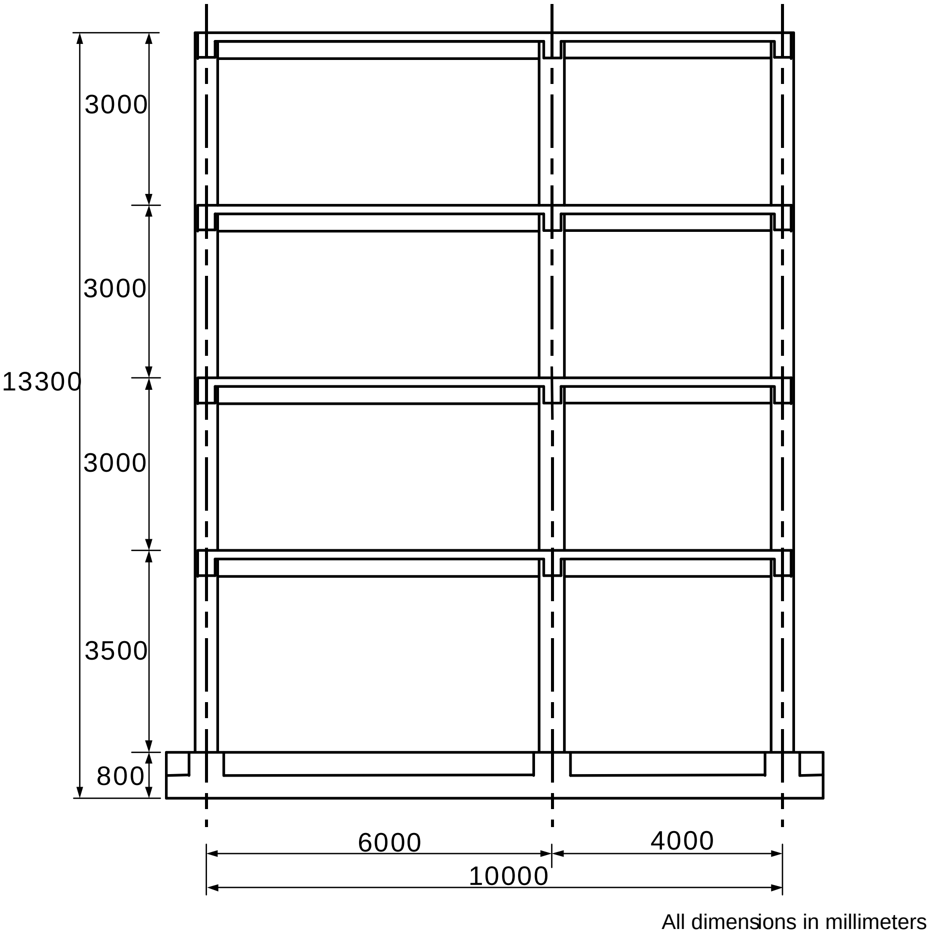

Figure 4.40 - Elevation of Building (Adapted from 4-14)

4.5.1 Description of Building and Testing Procedure

The test structure was a four-story frame system supported by a grid of deep foundation beams that were in turn attached to the strong floor of the laboratory. As shown in elevation in Figure 4.40, the interstory heights were 3.50 m for the first floor and 3.0 m for the other floors, for a total height of 12.5 m from the base of the columns to the roof. All dimensions in Figure 4.40 are in millimeters.

The plan of the building was square with 10.0 m sides from center to center of exterior columns. As shown in Figure 4.41, the building was symmetric in the direction of testing having two 5.0 m spans. In the transverse direction the building was asymmetric with spans of 6.0 m and 4.0 m. This created a more realistic layout and provided the possibility of evaluating the effect of plan irregularity in the building response if eventually tested in the transverse direction.

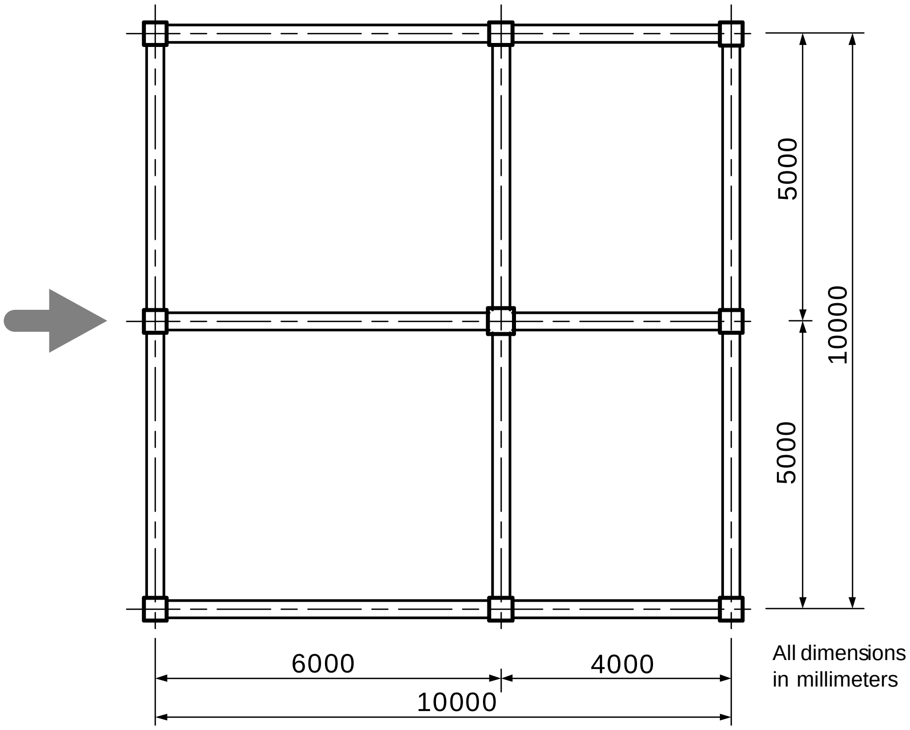

Figure 4.41 - Elevation of Building (Adapted from 4-14)

All exterior columns were square with 400 mm sides, and the single interior column, which is also square, had 450 mm sides. Beams in all floors were rectangular with a depth of 450 mm and a width of 300 mm. All beams were cast integrally with a solid 150 mm thick slab, and therefore they all behaved as T beams. Figure 4.42 shows a typical beam and slab cross section while Figure 4.43 displays typical cross sections for the interior and exterior columns.

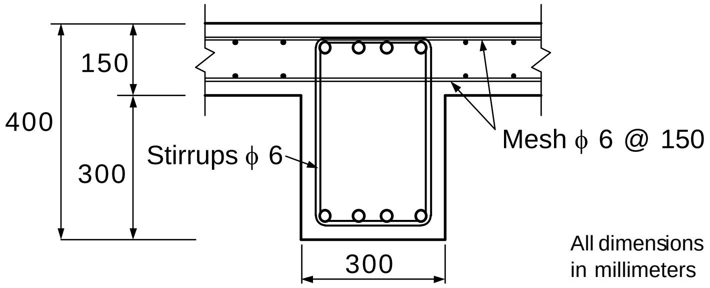

Figure 4.42 - Typical Cross Section of Beam and Slab (Adapted from 4-14)

All structural elements used normal-weight high-strength concrete. The average compressive strengths for all floors, shown in Table 4.1, were obtained using standard cube specimens. The reinforcing bars and welded meshes used for all beams, columns and slabs were grade 500 Tempcore. According to References 4-17 and 4-18, this steel has a nominal strain at failure of less than 12% and a low tensile failure strength-to-yield strength ratio (approximately 1.16).

Table 4.2 summarizes the main properties of the bars used. An average yield strength of 560 MPa was adopted for the analysis.

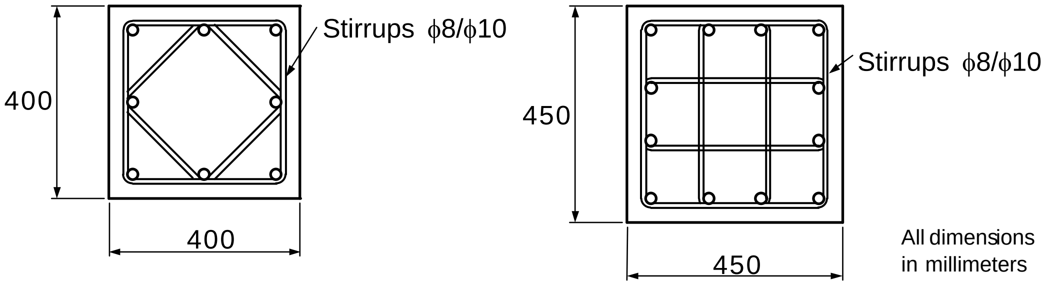

Figure 4.43 - Typical Cross Section of Exterior and Interior Columns (Adapted from 4-14)

Table 4.1 - Compressive Concrete Strength, MPa (Adapted from 4-14)

FLOOR	COLUMNS	SLABS
1st	49.8	56.4
2nd	47.6	53.2
3rd	32.0	47.2
4th	46.3	42.1

Table 4.2 - Reinforcing bar Tensile Properties (Adapted from 4-14)

Diameter (mm)	**Area (mm^2)**	**f_y (MPa)**	**f_u (MPa)**
6	29.2	566.1	633.5
8	51.4	572.5	636.1
10	80.3	545.5	618.8
12	113.1	589.7	689.4
14	153.3	583.2	667.4
16	199.2	595.7	681.0
20	310.0	553.5	660.0
26	517.2	555.6	657.3

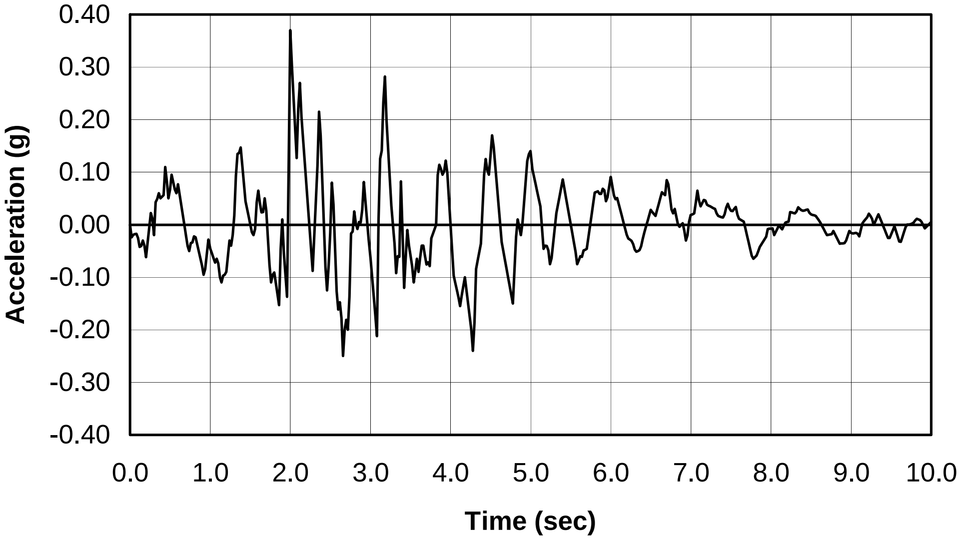

Figure 4.44 - Ground Acceleration Record (Adapted from 4-14)

The ground motion acceleration imposed on the test building during the pseudo-dynamic test was artificially generated using the wave forms from the actual 1976 Friuli Earthquake. Figure 4.44 shows the record of the ground motion acceleration that was digitized from Reference 4-14.

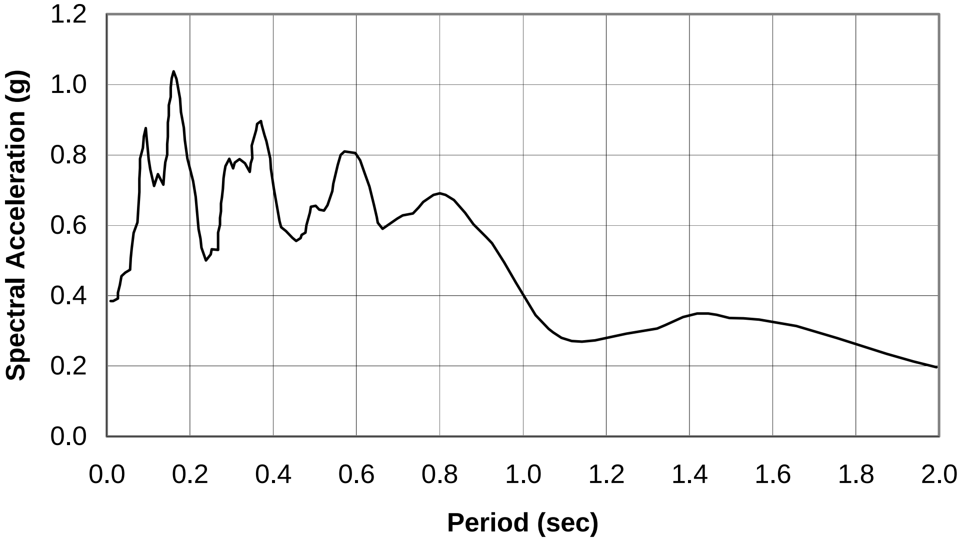

Figure 4.45 - Digitized Elastic Response Spectrum (Adapted from 4-14)

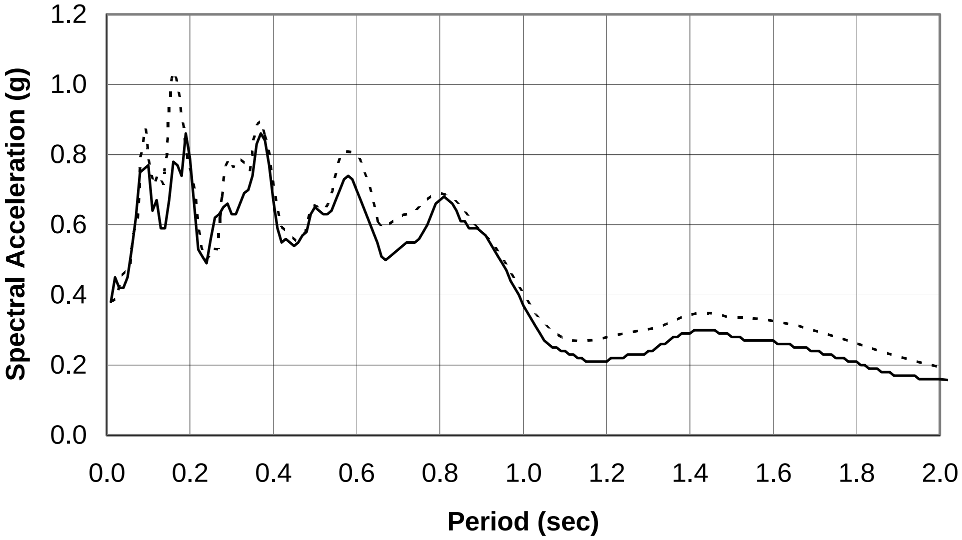

Figure 4.46 - Computed vs. Digitized Elastic Response Spectra

Figure 4.45 displays the elastic acceleration response spectrum corresponding to the ground acceleration record used for the test (Figure 4.34) and 5% damping. This spectrum was also digitized from Reference 4-14.

Figure 4.46 illustrates the difference between the elastic response spectrum from the digitized ground motion acceleration record (solid line) and that digitized from the original research report (4-14). Differences in spectral accelerations of up to 30% are obtained for certain period ranges.

4.5.2 Discussion of the Pseudo-Dynamic Test Method (4-7)

A pseudo-dynamic test is actually a quasi-static test during which on-line computer calculations use experimental measurements of the actual properties and nonlinear response of the structure as input to provide realistic simulation of the dynamic response. The equations of motion for a discrete parameter model of the test structure are solved on-line using a step-by-step numerical integration method assuming certain inertial and viscous damping forces (modeled analytically). The nonlinear structural restoring forces are measured experimentally, accounting automatically for the hysteretic damping due to inelastic deformation and damage of the members.

A record of ground acceleration history is given as input data to the algorithm which then calculates the story lateral displacements for a small time step. These displacements are then applied to the structure by servo-controlled hydraulic actuators attached to a reaction wall or frame. Load-cells on the actuators measure the forces necessary to achieve the required deformation (the structural restoring forces) and these are then used in the next step of the calculation. Because the inertia and damping forces are analytically modeled, there is no need to perform the test in real time.

One of the major advantages of this method is the possibility to test very large models using a limited hydraulic power requirement, as opposed to shaking-table tests that are restricted to components or small-scale models of large structures. The second major advantage is the possibility to monitor very closely the progression of damage in the structure and to stop at any moment for a detailed examination or to prevent complete collapse. However, shaking-table tests are needed when testing materials that have properties which are rate-dependent or when structures with fully distributed mass are investigated experimentally.

4.5.3 Experimental Results

A ‘low-level’ test was conducted before the actual test as a verification of the initial stiffness properties of the building, and as a rehearsal of the more demanding high-level test. The progression of cracking was evident, but apparently no yielding occurred. Inspection of the structure following the test revealed no new cracks other than the micro-cracking due to shrinkage which had been mapped prior to the test.

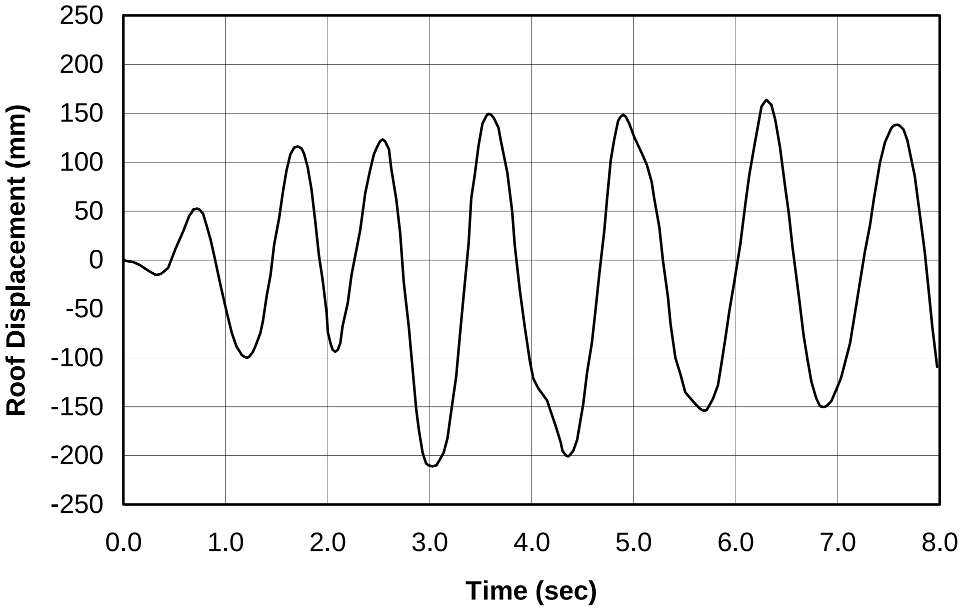

Figure 4.47 - Roof Displacement Time History (Adapted from 4-14)

The ‘high-level’ test was then performed. Apparently, very limited damage was sustained by the building during the high-level test. At the ends of the beams and columns in the first three stories cracks opened and subsequently closed. Only cracks at the interface between beams and columns remained open permanently and are evidence of local yielding of reinforcing bars. No spalling of concrete cover was observed. Likewise, no local buckling of reinforcing bars was detected. Figure 4.47 shows the displacement response at the roof, and Figure 4.48 displays the base-shear history.

Immediately following the high-level test, stiffness of the structure was measured. A fundamental period of 1.22 sec was measured, which was more than two times that of the virgin structure (0.56 sec). This indicated a change of stiffness beyond the "progression of cracking". However, the mode shapes measured were close to those of the virgin structure, which suggests that the structure was uniformly damaged (corresponding to an efficient energy-dissipating mechanism). The pattern of maximum rotations in the members appeared to correspond to a weak beam-strong column mechanism (limited to the first three stories).

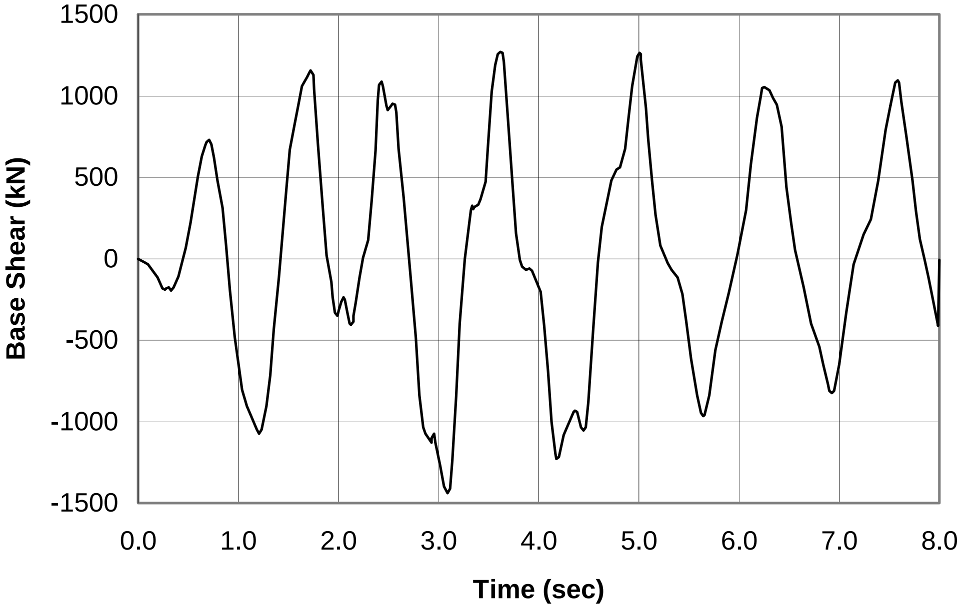

Figure 4.48 - Base Shear Time History (Adapted from 4-14)

Contribution of higher-mode forces was reported by the researchers (4-14) based on the time-history response of the individual story shears. The first two stories exhibited large energy dissipation, with large hysteretic loops, but some pinching. The third floor contributed little to the energy dissipation, and the fourth floor contribution was almost negligible (the amount of energy dissipated by the top level was an order of magnitude smaller than the energy dissipated by each of the other stories). The interstory drift at the second level was larger that at the first level. Figure 4.49 shows the load-displacement response of the structure, in terms of base shear versus roof displacement.

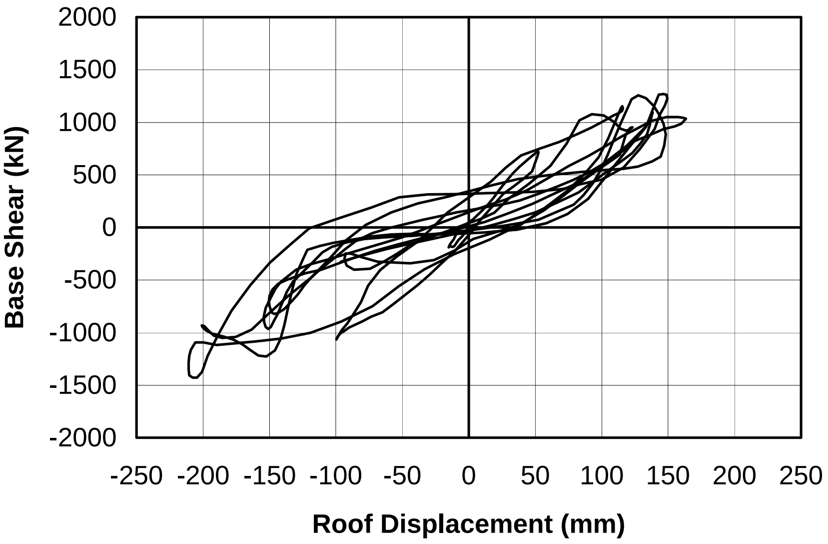

Figure 4.49 - Load-Displacement Response for High-Level Test (Adapted from 4-14)

One of the major unknowns about the complete behavior of an actual structure is the contribution of floor slabs to the lateral stiffness and strength of the building. For this structure, the participation appeared to be the same for the internal and external transverse frames for negative moments (tension on top). However, the effective width was greater for the internal transverse frame for positive moments (slab in compression).

The contributing slab width was estimated (4-14) assuming that axial deformations were due to membrane action of the slab only (neglecting independent bending of the slab) by summing up the portions of slab corresponding to each measurement location, multiplied by the ratio of the axial deformation to the axial deformation at the beam axis. It was also assumed that limited torsional resistance was provided by orthogonal beams (large torsion cracks occurred during the test).

4.5.4 Analytical Predictions of the Experimental Response

All analytical predictions of the seismic response of the structure presented in this section were performed using the interior frame only. Mass corresponding with 38.7% of the building mass was assigned to this frame, based on a three-dimensional elastic static analysis performed with the educational version of the program ETABS (4-23).

Furthermore, a constant effective slab width of 2.0 m was used based on the experimental results mentioned in Section 4.5.3.

Figure 4.50 shows the elastic time-history prediction of the roof displacement response for the high-level test. This response was obtained using the program SAP2000 (4-6) and assuming gross section properties for all elements. Lengthening of the vibration period and magnification of lateral displacement in the test structure are clear from comparisons of the measured response with the computed elastic response in this figure.

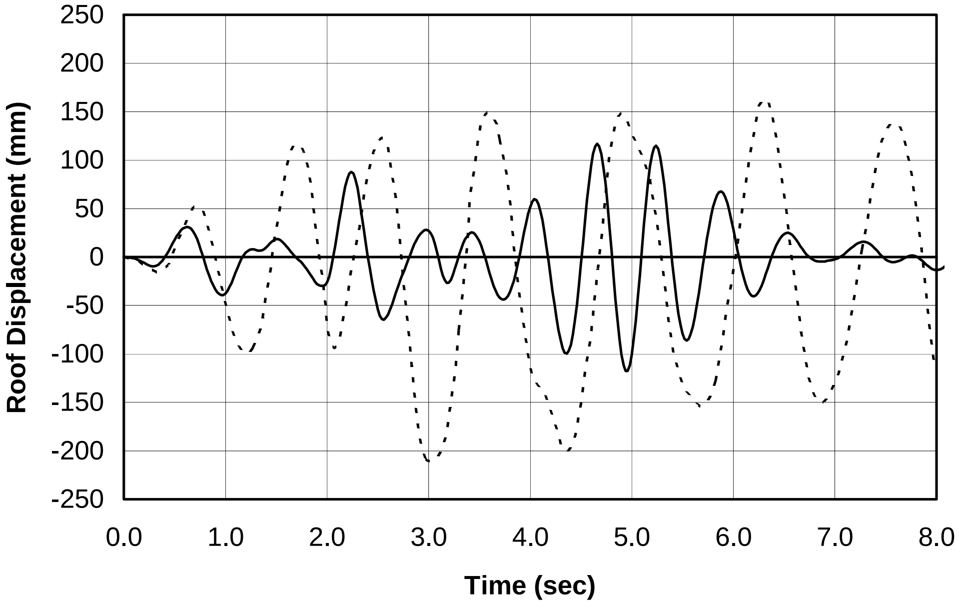

Figure 4.50 - Computed Elastic Time-History Response of Roof Displacement

The program IDARC2D was used then to predict the inelastic dynamic response of the building. Figure 4.51 shows the time-history response for the high-level ground motion. The overall shape of the displacement time history is somewhat similar to that obtained experimentally. In particular, a good prediction of the vibration period was achieved. However, the lateral deflection levels after approximately 4 seconds of response were only approximately one third of the measured response: While the program predicted the response to attenuate gradually, the measured displacements remained large throughout the eight seconds of analysis.

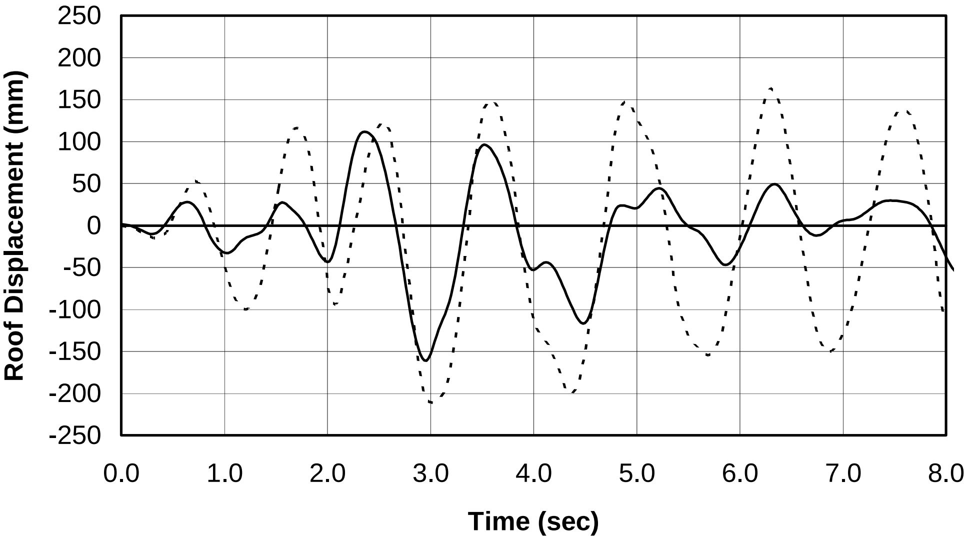

Figure 4.51 - IDARC2D Computed Roof Displacement Time History

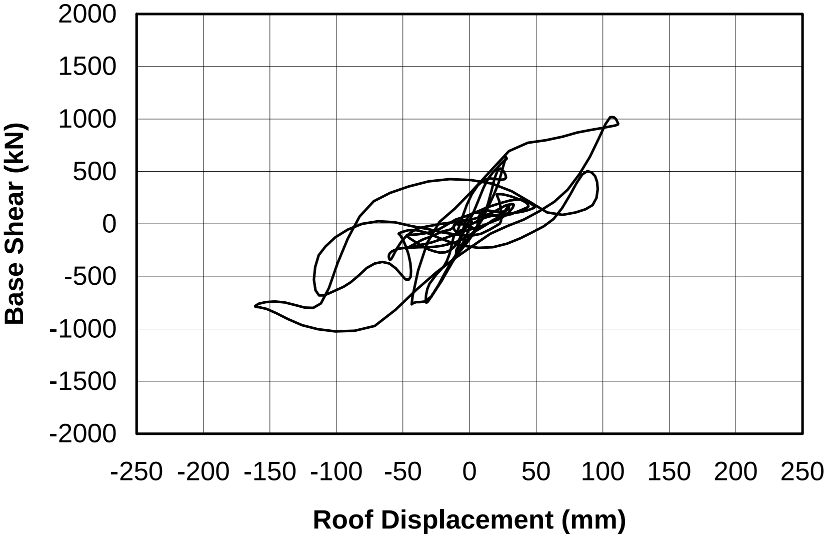

Figure 4.52 - Computed Load-Displacement Response using IDARC2D

The computed load-displacement response obtained using program IDARC2D is displayed in Figure 4.52. Comparing this figure to Figure 4.48, it is evident that IDARC2D generally predicted a stiffer response than that which was measured. Moreover, the base shear levels were significantly under-predicted (by approximately 28%).

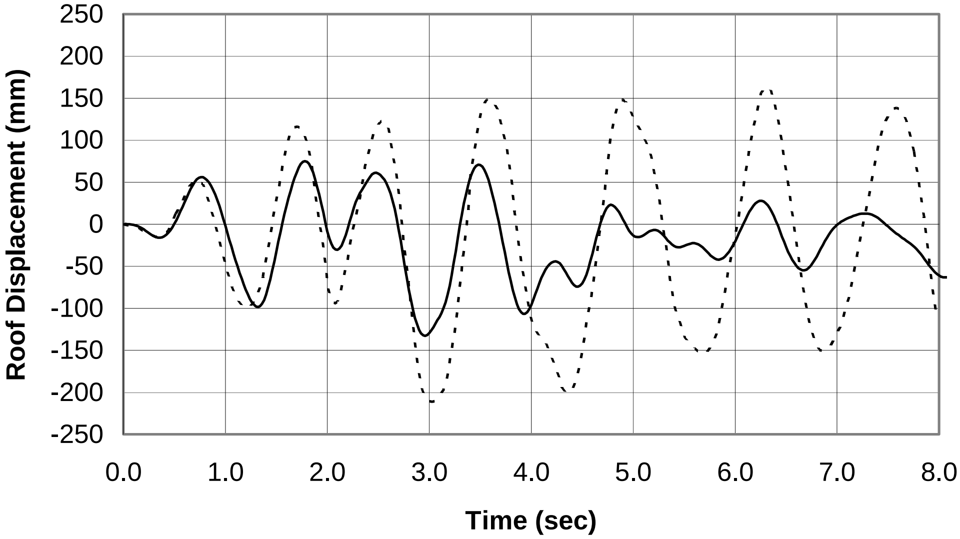

Figure 4.53 - DRAIN-2DX Computed Roof Displacement Time History

Figure 4.53 shows the roof displacement time-history response computed using program DRAIN-2DX. A fair simulation of the experimental response was obtained for the initial four seconds, although the magnitude of the predicted displacements was appreciably lower (by approximately 40% to 50%) than the experimentally observed response. For the latter four seconds of the record, the predicted displacements were much smaller (approximately one-third) than those measured experimentally. Also, the computed vibration period of the structure did not lengthen due to the lack of stiffness degradation in the model.

As shown in Figure 4.54, the program DRAIN-2DX significantly under-estimated the level of base shear developed in the building, reaching approximately half the force measured experimentally. This difference can be accounted for partially by the lack of axial force-bending moment interaction in the columns (which reduces column capacities).

The main effect of the deficiencies in base shear and deflections noted above is that there is an under-estimation of energy dissipation and damage in the structure.

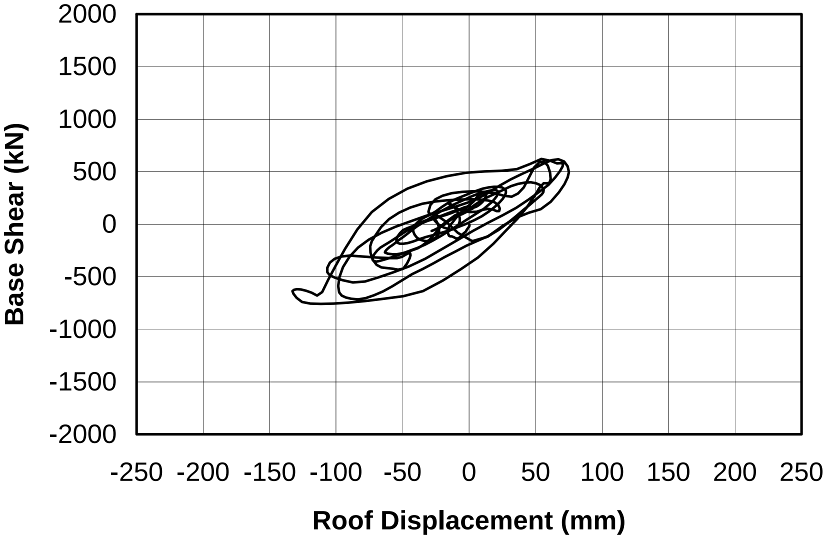

Figure 4.54 - Base Shear-Displacement Response Computed using DRAIN-2DX

The roof displacement time history computed by program FIBERC for the ground motion is shown in Figure 4.55. A reasonably close correlation with the experimental results for both displacements and vibration period was achieved through approximately 4 seconds. After that, the measured peak displacements were again significantly larger than the computed values. Furthermore, the model failed to predict the lengthening of the response period observed during the test.

The load-displacement response of the structure computed using program FIBERC is displayed in Figure 4.56. A good comparison with the experimental response was attained, in particular for stiffness of the initial cycles. For the large hysteretic loops, the measured behavior shows reduced stiffness and large displacements while the response computed using FIBERC maintains a relatively constant average stiffness. Finally, maximum base shear levels computed with the program exhibited good correlation with those observed experimentally and the maximum displacements are only slightly smaller than the measured values.

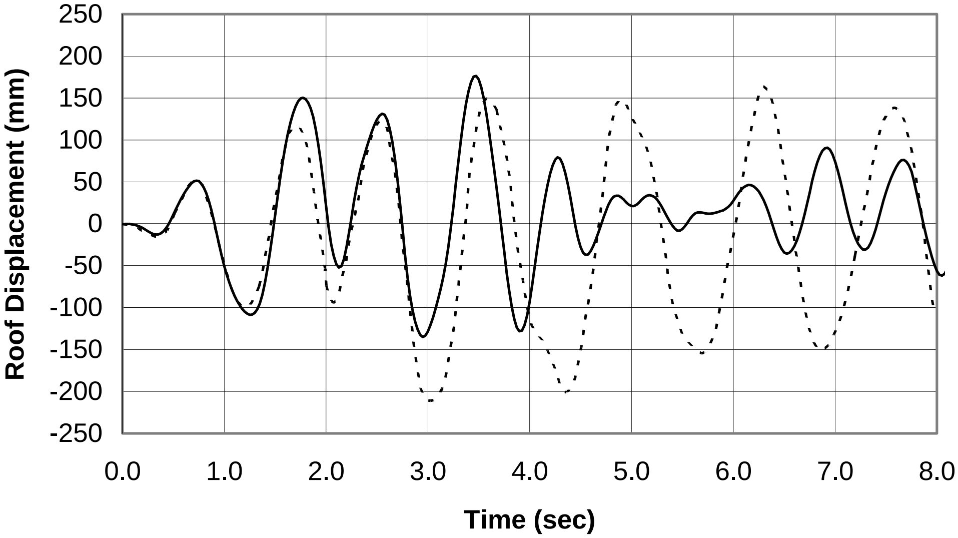

Figure 4.55 - FIBERC Computed Roof Displacement Time History

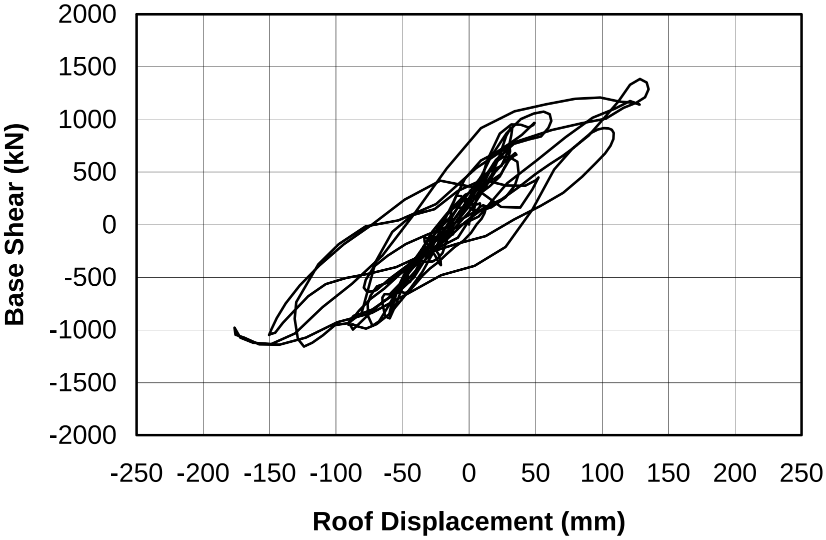

Figure 4.56 - Base Shear-Roof Displacement Response Computed using FIBERC

The roof-displacement computed response of the structure provided by all three programs, in particular for the late stages, is in general poor. However, the three responses (shown in Figures 4.51, 4.53, and 4.55) are somewhat similar to each other, especially when they all predict a reduction in displacement for the last four seconds.

This fact, together with potential differences in mass, damping and ground motion of the pseudo-dynamic model compared with those assumed for the computer models used in this study, suggest that a dynamic analysis may not be appropriate for comparing measured and computed responses in this case. Therefore, it was decided to reanalyze the structure applying displacement-controlled quasi-static loads at the floor levels in a manner similar to that used to apply actual loads during the test. The results of such analysis are presented below.

Figure 4.57 shows the computed time history of the base shear together with the experimental response. A reasonably good correlation was obtained up to approximately 3.5 seconds. After that, the difference between computed and measured responses increases significantly. However, the overall shape of the predicted response is still quite similar to that of the experimental response.

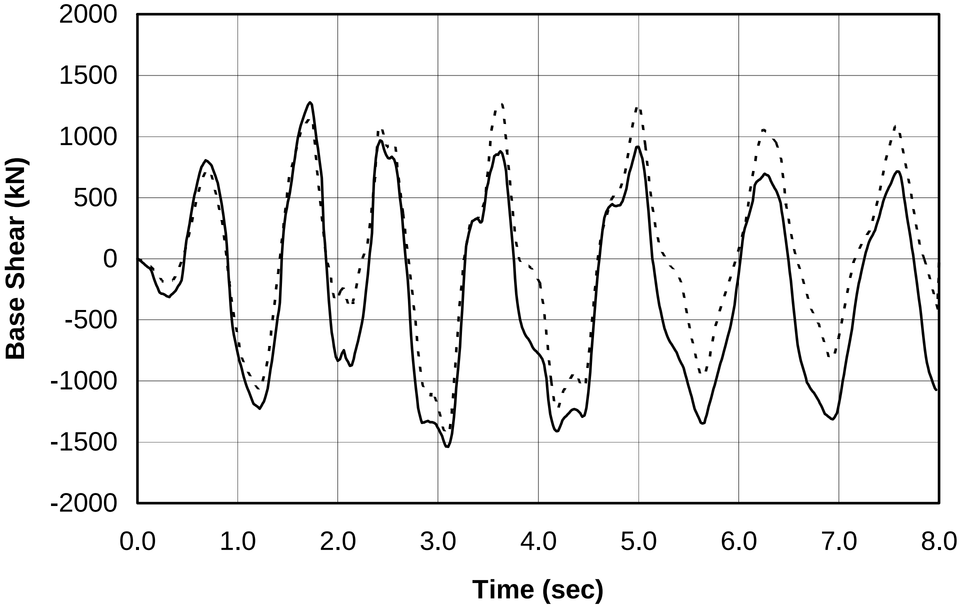

Figure 4.57 - Quasi-Static Computed Base Shear Time History using FIBERC Compared with Measured Response

The computed base shear-roof displacement response is presented in Figure 4.58. Comparing this prediction with the experimental response (Figure 4.49) and the dynamic computed response (Figure 4.56) it is evident that the quasi-static analysis provides a better simulation of the structure's behavior than the dynamic analysis. Not only is the shape of the hysteresis loops more similar to that observed experimentally, but the average secant stiffness is also closer.

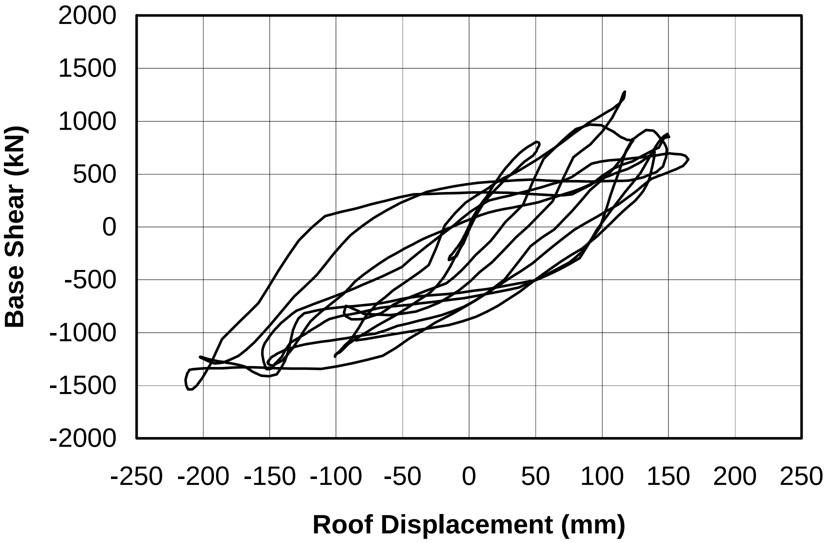

Figure 4.58 - Quasi-Static Computed Base Shear-Roof Displacement Response using F*IBE*RC

4.6 Summary of Prediction Results

A series of reinforced concrete members and frames that were tested by several researchers around the world were reviewed and analyzed. Two widely-used computer programs for nonlinear dynamic analysis of structures, namely DRAIN-2DX and IDARC2D, were evaluated using the experimental data. Additionally, the program FIBERC, developed as part of the research study presented in this report, was also evaluated.

In general, the program IDARC2D provided a good prediction of the experimental results at all levels of idealization considered; that is, at the section level, as well as globally for members and frames, when the program's hysteresis parameters are properly adjusted. In particular, good simulation of strength deterioration, stiffness degradation, and pinching of hysteresis loops was achieved by adjusting a set of parameters that control the program's built-in hysteretic model. This feature however, may be difficult to use or lead to incorrect and unconservative results in practical applications for which no guidance exists (such as test data) for selection of appropriate values of the hysteresis parameters.

One of the main shortcomings of the model implemented in program IDARC2D is the lack of moment-axial load interaction during the analysis. Additionally, the initial stiffness estimated by the program is usually higher than the actual stiffness.

An additional deficiency in the performance of IDARC2D was found during the analysis of a frame for which the quasi-static lateral load was applied initially in only one direction in a repeated fashion and then applied cyclically in both directions. For this case the program was unable to reproduce well the cyclic behavior of the frame in spite of producing an accurate prediction of the repeated load cycles. It was concluded that the model does not properly model cases in which the load is asymmetrically applied.

The beam-column element of program DRAIN-2DX, which was also used in this study to compute the response of reinforced concrete members and frames to seismic loads, is elasto-plastic bilinear with no strength or stiffness degradation, and therefore does not reproduce the actual hysteretic behavior of the members. However, it was found that the overall response of the two frames studied here was relatively well-predicted.

It is concluded that the program DRAIN-2DX is not an appropriate tool for the investigation of reinforced-concrete member hysteretic response. Particularly, it misrepresents the energy dissipation and damage in elements. However, based on the two frame studies performed here, it may be useful for estimating the peak inelastic response of reinforced-concrete frames.

The program FIBERC provides, in general, reasonably good prediction of the measured response of sections, members and frames, especially when flexural behavior dominates the response of the structure. It also accounts for the interaction of axial force and bending moment during analysis. However, the effects of pinching and stiffness deterioration are sometimes under-estimated (because the model ignores them).

During the investigation of the pseudo-dynamic test of a four-story building, it was found that a dynamic analysis provided poor predictions with all models, and it was concluded that uncertainties associated with mass, stiffness and damping may make dynamic analysis inappropriate. When a quasi-static analysis was used, the computed response was reasonably close to the measured response in terms of the base-shear time history and the base shear-roof displacement relationship.

To try to remedy the deficiencies in program FIBERC mentioned above, an extension of the model to include the effects of shear deformations in the members and anchorage slip of reinforcing bars is developed in Chapters 5 and 6, respectively.

CHAPTER 5

Member Shear Deformations Modeling

5.1 General Remarks

The analytical modeling of shear deformations in reinforced concrete members after initial cracking has been studied for the last two or three decades. A number of approximate solutions have been developed recently. In Section 5.2, a review of some of these approaches is presented.

Section 5.3 introduces a number of modifications to program FIBERC to take into account the effect of shear deformations in the static and dynamic response of reinforced concrete members and frames. Section 5.4 presents a series of analyses using the modified version of FIBERC to assess the performance of the model.

5.2 Previous Research on Concrete Shear Deformations

A semi-empirical approach was developed by Park, Ang and Wen (5-5) as part of a study on damage analysis of reinforced concrete buildings. In reference to the cantilever beam shown in Figure 5.1, the shear crack inclination is taken as 45° and the deflection due to shear cracking is computed as

$$\delta_s = \sum L_i \, \theta_s \tag{5.1}$$

where θ_s is the shear rotation (angle of open cracks) which is a function of the shear span ratio, the average bond stress in the bars, and the ratio of transverse reinforcement.

Based on the above formulation, Park, Reinhorn and Kunnath (5-6) obtained the equivalent curvature given by Equation 5.2

$$\varphi_s = 3\left\{\frac{1}{L} + \frac{1-\left(L_s^{'}/L\right)^2}{2z}\right\}\theta_s \tag{5.2}$$

in which *L* is the shear span, L'_s is the length of the beam without shear cracks, and *z* is the distance between the tension and compression reinforcement.

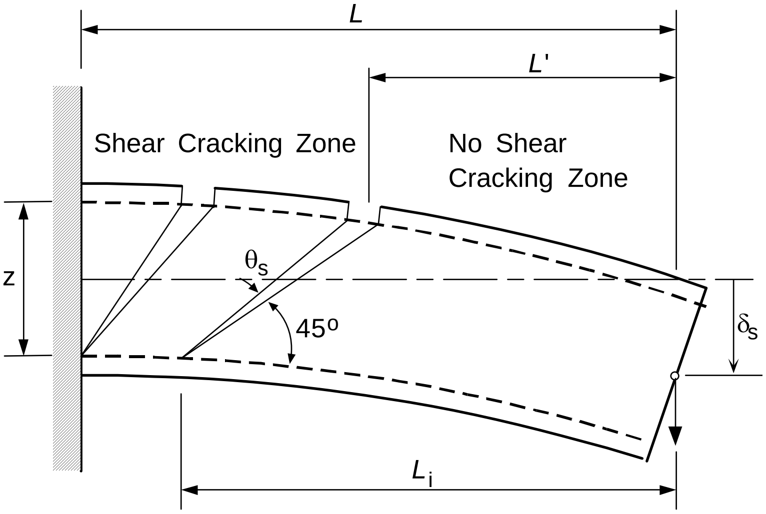

Figure 5.1 - Park's Shear Crack and Shear Deflection Model (adapted from 5-5)

Using a fiber element approach, Powell et al. (5-8) suggested a conceptual model in which the element is divided along its length into slices that contain shear reinforcement as transverse fibers, as shown in Figure 5.2c.

This model disregards the conventional shear distortion (displayed in Figure 5.2d) but accounts for diagonal cracking. Figure 5.2d shows how such diagonal cracking would cause shear deformations in the slice. That figure, however, assumes perfect aggregate interlock and ignores the sliding that would occur along cracks.

Powell et al. propose "adding cracking degrees of freedom to the slice" so that cracking, stirrup strains and even interaction between shear force, axial force and moments can be accounted for. However, the authors do not explicitly develop a theoretical model to implement this conceptual idealization.

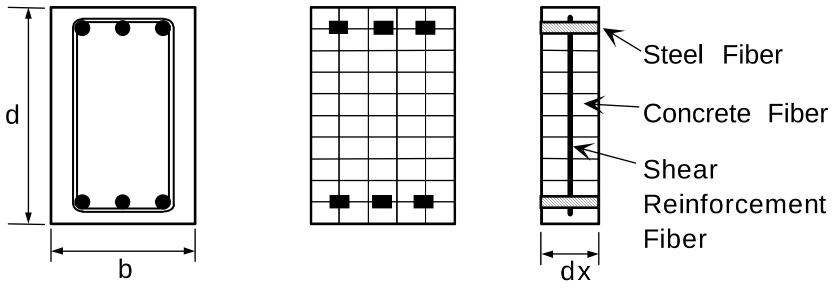

ⓐ Section ⓑ Fiber Representation

ⓒ Conventional Shear Deformation ⓓ Shear Deformation caused by Diagonal Cracks

Figure 5.2 - Conceptual Inelastic Shear Model by Powell et al. (adapted from 5-8)

Several more involved models have been developed by other researchers. The following subsections present an overview of three of those models, some of which will be used in program FIBERC as discussed in Section 5.3.

5.2.1 Analogous Truss Model for Shear Distortions in Cracked Members

A truss analogy was presented by Park and Paulay (5-7) for reinforced concrete members under shear. Figure 5.3 shows a portion of a beam with top and bottom reinforcement separated by a distance d from each other, with vertical stirrups at a spacing s and cracks inclined at an angle θ. The model assumes that the transverse steel is lumped at discrete locations along the beam with a separation $d \cdot cot\theta$ and that a compression strut exists within that length, thus forming a panel of the analogous truss.

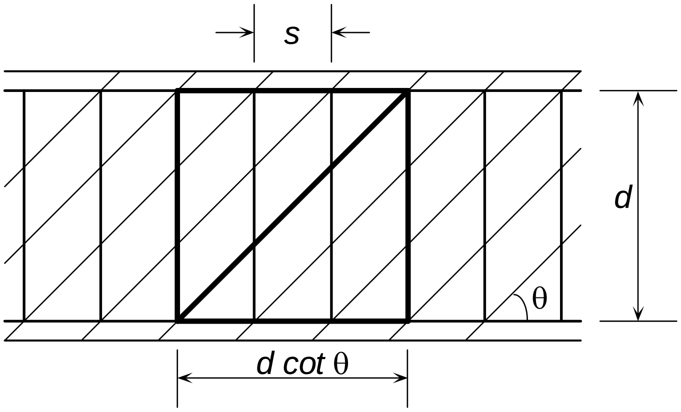

Figure 5.3 - Idealization of Crack inclination for an Analogous Truss (adapted from 5-7)

In Figure 5.4 the distortion of one panel is displayed. It is assumed that the top and bottom reinforcing bars (chords of the truss) are uniaxially rigid. Therefore, the total deflection of the panel is

$$\delta_v = \delta_s + \delta_R = \delta_s + \frac{\delta_c}{\sin\theta} \tag{5.3}$$

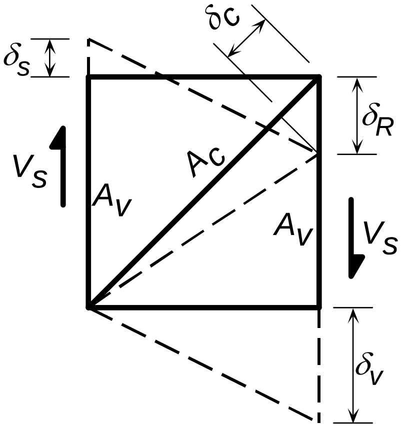

Figure 5.4 - Shear Distortion of Analogous Truss (adapted from 5-7)

Assuming linear elastic response of the stirrups in tension and the concrete in compression, Equation 5.3 can be rewritten as

$$\delta_v = \frac{f_S}{E_S} d + \left(\frac{f_C}{E_C} \frac{d}{\sin\theta} \right) \frac{1}{\sin\theta} \tag{5.4}$$

or, introducing the shear force V_s, the stirrup spacing s, the stirrup transverse area A_v, and the web width b_w, it becomes

$$\delta_v = \frac{V_S s}{E_S A_v \cot\theta} + \frac{V_S}{E_C b_w \sin^4\theta \cot\theta} = \frac{V_S}{E_S b_w} \left(\frac{b_w s}{A_v \cot\theta} + \frac{n}{\sin^4\theta \cot\theta} \right) \tag{5.5}$$

where, n is the modular ratio given by

$$n = \frac{E_S}{E_C} \tag{5.6}$$

Finally, the shear strain can be obtained as

$$\gamma = \frac{\delta_v}{d\cot\theta} = \frac{V_S}{E_S b_w d} \left(\frac{1}{\rho_v \cot^2\theta} + \frac{n}{\sin^4\theta \cot^2\theta} \right) \tag{5.7}$$

or in a slightly simpler form as

$$\gamma = \frac{V_s}{E_s A_s} \left(\frac{\sin^4\theta + \rho_v n}{\rho_v \sin^4\theta \cot^2\theta} \right) \tag{5.8}$$

where the transverse steel ratio ρ_v and the shear area A_s are given by Equation 5.9 and 5.10, respectively.

$$\rho_v = \frac{A_v}{b_w s} \tag{5.9}$$

$$A_s = b_w d \tag{5.10}$$

5.2.2 Modified Compression Field Theory

Collins and his associates at the University of Toronto developed the so-called “Modified Compression Field Theory” (5-2, 5-9). This theory, which was originally applied to concrete membrane elements and subsequently to reinforced concrete beams (5-10), is based on the average strains in the cracked member as shown in Figure 5.5..

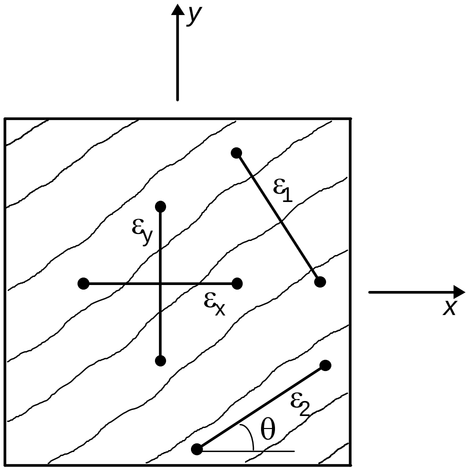

Figure 5.5 - Average Shear Strains In Cracked Element (adapted from 5-9)

One of the main assumptions of the method is that the angle of inclination of the diagonal cracks coincides with the angle of inclination of the principal strain and stresses. Consequently, the following compatibility condition is written

$$\tan^2\theta = \frac{\varepsilon_x - \varepsilon_2}{\varepsilon_y - \varepsilon_2} = \frac{\varepsilon_1 - \varepsilon_y}{\varepsilon_1 - \varepsilon_x} \tag{5.10}$$

Furthermore, the shear strain is related to strain components and to the angle θ by Equation 5.11 which is derived from Mohr's circle (Figure 5.6).

$$\gamma = 2\frac{\varepsilon_x - \varepsilon_2}{\tan\theta} \tag{5.11}$$

Likewise, relationships among the stress components acting in the member can be derived. Equation 5.12 relates the principal compressive stress f_{c2} to the shear stress τ and to the principal tensile stress f_{c1}. Similarly, Equations 5.13 and 5.14 relate the stresses in the x and y directions to the principal and shear stresses.

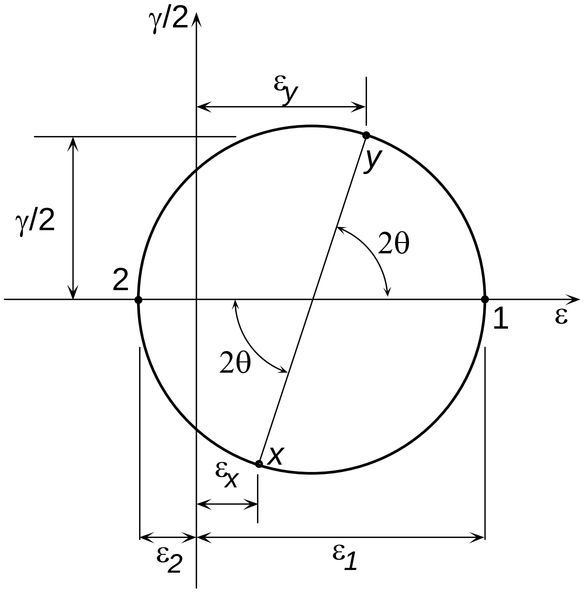

Figure 5.6 - Mohr's Circle for Average Strains (adapted from 5-9)

$$f_{c2} = \tau\left(\tan\theta + \frac{1}{\tan\theta}\right) - f_{c1} \tag{5.12}$$

$$f_{cx} = f_{c1} - \frac{\tau}{\tan\theta} \quad \text{and} \quad f_{cy} = f_{c2} - \frac{\tau}{\tan\theta} \tag{5.14}$$

Using equilibrium considerations, the force in the stirrups (with a transverse area A_v and spacing *s*) can be estimated using Equation 5.15. Then, equating τ to the average shear stress, that is, $\tau = V/b_w jd$, an expression for the shear strength of the member is obtained (Equation 5.16).

$$A_v f_v = \left(f_{c2}\sin^2\theta - f_{c1}\cos^2\theta\right)b_w s \tag{5.15}$$

$$V = f_1 b_w jd\cot\theta + \frac{A_v f_v}{s} jd\cot\theta \tag{5.16}$$

Finally, the stress-strain relations for concrete in compression and tension are given by Equations 5.17 and 5.18, respectively

$$f_{c2} = f_{c2,\max}\left[2\left(\frac{\varepsilon_2}{\varepsilon'_c}\right) - \left(\frac{\varepsilon_2}{\varepsilon'_c}\right)^2\right] \tag{5.17}$$

$$f_{c1} = \frac{\alpha_1\alpha_2 f_{cr}}{1+\sqrt{200\varepsilon_1}} \tag{5.18}$$

$$f_{c2,\max} = \frac{f'_c}{0.8 - 0.34(\varepsilon_1/\varepsilon'_c)} \leq 1.0 \tag{5.19}$$

The solution to this set of equations is iterative. It starts by assuming the angle *θ* and two of the strains, then it iterates until convergence is achieved.

A similar development was conducted by Hsu and his associates at the University of Houston (5-3). They introduced the so-called “softened truss model” to evaluate the shear deformations in membrane elements.

5.2.3 Cyclic Inelastic Strut-and-Tie Model

A recent study by Chang and Mander (5-1) used a strut-and-tie model approach. In this study a single bridge pier was analyzed for the combined action of axial loads, bending moments and shear forces applied cyclically.

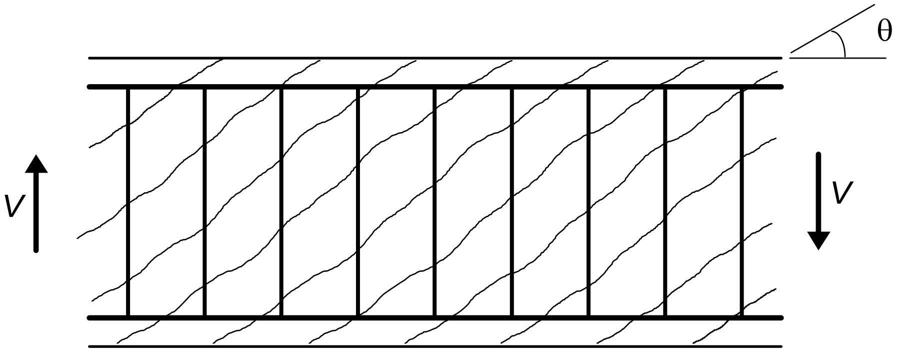

Figure 5.7 - Crack Inclination of Element Subjected to Shear (adapted from 5-1)

Figure 5.7 shows a segment of the element subjected to shear forces and displaying diagonal cracks with an angle of inclination of *θ*. This angle was assumed constant during the analysis (after cracking). This assumption was based on experimental observations (5-

1). Additionally, the model assumed that the stirrups are lumped at discrete locations separated a distance *jdcot*θ, as shown in Figure 5.8.

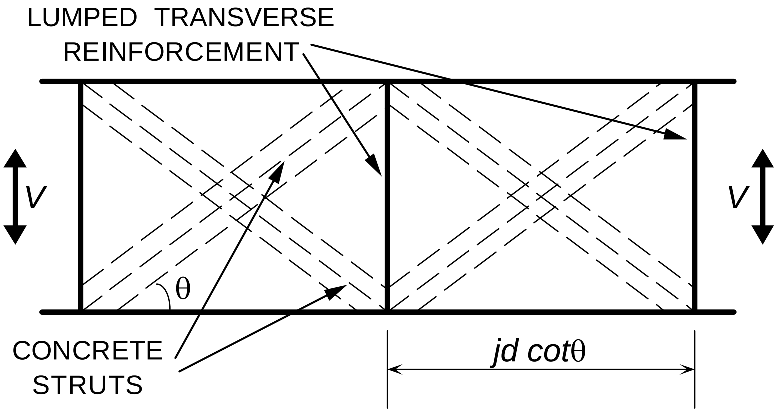

Figure 5.8 - Strut-and-Tie Model (adapted from 5-1)

The strut-and-tie model for the element is shown in Figure 5.8. The concrete struts alternate between tension and compression depending on the direction of the cyclic load.

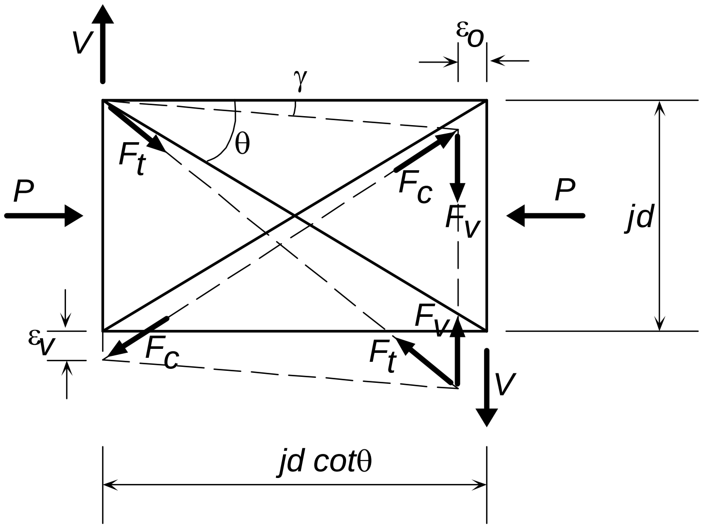

Figure 5.9 - Equilibrium of Forces of Strut-and-Tie Model (adapted from 5-1)

From Figure 5.9, which shows the internal forces in all struts and ties in the model, the following relations are obtained by satisfying internal and external equilibrium.

$$F_v - \left(F_c - F_t\right)\sin\theta = 0 \tag{5.20}$$

$$V = \left(F_c + F_t\right)\sin\theta \tag{5.21}$$

The forces F_c, F_t and F_v in Equations 5.20 and 5.21 can be written in terms of the constitutive models for concrete (in compression or tension) and steel (stirrups) as

$$F_c = f_c\left(\varepsilon_2\right)\cdot b_w\, jd\cos\theta \tag{5.22}$$

$$F_t = f_c\left(\varepsilon_1\right)\cdot b_w\, jd\cos\theta \tag{5.23}$$

$$F_v = f_{sv} A_v \frac{jd\cot\theta}{s} \tag{5.24}$$

Finally, compatibility conditions between the strains in the struts can be established using Mohr's circle as shown in Figure 5.10. Compatibility is expressed in Equations 5.25 and 5.26.

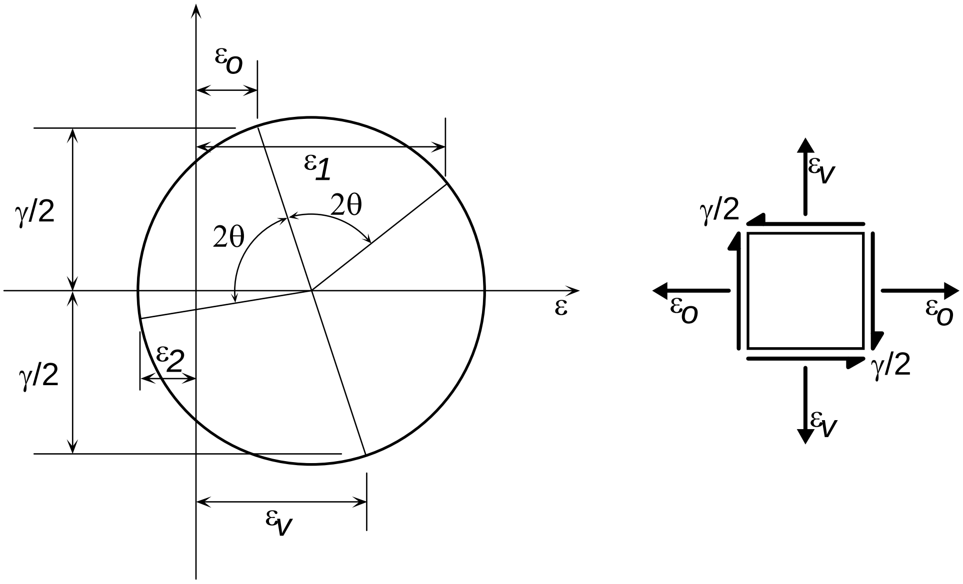

Figure 5.10 - Strain Transformation of Strut-and-Tie Model (adapted from 5-1)

$$\varepsilon_1 = \varepsilon_O\cos^2\theta + \varepsilon_v\sin^2\theta + \gamma\sin\theta\cos\theta \tag{5.25}$$

$$\varepsilon_2 = \varepsilon_O\cos^2\theta + \varepsilon_v\sin^2\theta - \gamma\sin\theta\cos\theta \tag{5.26}$$

The solution is found by iteration. The process is as follows: obtain centroidal strain from flexural analysis. Assume θ and strain, and then iterate until convergence of the equilibrium equations is obtained.

5.2.4 Crack Inclination Angle

All the models presented in the previous sections use the angle of crack inclination θ for the theoretical derivations, but few of them define it explicitly. For instance, in the 'Modified Compression Field Theory', presented in Section 5.2.2, θ is a function of the average strains in the member and is found during the iterative solution.

Following a plasticity approach, Marti and Meyboom (5-4) developed several expressions for the inclination of cracks in membrane elements. If both longitudinal and transverse reinforcement yield and the concrete does not crush, θ can be found from

$$\tan\theta = \sqrt{\frac{\rho_{sv} f_{yv}}{\rho_s f_y}} \tag{5.27}$$

where $\rho_s = A_{st}/b_w jd$ and $\rho_{sv} = A_{sv}/b_w s$. The applied shear stress in that case is $\tau_u = \sqrt{\rho_s \rho_{sv} f_y f_{yv}}$. If only the transverse reinforcement yields and concrete crushes,

$$\sin\theta = \sqrt{\frac{\rho_{sv} f_{yv}}{f_c'}} \tag{5.28}$$

and the shear stress is $\tau_u = \sqrt{\left(f_c' - \rho_{sv} f_{yv}\right)\rho_{sv} f_{yv}}$. Finally, if no yielding of reinforcement occurs but concrete crushes, θ = 45° and the shear stress is $\tau_u = \frac{1}{2} f_c'$. The governing mode corresponds to the minimum τ_u.

Chang and Mander (5-1) also used the above formulation but limited the angle to $\theta_{\min}$ given by

$$\tan\theta_{\min} = \frac{jd}{2L} \tag{5.29}$$

5.3 Modified Version of FIBERC

In this section a number of modifications to program FIBERC to accommodate the effect of shear deformation on the response of reinforced concrete members and frames are described.

5.3.1 Equivalent Shear Area Approach

The shearing distortion of an infinitesimally short section of an element is shown in Figure 5.11. The elastic transverse deflection caused by the shear strain γ is given by Equation 5.25.

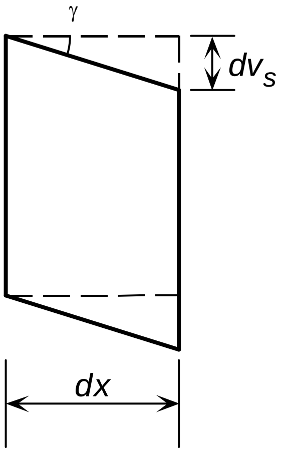

Figure 5.11 - Idealized Elastic Shear Distortion

$$dv_s = \gamma\, dx = \frac{\tau}{G} dx = \frac{V}{GA_s} dx \tag{5.25}$$

To account for cracking and inelasticity in the element, it is proposed to use an incremental form of Equation 5.25 and replace the elastic shear modulus G by the tangent shear modulus G_T and the shear area A_s by an effective shear area $A_{s,eff}$ at each section, as suggested by Equation 5.26.

$$d\left(\Delta v_s\right) = \frac{\Delta V}{G_T A_{s,eff}} dx \tag{5.26}$$

The tangent shear modulus of each fiber $G_{T,i}$ is computed using the corresponding tangent stiffness $E_{T,i}$ at each analysis increment as follows

$$G_{T,i} = \frac{E_{T,i}}{2(1+\mu)} \tag{5.27}$$

Thus, Equation 5.26 can be rewritten as shown below, where A^*_i is the area of the steel and concrete fibers in compression

$$d(\Delta v_s) = \frac{\Delta V}{\sum G_{T,i} A_i^*} dx \tag{5.28}$$

Finally, the deflection increment for the member can be obtained by integration as

$$\Delta v_s = \int d(\Delta v_s) = \int \frac{2(1+\mu)\Delta V}{E_T A_{s,eff}} dx = \left(\int \frac{2(1+\mu)}{E_T A_{s,eff}} dx \right) \Delta V \tag{5.29}$$

The deflection given by Equation 5.29, caused by the shear distortion alone, is then added to the deflection due to flexure (Equation 2.39) to obtain the total transverse deflection of the element used to compute the flexibility matrix of the member.

5.3.2 Truss Analogy Approach

In subsection 5.2.1, an expression for the shearing strain was found as a function of the crack inclination, the properties of the materials, and the geometry of the section (Eq. 5.8). If that equation is rewritten in incremental form and is then integrated along the length of the member, the increment in transverse deflection of the member is obtained as

$$\Delta v_s = \int_0^L \Delta\gamma \, dx = \left[\int_0^L \frac{1}{E_s A_s} \left(\frac{\sin^4\theta + \rho_v n}{\rho_v \sin^4\theta \cot^2\theta} \right) dx \right] \Delta V_s \tag{5.30}$$

This deflection, which is caused only by shearing distortion of the member, is added to the deflection due to flexure (Equation 2.39) to obtain the total transverse deflection of the element that will eventually be used to compute the member flexibility matrix.

5.4 Application of Modified FIBERC

Using the modified version of the program FIBERC that includes shearing deformations as outlined in Section 5.3, a series of runs were performed using some of the members and frames studied in Chapter 4. Comparisons between responses obtained assuming flexural response only and including shear strains are presented. Moreover, differences between these predictions and experimental results are also assessed.

Throughout this chapter computed response of members and frames to static and dynamic loads, using the program FIBERC, is presented graphically together with the corresponding experimental response. With no exceptions, the experimental response is always shown in dashed lines and the computed response in solid lines

5.4.1 Cantilever Beam by Hanks

Figure 5.12 shows the computed response of the beam studied in Section 4.3.1, considering only flexural behavior (solid lines), compared to experimental results (dashed lines). The computed load-displacement response for this beam obtained using the equivalent-area model is shown in Figure 5.13 together with the experimental response. The strength and stiffness estimates for the first cycle of loading are very similar to those predicted by the flexural analysis. However, for the subsequent cycles the computed strength in the positive-loading direction deteriorates substantially, coming very close to the measured strength in that direction, thus improving somewhat on the response computed considering only flexural deformations. Nevertheless, the computed strength in the negative direction unexpectedly increases to about 50% of the measured strength during the last cycle of loading.

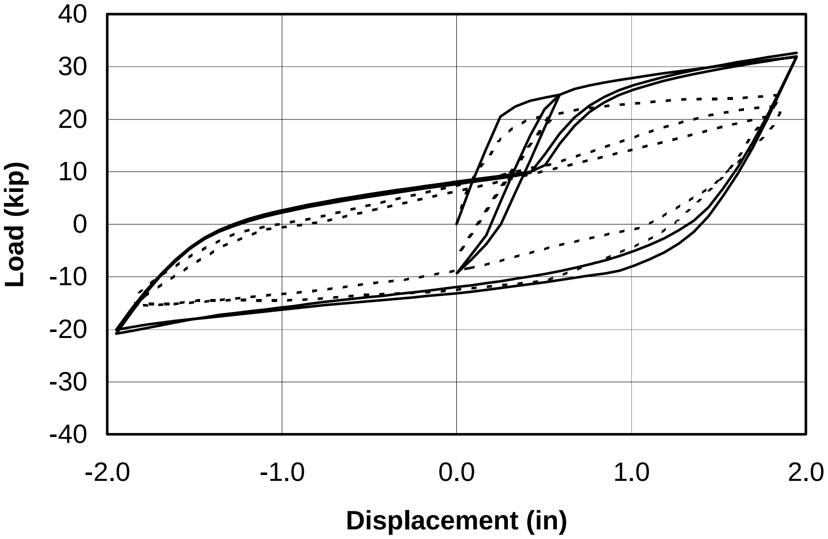

Figure 5.12 - Prediction with flexural deformations only

It must be noted, though, that the crack closing prediction provided by this model is still too abrupt (and slightly accelerated) compared to the measured response. In particular, in the positive-direction reloading branch during the third cycle a sudden drop in computed strength was observed and then upon crack closure a large stiffness is obtained (slightly larger than that computed with the flexure-only model).

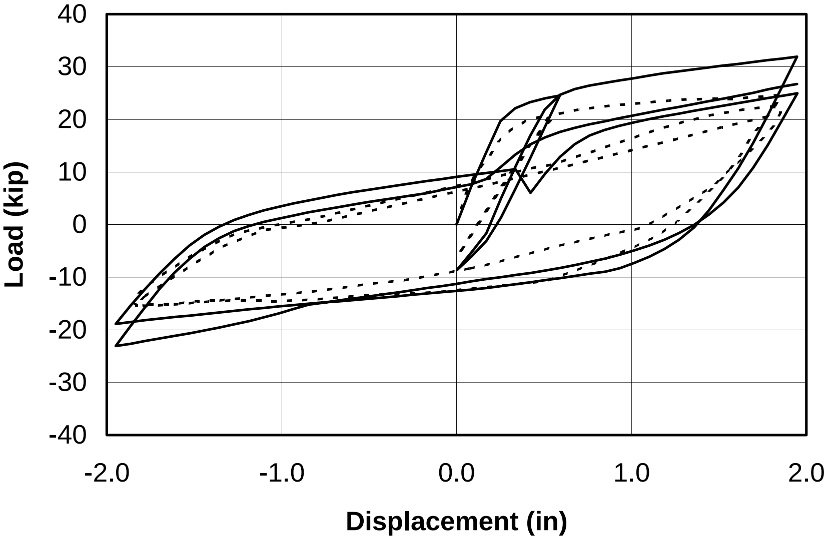

Figure 5.13 - Prediction including shear strains by Equivalent Area Approach

The load-displacement response computed using the truss-analogy approach is shown in Figure 5.14 and is compared to the experimental response. A 50° angle for the inclination of cracks was used for this analysis, as suggested by the test results which included cracks with a range of inclinations between 40° and 60°.

Although the beam capacity in the positive direction is still overpredicted, the overall shape of the simulated hysteresis loops is closer to those observed experimentally. In particular, the computed stiffnesses are less than those computed assuming only flexural deformations, a direct consequence of the added flexibility provided by the shearing deformations. Furthermore, the crack closing is more gradual, albeit still obvious.

In conclusion, the prediction of the load-displacement response of this beam was significantly improved by introducing a model for shearing deformations. In particular, the truss analogy gave an overall better simulation.

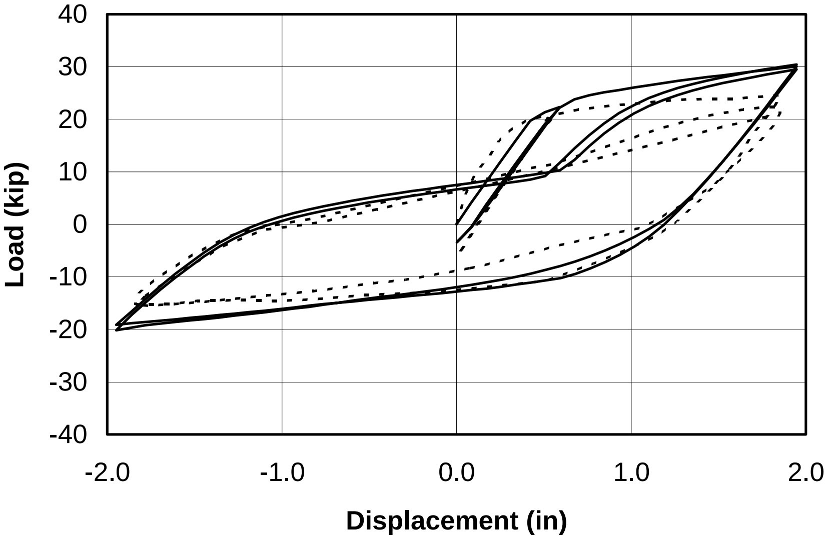

Figure 5.14 - Prediction including shear strains by Analogous Truss Approach

In order to study the effect of crack inclination on the load-displacement response of the model, an additional analysis was performed on this specimen, this time using a 40° inclination for the cracks. Figure 5.15 shows the computed response for θ equal to 40°. The computed stiffness of the element is slightly higher, particularly during the initial loading, Likewise, the strength is slightly higher than that computed response for θ equal to

50°. However, it is clear that a large variation in the crack inclination angle does not affect significantly the overall response of the member.

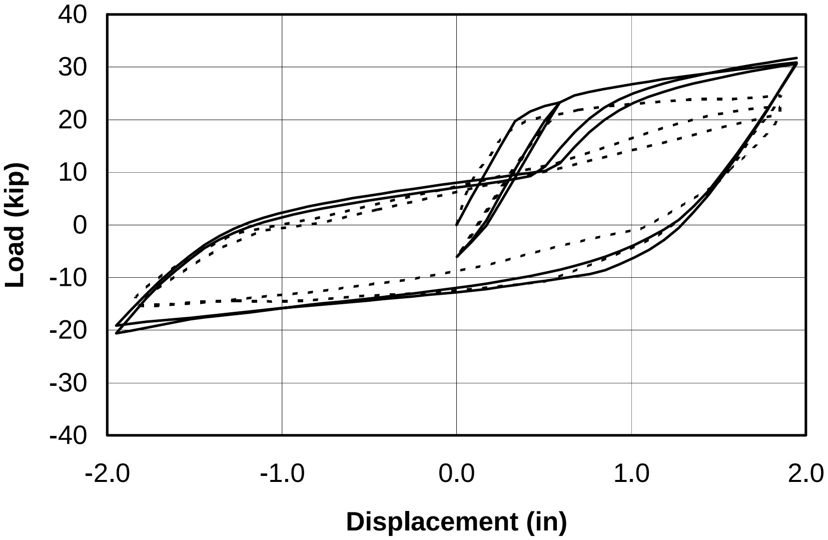

Figure 5.15 - Prediction by the Truss Analogy Method using θ=40 °

5.4.2 Cantilever Beam by Popov et al.

The beam studied in Section 4.3.2 was analyzed again to further evaluate the effect of the shear deformation model. Figure 5.16 presents the analytical load-displacement hysteretic loops, considering flexural behavior only, together with the experimental response.

The equivalent area approach was utilized next to compute the cyclic response of the beam. This is shown in Figure 5.17, along with the experimental results. It is obvious that this method provides only a slight improvement in the computed response. Although the estimated stiffness is slightly reduced in some cycles, strength levels are not accurately predicted. Additionally, the computed hysteretic loops display no signs of pinching.

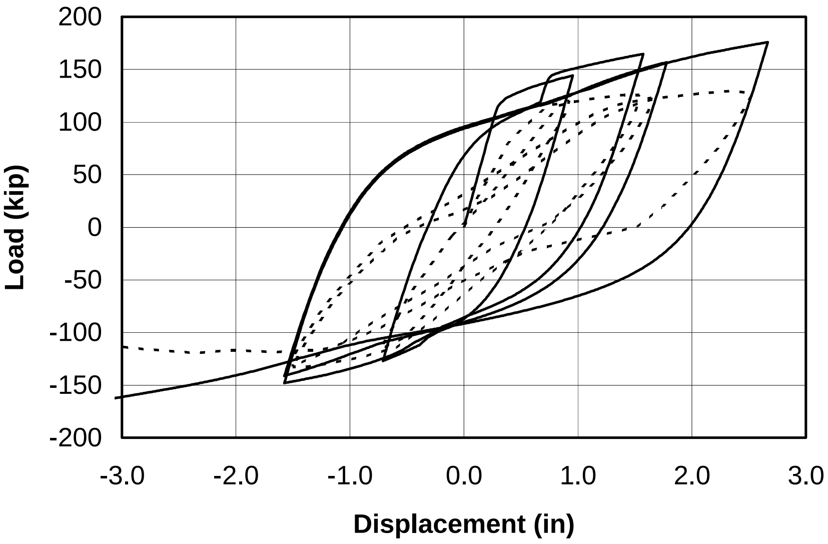

Figure 5.16 - Prediction assuming flexural deformations only

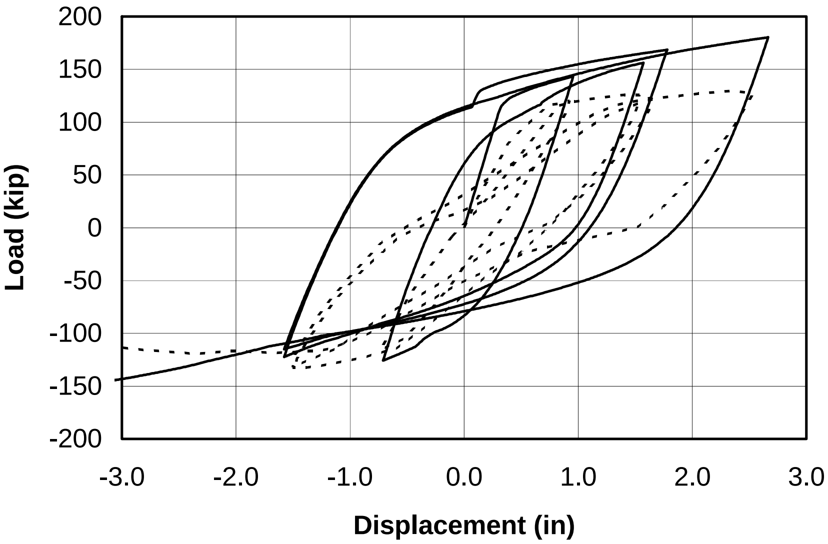

Figure 5.17 - Prediction including shear strains by Equivalent Area Approach

Figure 5.18 shows the computed load-displacement response for the same beam using the truss analogy method. A 45° angle for the crack inclination was used for the analysis. Crack angles between 30° and 45° were measured during testing.

In contrast to the response computed considering only flexural deformations, a significant reduction in the width of the hysteresis loops was obtained with this model. Moreover, the unloading stiffnesses computed were quite similar to the measured stiffnesses. The strength prediction in the positive direction is also improved in comparison with the flexural analysis. It is concluded that for this beam the analogous truss model gives an improved, although not perfect, estimation of the load-displacement behavior under cyclic load. In particular, the reloading stiffness and the pinching of the hysteresis loops were not accurately predicted.

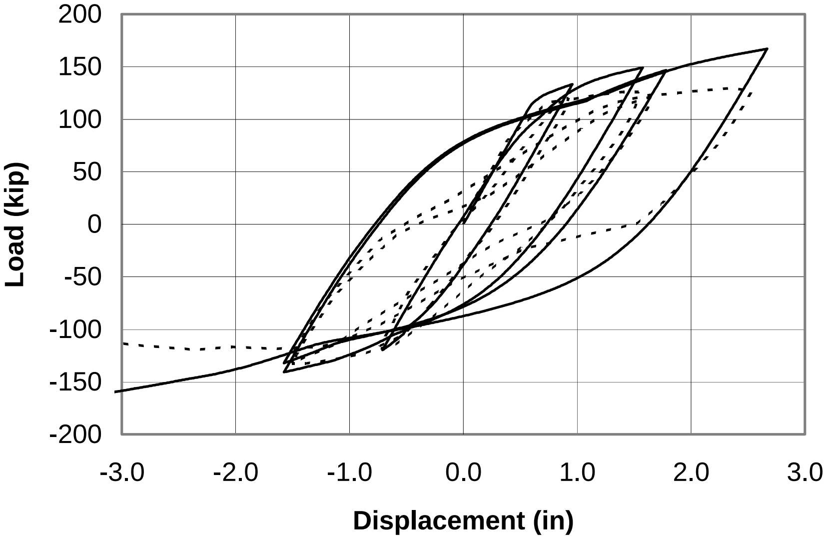

Figure 5.18 - Computed Response including Shear Deformations by Analogous Truss Approach

Figure 5.19 presents an additional computed load-displacement response for the same beam, using the truss analogy with a θ of 35° to further evaluate the influence of the crack inclination on the computed response. The agreement with the experimental response deteriorates slightly for this angle, introducing higher stiffness and fatness into the hysteresis loops.

The computed response for this specimen together with those of the previous specimen indicate that the predicted stiffness of the beams increases as the crack inclination angle decreases. Likewise, energy-absorption capacity of the member tends to increase with smaller crack inclination angles.

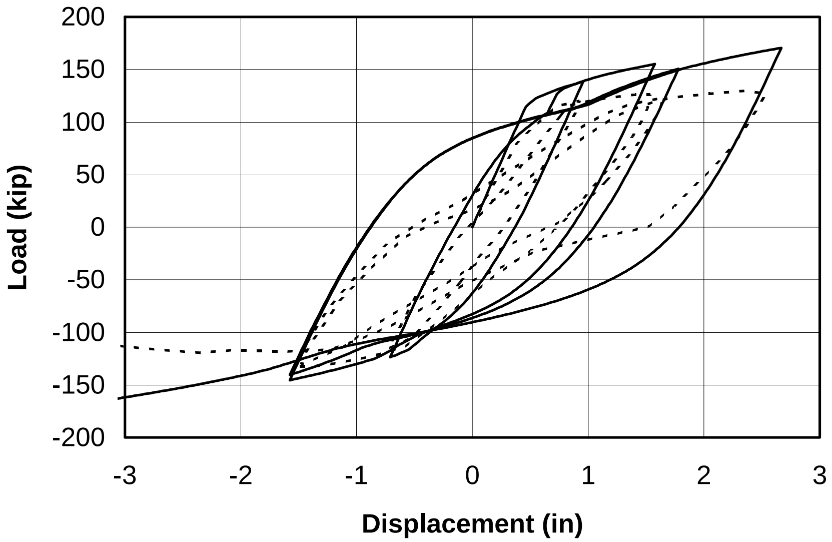

Figure 5.19 - Computed Response using the Truss Analogy Method using θ=35°

5.4.3 Two-Story Frame

The specimen presented in this section is the two-story frame, under quasi-static lateral load, previously described and studied for flexural behavior in Section 4.4. Results of that investigation are shown again here for completeness. Figure 5.20 displays the comparison between computed and experimental behavior under repeated load, while Figure 5.21 shows the case for load reversals.

The numerical load-displacement response using the equivalent-area approach plotted with the experimental response for the repeated and cyclic loading cases are presented in Figures 5.22 and 5.23, respectively. It is clear that the inclusion of the equivalent-area method for shear deformations in the computed response has virtually no discernible effect.

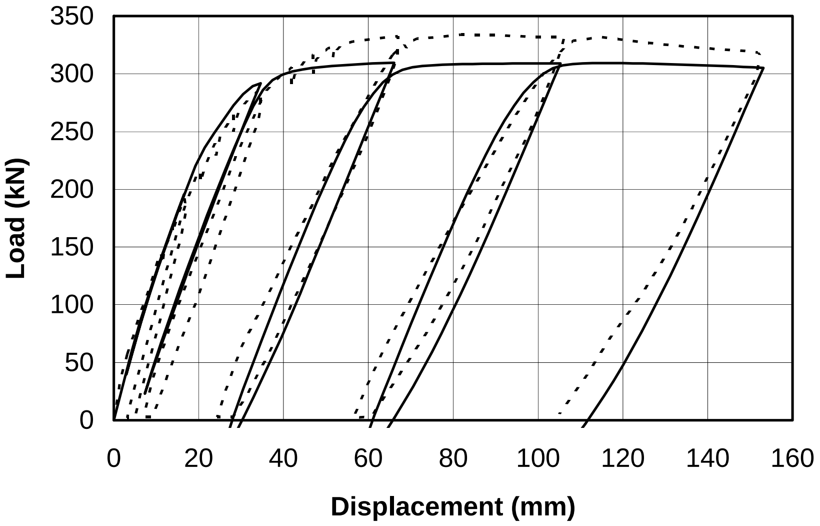

Figure 5.20 - Computed Flexural Response under Repeated Load

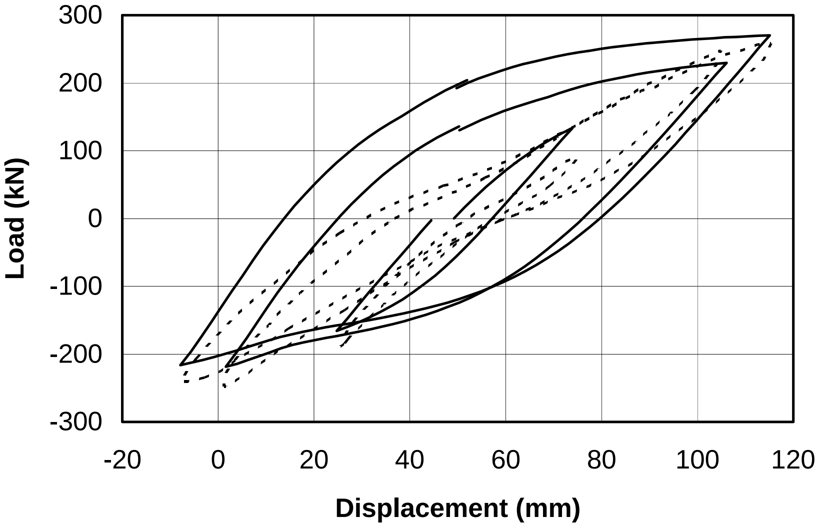

Figure 5.21 - Computed Flexural Response under Cyclic Loads (typical loops)

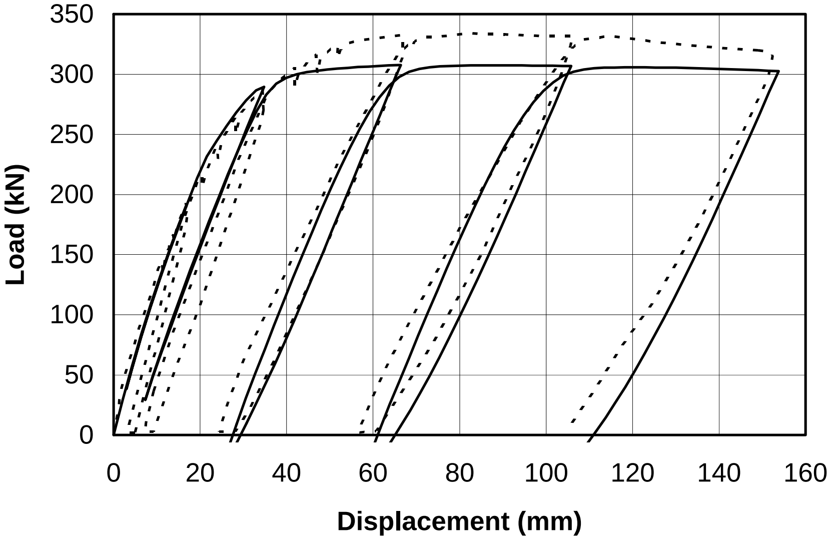

Figure 5.22 - Computed Response including shear strains using Equivalent-Area Approach

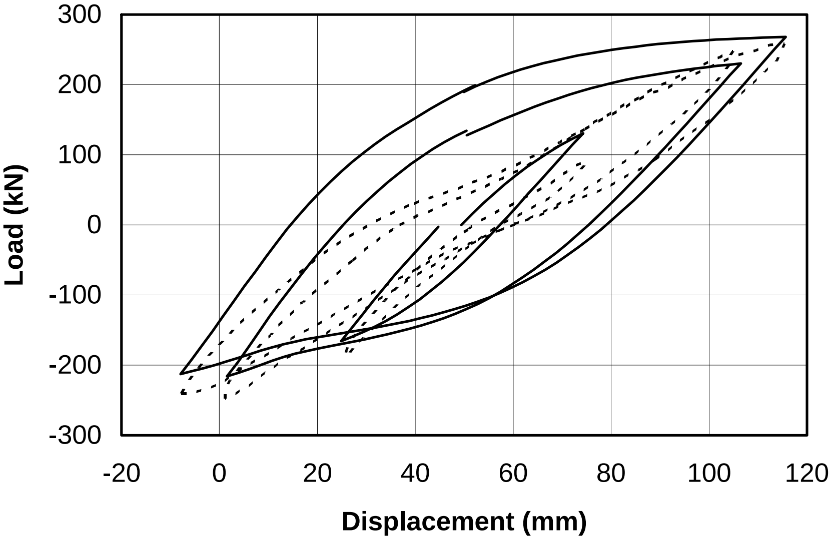

Figure 5.23 - Computed Response including shear strains using Equivalent-Area Approach

Results using the truss analogy model to compute the load-displacement response of the frame under repeated loads are shown in Figure 5.24, while those under cyclic loads are displayed in Figure 5.25. A 45° crack inclination was used in the computations.

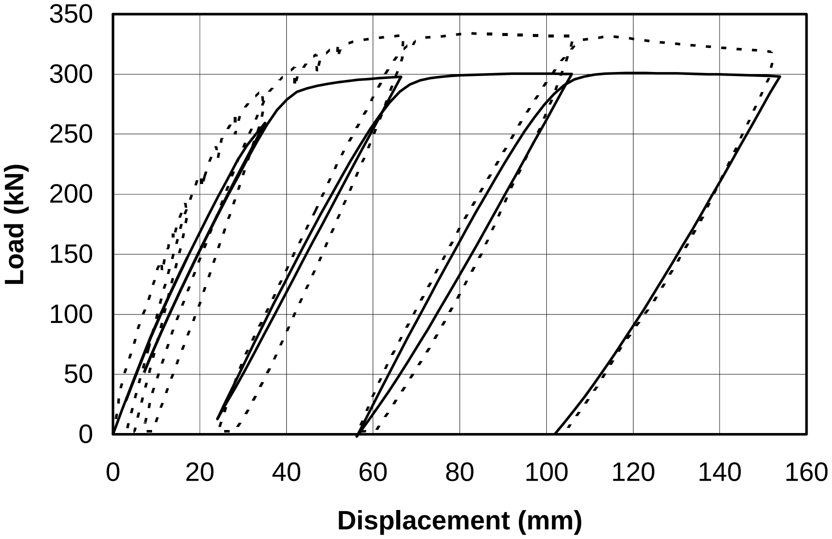

Figure 5.24 - Repeated Load with shear strains by Truss Analogy Approach

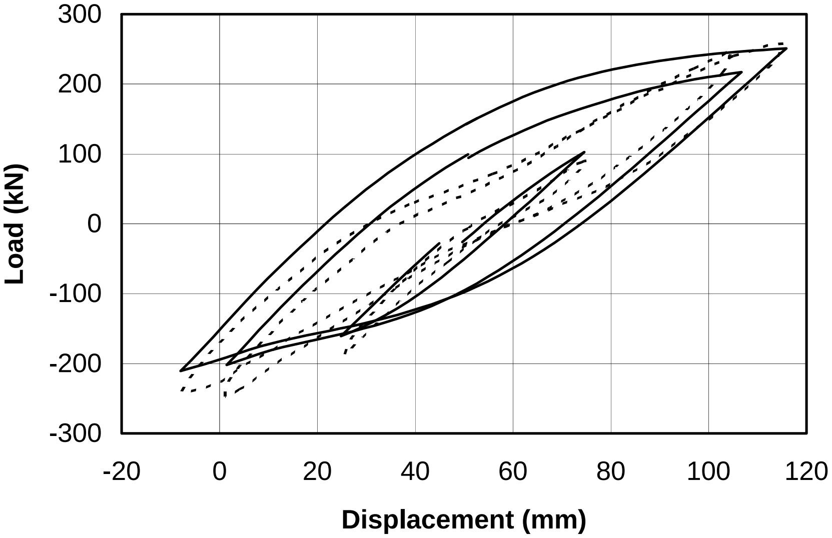

Figure 5.25 - Cyclic Load with shear strains by Truss Analogy Approach

In contrast to the equivalent-area model, the effect of shear deformations on the frame load-displacement behavior is more pronounced. For the repeated-loading test, the initial stiffness is appreciably reduced as compared to that observed experimentally. On the other hand, the unloading and reloading stiffnesses are now closer to the measured stiffnesses. The estimated capacity of the frame is slightly reduced compared with the response computed using the equivalent-area approach.

The effect of shear deformations for the computed response for cyclic loading is improved. The width of the simulated hysteresis loops is reduced compared with those computed considering only flexural deformations (Figure 5.19) and the unloading slopes at the loop ends are very close to those measured experimentally. There is still, however, a lack of pinching in the computed hysteresis loops.

5.4.4 Four-Story Building

The specimen reviewed in this section is the four-story building tested pseudo-dynamically and described in Section 4.5. In that section, a study of the building considering only flexural deformations was carried out. Figures 5.26 and 5.27 show once more the results of the dynamic analysis.

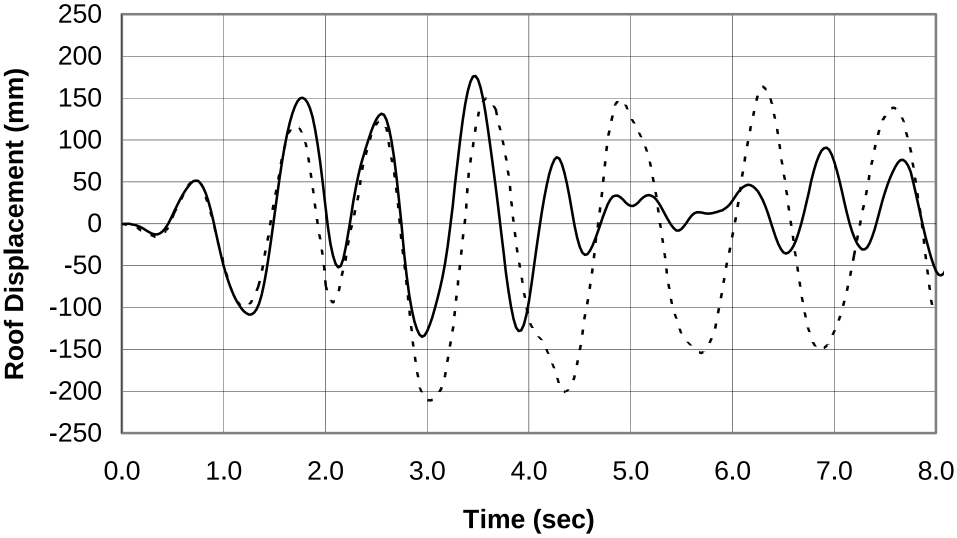

Figure 5.26 - Roof Displacement Time History Considering Only Flexural Deformations and using a Dynamic Analysis

As reported in Section 4.5.3 the damage sustained by the structure was apparently very limited. In particular, no diagonal cracks in members were reported, and just a few of the beam-column joints displayed some diagonal cracking. These results suggest that shear deformations in the members were probably minor, which is expected considering the slenderness of the elements. Nevertheless, analysis of the building was carried out using the truss analogy approach to evaluate the performance of the shear deformation model for this type of structure. A 45° crack inclination angle was chosen.

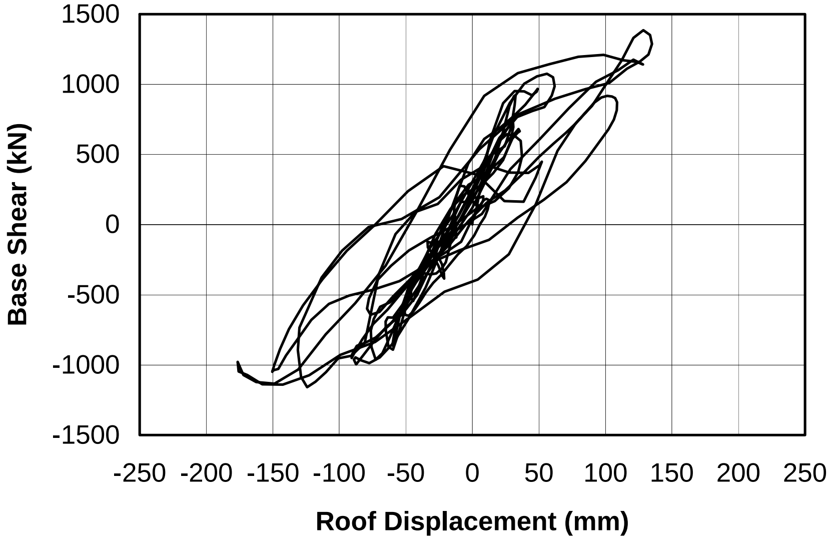

Figure 5.27 - Load-Displacement Prediction Considering Only Flexural Deformations and using a Dynamic Analysis

Results of the analysis are shown in Figures 5.28 and 5.29. In the first of these figures, the roof displacement time history is compared with the pseudo-dynamic response. In general, this prediction is somewhat similar to that obtained without the effects of shear deformations (Figure 5.26). For this case, however, the vibration period has increased slightly as expected. On the other hand, the computed displacement response during the initial four seconds decreased and shows apparent effects of higher modes of vibration. Finally, the computed displacement amplitudes for the last four seconds increased, but the prediction is still very different from the experimental data.

The computed load-displacement response, displayed in Figure 5.29, hardly resembles the response considering only flexural deformations (Figure 5.27) or the experimental response (Figure 4.49). However, a slight reduction in the computed average secant stiffness, from that observed in the computed flexural response is apparent.

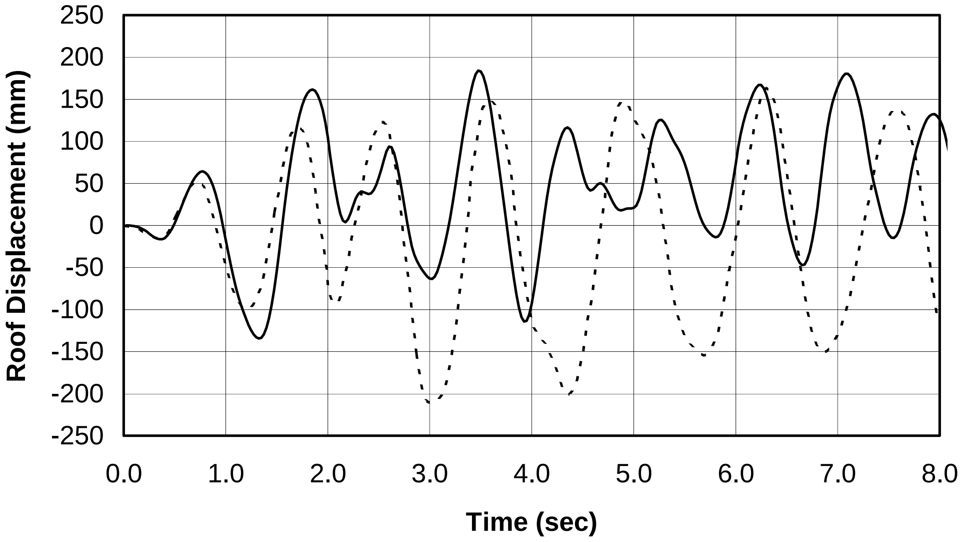

Figure 5.28 - Roof Displacement Time History including shear strains (Truss Analogy)

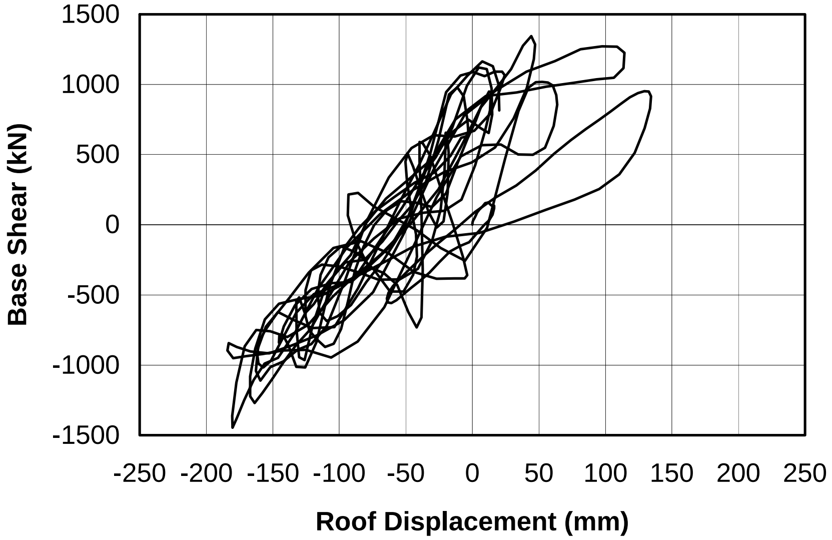

Figure 5.29 - Load-Displacement Prediction including shear strains (Truss Analogy)

Because of the poor prediction obtained using the dynamic analysis, a quasi-static analysis was performed similar to that carried out in Section 4.5.4. The base-shear time-history computed response generated with the inclusion of shear deformations using the truss analogy is shown in Figure 5.30. A slightly improved prediction is obtained for the first three seconds (see Figure 4.56). However, for the last five seconds the inclusion of shear deformations has practically no effect on the computed response.

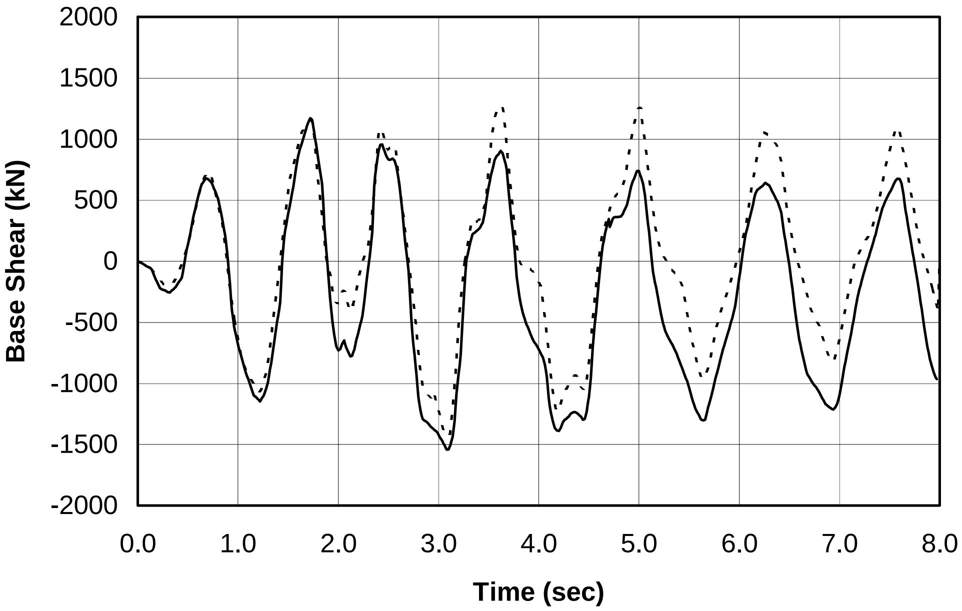

Figure 5.30 - Quasi-Static Computed Base Shear Time History Considering Shear Deformations Compared with Measured Response

Figure 5.31 shows the computed base shear-roof displacement response for the same model. A slight reduction in the computed unloading stiffnesses as well as a moderate reduction in the size of the hysteresis loops are observed.

The computed responses illustrated in Figures 5.30 and 5.31 confirm that the quasi-static analysis is more appropriate for the investigation of the experimental results for this structure.

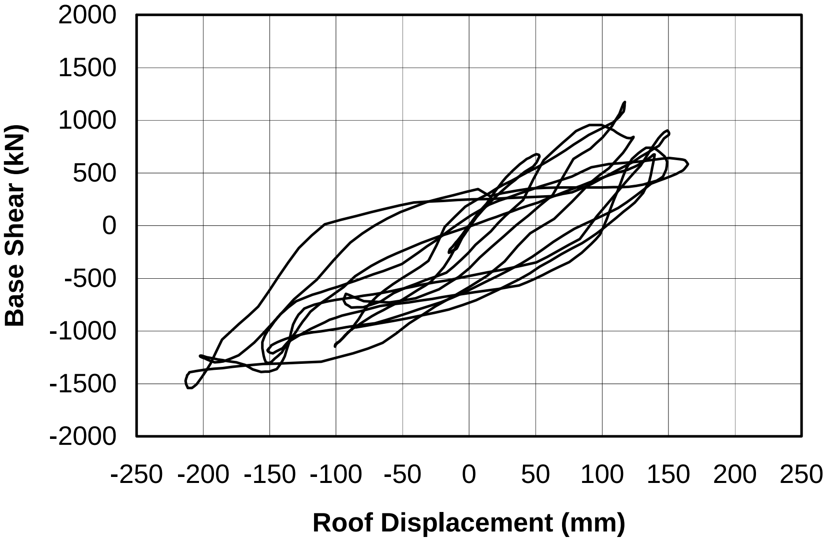

Figure 5.31 - Quasi-Static Computed Base Shear-Roof Displacement Response Considering Shear Deformations

5.5 Summary of Investigation Incorporating Shear-Deformation Models

Several analytical models to evaluate the shearing deformations in concrete members after cracking were presented, and two were implemented in a modified version of program FIBERC.

Although the models by Collins and Hsu are theoretically consistent and reportedly give good analytical results, they are very elaborate and introduce a large computational effort due to their iterative nature. Therefore, they were not considered further in this study.

A very simple model was developed in which an equivalent shear area, computed as the sum of the area of the fibers in compression at each step, together with the tangent shear modulus of those fibers, was used to estimate the shear deformations in the members, keeping the elastic formulation of the shear component of the member-flexibility matrix.

Another model considered in this chapter was a truss analogy consisting of rectangular panels composed of diagonal concrete compression struts, stirrup stringers, and reinforcing-bar chords.

It was found that the equivalent-area method did not generally improve significantly the agreement of the prediction with the experimentally-observed results. For some of the specimens evaluated in this section, for which shear deformations were expected to have a significant effect in the overall computed response, the model had practically no influence on the response.

The analogous truss model was found to have a greater effect on the prediction of inelastic response of reinforced concrete members and frames under repeated and reversed loads, primarily by reducing the structural stiffness. However, it was obvious that the model developed and used in this chapter did not completely account for the observed total response of the specimens studied. Therefore, in an attempt to complement this model, a method to include deformations induced by deterioration of bond between concrete and reinforcing steel is introduced in the following chapter.

CHAPTER 6

Model for Anchorage Slip of Members

6.1 Effects of Bar Extension and Slip in Member Deformations

Anchorage slip of reinforcing bars at the connections of reinforced concrete members can constitute a major source of inelastic deformations. Such deformations are specifically caused by straining and yielding of reinforcing bars inside the joint and slip of reinforcing bars with respect to the surrounding concrete in the joint and adjacent member ends.

The penetration of yielding of reinforcement into the joint produces extension of the bars that is not normally considered in the member models presented in the previous chapters. Slip of the reinforcing bars is due to the loss of bond between steel and concrete inside the joint and in the plastic hinge zone of the members.

The most important consequences of the two phenomena mentioned above in the behavior of members, as observed experimentally, have been summarized by Kaku and Asakusa (6-9). First, pinching of the force-deflection hysteresis loops of the members occurs, resulting in a loss of energy absorption capacity. Due to the bond loss, a change of shear transfer mechanism inside the joint occurs because the truss action disappears and a single diagonal compression-strut emerges. Also, large deformations associated with slip induce wider cracks and concentrated damage in the plastic hinge region which complicates repair and rehabilitation of the member. Finally, a reduction in moment capacity in adjoining members may be observed.

In addition to the effects of extension and slippage of the reinforcement, further deformations are caused by joint distortion. However, that effect will not be considered in this chapter.

6.2 Previous Research on Anchorage Slip

The effect of the deformations caused by anchorage slip and bond deterioration in the beam-column joint and in the plastic hinge regions of members has been studied extensively both experimentally and analytically. In this section, a brief review of the results and models developed in some of those studies are presented.

A complete set of studies on anchorage slip has been conducted in the last two decades at the University of California, Berkeley (6-2, 6-3, 6-4, 6-5, 6-6, 6-7, 6-8, 6-10). In the research conducted by Ciampi (6-2) and Eligehausen (6-3) a large number of pull-out tests were performed on single, deformed bars embedded five diameters into concrete blocks representing the confined region of beam-column joints. Based on the results of such tests, a relatively simple analytical model to simulate local bond-slip response of single bars embedded in concrete under generalized excitations was developed. This model is based on the assumption that bond deterioration depends on concrete damage as a function of the joint's total dissipated energy. This assumption, according to the authors, is correct for low-cycle fatigue loading (small number of cycles at large strains).

The model was then used to predict the bond behavior of bars anchored in joints of frames subjected to cyclic load, and good comparisons to experiments were obtained. Furthermore, a number of parametric studies were performed to evaluate the influence of loading history, bar diameter and strength, anchorage length, number of cycles and strain magnitude, among others, on the behavior of embedded bars.

Filippou (6-4, 6-7) developed a detailed model for the flexural analysis of reinforced concrete members and beam-column joints, including explicitly the effect of bond deterioration using the model developed by Ciampi and Eligehausen (6-2, 6-3). In his model, Filippou divides the element into subregions corresponding with the locations of vertical flexural cracks that penetrate through the depth of the section, as shown in Figure 6.1. One such region is the beam-column joint.

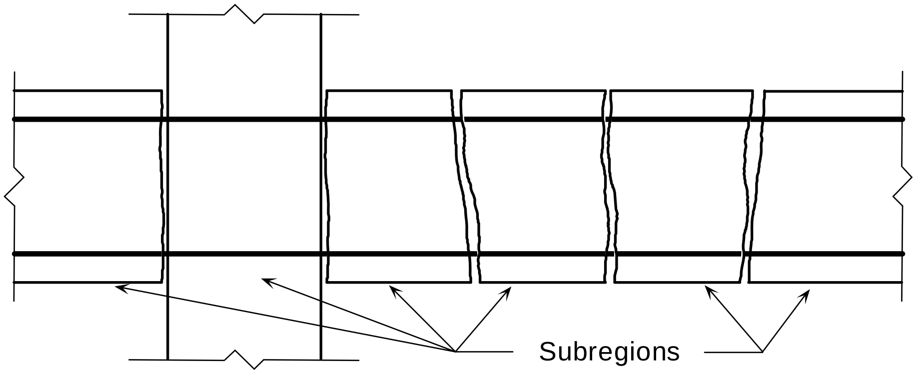

Figure 6.1 - Filippou's Critical Regions Model (adapted from 6-4)

Figure 6.2 shows the idealization of a typical interior joint of a frame. The bars within the joint are assumed to consist of top and bottom layers which are discretized into a number of segments. The displacements and stresses along the bar are formulated, using weighted residual and mixed finite element approaches, in such a way that a direct interaction relation between the variables at the two end sections of the joint is obtained. Finally, using such a relation, together with equilibrium of forces at the ends of the joint, the solution to any imposed history of deformations can be obtained.

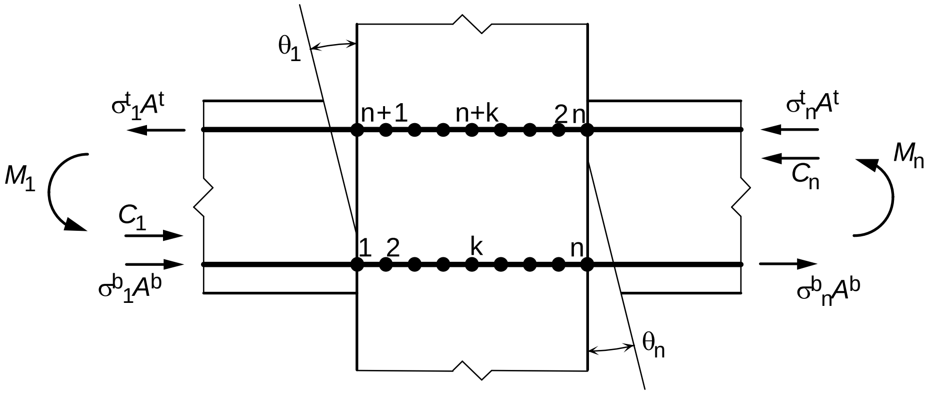

Figure 6.2 - Filippou's Joint Model (adapted from 6-4)

Tada and Takeda (6-13, 6-14) also developed a detailed analytical model to study the bond in beam-column joints. In their model, plastic hinge regions of fixed length are assumed at the element ends and they are discretized into a number of concrete and steel layers (fibers) whose behavior is governed by pre-determined constitutive hysteretic rules.

In the joint core the concrete is assumed rigid while the bars are discretized into small segments that are connected to the surrounding concrete by bond links, as shown in Figure 6.3. These links follow a simple bond-slip constitutive model developed by the authors.

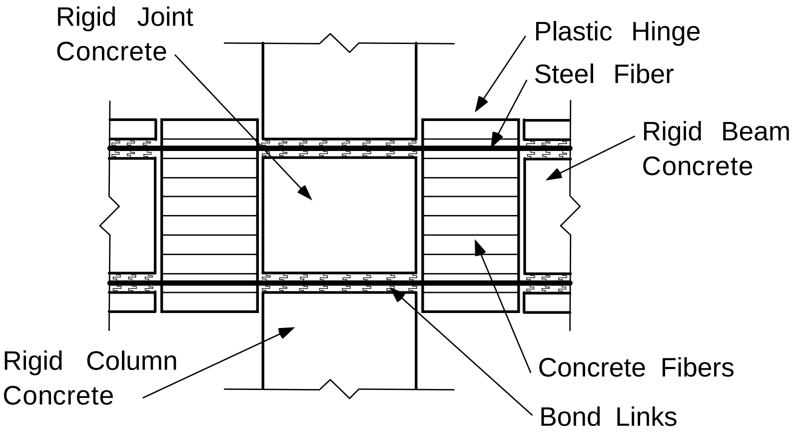

Figure 6.3 - Tada's Joint Model (adapted from 6-13)

Using the model outlined above, Tada and Takeda (6-14) conducted a series of comparisons to experimental results from beam-column subassemblage tests and obtained close prediction of the test results.

Saatcioglu and Alsiwat (6-1, 6-11, 6-12), at the University of Ottawa, developed a model to account for anchorage slip of reinforcing bars. Initially, a monotonic model for the force-deformation behavior of a single bar embedded in concrete was developed (6-1). The procedure accounts for the accumulation of elastic strains and plastic strains along the embedded length which result in net extension of the bar. The model includes an estimation of the bar slip when the stress builds up along its embedded length inducing a failure of the steel-concrete bond.

The force-deformation relationship found as outlined above was used by Saatcioglu et al (6-12) as the envelope for a hysteretic model. Finally, Saatcioglu and Alsiwat (6-11) applied their hysteretic model to the analysis of reinforced concrete frames.

Because of their simplicity and good performance, both the monotonic and cyclic models developed by Saatcioglu and associates will be used in this study in a slightly modified form. A brief but complete description of the models and their implementation in the program FIBERC is presented in Sections 6.2.1, 6.2.2 and 6.3. A more detailed account of the models is given elsewhere (6-1, 6-11).

6.2.1 Monotonic Model by Saatcioglu et al. (6-1)

Using the stress and strain distributions depicted in Figures 6.4b and 6.4c, the extension of the embedded reinforcing bar is computed for each one of four regions: elastic, yield plateau, strain hardening and pull-out cone.

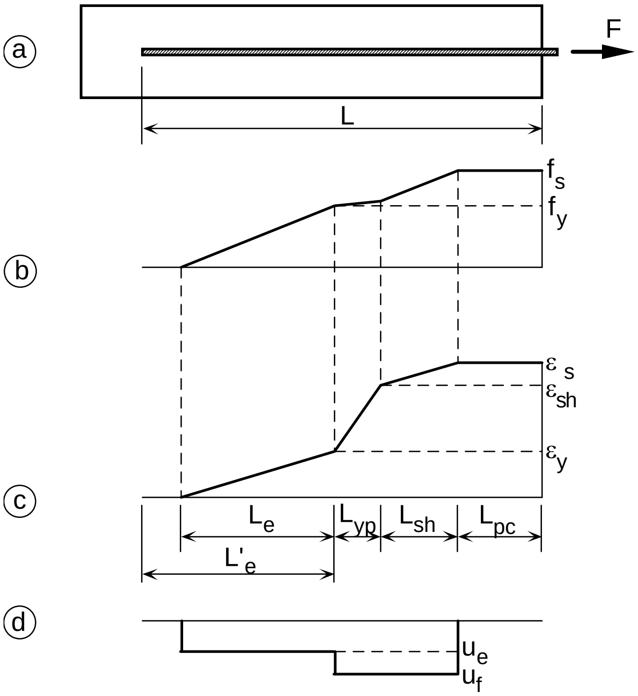

Figure 6.4 - Anchorage Extension Model by Saatcioglu et al. (adapted from 6-1)

In the region of length L_e, where the reinforcing bar stress is elastic, a constant average bond stress given by Equation 6.1 is assumed,

$$u_e = \frac{f_y d_b}{4 l_d} \tag{6.1}$$

in which d_b is the bar diameter and l_d is the development length given by Equation 6.2. In this and all other equations for the model, SI units are used.

$$l_d = \frac{440 A_b}{(3 d_b)\sqrt{f_c'}} \frac{f_y}{400} \geq 300\ mm \tag{6.2}$$

Using the average bond stress of Equation 6.1, the length L_e of the elastic region is

$$L_e = \frac{f_s d_b}{4 u_e} \tag{6.3}$$

in which f_s is the maximum elastic steel stress. If L_e is greater than the available elastic length, the bar will slip. Such a case is analyzed later in this section.

After yielding, large strains in the steel occur and the concrete between the ribs of the reinforcing bar crushes. Then, the bond stress becomes primarily frictional and can be taken as

$$u_f = \left(5.5 - 0.07 \frac{S_L}{H_L}\right)\sqrt{\frac{f_c'}{27.6}} \tag{6.4}$$

where S_L/H_L is the ratio of spacing to height of the reinforcing bar ribs. The segment of the bar in which stresses are at the yield plateau can be written as

$$L_{yp} = \frac{\Delta f_s d_b}{4 u_f} \tag{6.5}$$

in which Δf_s is the increment in stress between the starting and end points of the yield plateau. If there is no stress increase in this region, that is Δf_s=0, the length L_{yp} is zero.

If the reinforcement strain increases beyond the end of the yield plateau, the length of the bar segment in strain hardening can be computed again assuming frictional bond as

$$L_{sh} = \frac{\Delta f_s d_b}{4 u_f} \tag{6.6}$$

In this case Δf_s is the difference between the maximum stress f_s and the stress at the onset of strain hardening.

In the zone adjacent to the concrete face a pullout cone may be formed because of the tensile stresses that develop in the surrounding concrete. In that case, a segment L_{pc} of constant stress and strain exists in the bar as shown in Figures 6.4b and 6.4c. However, if adequate transverse reinforcement is provided close to the concrete face, this pullout may not occur.

Finally, the bar extension can be computed by integrating the strain distribution (Figure 6.4c) over the embedded length as

$$\delta_{ext} = \varepsilon_s L_{pc} + 0.5\left(\varepsilon_s + \varepsilon_{sh}\right) L_{sh} + 0.5\left(\varepsilon_{sh} + \varepsilon_y\right) L_{yp} + 0.5 \varepsilon_y L_e \qquad (6.7)$$

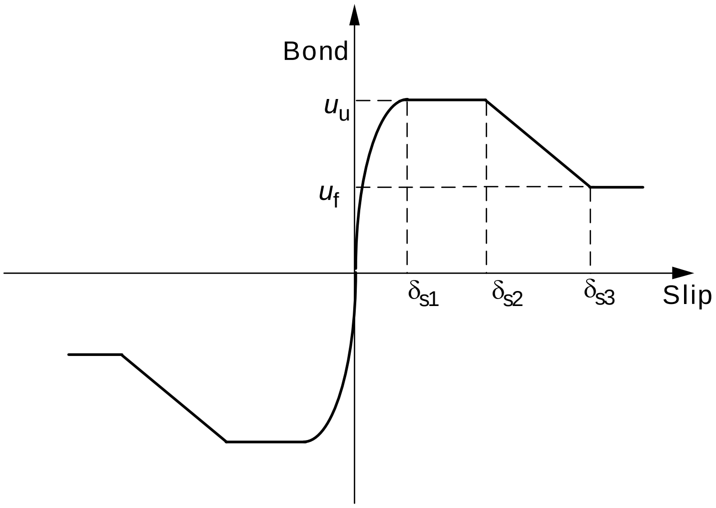

Figure 6.5 - Bond-Slip Model by Saatcioglu et al. (adapted from 6-1)

Slip of the reinforcement, which occurs when the entire embedded length is stressed, is estimated by means of the bond-slip model shown in Figure 6.5, using the bond stress acting at the end of the embedded length of the reinforcing bar.

The bond stress for the initial loading is given by

$$u = u_u \left(\frac{\delta_s}{\delta_{s1}} \right)^{0.4} \qquad (6.8)$$

where u_u, the ultimate bond stress, is defined by the expression

$$u_u = \left(20 - {}^{d_b}\!/_{4} \right) \sqrt{\frac{f_c'}{30}} \qquad (6.9)$$

where $\delta_{s1} = \sqrt{30/f_c^{'}}$, δ_{s2}=3.0 and δ_{s3}=S_L.

Therefore, the bar slip during the ascending branch can be computed as

$$\delta_s = \delta_{s1}\left(\frac{u_e'}{u_u}\right) \tag{6.10}$$

where u'_e is the bond stress at the end of the embedded length. This stress is obtained using Equation 6.11 in which L'_e is the available elastic length which is equal to the embedded length minus the plastic length (L_{yp}+L_{sh}+L_{pc}).

$$u_e' = \frac{f_s d_b}{4L_e'} \tag{6.11}$$

For bars that end in a hook, an additional deformation term δ_h must be added. Such deformation of the hook is a function of the force in the hook, and can be obtained from Equation 6.12

$$P_h = P_{hu}\left(\frac{\delta_h}{2.54}\right)^{0.2} \tag{6.12}$$

where P_h is the force in the hook and P_{hu} = 271(0.05d_b-0.25).

Upon unloading, the elastic deformation δ_r given by Equation 6.13 is recovered while the plastic extension and slip are residual permanent deformations.

$$\delta_r = \varepsilon_y\left(L_t - \frac{L_e}{2}\right) \tag{6.13}$$

6.2.2 Hysteretic Model by Saatcioglu et al. (6-12)

The hysteretic model for anchorage slip of reinforced concrete members is formulated in terms of the moment-rotation relationship at the member ends. The model consists of a primary curve, which is constructed based on the monotonic extension-slip bar model presented earlier, and a number of hysteretic rules.

The primary curve is obtained by performing a flexural section analysis to calculate the moment in the end section and the strains in the reinforcing bars. Using those strains, the extension and slip in the bar are computed and then, the rotation of the section is estimated with Equation 6.14

$$\theta = \frac{\delta}{d - c} \tag{6.14}$$

where (*d*-*c*) is the distance between the bar and the neutral axis of the section.

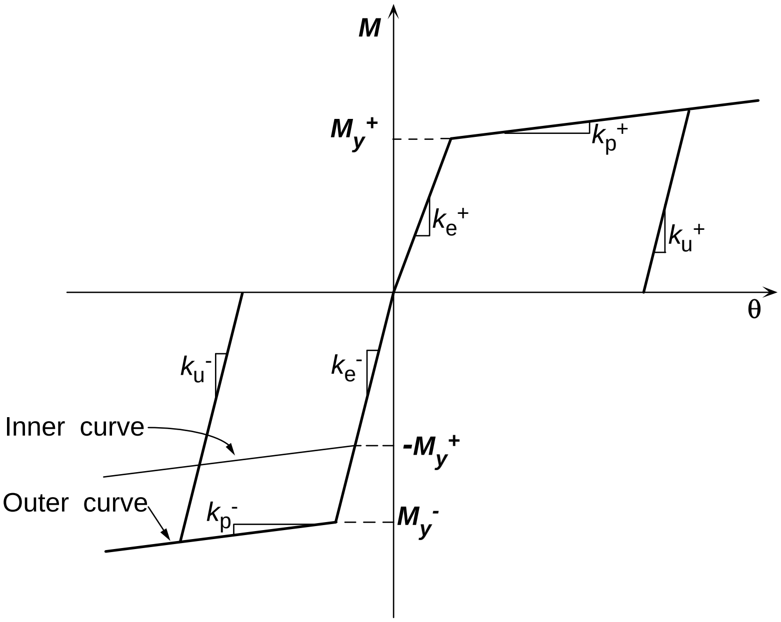

Figure 6.6 - Moment-Rotation Primary Curve model by Saatcioglu et al.

Figure 6.6 shows a typical primary curve resulting from this procedure. In this relationship, yielding is taken as the point at which the onset of strain hardening in the steel in tension has been reached. Before this point is reached the response is considered elastic with a stiffness k_e. The post-yield branch joins the yield point with the point at which the maximum concrete compression strain is equal to ε_{50} (post-peak strain at which 50% of the maximum concrete strength is resisted). The stiffness of this branch is k_p. Finally, the unloading branch, with stiffness k_u, is computed using the recovered deformation of the bars.

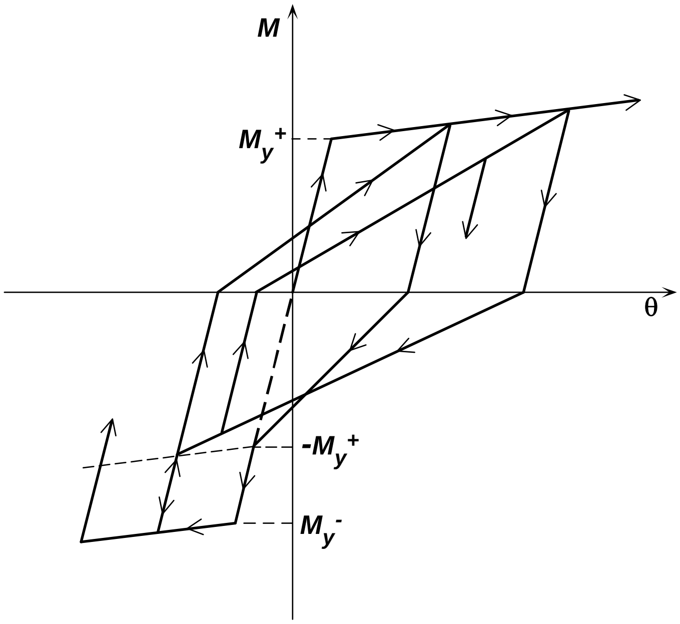

Figure 6.7 - Hysteretic Model by Saatcioglu et al. (adapted from 6-12)

A typical moment-rotation response to cyclic loading is shown in Figure 6.7. The set of rules that govern the response are empirical and developed based on experimental observations. The hysteretic rules are as follows:

1. Loading and unloading before first yielding is elastic with stiffness k_e^+ or k_e^-.
2. After first yielding, loading follows the slope k_p^+ (k_p^-) and unloading follows the slope k_u^+ (k_u^-). Subsequent reloading in the opposite direction aims at the previous maximum excursion (or yield point if no yielding in that direction has taken place).
3. Unloading after a moment reversal before reaching the previous maximum is parallel to the unloading branch from the previous maximum.
4. Reloading after small-amplitude cycles is directed at the second previous maximum and once this is reached, is directed at the previous maximum.
5. Reloading before complete unloading aims at the immediate previous maximum.

6.3 Implementation of Anchorage Slip Model

The program FIBERC was further modified to include the effect of anchorage slip following Saatcioglu et al's model. The new member idealization, shown in Figure 6.8, introduces rotational springs at both ends of the fiber element. Additionally, rigid zones in place of the joints are also introduced as discussed in Subsection 6.3.2.

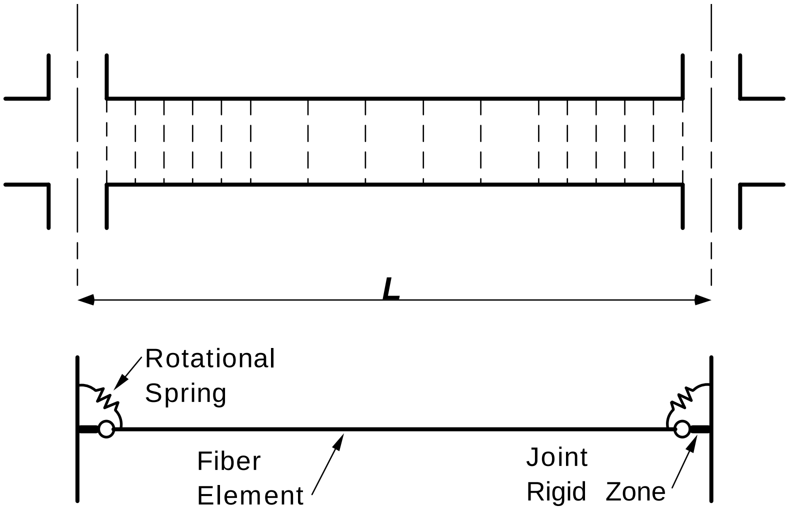

Figure 6.8 - Member Idealization for Anchorage Slip Model

The extension-slip model by Saatcioglu was modified as follows. First, it was assumed that the beam-column joint has adequate transverse reinforcement to prevent the pullout cone from occurring and therefore, L_{pc}=0 in Equation 6.7. Next, it was assumed that no increment in stress takes place during the yield plateau, and hence, Δf_s=0 in Equation 6.5 and consequently, L_{yp}=0 as well. Thus, Equation 6.7 can be rewritten as

$$\delta_{ext} = 0.5(\varepsilon_s + \varepsilon_{sh}) L_{sh} + 0.5 \varepsilon_y L_e \tag{6.15}$$

Finally, for hooked bars or bars that are welded to end plates, it was assumed that no slip or deformation at the end of the straight portion of the bar takes place, that is, δ_s=0 and δ_h=0.

6.3.1 Addition of Hysteretic Rotational Springs

To include the effect of the rotational spring in the member, a modification of the member stiffness matrix was developed as outlined below.

Equation 2.64 was rewritten in an expanded form as given by Equation 6.16. It must be noticed that the stiffness coefficients k_{ii} of the member stiffness matrix of this equation are not equal to those of Equations 2.54 through 2.61.

$$\begin{Bmatrix} \Delta X_A \\ \Delta Y_A \\ \Delta M_A \\ \Delta X_B \\ \Delta Y_B \\ \Delta M_B \end{Bmatrix} = \begin{bmatrix} k_{11} & k_{12} & k_{13} & k_{14} & k_{15} & k_{16} \\ k_{21} & k_{22} & k_{23} & k_{24} & k_{25} & k_{26} \\ k_{31} & k_{32} & k_{33} & k_{34} & k_{35} & k_{36} \\ k_{41} & k_{42} & k_{43} & k_{44} & k_{45} & k_{46} \\ k_{51} & k_{52} & k_{53} & k_{54} & k_{55} & k_{56} \\ k_{61} & k_{62} & k_{63} & k_{64} & k_{65} & k_{66} \end{bmatrix} \begin{Bmatrix} \Delta u_A \\ \Delta v_A \\ \Delta \theta_A \\ \Delta u_B \\ \Delta v_B \\ \Delta \theta_B \end{Bmatrix} \tag{6.16}$$

If each one of the rows of Equation 6.16 is written separately, a set of simultaneous equations is obtained (Equations 6.17)

$$\begin{aligned} \Delta X_A &= k_{11}\Delta u_A + k_{12}\Delta v_A + k_{13}\Delta\theta_A + k_{14}\Delta u_B + k_{15}\Delta v_B + k_{16}\Delta\theta_B \\ \Delta Y_A &= k_{21}\Delta u_A + k_{22}\Delta v_A + k_{23}\Delta\theta_A + k_{24}\Delta u_B + k_{25}\Delta v_B + k_{26}\Delta\theta_B \\ \Delta M_A &= k_{31}\Delta u_A + k_{32}\Delta v_A + k_{33}\Delta\theta_A + k_{34}\Delta u_B + k_{35}\Delta v_B + k_{36}\Delta\theta_B \\ \Delta Y_B &= k_{41}\Delta u_A + k_{42}\Delta v_A + k_{43}\Delta\theta_A + k_{44}\Delta u_B + k_{45}\Delta v_B + k_{46}\Delta\theta_B \\ \Delta Y_B &= k_{51}\Delta u_A + k_{52}\Delta v_A + k_{53}\Delta\theta_A + k_{54}\Delta u_B + k_{55}\Delta v_B + k_{56}\Delta\theta_B \\ \Delta M_B &= k_{61}\Delta u_A + k_{62}\Delta v_A + k_{63}\Delta\theta_A + k_{64}\Delta u_B + k_{65}\Delta v_B + k_{66}\Delta\theta_B \end{aligned} \tag{6.17}$$

In the previous equations $\Delta\theta$ represented the rotation at the end of the member. If the member is rigidly attached to the joint, as assumed in the theoretical development presented in Chapter 2, $\Delta\theta$ is also the rotation of the joint.

When a rotational spring is introduced at the end of the member, $\Delta\theta$ is no longer equal to the joint rotation. Instead, the rotation of the joint $\Delta\theta'$ can be expressed as the rotation of the end of the member plus the additional rotation in the spring. The spring rotation increment can in turn be written as the member-end moment increment divided by the spring's tangent rotational stiffness, k_{R} (Equation 6.15).

$$\Delta\theta' = \Delta\theta + \delta\theta = \Delta\theta + \frac{\Delta M}{k_R} \qquad (6.18)$$

Using Equation 6.18, the set of Equations 6.17 can be rewritten in terms of the joint rotations at both ends of the element, and a new set of equations is obtained (Equations 6.19).

$$\begin{aligned}
\Delta X_A &= k_{11}\Delta u_A + k_{12} v_A + k_{13}\left(\Delta\theta'_A - \frac{\Delta M_A}{k_A}\right) + k_{14}\Delta u_B + k_{15}\Delta v_B + k_{16}\left(\Delta\theta'_B - \frac{\Delta M_B}{k_B}\right) \\
\Delta Y_A &= k_{21}\Delta u_A + k_{22} v_A + k_{23}\left(\Delta\theta'_A - \frac{\Delta M_A}{k_A}\right) + k_{24}\Delta u_B + k_{25}\Delta v_B + k_{26}\left(\Delta\theta'_B - \frac{\Delta M_B}{k_B}\right) \\
\Delta M_A &= k_{31}\Delta u_A + k_{32} v_A + k_{33}\left(\Delta\theta'_A - \frac{\Delta M_A}{k_A}\right) + k_{34}\Delta u_B + k_{35}\Delta v_B + k_{36}\left(\Delta\theta'_B - \frac{\Delta M_B}{k_B}\right) \\
\Delta Y_B &= k_{41}\Delta u_A + k_{42} v_A + k_{43}\left(\Delta\theta'_A - \frac{\Delta M_A}{k_A}\right) + k_{44}\Delta u_B + k_{45}\Delta v_B + k_{46}\left(\Delta\theta'_B - \frac{\Delta M_B}{k_B}\right) \\
\Delta Y_B &= k_{51}\Delta u_A + k_{52} v_A + k_{53}\left(\Delta\theta'_A - \frac{\Delta M_A}{k_A}\right) + k_{54}\Delta u_B + k_{55}\Delta v_B + k_{56}\left(\Delta\theta'_B - \frac{\Delta M_B}{k_B}\right) \\
\Delta M_B &= k_{61}\Delta u_A + k_{62} v_A + k_{63}\left(\Delta\theta'_A - \frac{\Delta M_A}{k_A}\right) + k_{64}\Delta u_B + k_{65}\Delta v_B + k_{66}\left(\Delta\theta'_B - \frac{\Delta M_B}{k_B}\right)
\end{aligned} \qquad (6.19)$$

Rearranging the force and displacement terms, these become

$$\begin{aligned}
\Delta X_A + \frac{k_{13}}{k_A}\Delta M_A + \frac{k_{16}}{k_B}\Delta M_B &= k_{11}\Delta u_A + k_{12}\Delta v_A + k_{13}\Delta\theta'_A + k_{14}\Delta u_B + k_{15}\Delta v_B + k_{16}\Delta\theta'_B \\
\Delta Y_A + \frac{k_{23}}{k_A}\Delta M_A + \frac{k_{26}}{k_B}\Delta M_B &= k_{21}\Delta u_A + k_{22}\Delta v_A + k_{23}\Delta\theta'_A + k_{24}\Delta u_B + k_{25}\Delta v_B + k_{26}\Delta\theta'_B \\
\Delta M_A + \frac{k_{33}}{k_A}\Delta M_A + \frac{k_{36}}{k_B}\Delta M_B &= k_{31}\Delta u_A + k_{32}\Delta v_A + k_{33}\Delta\theta'_A + k_{34}\Delta u_B + k_{35}\Delta v_B + k_{36}\Delta\theta'_B \\
\Delta Y_B + \frac{k_{43}}{k_A}\Delta M_A + \frac{k_{46}}{k_B}\Delta M_B &= k_{41}\Delta u_A + k_{42}\Delta v_A + k_{43}\Delta\theta'_A + k_{44}\Delta u_B + k_{45}\Delta v_B + k_{46}\Delta\theta'_B \\
\Delta Y_B + \frac{k_{53}}{k_A}\Delta M_A + \frac{k_{56}}{k_B}\Delta M_B &= k_{51}\Delta u_A + k_{52}\Delta v_A + k_{53}\Delta\theta'_A + k_{54}\Delta u_B + k_{55}\Delta v_B + k_{56}\Delta\theta'_B \\
\Delta M_B + \frac{k_{63}}{k_A}\Delta M_A + \frac{k_{66}}{k_B}\Delta M_B &= k_{61}\Delta u_A + k_{62}\Delta v_A + k_{63}\Delta\theta'_A + k_{64}\Delta u_B + k_{65}\Delta v_B + k_{66}\Delta\theta'_B
\end{aligned}$$

Finally, these equations are assembled in matrix form in Equation 6.20.

$$\begin{bmatrix} 1 & 0 & \frac{k_{13}}{k_A} & 0 & 0 & \frac{k_{16}}{k_B} \\ 0 & 1 & \frac{k_{23}}{k_A} & 0 & 0 & \frac{k_{26}}{k_B} \\ 0 & 0 & 1+\frac{k_{33}}{k_A} & 0 & 0 & \frac{k_{36}}{k_B} \\ 0 & 0 & \frac{k_{43}}{k_A} & 1 & 0 & \frac{k_{46}}{k_B} \\ 0 & 0 & \frac{k_{53}}{k_A} & 0 & 1 & \frac{k_{56}}{k_B} \\ 0 & 0 & \frac{k_{63}}{k_A} & 0 & 0 & 1+\frac{k_{66}}{k_B} \end{bmatrix} \begin{Bmatrix} \Delta X_A \\ \Delta Y_A \\ \Delta M_A \\ \Delta X_B \\ \Delta Y_B \\ \Delta M_B \end{Bmatrix} = \begin{bmatrix} k_{11} & k_{12} & k_{13} & k_{14} & k_{15} & k_{16} \\ k_{21} & k_{22} & k_{23} & k_{24} & k_{25} & k_{26} \\ k_{31} & k_{32} & k_{33} & k_{34} & k_{35} & k_{36} \\ k_{41} & k_{42} & k_{43} & k_{44} & k_{45} & k_{46} \\ k_{51} & k_{52} & k_{53} & k_{54} & k_{55} & k_{56} \\ k_{61} & k_{62} & k_{63} & k_{64} & k_{65} & k_{66} \end{bmatrix} \begin{Bmatrix} \Delta u_A \\ \Delta v_A \\ \Delta \theta'_A \\ \Delta u_B \\ \Delta v_B \\ \Delta \theta'_B \end{Bmatrix} \qquad (6.20)$$

Equations 6.20 can be written in matrix notation as

$$[L]\{\Delta F\} = [K]\{\Delta U\} \qquad (6.21)$$

from which the force vector can be obtained in terms of the displacement vector pre-multiplied by a modified member stiffness matrix [K^*] as in Equation 6.22.

$$\{\Delta F\} = [L]^{-1}[K]\{\Delta U\} = [T][K]\{\Delta U\} = \left[K^*\right][\Delta U] \qquad (6.22)$$

In this expression, matrix [T] is given by Equation 6.23 shown below.

$$T = \frac{1}{D}\begin{bmatrix} 1 & 0 & \frac{-\left(k_{13}k_B + k_{13}k_{66} - k_{63}k_{16}\right)}{k_A k_B} & 0 & 0 & \frac{-\left(k_{16}k_A + k_{16}k_{33} - k_{13}k_{36}\right)}{k_A k_B} \\ 0 & 1 & \frac{-\left(k_{23}k_B + k_{23}k_{66} - k_{63}k_{26}\right)}{k_A k_B} & 0 & 0 & \frac{-\left(k_{26}k_A + k_{26}k_{33} - k_{23}k_{36}\right)}{k_A k_B} \\ 0 & 0 & \frac{k_B + k_{66}}{k_B} & 0 & 0 & \frac{-k_{36}}{k_B} \\ 0 & 0 & \frac{-\left(k_{43}k_B + k_{43}k_{66} - k_{63}k_{46}\right)}{k_A k_B} & 1 & 0 & \frac{-\left(k_{46}k_A + k_{46}k_{33} - k_{43}k_{36}\right)}{k_A k_B} \\ 0 & 0 & \frac{-\left(k_{53}k_B + k_{53}k_{66} - k_{63}k_{56}\right)}{k_A k_B} & 0 & 1 & \frac{-\left(k_{56}k_A + k_{56}k_{33} - k_{53}k_{36}\right)}{k_A k_B} \\ 0 & 0 & \frac{-k_{63}}{k_A} & 0 & 0 & \frac{k_A + k_{33}}{k_A} \end{bmatrix} \qquad (6.23)$$

where,

$$D = \frac{(k_A + k_{33})(k_B + k_{66}) - k_{63}k_{36}}{k_A k_B} \tag{6.24}$$

6.3.2 Addition of Joint Rigid Zones

The beam-column joints in reinforced concrete frames are very rigid before cracking. Once they crack and bond deteriorates, considerable distortion of the joints can take place. The modeling of such deformations is quite complex and is beyond the scope of this study. However, a simple model was introduced to program FIBERC to account for this behavior as described below.

The displacements at the end of the members can be written in terms of the displacements at the joints as

$$\{\Delta U\} = [G]\{\Delta U'\} \tag{6.25}$$

Likewise, the forces at the joints can be written as a function of the member end forces as

$$\{\Delta F'\} = \left[G^T\right]\{\Delta F\} \tag{6.26}$$

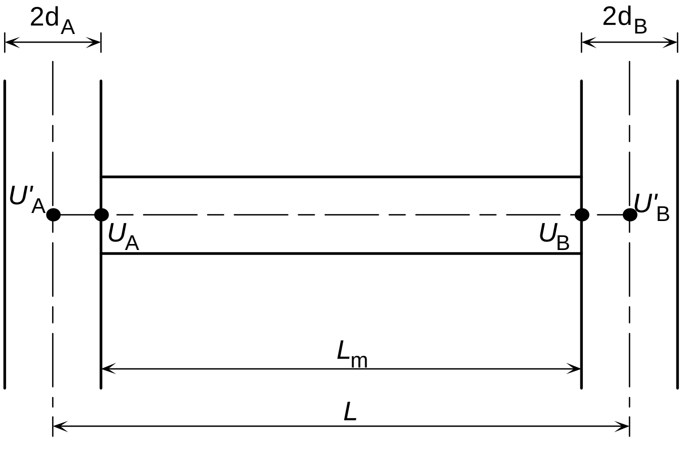

Figure 6.9 - Effect of Joint Size

The matrices G and G_T are given by Equations 6.27 and 6.28. In those equations, d_a and d_b are the dimensions of the joints (Figure 6.9) and α is a joint stiffness factor. The magnitude of α can be taken as between 0 and 1, and in this way the stiffness of the joint can be indirectly reduced.

$$G = \begin{bmatrix} 1 & 0 & 0 & 0 & 0 & 0 \\ 0 & 1 & \alpha d_A & 0 & 0 & 0 \\ 0 & 0 & 1 & 0 & 0 & 0 \\ 0 & 0 & 0 & 1 & 0 & 0 \\ 0 & 0 & 0 & 0 & 1 & -\alpha d_b \\ 0 & 0 & 0 & 0 & 0 & 1 \end{bmatrix} \tag{6.27}$$

$$G^T = \begin{bmatrix} 1 & 0 & 0 & 0 & 0 & 0 \\ 0 & 1 & 0 & 0 & 0 & 0 \\ 0 & \alpha d_A & 1 & 0 & 0 & 0 \\ 0 & 0 & 0 & 1 & 0 & 0 \\ 0 & 0 & 0 & 0 & 1 & 0 \\ 0 & 0 & 0 & 0 & -\alpha d_b & 1 \end{bmatrix} \tag{6.28}$$

Equation 6.29, which relates member-end forces to member-end displacements, was obtained in Chapter 2 (Equation 2.64) and is equivalent to Equation 6.16.

$$\{\Delta F\} = [K]\{\Delta U\} \tag{6.29}$$

Introducing Equations 6.29 and 6.25 into Equation 6.26, a new stiffness matrix for the member $[K']$ is obtained as follows

$$\{\Delta F'\} = \left[G^T\right][K][G]\{\Delta U'\} = [K']\{\Delta U'\} \tag{6.30}$$

6.4 Application of Anchorage Slip Model

In this section the response predictions of some of the elements and frames studied in Chapters 4 and 5 are reviewed using the models developed above to account for the effect of anchorage slip and rigid joints.

As in Chapter 5 the computed response of members and frames to static and dynamic loads, using the program FIBERC, is presented graphically together with the corresponding experimental response. Once again, the experimental response is shown in dashed lines and the computed response in solid lines

6.4.1 Cantilever Beam by Hanks

The first specimen to be analyzed here is the beam described in Section 4.3.1 tested by Hanks. Figure 6.10 shows the results of the analysis of this beam including flexural and shear deformations obtained in Section 5.3 (the measured response is also plotted with a dashed line). In Figure 6.11 the computed response, including the effects of anchorage slip is presented together with the experimental response.

Although the initial stiffness of the beam is underestimated by the model, the overall shape of the hysteretic loops is closely simulated, including a reduction in the width of the loops. Unloading stiffnesses, reloading stiffness in the negative direction, and strength levels are reasonably well predicted. Moreover, the computed crack-closing effect in the positive loading direction is delayed and more gradual than in previous models.

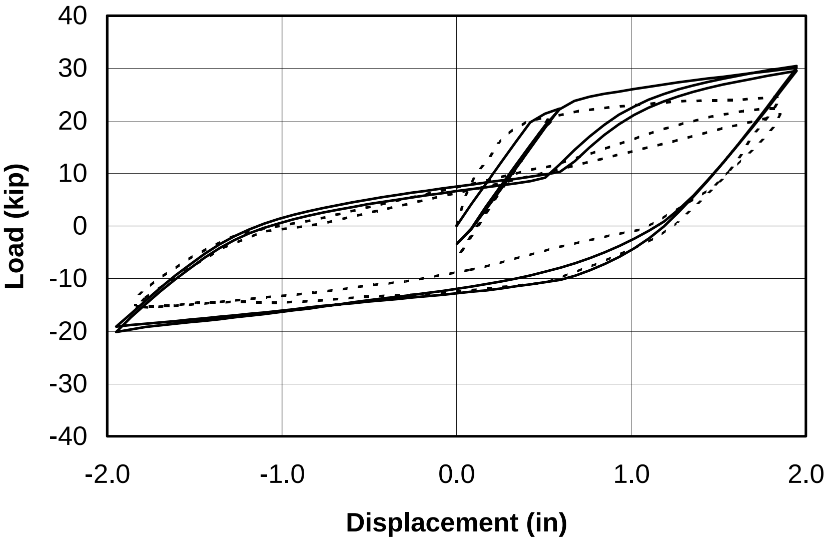

Figure 6.10 - Computed Response Including Shear Deformations

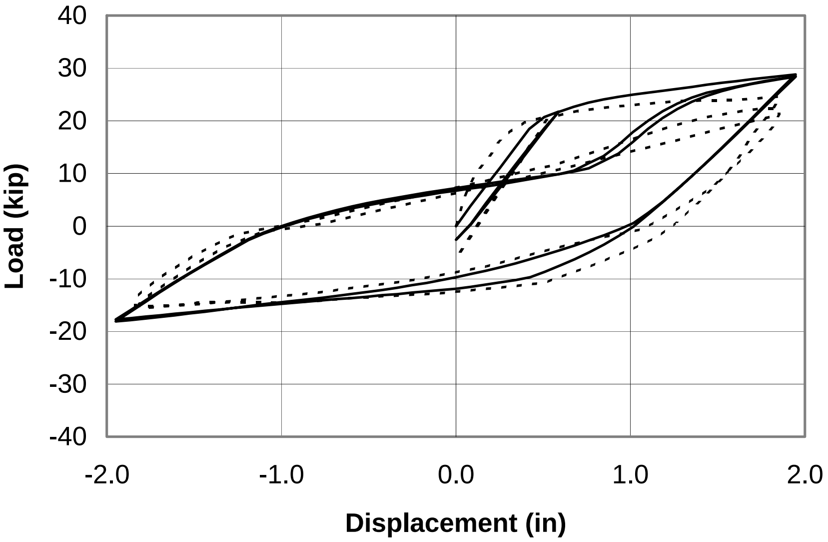

Figure 6.11 - Computed Hanks' Beam Response Including Anchorage Slip

6.4.2 Cantilever Beam by Popov et al.

The next specimen considered is the beam tested by Popov et al. that was described and studied for flexural response in Section 4.3.2, and for combined flexural and shear response in Section 5.3. Figure 6.12 shows the results of the computed response including flexural and shear deformations (measured experimental response is also plotted).

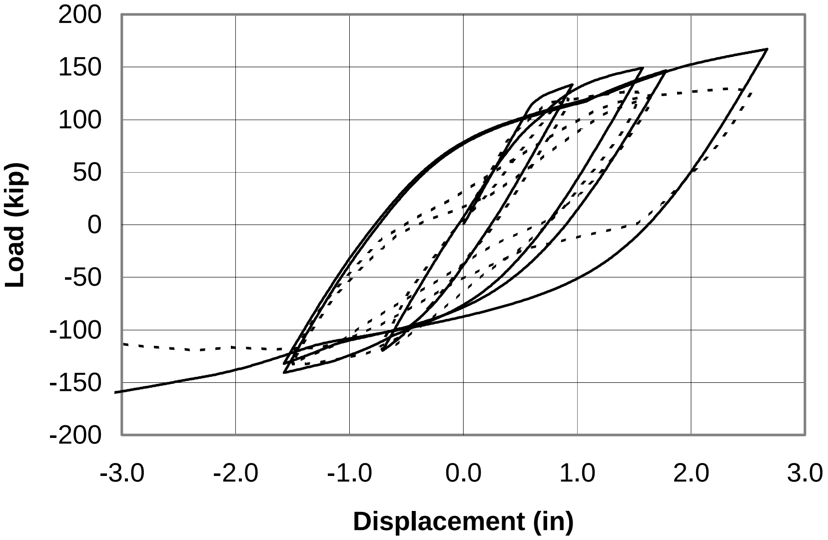

Figure 6.12 - Computed Response Including Shear Deformations

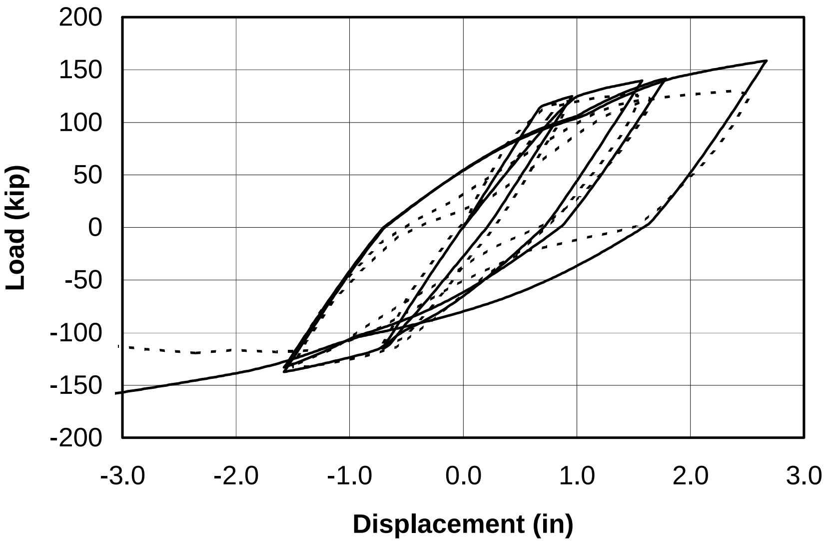

Figure 6.13 - Computed Response Including Anchorage Slip

In Figure 6.13 the computed load-displacement response, including the anchorage slip effect, is shown together with the experimental response. The two initial loops of the simulation are very close to those observed experimentally in terms of both strength and stiffness. For the large displacement loops the model fails to capture the significant pinching that occurred in the test. Likewise, the model is unable to predict the drop in capacity for the last cycle. Nevertheless, the overall shape of the loops is closer to the shape of the experimentally observed loops than the computed response which did not include bar slip.

The two specimens analyzed above were beams that were connected to large blocks of concrete (Figures 4.11 and 4.17) and therefore, they did not contain a real beam-column joint . In contrast, the specimens studied in Sections 4.4 and 4.5 were actual frames for which the model for beam-column joints developed in Section 6.3.2 can be directly applied as discussed in the following sections.

6.4.3 Two-Story Frame

A series of runs using the modified version of FIBERC that accounts for joint rigidity and anchorage slip was performed on the two-story frame described in Section 4.4.

Figures 6.14 and 6.15 show the load-displacement response, involving both flexural and shear deformations, of that frame as reported in Section 5.3.

Figure 6.16 shows the comparison between the computed response for rigid joints and the experimental response under repeated loads. The computed lateral strength of the frame increases with a much better agreement with the experimental response, which is even slightly overestimated (whereas before it was more seriously underestimated). The initial stiffness increases as well and closely follows that observed in the experiment. Moreover, the unloading and reloading slopes also increased and are now slightly steeper than those measured during the test.

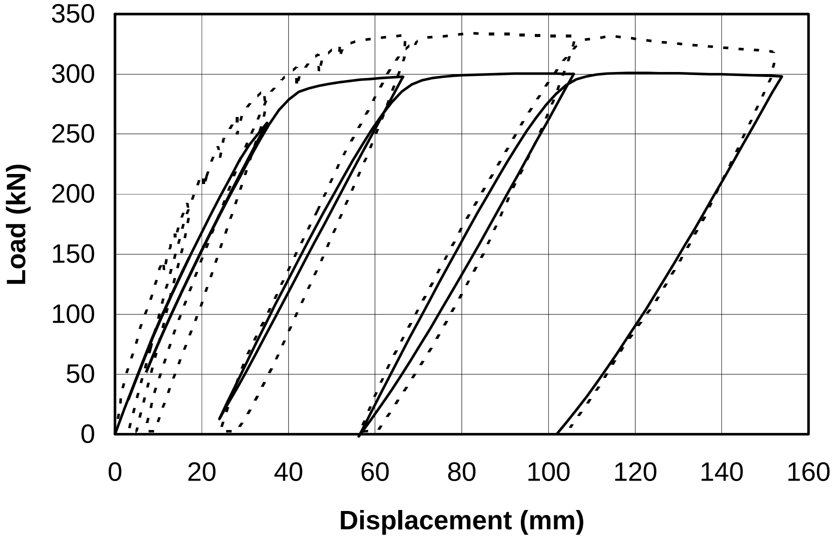

Figure 6.14 - Computed Repeated Load Response including Shear Deformations

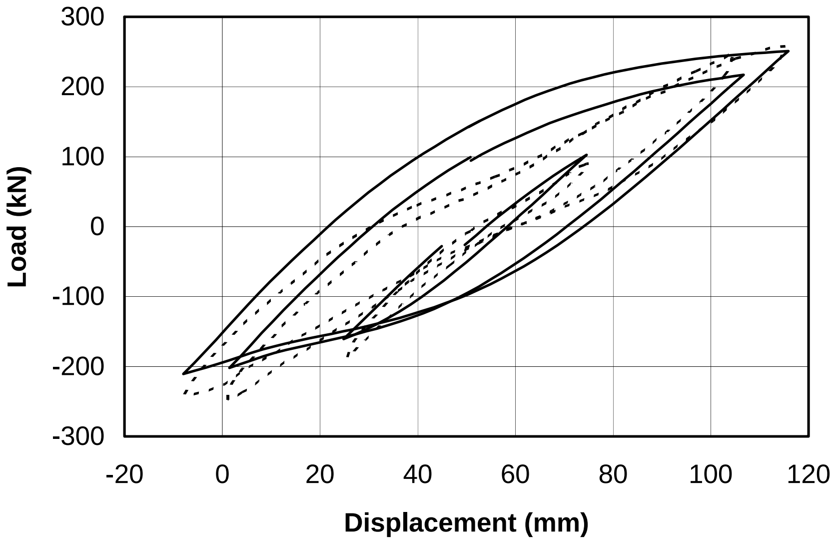

Figure 6.15 - Computed Reversed Load Response including Shear Deformations

For the same structural model, Figure 6.17 shows the computed load-displacement response and the measured response of the frame to cyclic loads. The hysteresis loops regained some of the width of the flexure-only response, and the unloading and reloading stiffnesses increased, particularly in the small-displacement cycle.

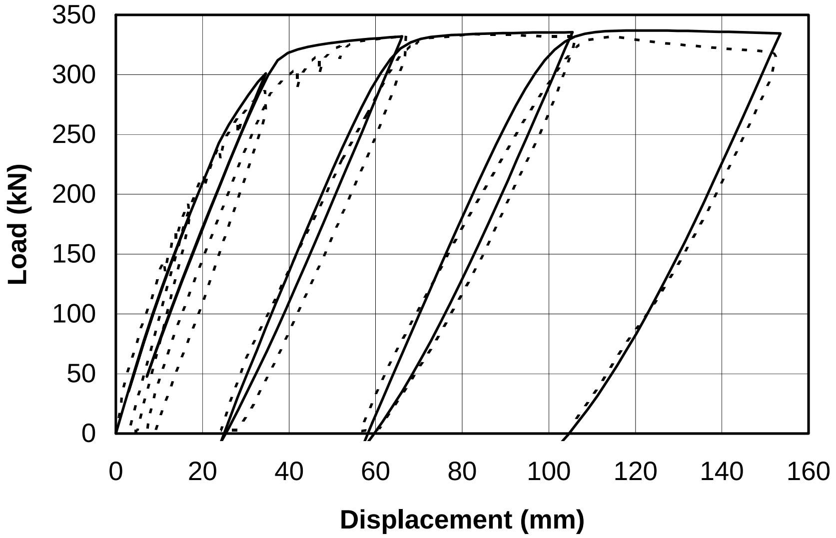

Figure 6.16 - Computed Response with Shear Deformations (Truss Analogy) and Rigid Joints

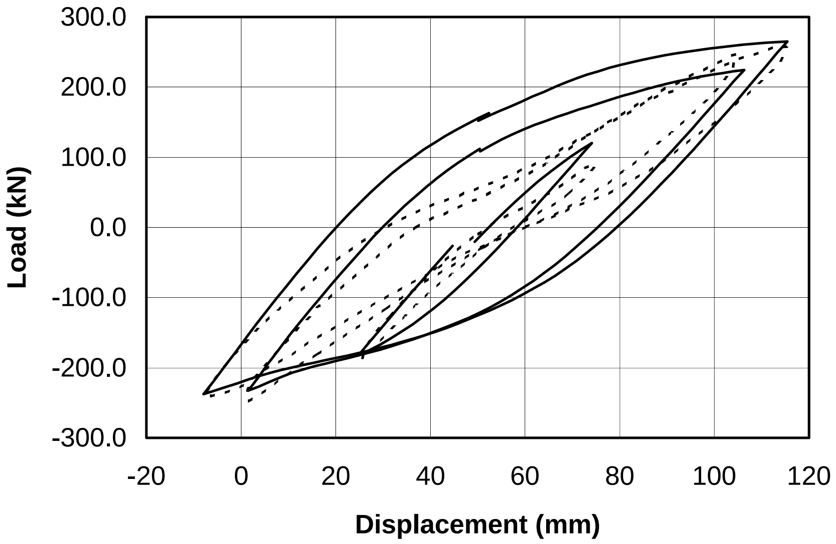

Figure 6.17 - Computed Cyclic Response with Shear Deformations (Truss Analogy) and Rigid Joints

A 50% reduction in the rigidity of the joints was applied to the model to investigate the effect of joint stiffness on the structural response. Figure 6.18 displays the computed load-displacement response for this structural model under repeated loads. Naturally, the initial stiffness of the model decreased, although not by much. The computed response is still a very good estimate of the measured response. Likewise, the estimated capacity of the frame reduced slightly and is just 2% less than that obtained experimentally. The unloading and reloading stiffnesses are very close to the measured stiffnesses.

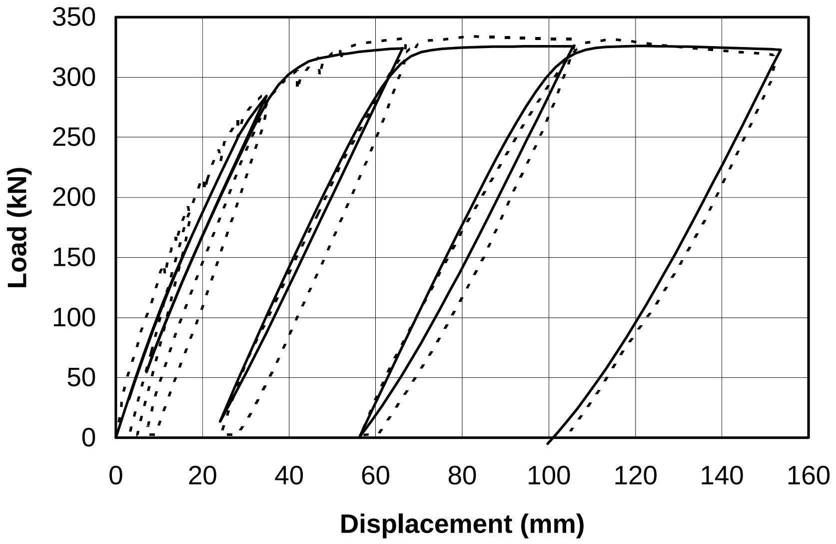

Figure 6.18 - Computed Response including Shear Deformations (Truss Analogy) and 50% Reduction in Joint Stiffness

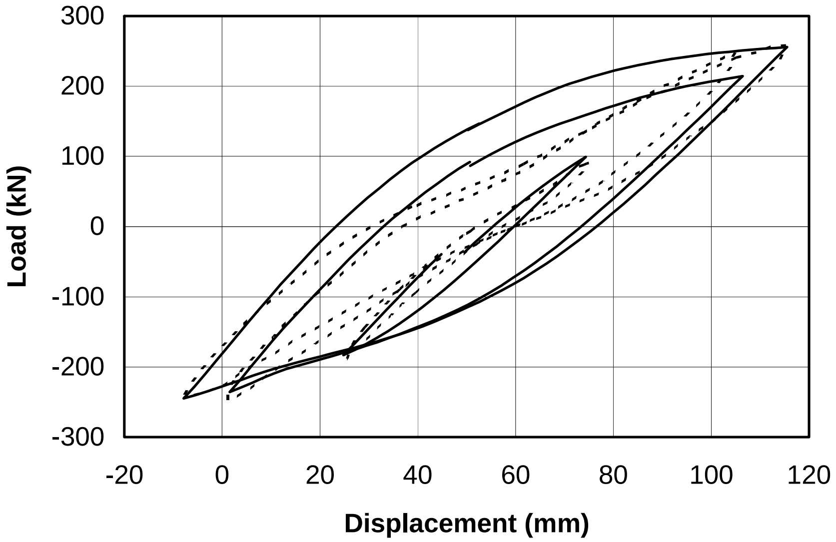

Figure 6.19 - Computed Cyclic Response Including Shear Deformations (Truss Analogy) and 50% Reduction in Joint Stiffness

Figure 6.19 shows the frame's computed and experimental response to cyclic loads. In general, the frame strength and unloading stiffness are well predicted for all cycles. Once again, pinching of the hysteresis loops is not reproduced.

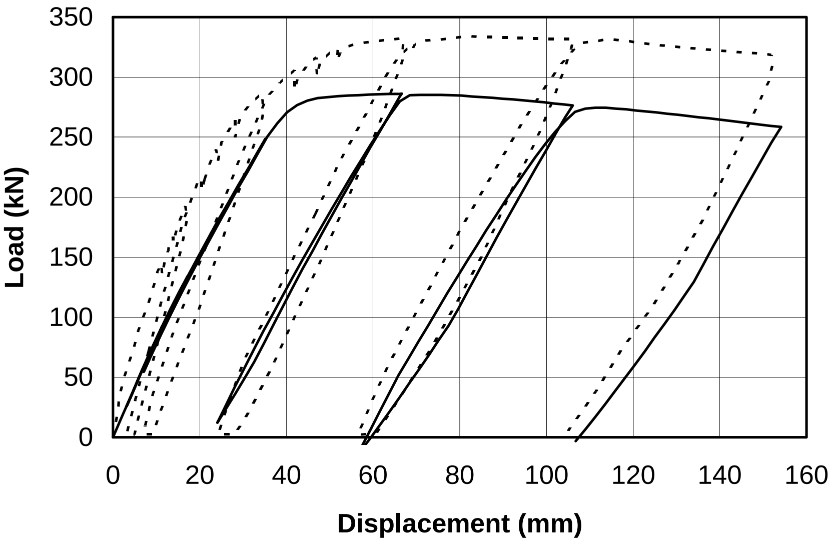

Figure 6.20 - Computed Repeated Load Response Including Shear Deformations (Truss Analogy), Anchorage Slip, and 50% Reduction in Joint Stiffness

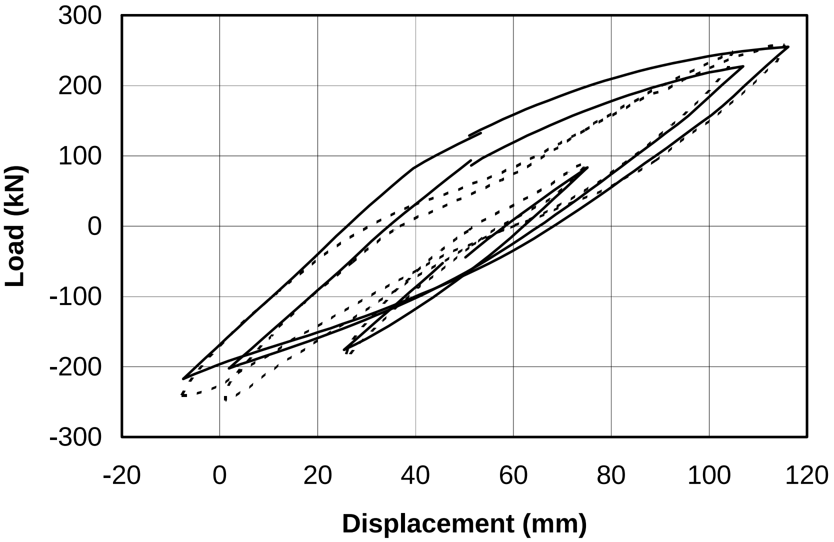

Figure 6.21 - Computed Cyclic Load Response Including Shear Deformations (Truss Analogy), Anchorage Slip, and 50% Reduction in Joint Stiffness

At this point, anchorage slip effects were introduced into the structural model of the frame that was just studied (with 50% rigidity of the joints). Figure 6.20 shows the computed load-displacement response as compared to the measured response for the repeated load case. A drastic reduction in the initial stiffness and strength of the specimen was obtained, confirming the significant influence of the anchorage slip effect in the model's response. The unloading and reloading stiffnesses of the subsequent cycles were somewhat reduced although to a lesser degree. However, the agreement with the experimental response deteriorates considerably.

For the cyclic-response case, shown in Figure 6.21, the computed response matched reasonably well the strength in the positive direction and the unloading stiffnesses. Furthermore, the width of the cycles decreases and hence the predicted energy absorption decreases. However, the strength of the frame in the negative direction was underpredicted by approximately 15%.

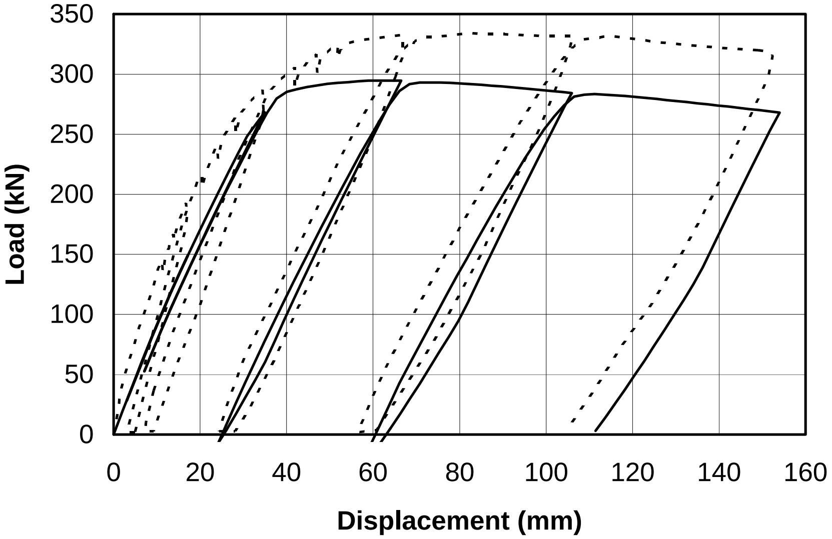

Figure 6.22 - Repeated Load Response including Shear Deformations (Truss Analogy), Anchorage Slip, and Rigid Joints

The final computations for this series, illustrated in Figures 6.22 and 6.23, were performed on a structural model with rigid joints and considering again anchorage slip. For the repeated load case, the estimated initial strength and lateral capacity of the frame were increased over those predicted by the model with only 50% joint rigidity. However, the predictions still underestimated appreciably the actual response of the specimen. In contrast, the unloading and reloading stiffness were practically unaffected and agreed well with those observed during testing.

The computed response to cyclic loads was not affected significantly by the increase in joint rigidity. Although the simulated hysteretic loops were slightly wider, the estimated strength in the negative direction was closer to that measured experimentally.

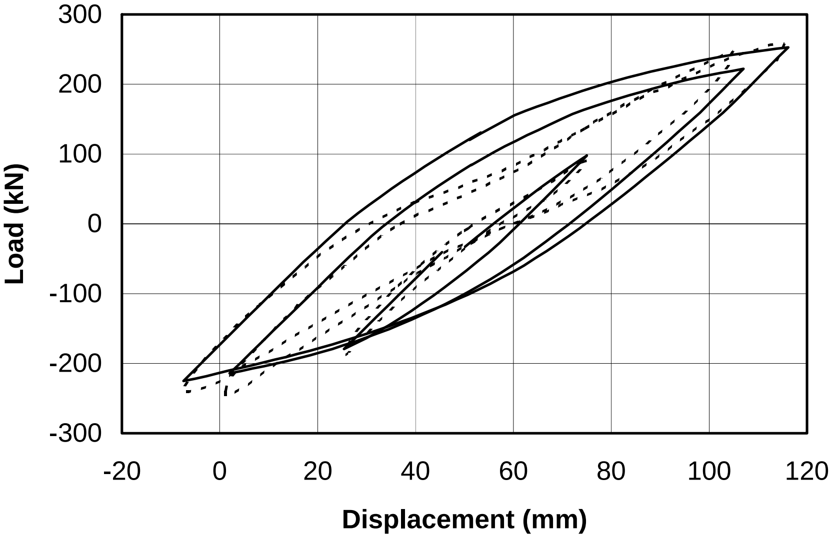

Figure 6.23 - Cyclic Load Response including Shear Deformations (Truss Analogy), Anchorage Slip, and Rigid Joints

6.4.4 Four-Story Building - Dynamic Analysis

The final specimen examined in this chapter is the four-story building studied in Section 4.5 for flexural behavior and in Section 5.4 for combined flexural and shear deformations. As discussed in those sections, the dynamic analysis method may be inappropriate for this study. However, it is carried out here for completeness. Section 6.4.5 presents an additional series of analyses using a quasi-static approach.

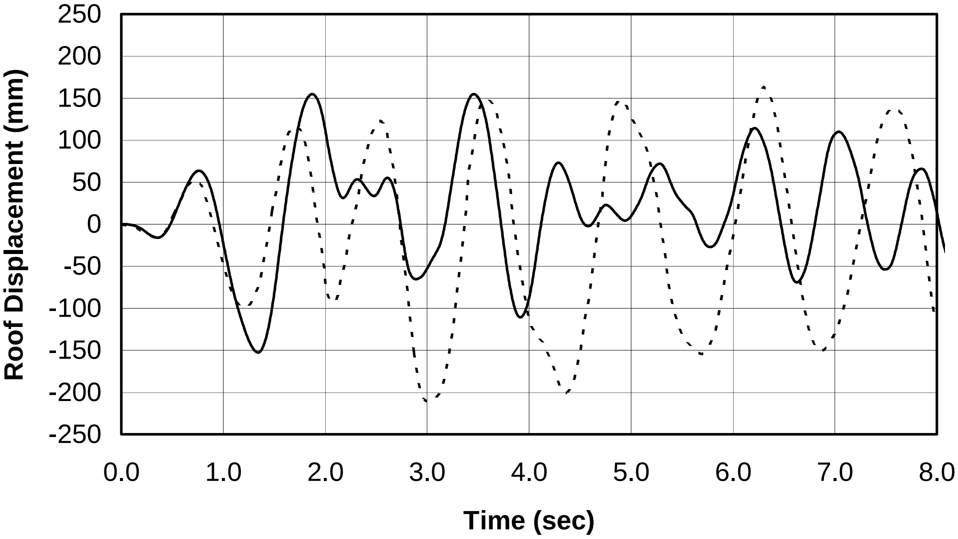

Figure 6.24 - Computed Displacement Time History considering Shear Deformations Joints

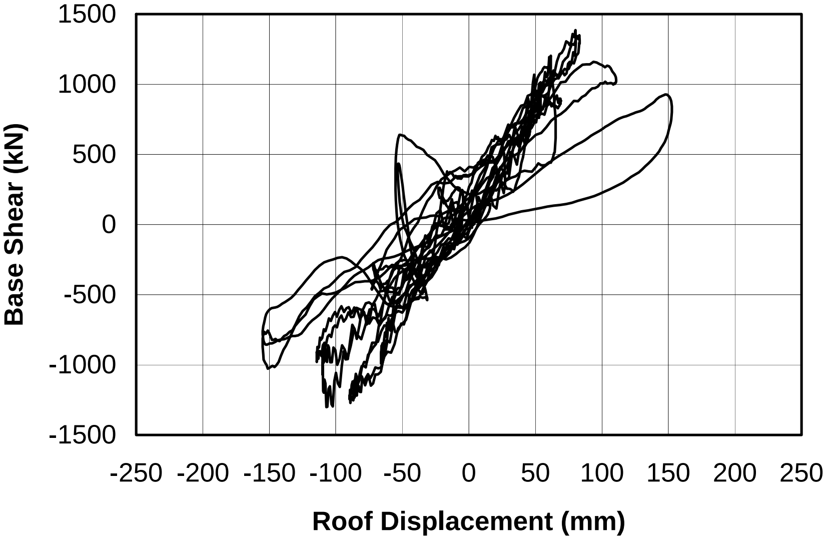

Figure 6.25 - Load-Displacement Response with Shear Deformations and 100% rigid joints

The structural model developed in Section 5.4 is modified to include rigid joints. The results of the computed response to ground motion are shown in Figures 6.24 and 6.25.

The computed displacement time history obtained (Figure 6.24) is actually very similar to that computed without joint rigidity in Section 5.4 (see Figure 5.28); only minor differences in displacement amplitudes are observed. Thus, it seems that for this structure the joint stiffness apparently does not play a major role in the structural behavior. However, the computed load-displacement response of the model , shown in Figure 6.25, does suggest a somewhat larger average secant stiffness estimate for the structure.

From the above discussion it is confirmed that the joint rigidity contributes to the structural stiffness but in a relatively minor way.

The predicted responses of the structure, shown in Figures 6.24 and 6.25, are not in good agreement with those observed experimentally (Figures 4.41 and 4.43). This is mainly reflected in the vibration period and the average stiffness of the computed response since both tend to be smaller than those observed during the test. Likewise, the predicted displacement amplitudes are generally smaller than those measured.

In an attempt to improve the structural model, a further modification was introduced by including rotational springs at the ends of the members to account for anchorage slip. Figures 6.26 and 6.27 show the predicted response of such a model to the ground motion.

Figure 6.26 shows that a slight improvement in amplitude response in the first four seconds is obtained, but the agreement is still worse than the flexure-only response. However, the amplitude is actually reduced significantly for the last four seconds of response. Figure 6.27 shows that the computed average secant stiffness of the structure is closer to that observed experimentally. One can conclude from these responses that anchorage slip has a large influence in both displacement amplitude and stiffness of the model.

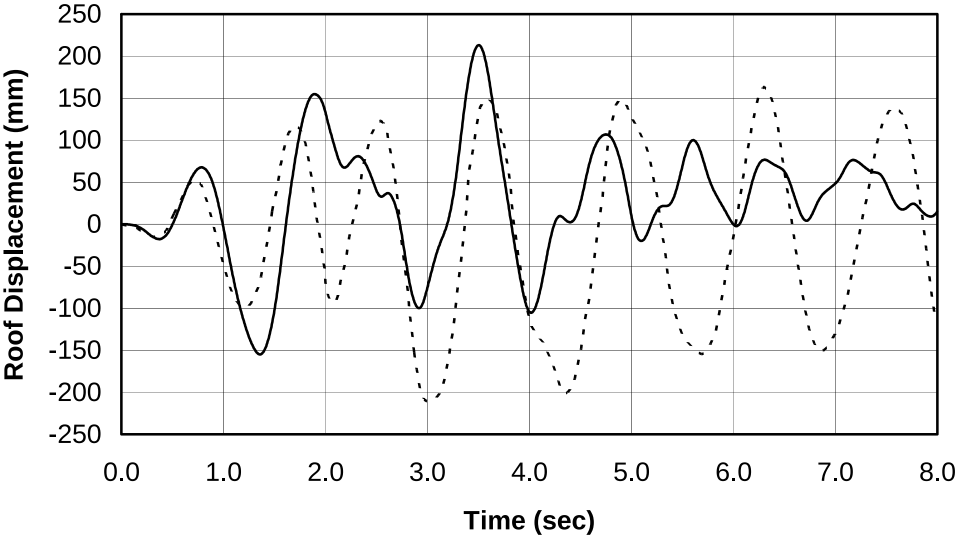

Figure 6.26 - Displacement Time History with shear strains, 100% rigid joints and Anchorage Slip

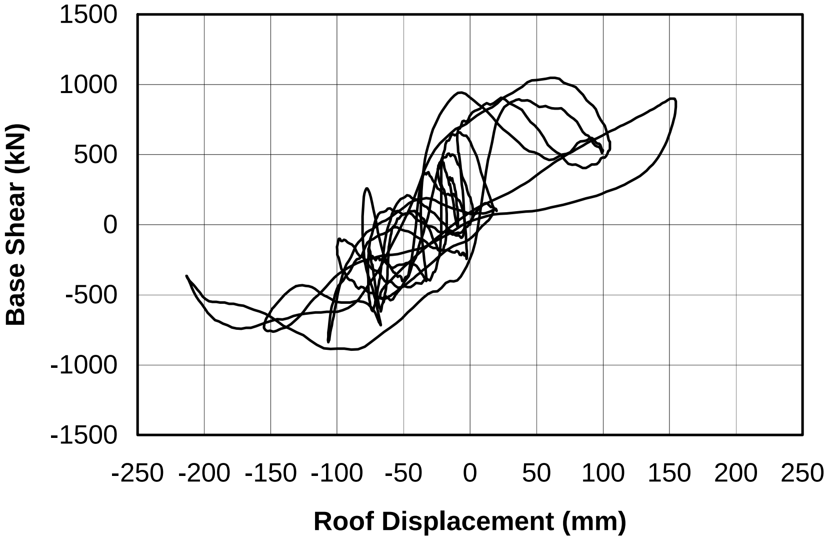

Figure 6.27 - Load-Displacement Response with shear strains, 100% rigid joints and Anchorage Slip

6.4.5 Four-Story Building - Quasi-Static Analysis

As mentioned at the beginning of Section 6.4.4, an additional series of analyses were carried out on this structure using displacement-controlled quasi-static loads. Initially, a flexure-only analysis including rigid joints was performed, and the results are shown in Figures 6.28 and 6.29.

The computed base-shear time history response shown in Figure 6.28 is very similar to that obtained in Section 4.5.4 (Figure 4.56) in which a model without rigid joints was used. This result suggests that the inclusion of the joint rigidity does not affect the response of the structure.

Figure 6.29 shows the computed base shear-roof displacement relationship for the model with rigid joints. Again, the prediction is almost identical to that provided by the flexure only model (with no rigid joints) of Section 4.5.4, confirming that the response of this four-story structure is not affected significantly by the stiffness of the joints. This result can be explained by the fact that the size of the joint rigid zone is generally very small compared to the length of the members and the large stiffness of the beams (which include part of the slab as a flange).

At this stage, inelastic rotational springs are introduced to the structural model at the member ends to account for anchorage slip effects. Figures 6.30 and 6.31 illustrate the performance of this modified model.

The computed base-shear time history response shown in Figure 6.30 is a close prediction of the measured response and represents a significant improvement over the model which considers flexural deformations only (Figure 6.28). In addition, the base shear-roof displacement prediction shown in Figure 6.29, is also closer to the experimental response (Figure 4.48) due to reduction in unloading and average secant stiffnesses.

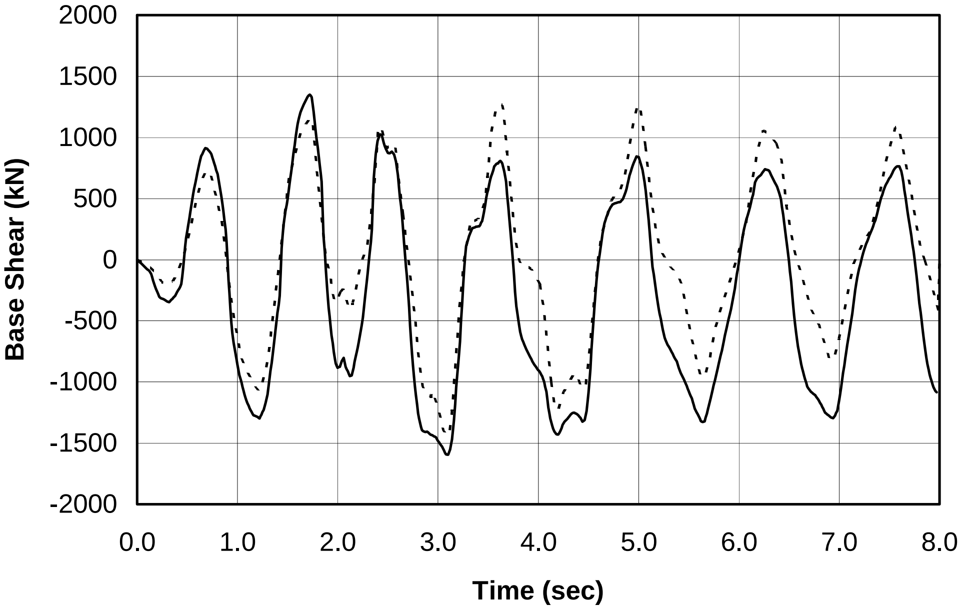

Figure 6.28 - Quasi-Static Computed Base Shear Time History with Rigid Joints Compared with Measured Response

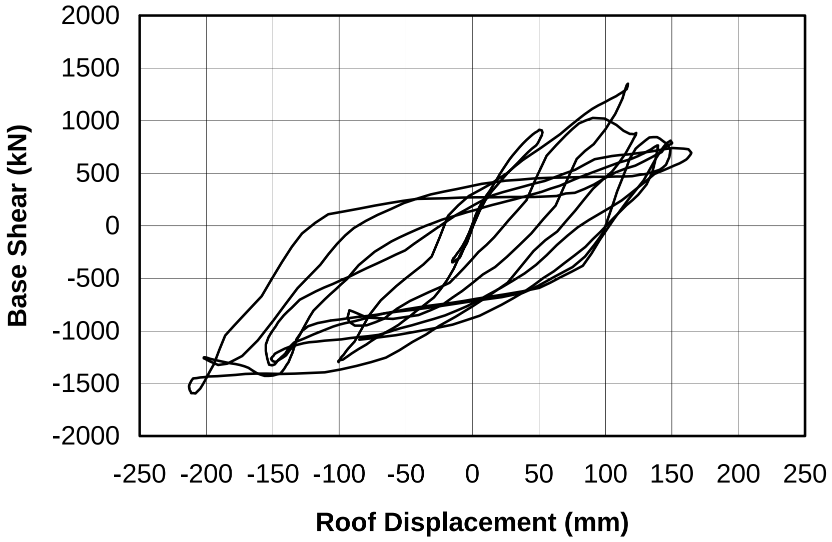

Figure 6.29 - Quasi-Static Computed Base Shear-Roof Displacement Response with Rigid Joints

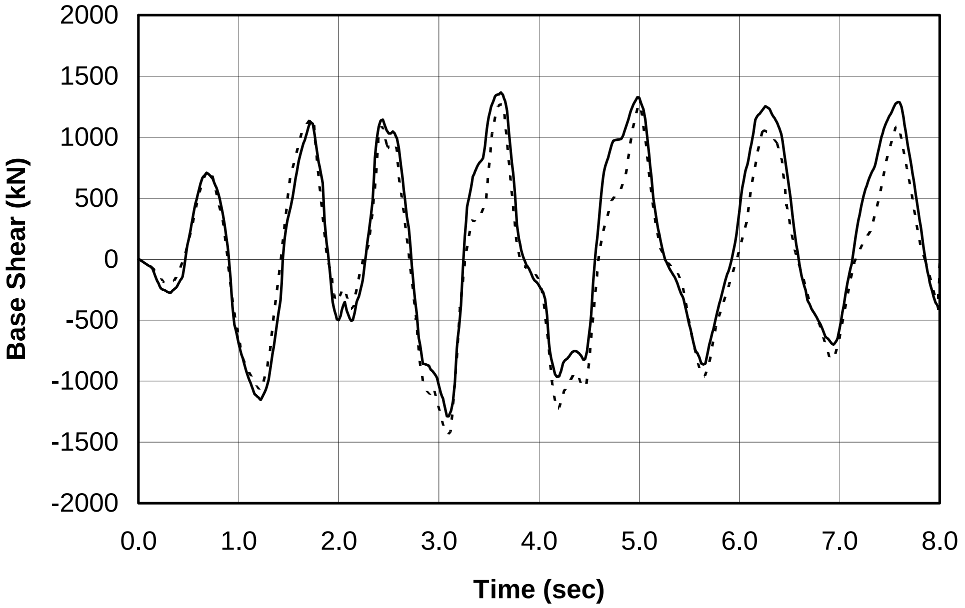

Figure 6.30 - Quasi-Static Computed Base Shear Time History Considering Anchorage Slip and Rigid Joints Compared with Measured Response

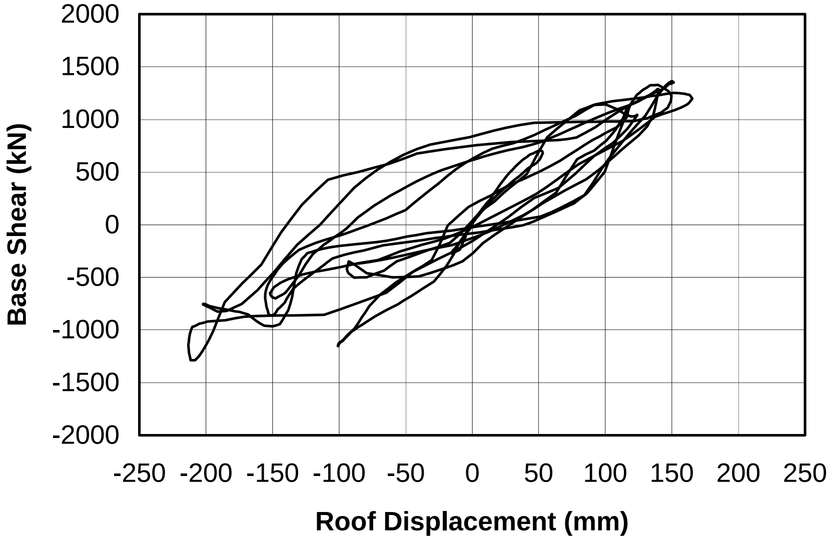

Figure 6.31 - Quasi-Static Computed Base Shear-Roof Displacement Response Considering Anchorage Slip and Rigid Joints

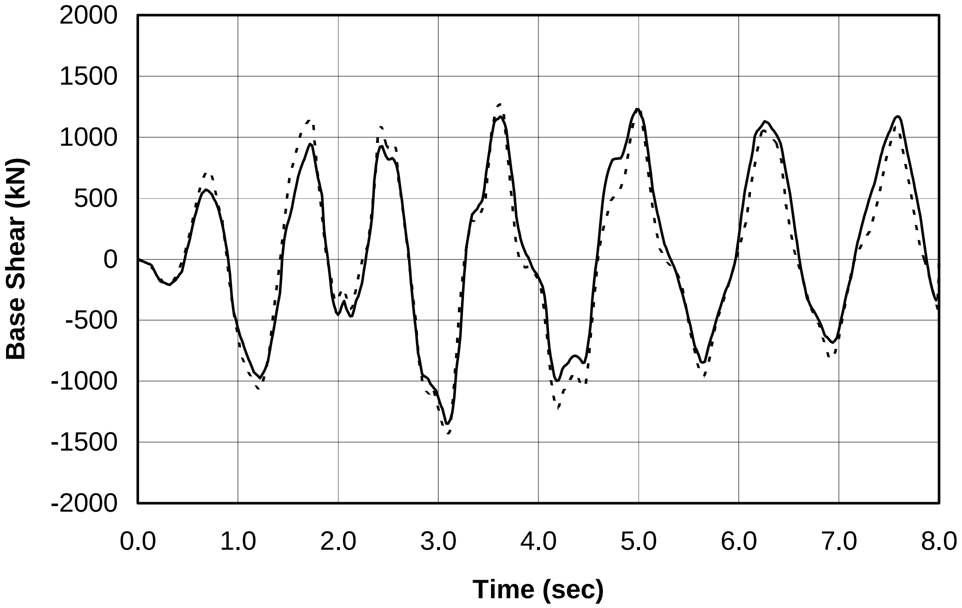

Figure 6.32 - Quasi-Static Computed Base Shear Time History Considering Shear Deformations, Anchorage Slip and Rigid Joints Compared with Measured Response

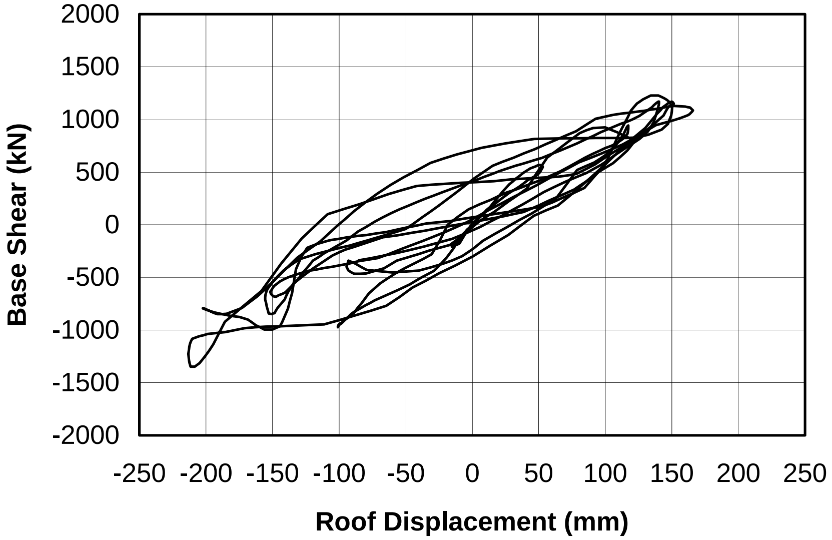

Figure 6.33 - Quasi-Static Computed Base Shear-Roof Displacement Response Considering Shear Deformations, Anchorage Slip and Rigid Joints

Finally, the truss analogy method for shear deformations is introduced into the structural model and the results are shown in Figures 6.32 and 6.33. The computed base-shear time history response worsens slightly during the first three seconds with respect to the model with anchorage slip and no shear deformation effects. However, the prediction is very close to the measured response for the last five seconds of the analysis. These results, together with the fact that the computed base shear-roof displacement relationship (Figure 6.33) is much closer to the experimental response (Figure 4.48), imply that the model that considers both shear deformations and anchorage slip provides an overall better simulation of the experimental results.

6.5 Summary on Anchorage Slip Modeling

A number of theoretical models developed by several researchers to account for anchorage slip in reinforced concrete members were briefly described. The model by Filippou uses a bond-slip idealization, based on a large number of tests, developed by other researchers at the University of California. The model is involved and requires a large computational effort. In addition, the mathematical formulation in which it is based is not completely compatible with that of FIBERC.

The model developed by Tada is based partially on a fiber formulation of the plastic hinge zone at the member ends. Additionally, the reinforcing bars inside the joint are discretized in short segments which are connected to the surrounding concrete by bond links. This model seems appropriate for future refinement of Program FIBERC because of the compatibility with the fiber formulation.

Saatcioglu’s model is simple and has been found to be reasonably accurate. It is based on a monotonic force-deformation envelope obtained for a single bar embedded in a concrete block. Using that relationship and a sectional analysis, a moment-rotation envelope for the member end at the column face is defined. Finally, a set of hysteretic rules define the response of the model under cyclic loading.

Although the behavior of beam-column joints following cracking and bond deterioration is very difficult to model, a simplified model was introduced in program FIBERC to account for this behavior in an approximate manner.

The computation of member behavior using the extension-slip model implemented in FIBERC yielded overall good results. In particular, the reduction of width of hysteresis loops due to anchorage slip was achieved although pinching was not reproduced. The unloading stiffnesses were reasonably closely estimated.

The effect of joint rigidity was assessed using a simple model. The results show that including perfectly rigid joints in the model induces a significant increase in stiffness and strength of frames. However, such effect appears to be excessive in some of the cases studied. Additional simulations performed using a 50% reduction in joint stiffness suggest that by adding flexibility to the joints, an improved computed response may be obtained.

The effect of bar slip on the predicted behavior of a frame was found to be significant. It affects not only the stiffness of the structure but also the strength. In the particular case of repeated loads applied to a two-story frame, the strength was appreciably underestimated. However, for cyclic load response prediction, a reasonable prediction of the results was achieved.

Finally, for the four-story frame, the results of the dynamic analyses confirm the conclusions obtained in Chapters 4 and 5 regarding the inability of the method to reproduce reliably the measured response during the pseudo-dynamic tests. In contrast, the quasi-static analysis yielded a remarkably close simulation to the experimental results.

CHAPTER 7

Summary and Conclusions

7.1 Summary

The behavior of reinforced concrete frame structures under seismic loads has been analyzed using a number of mathematical models of increasing levels of complexity. The first model, represented by the program DRAIN-2DX, idealizes the plasticity in the members as concentrated at the member ends and governed by a simple elastoplastic hysteretic rule with no strength or stiffness degradation. The second model, implemented in program IDARC2D, permits yielding to penetrate into the member and accounts for stiffness and strength degradation as well as pinching of the hysteretic loops. The last model used, based on a fiber formulation, was developed as part of this study and was implemented in the program FIBERC.

Several large-scale members and frame specimens were then analyzed with the three models under static and dynamic loading. It was found that, in general, the beam-column element of program DRAIN-2DX does not reproduce the member behavior very well, particularly in terms of stiffness and energy dissipation. In contrast, program IDARC2D generally gives a good estimate of member and frame behavior, including pinching of the hysteretic loops, thanks to a set of parameters used to adjust the predicted response. Finally, program FIBERC simulates closely the member response when it is governed mainly by flexure and axial force. It does not, however, give good predictions when pinching of the hysteresis loops takes place.

To extend and improve the performance of the fiber element model implemented in program FIBERC, a simple model that accounts for the effects of shear deformation was added. This model is based on a truss analogy of the cracked structural members. A series of runs using some of the members and frames studied previously was performed to assess the validity of the model as well as its influence on the predicted response.

Additionally, a model that estimates the effects of anchorage slip on member deformation and stiffness was introduced into the program. Again, a series of runs were performed on the same specimens to evaluate the effectiveness of the model as well as its effect on the computed response.

7.2 Conclusions

The main conclusions drawn from the results of the research study are as follows:

1. A fiber formulation of structural elements in reinforced concrete frames can accurately predict their seismic response when flexure and axial load govern the member behavior.
2. The program IDARC2D provided a very good simulation of the response when the set of control parameters is properly adjusted. This adjustment implies a previous knowledge of the expected behavior of the class of members to be analyzed.
3. The program DRAIN-2DX gave a poor estimate of member response and damage and a crude estimate of frame response for the cases studied here.
4. The mesured response of a full-scale four story frame tested psudo-dynamically was not well reproduced by any of three different models when a dynamic analysis was used. In contrast a reasonably good simulation is obtained when a quasi-static analysis is performed.
5. A simple model that accounts for shear deformations in the members and implemented in program FIBERC provided a good prediction of the stiffness reduction and hysteresis loops for member response. It also had a pronounced effect on frame computed response improving reasonably the simulation of the experimental results.
6. The stiffness of the beam-column joints demonstrated a large influence on frame response, even using a very approximate model. It must definitely be taken into account in refined analysis of reinforced concrete frames.
7. A relatively simple but complete model that accounts for the effects of anchorage slip of rebars, at the beam-column interface, on the member deformations achieved a good

prediction of cyclic response of single elements, and yielded a relative enhancement of results for frames.

8. No pinching of the hysteresis loops of beams and frames was reproduced by the models.

7.3 Recommendations for Future Research

A number of improvements on the models developed in this study need to be implemented. At the material modeling level, the following items should be considered in a future refinement of the program:

1. Unconfined concrete to simulate concrete spalling, Confined concrete to simulate increase in concrete strength and stiffness.
2. Improve the constitutive steel model by introducing isotropic hardening when significant compressive straining takes place.
3. Model rebar buckling in compression and stirrup fracture in tension.
4. Tension softening in concrete

At the element model the following improvements are proposed:

5. Implement one of the more involved models for shear deformation such as that by Mander (Section 5.2.3).
6. Introduce a more sophisticated model for anchorage slip including the bond stress inside the joint. It is recommended to use Tada's model (Section 6.2) because of its compatibility with the fiber model implemented in program FIBERC.
7. Introduce a model for joint distortions. This is important particularly in members sustaining significant damage.

APPENDIX A

FIBERC User′s Guide

A.1 Introduction

This program was written in the programming language FORTRAN. It was compiled using Microsoft Fortran PowerStation, version 4.0 (1995) licensed to the Learning Resource Center of the Department of Civil Engineering at the University of Texas at Austin.

This appendix contains a guide for preparing the input data to run the program as well as a brief description of the analysis options currently available. Furthermore, a description of the output files that can be generated is also presented. Finally, the limitations of the current version of the program are listed.

A.2 Input Data Description

In this section, the two input files needed to run program FIBERC are described. Each file is specified line by line, and repeated lines are noted. A short definition of each variable is given at the end of this section.

All input data are specified in a free format. Items in a single line are to be separated by spaces and/or commas. No blank lines should be left between data lines. No data check is performed, but an ‘echo’ file is printed with all input data read and generated for verification purposes

A.2.1 Main input file

```
File name: PROJECTNAME.DAT

 1.    EQFILENAME
 2.    MUNIT
 3.    MSTR
 4.    If MSTR = 1: NST, NBAY, IGIR, NSEC(1) , NSEC(2) , NSEC(3)
       If MSTR = 2: NBAY, NCOL, IGIR, NSEC(1) , NSEC(2) , NSEC(3)
 5.    If MSTR = 1: (H(I),I=1,NST)
       If MSTR = 2: (H(I),I=1,NCOL)
 6.    (SPAN(I),I=1,NBAY)
```

```
 7.    MODEL, DMAT, MRAY, JWR
 8.    INTEG, IPD, IPG, IMP, IGR, ISTL, HFAC, VFAC
11.    DAMP, DAMP2, NTEN, NSHD, NSLP, RJNT
12.    NELTYPE

For each Element Type (ITYP=1,NELTYPE):
13.    KSEC,AD,AJD,AB,CAM,CAIM,FC,WC,IA,ISF,FY1,FU1,OVC,OVS,PER,ESH,NCF,
       (NSF(I,J),I=1,3)
14.    Only If KSEC=3  (Fibers MUST be input from top to bottom of the
       section):
       14.a   (BCF(ICF,ITYP),IF=1,NCF)
       14.b   (DCF(ICF,ITYP),IF=1,NCF)
       14.c   (YCF(ICF,ITYP),IF=1,NCF)
       14.d   (BCCOF(ICF,ITYP),IF=1,NCF)
15.    For Each Segment (ISEG=1,3) and for NSTF=NSF(ISEG,ITYP).
       Longitudinal fibers MUST be input from top to bottom of the section.
       (AS(ISS,ISEG,ITYP),ISS=1,NSTF)
       (YS(ISS,ISEG,ITYP),ISS=1,NSTF)
       AV(ISEG,ITYP),SP(ISEG,ITYP)

For Each Group of Columns
16.    If MSTR = 1:
       NF1,NF2,NC1,NC2,IELTYP,CP,ALC1,ALC2,ILINGR,WGR,DA,DB,ZA,ZB
       If MSTR = 2: NC1,NC2,IELTYP,CP,ALC1,ALC2,ILINGR,WGR,DA,DB,ZA,ZB

For Each Group of Girders
17.    If MSTR = 1:
       NF1,NF2,NC1,NC2,IELTYP,CP,ALC1,ALC2,ILINGR,WGR,DA,DB,ZA,ZB
       If MSTR = 2: NC1,NC2,IELTYP,CP,ALC1,ALC2,ILINGR,WGR,DA,DB,ZA,ZB

18.    NEP, DTE, DT

19.    NJOP

For Each response requested
20.    JOP(IJOP), IT1(IJOP), IT2(IJOP), IT3(IJOP)
```

A.2.2 Earthquake Record File

```
File name: as specified in first line of input data file.

1.     TCOR, NPOINT, TSTEP

For each point (up to NEP points)
2.     EH, EV
```

A.2.3 Quasi-Static Load Record File

```
File name: as specified in first line of input data file

1.     MLOAD

For each loading (up to MLOAD lines)
2.     MFLR(ILD), MCL(ILD), MDOF(ILD)
```

```
For each loading step (up to NEP steps (lines) and up to MLOAD loads)
3.     DI(2,ILD)
```

A.2.4 Description of Input Variables

AB(20)	Width of Member Type
AD(20)	Depth of Member Type
ALC1	Length of segment 1 used to define longitudinal Rebars (Figure A.1)
ALC2	Length of segment 1 used to define longitudinal Rebars (Figure A.1)
AS(10,3,20)	Area of Steel fiber (fiber, segment, member type)
BCF(30,20)	Width of Concrete fibers (fiber, member type)
BCCOF(30,20)	Confined Width of Concrete fibers (fiber, member type)
DA,DB	Joint size at member ends (Figure A.1)
DCF(30,20)	Depth of Concrete fibers (fiber, member type)
EER(2,2)	Earthquake Record data handling array
EQFILENAME	File name of the earthquake record (up to 20 characters)
FY1(200)	Yield strength of reinforcing bars (ksi)
H(30)	Interstory heights
HFAC	Horizontal Acceleration Scaling Factor
IA(20)	Aggregate Type (1=Gravel Aggregate, 2=Crushed Aggregate)
IGIR	Girder Axial Deformation (0=Yes/1=No)
IGR	Gravity Loads (1= Yes/0=No)
ILINGR	Flag for Linear Analysis (1=Linear/0=Nonlinear)
IMP	Axial-Moment Interaction (1=Yes/0=No)

INTEG	Integration methods (1=Constant Average Accelertation)
IPG	Change in Geometry (Update coordinates) (1=Yes/0=No)
IPD	P-Delta (1=Yes/0=No)
ISF(20)	Silica content (1=With Silica Fume, 2=Without Silica Fume)
ISTL	Steel Constitutive Model. See Section A.3. (1=Mod.Bilinear/2=Kin.Bilinear/3=Menegotto-Pinto)
JOP(10)	Selection of Output
KSEC	Shape of Cross Section (1=Rectangular/2=Circular/3=General)
MODEL	Mass Matrix (2=Lumped mass/3=Consistent mass)
MRAY	Number of mode for 2nd Critical Damping
MSTR	Type of structure: 1=Orthogonal frame/2=Bridge
MUNIT	Unit system (1=US/2=SI)
NBAY	Number of bays
NC1	Initial column line
NC2	Final column line
NEP	Number of earthquake points
NF1	Initial floor
NF2	Final floor
NSEC(3)	Number of sections per segment
NST	Number of Storie
NSHD	Flag for shearing deformation effect (0=Neglected/1=Included)
NSLP	Flag for anchorage slip effect (0=Neglected/1=Included)
NTEN	Flag for Tension Strength of Concrete (0=No/1=Yes)

NTJOP(7)	Number of requests of each dynamic response type
OVC(200)	Concrete Overstrength coefficient (previously confinement)
OVS(200)	Steel Overstrength coefficient
PER(LET)	Strain Hardening % for each member
PROJECTNAME	Project name to be used as output file name (4 characters)
RJNT	Multiplier of joint size for equivalent stiffness
WGR	Distributed load for Column or Beam group
YCF(30,20)	Location of Concrete fiber w.r.t. mid-depth (fiber, member type)
YS(10,3,20)	Location of Steel fiber w.r.t. to mid-depth (fiber, segment, member type)

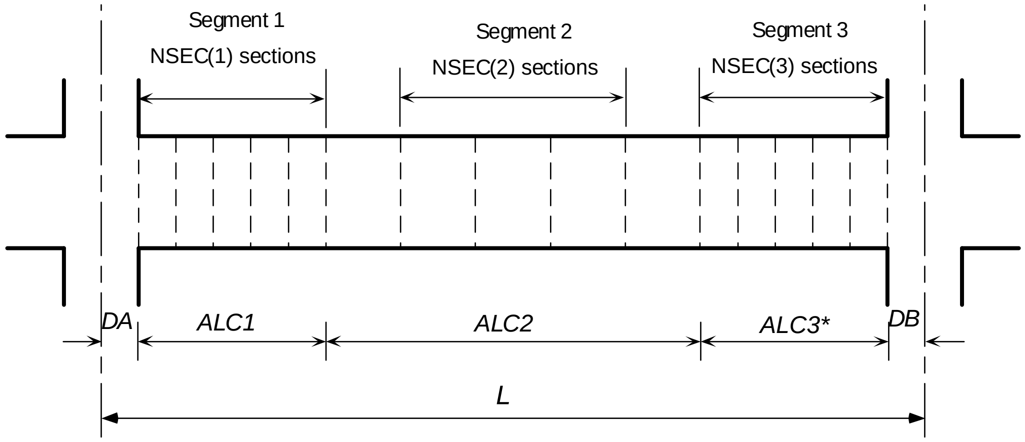

*ALC3 = L-DA-DB-ALC1-ALC2

Figure A.1 - Segments and Slices for a typical member

A.3. Analysis Options

A number of analysis options are available to control the process according to user's preferences by means of the following flags:

```
Unit System .................    (1) U.S. CUSTOMARY        -->MUNIT=1
                                 (2) SI INTERNATIONAL SYSTEM-->MUNIT=2
```

```
Type of Structure ...........    (1) BUILDING FRAME  -->MSTR=1
                                 (2) BRIDGE                 -->MSTR=2
                                 (3) GENERAL FRAME (N/A)    -->MSTR=3

Element Group Response ......    (1) NONLINEAR INELASTIC    -->ILINGR=0
                                 (2) LINEAR ELASTIC         -->ILINGR=1

Mass Matrix ................     (1) LUMPED MASS            -->MODEL=2
                                 (2) CONSISTENT MASS        -->MODEL=3

Girder Axial Deformation .....   (1) YES                    -->IGIR =0
                                 (2) NO                     -->IGIR =1

Damping Matrix ..............    (1) RAYLEIGH DAMPING       -->DMAT =1
                                 (2) MASS PROPORTIONAL      -->DMAT =2
                                 (3) STIFFNESS PROPORTIONAL -->DMAT =3

Change in Geometry .........     (1) UPDATE COORDINATES(1) YES-->IPG  =1
                                 (2) NO -->IPG  =0

Linearized Stability ........    (2) P-DELTA  (1) YES       -->IPD  =1
                                              (2) NO        -->IPD  =0

Axial-Moment Interaction ...     (1) YES                    -->IMP  =1
                                 (2) NO                     -->IMP  =0

Gravity Loads .............      (1) YES                    -->IGR  =1
                                 (2) NO                     -->IGR  =0

Steel Constitutive Model         (1) MODIFIED BILINEAR      -->ISTL  =1
                                 (2) BILINEAR KINEM. HARD.  -->ISTL  =2
                                 (3) MENEGOTTO-PINTO        -->ISTL  =3

Tension Strength in Concrete     (1) YES                    -->NTEN  =1
                                 (2) NO                     -->NTEN  =0

Shearing Deformation Effect      (1) YES                    -->NSHD  =1
                                 (2) NO                     -->NSHD  =0

Anchorage Slip Effect            (1) YES                    -->NSLP  =1
                                 (2) NO                     -->NSLP  =0
```

A.4 Unit Systems

US and SI Unit Definition

```
INPUT                       US             SI

Spans, Heights ............ in             m
Section dimensions ........ in             mm
mass/length ............... kip-s2/in/in   kN-s2/mm/mm
f'c, fy ................... ksi            MPa (kN/mm2)
unit weight (concrete) .... pcf            kg/m3
As ........................ in2            mm2
Ys ........................ in             mm
cP ........................ kip            kN
Member load ............... kip/in         kN/m

INTERNAL VARIABLES          US             SI

Dimensions ................ in             mm
Forces .................... kip            kN
Areas ..................... in2            mm2
Tangent modulus ........... ksi            MPa
Stress .................... ksi            MPa
Moments ................... kip-in         kN-mm

OUTPUT                      US             SI

Displacements ............. in             mm
Forces .................... kip            kN
Moments ................... kip-ft         kN-m
```

A.5 Output Description

One or more output files are created during the run. The file <PROJECTNAME>.ECH is always generated. This file contains an echo of the input data (parameters and structural geometry) as well as the results of the eigenvalue problem and the results of the static structural analysis of the structure under gravity loads.

Up to 20 additional output files corresponding to different nonlinear dynamic responses can be generated. Table 4.1 describes the types of responses that can be generated together with the file extensions and the parameters required for each selection. File names are made of the four characters of the variable PROJECTNAME plus a 2-digit counter and an extension (according to Table A.1).

Table A.1 - Nonlinear dynamic solution Output

JOP	FILE EXTENSION	PARAMETERS			OUTPUT
		IT 1	IT 2	IT 3	
1	.DSP	I	0	0	Time History of Displacement of Top Joint of Element I
2	.FRC	I	J	0	Time History of Force J (1-6) at End of member I
3	.EAI	I	J	0	Time History of Equivalent EA and EI for Member I at Section J
4	.FCO	I	J	K	Time History of Concrete Fiber K of Section J of Member I
5	.FST	I	J	K	Time History of Steel Fiber K of Section J of Member I
6	.MPH	I	J	0	Time History of Moment-Curvature of Section J of Member I
7	.LMI	I	J	0	Time History of Load-Moment Interaction of Section J, Member I

A.6. Program Limitations

There are a number of arrays whose dimensions are fixed and must be changed by modifying the code. The most important limitations caused by such dimensions are:

Maximum number of stories = 30

Maximum number of spans = 20

There are several other array sizes that are defined in the include file PARAM.INC and are passed as parameters to all the subroutines in the program. Therefore, these dimensions will change in all the program if modified in PARAM.INC (Caution must be exercised with some of these parameters. See notes below).

Number of segments in a member, LSEG = 3(1)

Number of sections (slices) in a member, LSEC = 20

Maximum number of concrete fibers in a section, LCFB = 27(2)

Maximum number of steel fibers (layers) in a section, LSFB = 10

Maximum number of types of member types, LET = 20

Maximum number of members, LMEM = 25

Maximum number of Joints, LJNT = 50

Maximum number of output response files, LOP = 30

Maximum Size of Mass and Stiffness Matrix, LMTRX = 45000

A.6.1 Notes:

(1) Several subroutines assume that there are three segments. Therefore this parameter should be always set to 3.

(2) Two of the fibers are used by the program for inclined concrete struts of the “Cyclic Inelastic Strut-and-Tie” model for inelastic shear deformations. Therefore, the actual number of available longitudinal fibers is LCFB minus 2.

APPENDIX B

Details and Damage of Full-Scale Four-Story Building

B.1 Introduction

This appendix contains the reinforcement details of the full-scale four-story building tested at the European Laboratory for Structural Assessment (ELSA) that was described in Section 4.5. Section B.2 presents sketches based on the technical drawings (4-14) where the reinforcing bars utilized are specified. In addition, a few pictures taken from reference 4-14 are reproduced in Section B.3 to give an idea of the experimental setup. Finally, more pictures from the same reference, displaying the damage sustained by the building during the test, are presented in Section B.4.

B.2 Reinforcement Layout

Figure B.1 shows both longitudinal and transverse reinforcement for the columns of the interior frame of the building. Bar nominal diameters, stirrup spacing, and length of the constant-spacing stirrup zones are all in millimeters. The area and strength of the bars as a function of their nominal diameters are given in Table 4.2, while the cross sections of the columns are shown in Figure 4.38. It must be noticed that the longitudinal bars and stirrups of the right column are identical to those of the leftmost column.

Similarly, Figure B.2 presents the transverse and longitudinal reinforcement for the beams of the same frame. All beams exhibit the same stirrup pattern shown in the lower part of that figure. A typical cross section of a beam and slab is shown in Figure 4.37.

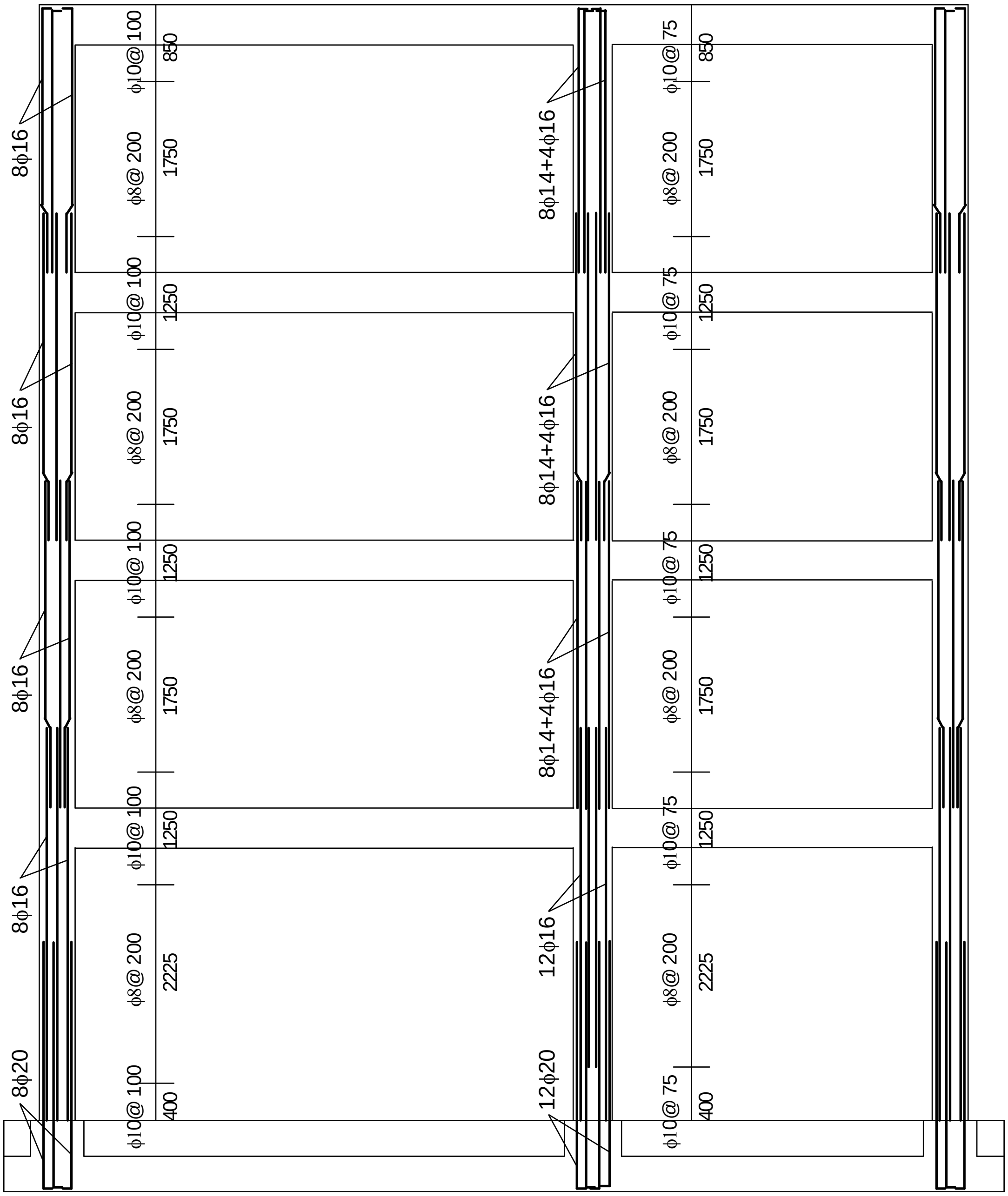

Figure B.1 - Column Reinforcement Layout (adapted from 4-14)

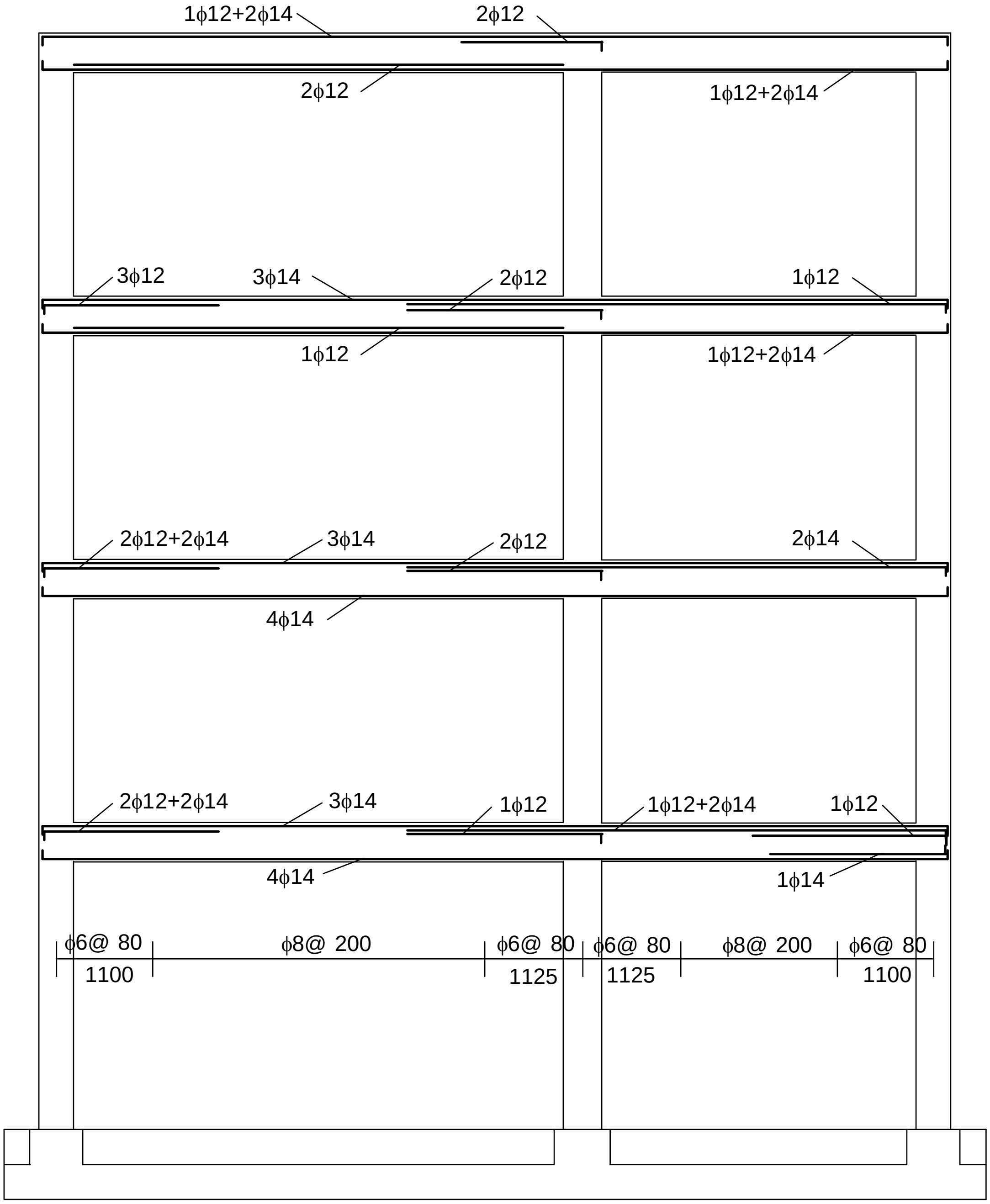

Figure B.2 - Beam Reinforcement Layout (adapted from 4-14)

B.3 Member Flexural Strength and Stiffness

A moment-curvature sectional analysis of all elements of the building was performed. Equivalent bilinear behavior for each element was obtained as illustrated in Figure B.3. The elastic stiffness $(EI)_o$ and post-elastic stiffness $(EI)_p$ were taken as the average of the exact M-ϕ curve before and after the yielding region, respectively.

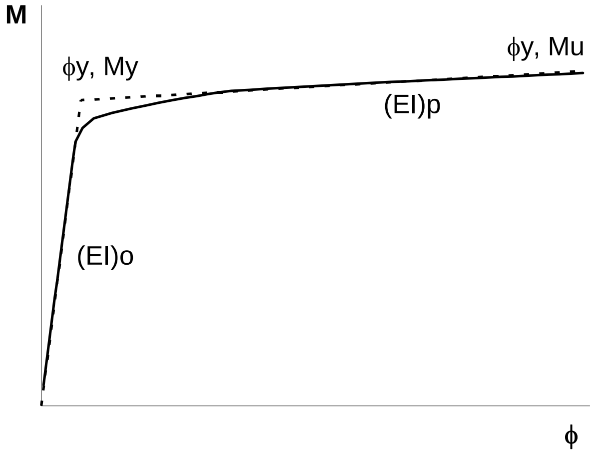

Figure B.3 - Actual and Idealized Moment-Curvature Relationships

Based on the ultimate point (ϕ_u, M_u), $(EI)_o$ and $(EI)_p$ an equivalent yield point (ϕ_y, M_y), using Equations B.1 and B.2, was obtained.

$$\phi_y = \frac{M_u - (EI)_p \phi_u}{(EI)_o - (EI)_p} \tag{B.1}$$

$$M_y = (EI)_o \phi_y \tag{B.2}$$

These computations were performed for eight column types and eight beam types as shown in Figure B.4. Tables B.1 and B.2 present the results for the columns and beams, respectively. In these tables, the stiffness (*EI*) is given in *kN-m*^{2}, the moment of inertia is given in *m*^{4}, the elastic modulus *E* is given in *kN/m*^{2} and the moment is given in *kN-m* (r_b is nondimensional).

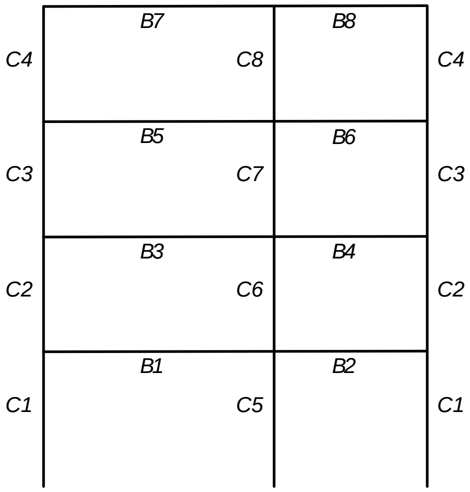

Figure B.4 - Beam and Column Type Numbers

Table B.1 - Stiffness and Strength of Columns

Col	$(EI)_o$	$(EI)_p$	I	E_o	r_b	M_y	M_b/M_y	P_{yc}	P_b/P_{yc}	P_{yt}
C1	18100	190	0.00213	7.231×10^6	0.011	241	1.72	7522	0.25	1458
C1	12750	150	0.00213	7.231×10^6	0.011	159	2.29	7032	0.27	933
C2	12700	130	0.00213	5.953×10^6	0.010	159	2.23	6763	0.28	933
C3	12400	100	0.00213	5.813×10^6	0.008	158	1.82	4851	0.29	933
C4	12700	130	0.00213	5.953×10^6	0.010	160	2.19	6575	0.28	933
C5	34900	250	0.00342	8.699×10^6	0.007	414	1.55	9840	0.24	2187
C5	24550	150	0.00342	8.699×10^6	0.007	277	2.01	9105	0.27	1400
C6	24500	160	0.00342	6.738×10^6	0.007	276	1.96	8764	0.27	1400
C6	21550	130	0.00342	6.738×10^6	0.007	236	2.21	8560	0.28	1182
C7	21100	160	0.00342	6.175×10^6	0.008	229	1.80	6140	0.29	1182
C8	21500	130	0.00342	6.292×10^6	0.006	236	2.18	8321	0.28	1182

Table B.2 - Stiffness and Strength of Beams

Beam	**End**	**Direction**	**$(EI)_o$**	**$(EI)_p$**	**I**	**E_o**	**r_b**	**M_y**
B1	I, J	Positive	18400	310	0.00467	4.336×10^6	0.016	147
B1	I, J	Negative	22100	300	0.00467	4.336×10^6	0.016	222
B2	I	Positive	18400	270	0.00467	4.438×10^6	0.017	145
B2	I	Negative	20400	360	0.00467	4.438×10^6	0.017	195
B2	J	Positive	21950	350	0.00467	4.438×10^6	0.017	177
B2	J	Negative	22150	400	0.00467	4.438×10^6	0.017	218
B3	I, J	Positive	18400	310	0.00467	4.326×10^6	0.016	147
B3	I, J	Negative	22000	310	0.00467	4.326×10^6	0.016	220
B4	I, J	Positive	18350	180	0.00467	3.956×10^6	0.011	145
B4	I, J	Negative	18600	220	0.00467	3.956×10^6	0.011	173
B5	I	Positive	12900	320	0.00467	3.284×10^6	0.018	102
B5	I	Negative	17550	210	0.00467	3.284×10^6	0.018	175
B5	J	Positive	12900	260	0.00467	3.284×10^6	0.018	102
B5	J	Negative	18000	240	0.00467	3.284×10^6	0.018	178
B6	I, J	Positive	12800	130	0.00467	2.907×10^6	0.012	100
B6	I, J	Negative	14350	200	0.00467	2.907×10^6	0.012	132
B7	I	Positive	12800	110	0.00467	2.762×10^6	0.013	104
B7	J	Negative	11000	140	0.00467	2.762×10^6	0.013	98
B7	I	Positive	12900	250	0.00467	2.762×10^6	0.013	104
B7	J	Negative	14900	160	0.00467	2.762×10^6	0.013	146
B8	I, J	Positive	12800	110	0.00467	2.548×10^6	0.011	100
B8	I, J	Negative	11000	140	0.00467	2.548×10^6	0.011	98

B.4 Experimental Setup

Figure B.5 shows a general view of the ELSA laboratory together with the full-scale four-story building tested. At its left side, a smaller steel building is also being tested. The large reaction wall, used to resist the actuator reactions, is behind the two buildings.

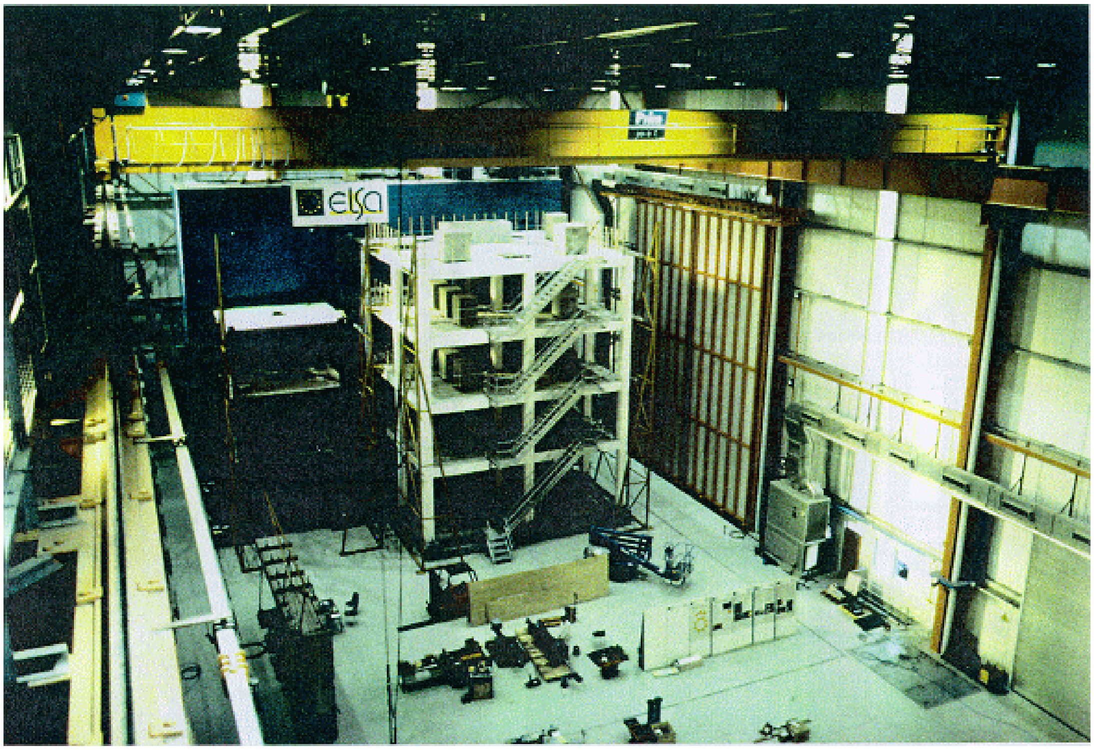

Figure B.5 - Test Setup (taken from 4-14)

In Figure B.6 a close-up of one of the sides of the building is shown. Steel components were used to attach the actuator rams to the floor slabs.

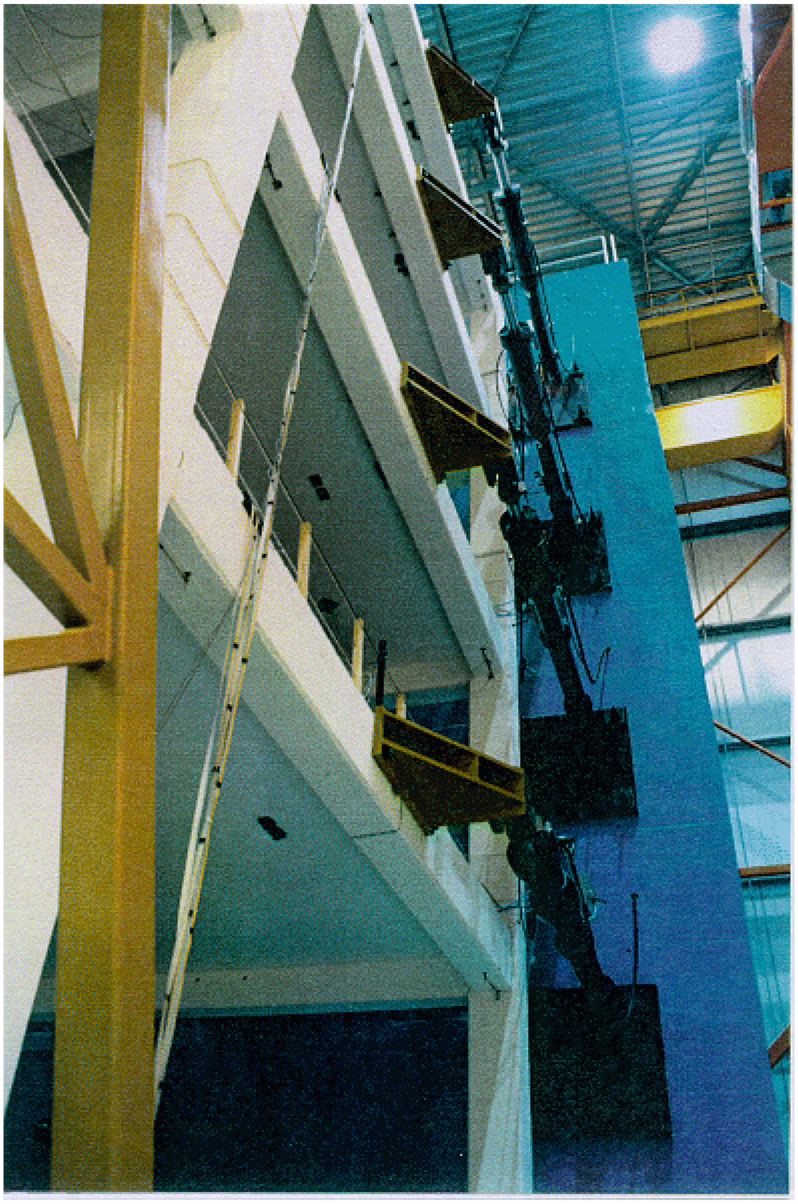

Figure B.6 - Detail of Actuators on one side of the building (taken from 4-14)

B.5 Visual Damage of the Building

In this section a few pictures taken after the test show the damage sustained by the structural elements. It must be pointed out, however, that a very low level of visual damage was reported by the researchers (4-14) particularly considering the severity of the ground motion applied to the structure.

Figure B.7 shows diagonal cracks in a beam-column joint. The crack inclination is approximately 45°. No damage is apparent at the interface of the joint and the beams.

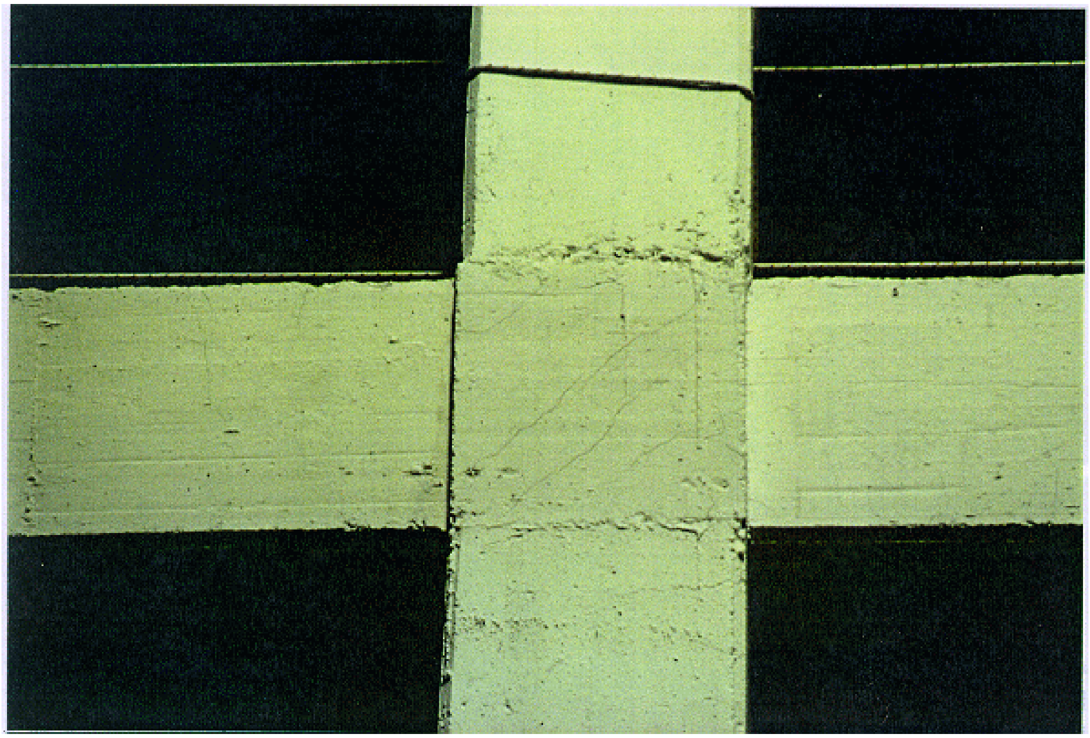

Figure B.7 - Cracking at Beam-Column Joint (taken from 4-14)

In Figure B.8 torsional cracking of the transverse beams, near the beam-column joint, is shown.

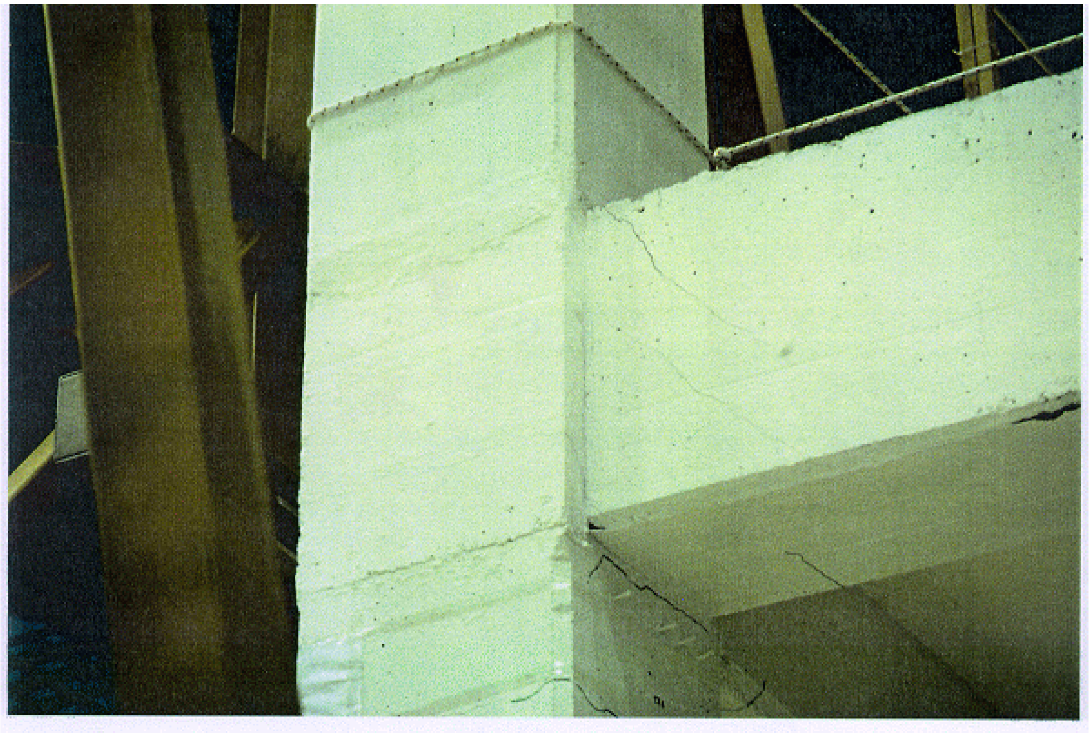

Figure B.8 - Torsional Cracking at Beam End (taken from 4-14)

Figure B.9 shows flexural cracking at the ends of beams and columns. However, these cracks are narrow and apparently easy to repair. This confirms the low level of damage sustained by the structure. No spalling occurred in any beam or column.

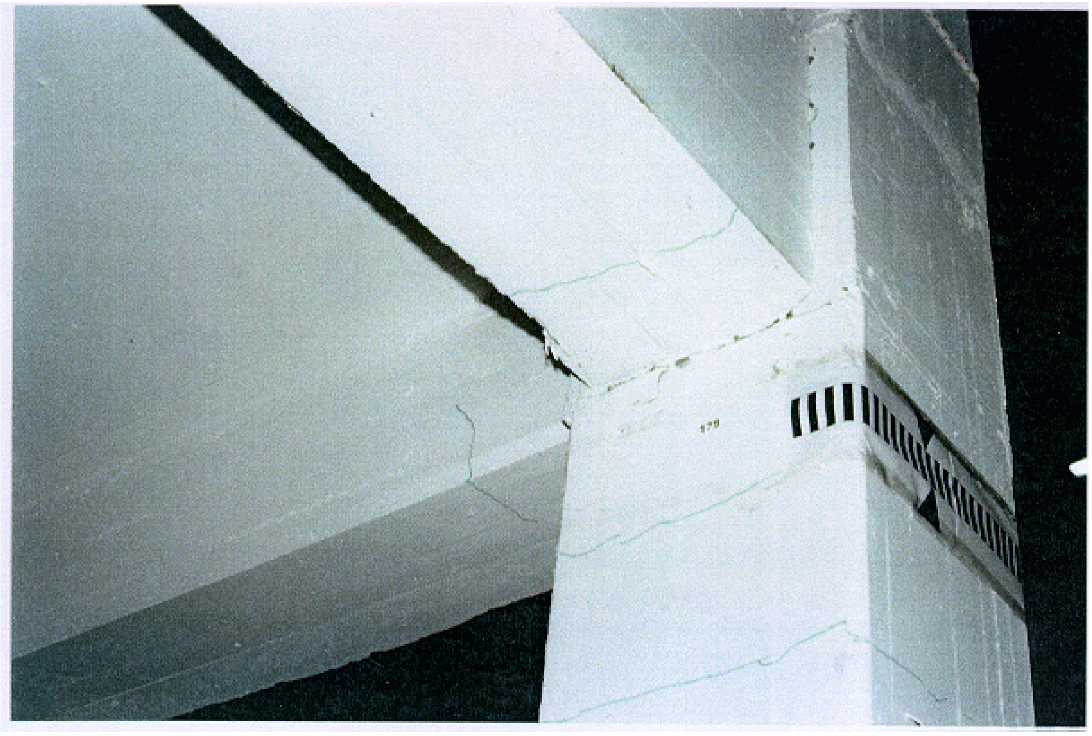

Figure B.9 - Flexural Cracking at Beams and Columns (taken from 4-14)

REFERENCES

1-1 J. Adams, (1973), "Non-Linear Behavior of Steel Frames," Ph.D. Dissertation, Department of Civil Engineering, Massachusetts Institute of Technology, Cambridge, MA.

1-2 S. H. Ahmad and Shah, (1982), "Stress-Strain Curves of Concrete Confined by Spiral Reinforcement," ACI Journal, Vol. 79, No. 6, pp. 484-490

1-3 P. Armendariz, (1995) "Behavior of High-Strength Concrete Structures under Seismic Loads," Ph.D. Dissertation, The University of Texas at Austin.

1-4 P. Armendariz, R. L. Carrasquillo and J. M. Roesset, (1996) "Behavior of High-Strength Concrete Structures under Seismic Loads," Paper No. 772, Eleventh World Conference on Earthquake Engineering, June 23-28, 1996, Acapulco, Mexico.

1-5 S. Kaba and S. A. Mahin, (1983), "Interactive Computer Analysis Methods for Predicting the Inelastic Cyclic Behaviour of Structural Sections," EERC Report No. 83/18, University of California, Berkeley.

1-6 S. Kaba and S. A. Mahin, (1984), "Refined Modeling of Reinforced Concrete Columns for Seismic Analysis," EERC Report No. 84/03, University of California, Berkeley.

1-7 W. Kim and L.-W. Lu, (1994), "Hysteretic Analysis and Modeling of Composite Beam-Columns," Proceedings of the Fifth U.S. National Conference on Earthquake Engineering, July 10-14, 1994, Chicago, Illinois, Vol. 1, pp. 273-282

1-8 R. W. Latona, (1970), "Non Linear Analysis of Building Frames for Earthquake Loading," Research Report R70-65, Department of Civil Engineering, Massachusetts Institute of Technology, Cambridge, MA.

1-9 P. Madas and A. S. Elnashai, (1992), "A New Passive Confinement Model for the Analysis of Concrete Structures Subjected to Cyclic and Transient Dynamic

Loading," Earthquake Engineering and Structural Dynamics, Vol. 21, No. 5. pp 409-431

1-10 J. B. Mander, M. J. N. Priestley and R. Park, (1988) "Theoretical Stress-Strain Model for Confined Concrete," Journal of Structural Engineering, ASCE, Vol. 114, No. 8. pp. 1804-1826

1-11 K. M. Mark, (1976), "Nonlinear Dynamic Response of Reinforced Concrete Frames," Ph.D. Dissertation, Department of Civil Engineering, Massachusetts Institute of Technology, Cambridge, MA.

1-12 Ch. G. Papaleontiou, (1992), "Dynamic Analysis of Building Structures Under Combined Horizontal and Vertical Vibrations," Ph.D. Dissertation, The University of Texas at Austin.

1-13 R. Park, D. C. Kent and R. A. Sampson, (1972) "Reinforced Concrete Members with Cyclic Loading," Journal of the Structural Division, ASCE, Vol. 98, No. ST7, pp. 1341-1360

1-14 R. Park and T. Paulay, (1975), "Reinforced Concrete Structures," John Wiley and Sons, New York, 769 pp.

1-15 R. M. Richard and B. J. Abbott, (1975) "Versatile Elastic-Plastic Stress-Strais Formula," Journal of the Engineering Mechanics Division, ASCE, Vol. 101, No. EM4. pp. 511-515

1-16 F. F. Taucer, E. Spacone and F. C. Filippou, (1991) "A Fiber Beam-Column Element for Seismic Response Analysis of Reinforced Concrete Structures," EERC Report No. 91/17, University of California, Berkeley.

1-17 C.-P. Yu, (1996), "Effect of Vertical Earthquake on Bridge Responses," Ph.D. Dissertation, The University of Texas at Austin.

1-18 C. A. Zeris and S. A. Mahin, (1988), “Analysis of Reinforced Concrete Beam-Columns Under Uniaxial Excitation,” Journal of Structural Engineering, ASCE, Vol. 114, No. 4. pp. 804-820

1-19 T.-Q. Zhou, T. Kabeyasawa and Y. Suenaga, (1990) “Inelastic Analytical Model for Reinforced Concrete Column Subjected to Tri-Axial Varying Loads,” Transactions of the Japan Concrete Institute, Vol. 12, pp 355-362

2-1 P. Armendariz, (1995) “Behavior of High-Strength Concrete Structures under Seismic Loads,” Ph.D. Dissertation, The University of Texas at Austin.

2-2 F. C. Filippou, E. P. Popov and V. V. Bertero, (1983) “Effects of Bond Deterioration on Hysteretic Behavior of Reinforced Concrete Joints,” EERC Report No. 83/19, University of California, Berkeley.

2-3 R. W. Latona, (1970), “Non Linear Analysis of Building Frames for Earthquake Loading,” Research Report R70-65, Department of Civil Engineering, Massachusetts Institute of Technology, Cambridge, MA.

2-4 J. B. Mander, M. J. N. Priestley and R. Park, (1988) “Theoretical Stress-Strain Model for Confined Concrete,” Journal of Structural Engineering, ASCE, Vol. 114, No. 8. pp. 1804-1826

2-5 F. M. Mazzolani and V. Piluso, (1996) “Theory and Design of Seismic Resistant Steel Frames,” W & FN Spon (Chapman & Hall), London, 497 pp.

2-6 M. Menegotto and P. E. Pinto, (1973) “Method of Analysis for Cyclically Loaded R.C. Plane Frames Including Changes in Geometry and Non-Elastic Behavior of Elements under Combined Normal Force and Bending,” IABSE Symposium on Resistance and Ultimate Deformability of Structures Acted on by Well-Defined Repeated Loads (Final Report), Lisbon, pp. 15-22.

2-7 M. Menegotto and P. E. Pinto, (1977) “Slender RC Compressed Members in Biaxial Bending,” Journal of the Structural Division, ASCE, Vol. 103, No. 3. pp. 587-605

2-8 J. F. Stanton and H. D. McNiven, (1979) “The Development of a Mathematical Model to Predict the Flexural Response of Reinforced Concrete Beams to Cyclic Loads, Using System Identification,” EERC Report No. 79/02, University of alifornia, Berkeley.

2-9 W. T. Tsai, (1987) “Uniaxial Compressional Stress-Strain Relation of Concrete,” Journal of Structural Engineering, ASCE, Vol. 114, No. 9. pp. 2133-2136

3-1 Advanced Structural Concepts, Inc., (1997), “NONLIN-Pro Version 2.00 User’s Manual,” Golden, Colorado.

3-2 R. Allahabadi and G. H. Powell, (1988), “DRAIN-2DX User Guide,” EERC Report No. 88/06, University of California, Berkeley.

3-3 P. Armendariz, (1995) “Behavior of High-Strength Concrete Structures under Seismic Loads,” Ph.D. Dissertation, The University of Texas at Austin.

3-4 A. E. Kanaan and G. H. Powell, (1973) “General Purpose Computer Program for Inelastic Dynamic Response of Plane Structures,” EERC Report No. 73/6, University of California, Berkeley.

3-5 S. K. Kunnath, A. M. Reinhorn and R. F. Lobo, (1992), “IDARC Version 3.0: A Program for the Inelastic Damage Analysis of Reinforced Concrete Structures,” Technical Report NCEER-92-0022 National Center for Earthquake Engineering Research, State University New York at Buffalo

3-6 S. K. Kunnath and A. M. Reinhorn, (1994), “IDARC2D Version 3.1: Inelastic Damage Analysis of RC Building Structures. General Version for Personal Computers, UNIX or VMS Systems. Users Manual,” National Center for Earthquake Engineering Research, State University New York at Buffalo

3-7 Ch. G. Papaleontiou, (1992), "Dynamic Analysis of Building Structures Under Combined Horizontal and Vertical Vibrations," Ph.D. Dissertation, The University of Texas at Austin.

3-8 Y. J. Park, A. M. Reinhorn and S. K. Kunnath (1987) "IDARC: Inelastic Damage Analysis of Reinforced Concrete Frame - Shear-Wall Structures," Technical Report NCEER-87-0008 National Center for Earthquake Engineering Research, State University New York at Buffalo

3-9 Powell, G. H., (1993) "DRAIN-2DX Element Description and User Guide for Element Type01, Type02, Type04, Type06, Type09, and Type15: Version 1.10," Report No. UCB/SEMM-93/18, Dept. of Civil Engineering, Univ. of California at Berkeley, Dec. 1993, 68 pages

3-10 V. Prakash, G. H. Powell and S. Campbell, (1993) "DRAIN-2DX Base Program Description and User Guide: Version 1.10," Report No. UCB/SEMM-93/17, Dept. of Civil Engineering, Univ. of California at Berkeley, Nov. 1993, 97 pages

3-11 R. E. Valles, A. M. Reinhorn, S. K. Kunnath, C. Li and A. Madan, (1996), "IDARC2D Version 4.0: A Computer Program for the Inelastic Damage Analysis of Buildings," Technical Report NCEER-96-0010 National Center for Earthquake Engineering Research, State University New York at Buffalo

4-1 D. Abrams, (1996) "Effects of Scale and Loading Rate with Tests of Concrete and Masonry Structures," Earthquake Spectra, Vol. 12, No. 1, pp. 13-28, Earthquake Engineering Research Institute, Oakland, CA

4-2 ACI Committee 318, (1995) "Building Code Requirements for Structural Concrete (ACI 318-95) and Commentary (ACI 318R-95)," American Concrete Institute, Farmington Hills, MI.

4-3 American Concrete Institute, (1985) "Earthquake Effects on Reinforced Concrete Structures, U.S.-Japan Research" ACI Publication SP-84, Detroit, 428 p.

4-4 P. Armendariz, (1995) “Behavior of High-Strength Concrete Structures under Seismic Loads,” Ph.D. Dissertation, The University of Texas at Austin.

4-5 H. Aoyama, (1964) “Moment-Curvature Characteristics of Reinforced Concrete Members Subjected to Axial Load and Reversal of Bending,” Proceedings of the International Symposium on Flexural Mechanics of Reinforced Concrete, Miami, Nov. 1964, Publication ACI SP-12 (and ASCE-1965-50), pp. 183-212

4.6 Computers and Structures, Inc., (1997) “SAP2000: Integrated Finite Element Analysis and Design of Structures. Version 6.1,” Berkeley, CA.

4-7 J. Donea, G. Magonette, P. Negro, P. Pegon, A. Pinto and G. Verzeletti, (1996) “Pseudo-dynamic Capabilities of the ELSA Laboratory for Earthquake Testing of Large Structures,” Earthquake Spectra, Vol. 12, No. 1, pp. 163-180, Earthquake Engineering Research Institute, Oakland, CA

4-8 M. O. Eberhard and M. L. Marsh (1997) "Lateral-Load Response of a Reinforced Concrete Bridge," Journal of Structural Engineering, ASCE, Vol. 123, No. 4, pp. 451-460

4-9 M. O. Eberhard and M. L. Marsh (1997) "Lateral-Load Response of Two Reinforced Concrete Bents," Journal of Structural Engineering, ASCE, Vol. 123, No. 4, pp. 461-468

4-10 M. B. Emara, (1990) “Shear Deformations in Reinforced Concrete Frames,” MS Thesis, Department of Civil Engineering, University of Toronto.

4-11 D. L. Hanks, (1988) “Cyclic Behavior of High Strength Concrete Beams,” MSc Thesis, Department of Civil Engineering, University of Kansas, Lawrence, KS, 120 pp.

4-12 P. Negro, A. V. Pinto, G. Verzeletti and G. E. Magonette, (1996) “PsD Test on Four-Story R/C Building Designed According to Eurocodes,” Journal of Structural Engineering, ASCE, Vol. 122, No. 12, pp. 1409-1417

4-13 P. Negro and G. Verzeletti, (1996) “Effect of Infills on the Global Behaviour of R/C Frames: Energy Considerations from Pseudo-dynamic Tests,” Earthquake Engineering and Structural Dynamics, Vol. 25, pp. 753-773

4-14 P. Negro, G. Verzeletti, G. E. Magonette, and A. V. Pinto, (1994) “Tests on a Four-Storey Full-Scale R/C Frame Designed According to Eurocodes 8 and 2: Preliminary Report,” Report EUR 15879 EN, Joint Research Center of the European Commission, Ispra, Italy, 80 pp.

4-15 R. Park, D. C. Kent and R. A. Sampson, (1972) “Reinforced Concrete Members with Cyclic Loading,” Journal of the Structural Division, ASCE, Vol. 98, No. ST7, pp. 1341-1360

4-16 R. Park and T. Paulay, (1975), “Reinforced Concrete Structures,” John Wiley and Sons, New York, 769 pp.

4-17 M. Pipa and E. C. Carvalho, (1995), “Reinforcing Steel Characteristics for Earthquake Resistant Structures,” in G. Duma (Ed.), “Proceedings of the 10th European Conference on Earthquake Engineering,” Vol. 4 (pp. 2887-2892), Vienna, Austria.

4-18 M. Pipa, E. C. Carvalho and A. Otes, (1995), “Experimental Behaviour of R/C beams with Grade 500 Steel,” in G. Duma (Ed.), “Proceedings of the 10th European Conference on Earthquake Engineering,” Vol. 3 (pp. 2405-2411), Vienna, Austria.

4-19 E. P. Popov, V. V. Bertero and H. Krawinkler, (1972) “Cyclic Behavior of Three R. C. Flexural Members with High Shear,” Report No. EERC 72-5, Earthquake Engineering Research Center, University of California at Berkeley, Oct. 1972, 78 pp

4-20 F. Seible, G. Hegemier and A. Igarashi, (1996) “Simulated Seismic Laboratory Testing of Full-Scale Buildings,” Earthquake Spectra, Vol. 12, No. 1, pp. 57-85, Earthquake Engineering Research Institute, Oakland, CA

4-21 F. J. Vecchio and M. B. Emara, (1992) “Shear Deformations in Reinforced Concrete Frames,” ACI Structural Journal, Vol. 89, No. 1, pp. 46-56

4-22 G. J. Volio, (1980), "Effect of Modifications in Story Strength of the Inelastic Dynamic Response of Frame Structures," M.S.E. Thesis, The University of Texas at Austin.

4.23 Computers and Structures, Inc., (1993) "ETABS: Three Dimensional Analysis of Building Systems. Educational Version 5.41," Berkeley, CA.

5-1 G. A. Chang and J. B. Mander, (1994) "Seismic Energy Based Fatigue Damage Analysis of Bridge Columns: Part I - Evaluation of Seismic Capacity," Technical Report NCEER-94-0006 National Center for Earthquake Engineering Research, State University New York at Buffalo

5-2 M. P. Collins and D. Mitchell, (1991) "Prestressed Concrete Structures," Prentice-Hall, Englewood Cliffs, New Jersey.

5-3 T. T. C. Hsu, (1993) "Unified Theory of Reinforced Concrete," CRC Press, Boca Raton, Florida.

5-4 P. Marti and J. Meyboom, (1992) "Response of Prestressed Concrete Elements to In-Plane Shear Forces," ACI Structural Journal, Vol. 89, No. 5, pp. 503-514

5-5 Y. J. Park, A. H-S. Ang and Y. K. Wen, (1984) "Seismic Damage Analysis and Damage-Limiting Design of R/C Buildings," Civil Engineering Studies , SRS No. 516, University of Illinois, Urbana, Illinois.

5-6 Y. J. Park, A. M. Reinhorn and S. K. Kunnath (1987) "IDARC: Inelastic Damage Analysis of Reinforced Concrete Frame - Shear-Wall Structures," Technical Report NCEER-87-0008 National Center for Earthquake Engineering Research, State University New York at Buffalo

5-7 R. Park and T. Paulay, (1975), "Reinforced Concrete Structures," John Wiley and Sons, New York, 769 pp.

5-8 G. H. Powell, F. Filippou, K. Martini and S. Campbell, (1992)..”Nonlinear Modeling and Analysis of Reinforced Concrete Frame Structures,” in F. Y. Cheng & F. Zizhi (Eds.), “Computational Mechanics in Structural Engineering: Recent Developments and Future Trends,” (pp. 260-272), Elsevier Applied Science, London.

5-9 F. J. Vecchio and M. P. Collins, (1986) “The Modified Compression Field Theory for Reinforced Concrete Elements Subjected to Shear,” ACI Structural Journal, Vol. 83, No. 2, pp. 219-231

5-10 F. J. Vecchio and M. P. Collins, (1988) “Predicting the Response of Reinforced Concrete Beams Subjected to Shear Using Modified Compression Field Theory,” ACI Structural Journal, Vol. 85, No. 3, pp. 258-268

5-11 F. J. Vecchio and M. B. Emara, (1992) “Shear Deformations in Reinforced Concrete Frames,” ACI Structural Journal, Vol. 89, No. 1, pp. 46-56

6-1 J. M. Alsiwat and M. Saatcioglu, (1992) “Reinforcement Anchorage Slip Under Monotonic Loading,” Journal of the Structural Division, ASCE, Vol. 118, No. 9, pp. 2421-2438

6-2 V. Ciampi, R. Eligehausen, V. V. Bertero and E. P. Popov, (1982) “Analytical Model for Concrete Anchorages of Reinforcing Bars Under Generalized Excitations,” EERC Report No. 82/23, University of California, Berkeley.

6-3 R. Eligehausen, E. P. Popov and V. V. Bertero, (1983) “Local Bond Stress-Slip Relationships of Deformed Bars Under Generalized Excitations,” EERC Report No. 83/23, University of California, Berkeley.

6-4 F. C. Filippou, (1983) “Effects of Bond Deterioration on Seismic Response of Reinforced Concrete Frames,” Ph.D. Dissertation, University of California, Berkeley.

6-5 F. C. Filippou, (1985) “A Simple Model for Reinforcing Bar Anchorages under Cyclic Excitations,” EERC Report No. 85/05, University of California, Berkeley.

6-6 F. C. Filippou and A.Issa, (1988) “Nonlinear Analysis of Reinforced Concrete Frames under Cyclic Load Reversals,” EERC Report No. 88/12, University of California, Berkeley.

6-7 F. C. Filippou, E. P. Popov and V. V. Bertero, (1983) “Effects of Bond Deterioration on Hysteretic Behavior of Reinforced Concrete Joints,” EERC Report No. 83/19, University of California, Berkeley.

6-8 F. C. Filippou and N. Zulfiqar, (1992) “Models of Critical Regions and Their Effect on the Seismic Response of Reinforced Concrete Frames,” Tenth World Conference on Earthquake Engineering, July 19-24, 1992, Madrid, Spain. Balkema, Rotterdam, pp. 4221-4226

6-9 T. Kaku and H. Asakusa, (1991) “Bond and Anchorage of Bars in Reinforced Concrete Beam-Column Joints,” in J. O. Jirsa (Ed.), “Design of Beam-Column Joints for Seismic Resistance” (pp. 401-423) American Concrete Institute SP-123, Detroit.

6-10 G. Monti, E. Spacone and F. C. Filippou, (1993) “Model for Anchored Reinforcing Bars under Seismic Excitations,” EERC Report No. 93/08, University of California, Berkeley.

6-11 M. Saatcioglu and J. M. Alsiwat, (1996) “Significance of Anchorage Slip on Dynamic Inelastic Response of R/C Frame Structures,” Paper No. 1854, Eleventh World Conference on Earthquake Engineering, June 23-28, 1996, Acapulco, Mexico

6-12 M. Saatcioglu, J. M. Alsiwat and G. Ozcebe, (1992) “Hysteretic Behavior of Anchorage Slip in R/C Members,” Journal of the Structural Division, ASCE, Vol. 118, No. 9, pp. 2439-2458

6-13 T. Tada, (1987) “Bond Deterioration in Reinforced Concrete Members Subjected to Seismic Loading,” IABSE Colloquium Delft 1987: Computational Mechanics of Concrete Structures — Advances and Applications, IABSE reports Vol. 54, Zurich, Switzerland, pp. 539-545

6-14 T. Tada and T. Takeda, (1991) “Analysis of Bond Deterioration Process in Reinforced Concrete Beam-Column Joints Subjected to Seismic Loading,” in J. O. Jirsa (Ed.), “Design of Beam-Column Joints for Seismic Resistance” (pp. 443-464) American Concrete Institute SP-123, Detroit.